THESIS FOR THE DEGREE OF DOCTOR OF PHILOSOPHY

Power System Stability Enhancement Using Shunt-connected Power Electronic Devices with Active Power Injection Capability

MEBTU BEZA

Department of Energy and Environment
Division of Electric Power Engineering
CHALMERS UNIVERSITY OF TECHNOLOGY
Gothenburg, Sweden, 2015

Power System Stability Enhancement Using Shunt-connected Power Electronic Devices with Active Power Injection Capability
MEBTU BEZA
ISBN 978-91-7597-139-1

Doktorsavhandlingar vid Chalmers Tekniska Högskola
Ny serie nr. 3820
ISSN 0346-718X

Department of Energy and Environment
Division of Electric Power Engineering
Chalmers University of Technology
SE–412 96 Gothenburg
Sweden
Telephone +46 (0)31–772 1000

Printed by Chalmers Reproservice
Gothenburg, Sweden, 2015

Power System Stability Enhancement Using Shunt-connected Power Electronic Devices with Active Power Injection Capability
MEBTU BEZA
Department of Energy and Environment
Chalmers University of Technology

Abstract

Power electronic devices such as Flexible AC Transmission Systems (FACTS), both in shunt and series configuration, are widely used in the power system for power flow control, to increase the loading capability of an existing line and to increase the security of the system by enhancing its transient stability. Among the shunt-connected FACTS controllers family, the Static Synchronous Compensator (STATCOM) and the Static Var Compensator (SVC) are two key devices for reinforcing the stability of the AC power system. Among other functions, these devices provide transient stability enhancement (TSE) and Power Oscillation Damping (POD) functions by controlling the voltage at the Point of Common Coupling (PCC) by using reactive power injection.

This thesis investigates the application of shunt-connected power electronic devices with optional active power injection capability to improve the dynamic performance of the power system. In particular, the focus of the work will be on developing an effective POD and TSE control algorithm using local measurements. The selection of local signals to maximize the effectiveness of active and reactive power for the intended stability enhancement purpose is described. To implement the control methods, an estimation technique based on a modified Recursive Least Square (RLS) algorithm that extracts the required signal components from measured signals is developed. The estimation method provides a fast, selective and adaptive estimation of the low-frequency electromechanical oscillatory components during power system disturbances. This allows to develop an independent multimode POD controller, which enables the use of multiple compensators without any risk of negative interaction between themselves. With the proposed selection of local signals together with the estimation method, it is shown that the use of active power injection can be minimized at points in the power system where its impact on stability enhancement is negligible. This leads to an economical use of the available energy storage. Finally, the performance of the POD and TSE controllers is validated both via simulation and through experimental verification using various power system configurations. The robustness of the POD controller algorithm against system parameter changes is verified through the tests. With the proposed control methods, effective stability enhancement is achieved through the use of single or multiple compensators connected at various locations in the power system.

Index Terms: Adaptive estimation, energy storage, FACTS, Power Oscillation Damping (POD), Recursive Least Square (RLS), Static Synchronous Compensator (STATCOM), Static Var Compensator (SVC), Transient Stability Enhancement (TSE).

Acknowledgments

My sincere gratitude goes to my main supervisor Assoc. Prof. Massimo Bongiorno for his exemplary guidance and useful insight to the project, his motivation and patience for exhaustively reviewing various manuscripts, especially during late evenings and weekends. I admire the attention he gives to details, which might have been grueling at times but rewarding. I would also like to thank my examiner and assistant supervisor Prof. Torbjörn Thiringer for reviewing the thesis, his all-round help whenever needed and his very friendly treatment at various occasions in the division. I appreciate the encouragement and friendship from my supervisors that have made the working environment enjoyable.

This work has been funded by Energimyndigheten, project number P37677-1/36145. The first part of the project has been carried out within the Elektra Project 36075. The financial support from Energimyndigheten and the sponsoring companies is greatly appreciated. I would also like to thank Sven Jansson from ELFORSK AB for the continuous support during the project application.

My acknowledgments go to members of the reference group: Dr. Jean-Philippe Hasler (ABB Power Technologies FACTS), Dr. Katherine Elkington (SvK), Prof. Lennart Ängquist (KTH) and Prof. Per Norberg (Vattenfall) for the nice discussions and inputs through the course of the project. I would also like to thank the former reference group members Dr. Tomas Larsson (ABB Power Technologies FACTS) and Dr. Johan Setreus (SvK) for their inputs.

I am grateful to Magnus Ellsen, Aleksander Bartnicki and Robert Karlsson for the help in the various practical issues while working in the laboratory. I would also like to thank Mattias Persson for his help in the laboratory every time I needed an extra hand. Many thanks go to all members at the division for a very friendly working environment and my roommates for making the office an enjoyable place to work.

Finally, I would like to thank my family and friends for the continuous support during the past few years.

Mebtu Beza
Gothenburg, Sweden
January, 2015

List of Acronyms

PSS	Power System Stabilizer
FACTS	Flexible AC Transmission System
TCSC	Thyristor Controlled Series Capacitor
SSSC	Static Synchronous Series Compensator
STATCOM	Static Synchronous Compensator
SVC	Static Var Compensator
E-STATCOM	Static Synchronous Compensator with Energy Storage
VSC	Voltage Source Converter
POD	Power Oscillation Damping
TSE	Transient Stability Enhancement
VI	Virtual Inertia
LPF	Low-pass Filter
RLS	Recursive Least Square
PLL	Phase-Locked Loop
PCC	Point of Common Coupling
PWM	Pulse Width Modulation
FFT	Fast Fourier Transform

Contents

Chapter 1

Introduction

1.1 Background and motivation

The continuous growth of the electrical system (especially, of large loads like industrial plants) results in that today's transmission systems are used close to their stability limits. Due to political, economic and environmental reasons, it is not always possible to build new transmission lines to relieve the overloaded lines and provide sufficient transient stability margin [1][2]. In this regard, the use of Power Electronic Devices in the transmission system can help to use the existing facilities more efficiently and improve the stability of the power system against low-frequency electromechanical disturbances [3][4]. To increase the stability of the power system against these disturbances, FACTS controllers both in series [5][6] and shunt [7][8] configuration have been used. In the specific case of shunt-connected FACTS controllers, such as a Static Synchronous Compensator (STATCOM) and Static Var Compensator (SVC), Transient Stability Enhancement (TSE) and Power Oscillation Damping (POD) can be achieved by controlling the voltage at the Point of Common Coupling (PCC) using reactive power injection. However, one drawback of the shunt configuration for this kind of applications is that the voltage at the PCC should be varied up to a limited extent around the nominal voltage and this reduces the amount of stability enhancement that can be provided by the compensator. Moreover, the amount of injected reactive power to impact the PCC voltage depends on the short-circuit impedance seen by the compensator at the PCC. On the other hand, injection of active power affects the PCC voltage angle without varying the voltage magnitude significantly; therefore, this could be a better alternative for enhancing system stability in some cases. One example of this is when a compensator is connected close to generators and a load area [9]. The characteristics of loads usually depend on the voltage magnitude and their impact to interact with compensators and is less significant when active power injection is used for stability enhancement [10].

Among the shunt-connected power electronic devices, a STATCOM has been applied both at distribution level to mitigate power quality phenomena and at transmission level for voltage control and increasing the transient stability of the power system [11][12]. Although typically used for reactive power injection only, by equipping the STATCOM with an energy storage connected to the DC-link of the converter (here named E-STATCOM), a more flexible control of the transmission system can be achieved [13][14][15]. An installation of a STATCOM with energy storage is already found in the UK for power flow management and voltage control [16][17]. In addition, the introduction of wind energy and other distributed generations will pave the way for more energy storage into the power system and auxiliary stability enhancement function is possible from those power electronic equipped energy sources [18][19]. Because injection of active power is used temporarily during transient, incorporating the stability enhancement functions in systems where active power injection is primarily used for other purposes [20] could be an attractive solution. Another application where the availability of active power can be used is to mimic the mechanical behavior of a synchronous machine in the control algorithms of the power electronic device. This helps to add inertia effect to the power system and hence it can increase the stability of the power system [21][22].

Possible applications of shunt-connected power electronic devices with active power injection capability in the power system has been studied and presented in literature, for instance in [23][24][25]. One such device is the E-STATCOM and its control for power system stability enhancement has been proposed. In those works, the impact of the location of the E-STATCOM on its dynamic performance is typically not treated. When using active power for stability enhancement, the location of the compensator has an impact on the size of the energy storage required and hence the cost of the FACTS device. Moreover, the proposed POD control structure for the device is similar to the one utilized for PSS [26], where a series of wash-out and lead-lag filter links are used to generate the control input signals. However, this kind of control action is effective only at the operating point where the design of the filter links is optimized and its speed of response is limited by the frequency of the electromechanical oscillations. The problem becomes more significant when more than one oscillatory mode is excited in the power system and a proper separation of the frequency components is required.

The use of single FACTS controllers for damping of multiple low-frequency oscillations has been described in the literature [11][27], where the design procedure involves the use of carefully tuned wash-out and lead-lag filter links to provide damping at a particular oscillation frequency. The use of multiple compensators has been described in [28][29], where each FACTS device is coordinately designed to maximize the damping of a particular oscillation mode of interest. As described previously, these tuned-filter links provide accurate phase compensation for damping at the correct oscillation frequency and their performance highly depends on the knowledge of the system parameters. Moreover, the designed filters at a particular frequency of interest could worsen the damping of the system at other critical oscillation modes that might be excited in the system. Hence, a complicated coordinated design of the POD controllers is usually necessary when multiple compensators are to be implemented in the power system [30][31].

When an electromechanical disturbance occurs in the power system, the transient stability of the system should be prioritized. To aid in this, a TSE controller for the E-STATCOM will be developed in this thesis. When the active power injection capability is available, the transient stability enhancement that can be added to the power system will also be investigated through two different control approaches. Once the transient stability of the power system is guaranteed, a POD controller is used to damp poorly-damped power oscillations. For this purpose, a modified Recursive Least Square (RLS) based algorithm that provides a selective and adaptive estimation of the oscillatory modes from local measurements will be developed for designing an independent multimode POD controller. By using the estimate of each oscillation mode in the control structure, the injected active and reactive power from the compensators will consist of only the frequency of the oscillation mode to be damped. This minimizes the needed active and reactive power to damp a particular oscillation mode. As the performance of the damping controller on the various modes is decoupled with this method, multiple compensators that are designed to damp a particular oscillation mode results in a net additive damping, and hence avoiding any risk of negative interaction between themselves. This also helps to avoid the need for a coordinated design and hence simplify the design stage when various compensators are used together in the power system. Finally, the different control strategies will be validated through simulation and experiments.

1.2 Purpose of the thesis and main contributions

The purpose of the thesis is to investigate the application of shunt-connected power electronic devices with active power injection capability to the transmission system. The ultimate goal is to design an effective controller to achieve power system stability enhancement function such as POD and TSE using single and multiple compensators. To the best of the author's knowledge, the main contributions of the thesis are summarized below.

- A modified Recursive Least Square (RLS) based estimation algorithm for low-frequency oscillation estimation in power systems has been developed. A variable forgetting factor and a frequency adaptation mechanism has been added to the conventional RLS algorithm in order to achieve a fast transient estimation together with a selective and adaptive steady-state estimation. (Papers I and VII)

- An adaptive POD controller for an E-STATCOM has been designed. For this, the modified RLS algorithm has been used to obtain a fast, selective and adaptive estimation of the low-frequency electromechanical oscillations from locally measured signals during power system disturbances. The POD controller is robust against system parameter changes and stability enhancement is provided at oscillation frequencies of interest irrespective of the connection point of the E-STATCOM with optimum use of the available active power. (Papers II and VIII)

- The modified RLS algorithm has been adapted for a generic signal estimation such as sequence and harmonic estimation in both single and three-phase systems. This helps to achieve a fast, selective and adaptive estimation of the various frequency components. (Papers III and IX)

- Using the sequence and harmonic estimation by the modified RLS algorithm, a modification to the current controller for a VSC connected to a distorted grid is proposed and its effectiveness has been demonstrated. The modification helps to avoid the exchange of harmonic or unbalanced currents between the VSC and the grid. (Paper IV)

- The impact of different static loads on the performance of a POD controller by shunt-connected FACTS devices has been investigated. From the results of the analysis, a recommendation has been suggested on the use of active and reactive power for POD when the compensator is connected close to a load area. (Paper V)

- An independent multimode oscillation damping controller for single or multiple shunt-connected FACTS devices has been proposed and its benefits have been proven. With an adaptive and selective estimation of the critical oscillation modes of interest, the control method enables to damp a particular oscillation mode of interest without affecting the damping of the system at other oscillation modes, even in the presence of system parameter uncertainties. An accurate estimate of each oscillation mode also enables the use of multiple compensators without risk of interactions between themselves. (Papers VI and X)

- Two control approaches for the E-STATCOM when using its active power injection capability have been investigated and compared. Based on the advantages and disadvantages of the two methods, a recommendation is made on the use of active power for transient stability enhancement. (Paper XI)

1.3 Structure of the thesis

The thesis is organized into eight chapters with the first chapter describing the background information, motivation and contribution of the thesis. Chapters 2 and 3 give a theoretical base on problems of power system dynamics and the strategies used to improve power system stability. Chapter 2 briefly discusses stability of the power system using a simplified single-machine infinite-bus system and Chapter 3 describes the application of FACTS controllers, both in series and shunt configuration, in power systems. Among the shunt-connected FACTS controllers, the E-STATCOM, which will be the focus of the thesis, will also be described briefly. Chapters 4 to 7 represent the main body of the thesis. Chapter 4 discusses a generic signal estimation algorithm based on an RLS algorithm with variable forgetting factor. Its application for specific examples is included with validation using simulation and experiments. Chapter 5 describes the overall control structure for the E-STATCOM with more focus on the inner vector current controller. A method to improve the current controller performance in case of distorted grids is developed using the results in Chapter 4. The chapter concludes with simulation and experimental verification of the theoretical analysis. Chapters 6 and 7 address the main objective of the work, where the application of the E-STATCOM for stability enhancement such as power oscillation damping and transient stability enhancement are investigated. The POD and TSE controllers will be derived using a simplified power system in Chapter 6 and verification of the control methods using simulations and experimental tests will be made in Chapter 7. Finally, the thesis concludes with a summary of the results achieved and plans for future work in Chapter 8.

1.4 List of publications

The Ph.D. project has resulted in the following publications which constitute the majority of the thesis.

I. M. Beza and M. Bongiorno, ”A fast estimation algorithm for low-frequency oscillations in power systems,” in *Proc. of Power Electronics and Applications (EPE 2011), Proceedings of the 2011*-14^{th} *European Conference on*, pp. 1-10, Aug. 30 2011-Sept. 1 2011.

II. M. Beza and M. Bongiorno, ”Power oscillation damping controller by static synchronous compensator with energy storage,” in *Proc. of Energy Conversion Congress and Exposition (ECCE), 2011 IEEE*, pp. 2977-2984, 17-22 Sept. 2011.

III. M. Beza and M. Bongiorno, M., ”Application of Recursive Least Square (RLS) algorithm with variable forgetting factor for frequency components estimation in a generic input signal,” in *Proc. of Energy Conversion Congress and Exposition (ECCE), 2012 IEEE*, pp. 2164-2171, 15-20 Sept. 2012.

IV. M. Beza and M. Bongiorno, ”Improved discrete current controller for grid-connected voltage source converters in distorted grids,” in *Proc. of Energy Conversion Congress and Exposition (ECCE), 2012 IEEE*, pp. 77-84, 15-20 Sept. 2012.

V. M. Beza and M. Bongiorno, ”Impact of different static load characteristics on power oscillation damping by shunt-connected FACTS devices,” in *Proc. of Power Electronics and Applications (EPE), 2013* 15^{th} *European Conference on*, pp. 1-10, 2-6 Sept. 2013.

VI. M. Beza and M. Bongiorno, ”Independent Damping Control of Multimode Low-frequency Oscillations using Shunt-connected FACTS devices in Power System,” in *Proc. of Energy Conversion Congress and Exposition (ECCE), 2014 IEEE*, pp.716,723, 14-18 Sept. 2014.

VII. M. Beza and M. Bongiorno, ”A Modified RLS Algorithm for Online Estimation of Low-frequency Oscillations in Power Systems,” submitted to *IEEE Trans. Power Syst.*

VIII. M. Beza and M. Bongiorno, ”An Adaptive Power Oscillation Damping Controller by STATCOM With Energy Storage,” *IEEE Trans. Power Syst.*, vol.30, no.1, pp. 484-493, Jan. 2015.

IX. M. Beza and M. Bongiorno, ”Application of Recursive Least Squares Algorithm With Variable Forgetting Factor for Frequency Component Estimation in a Generic Input Signal,” *IEEE Trans. Ind. Appl.*, vol.50, no.2, pp. 1168-1176, March-April 2014.

X. M. Beza and M. Bongiorno, ”Independent Damping Control of Multimode Low-frequency Oscillations using Shunt-connected FACTS devices in Power System,” submitted to *IEEE Trans. Ind. Appl.*

XI. M. Beza and M. Bongiorno, ”Comparison of Two Control Approaches for Stability Enhancement Using STATCOM with Active Power Injection Capability,” submitted to *Proc. of IEEE Energy Conversion Congress and Exposition (ECCE), 2015*.

The author has also contributed to the following publications.

1. M. Beza and S. Norrga, ”Three-level converters with selective Harmonic Elimination PWM for HVDC application,” in *Proc. of Energy Conversion Congress and Exposition (ECCE), 2010 IEEE*, pp. 3746-3753, 12-16 Sept. 2010.

Chapter 2

Power system modeling and dynamics

2.1 Introduction

To study the dynamics of the electric power system, modeling of the different power system components such as synchronous generators, transmission lines, various loads and controllable devices is necessary. While the impact of each component on the power system dynamics is described in later chapters, a simplified model will be developed in this chapter to ease understanding the nature of power system dynamics. The simplified models will be used later in this thesis to derive the control algorithms.

2.2 Simplified model of power system components

A brief description of simplified models of some of the main power system components for power system stability studies will be given in this section. This comprises of synchronous generator, transmission network, loads and FACTS devices.

2.2.1 Synchronous generator

Depending on the type of study to be performed, the level of detail in the synchronous generator model varies greatly. Besides the stator and rotor flux dynamics in the model of the synchronous generator, Automatic Voltage Regulators (AVR) and Power System Stabilizers (PSS) can also be included. With the assumption that the rotor flux in a generator changes slowly following a disturbance in the time frame of transient studies [26], a constant flux model (so called *classical model*) of a synchronous generator is adopted in this section. In this model, the rotor flux dynamics are neglected and the synchronous generator is represented by a voltage source of constant magnitude V_{g} and dynamic rotor angle δ_{g} behind a transient impedance X'_{d}. The voltage V_{g} represents the internal voltage magnitude of the synchronous generator just before the disturbance. As described in [32], including the rotor flux dynamics does not impact the low-frequency electromechanical oscillation significantly for the intended study. A damping torque component is provided while the synchronizing torque component is reduced slightly when compared to the case with constant rotor flux model. This provides a conservative approach for the design of the controllers in the following chapters.

In addition to the electrical quantities, the implemented model of the synchronous generator includes the mechanical dynamics. In case of unbalances between the mechanical and the electrical torque acting on the rotor of a synchronous generator, the electromechanical dynamics is described by the equation of motion [26], expressed in per-unit (pu) as

$$\begin{aligned} 2H_{\mathrm{g}}\tfrac{d\omega_{\mathrm{g}}}{dt} &= T_{\mathrm{m}} - T_{\mathrm{g}} - K_{\mathrm{Dm}}\omega_{\mathrm{g}} \\ \tfrac{d\delta_{\mathrm{g}}}{dt} &= \omega_0\omega_{\mathrm{g}} - \omega_0 \end{aligned} \tag{2.1}$$

where ω_{g}, K_{Dm}, T_{m} and T_{g} represent the angular speed, mechanical damping torque coefficient, mechanical torque input and electrical torque output of the generator, respectively. The inertia time constant of the generator system expressed in seconds is denoted as H_{g}. The angle δ_{g} represents the angular position of the generator rotor with respect to a reference frame rotating at constant frequency of ω_0. Note that the expression for the electrical torque of the generator T_{g} depends on the model used for the synchronous generator, the parameters of the transmission network and other power system components and this greatly affects the power system dynamics, as it will be described in the following.

2.2.2 Transmission network

A transmission system comprises of components such as transmission lines, transformers, series and shunt capacitors and shunt reactors. For the purpose of transient stability studies, the model of these components is represented by their steady-state equivalent impedances. As an example, a simplified transmission system where a synchronous generator is connected to an infinite bus (characterized by a constant voltage $\underline{V}_{\mathrm{i}}$ and frequency ω_0) is shown in Fig. 2.1. The transmission system is represented by two transformers with leakage reactances $[X_{\mathrm{t1}}, X_{\mathrm{t2}}]$ and a transmission line with resistance R_{L} and reactance X_{L} at nominal frequency.

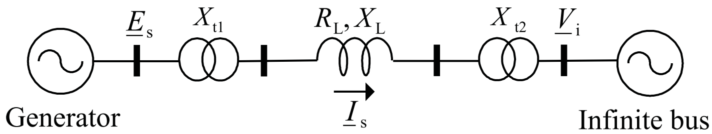

Fig. 2.1 Single line diagram of a synchronous generator connected to an infinite bus.

Considering the system in Fig. 2.1, the steady-state relation between the terminal voltages of the transmission system is described as

$$\underline{E}_{\mathrm{s}} = \underline{V}_{\mathrm{i}} + (R_{\mathrm{L}} + jX_{\mathrm{e}})\underline{I}_{\mathrm{s}} \tag{2.2}$$

where

$$X_{\mathrm{e}} = X_{\mathrm{t1}} + X_{\mathrm{L}} + X_{\mathrm{t2}}$$

Using the steady-state relations for the transmission system in question, the active power output from the generator (P_{g}) in Fig. 2.1 can be derived as

$$P_{\mathrm{g}} = \mathrm{Real}\left[\underline{E}_{\mathrm{s}}\underline{I}_{\mathrm{s}}^{*}\right] \tag{2.3}$$

2.2.3 Power system loads

Loads constitute a major part of the power system and their characteristics greatly influence the stable operation of the system. For this purpose, the various load types in the power system are modeled as [33][34]

$$\begin{aligned} P_{\mathrm{L}} &= P_{\mathrm{L0}}\left[p_1\left(\frac{V_{\mathrm{L}}}{V_{\mathrm{L0}}}\right)^{m_1} + p_2\left(\frac{V_{\mathrm{L}}}{V_{\mathrm{L0}}}\right)^{m_2} + p_3\left(\frac{V_{\mathrm{L}}}{V_{\mathrm{L0}}}\right)^{m_3}\right] \\ Q_{\mathrm{L}} &= Q_{\mathrm{L0}}\left[q_1\left(\frac{V_{\mathrm{L}}}{V_{\mathrm{L0}}}\right)^{n_1} + q_2\left(\frac{V_{\mathrm{L}}}{V_{\mathrm{L0}}}\right)^{n_2} + q_3\left(\frac{V_{\mathrm{L}}}{V_{\mathrm{L0}}}\right)^{n_3}\right] \end{aligned} \tag{2.4}$$

where P_{L} and Q_{L} represent the total active and reactive power of the load, respectively. The corresponding steady-state values at nominal load voltage V_{L0} are given by P_{L0} and Q_{L0}. As the change in the frequency of the system is very small for transient stability studies [26], the frequency dependency of the loads is neglected in the load model. The exponents m_{i} and n_{i} with i = [1,3] can be chosen to represent different load types and the contribution of each load type to the total load is represented by the parameters p_{i} and q_{i}. By combining loads with different exponents, a wide range of loads can be represented well by the model in (2.4) for transient stability studies.

2.2.4 Controllable devices

Various power electronic equipped controllable devices such as FACTS controllers and HVDC systems exist in today's transmission systems [1]. In addition, the integration of energy sources such as wind and other types of distributed generation units in the power system employ some power electronics in their structure [18]. Therefore, by utilizing their existing hardware and with a proper control system, these devices can help to improve stability of the power system. The model of these devices to study power system stability varies depending on the specific device considered and this will be described in the next chapter with focus on FACTS.

2.3 Simplified model for large system

While a complete model of the various components in a large power system can be used during time-domain simulations, a simplified model representation is needed for the purpose of controller design. For this purpose, the *classical model* is used for the various generators in the large power system and the electromechanical dynamics for the i^{th} generator is given by

$$\begin{aligned} 2H_{\text{g}i}\frac{d\omega_{\text{g}i}}{dt} &= T_{\text{m}i} - T_{\text{g}i} - K_{\text{Dm}i}\omega_i \\ \frac{d\delta_{\text{g}i}}{dt} &= \omega_0\omega_{\text{g}i} - \omega_0 \end{aligned} \tag{2.5}$$

where the subscript i indicates that all parameters in the model are related to the i^{th} generator. With the transmission system represented by their equivalent steady-state impedances and the generators by a voltage source of constant magnitude and dynamic rotor angle, the output active power and hence the output electrical torque of the i^{th} generator ($T_{\text{g}i}$) is calculated from the power flow equations. The expression of the electrical torque output of each generator depends on the network configuration, the available loads and controllable objects. Similarly, the various loads and controllable objects in a large power system can also be modeled separately where each component model is interrelated to one another thought the transmission network equation. By linearizing around a steady-state operating point, the small-signal stability of the whole system can be studied, as it will be shown in later chapters.

2.4 Power system dynamics

The model of a simplified transmission system is developed in this section to describe the phenomena of power system stability. For this, the system in Fig. 2.1 which consists of a synchronous generator connected to an infinite bus through two transformers and a reactive transmission line is considered.

2.4.1 Dynamic model of a simplified power system

Figure 2.2 shows the equivalent circuit of the simplified lossless system. In this equivalent circuit, the angle of the infinite bus is taken as reference. From the equivalent circuit, the expression for the transient electrical torque of the generator T_{g} in pu is given by

$$T_{\text{g}} \approx P_{\text{g}} = \frac{V_{\text{g}}V_i\sin(\delta_{\text{g}})}{X} \tag{2.6}$$

where

$$X = X'_{\text{d}} + X_{\text{t1}} + X_{\text{L}} + X_{\text{t2}}$$

Using the equation of motion for the synchronous generator as in (2.1) and the expression of the generator electrical output torque as in (2.6), the small-signal dynamic model of the single-machine infinite-bus system is developed as

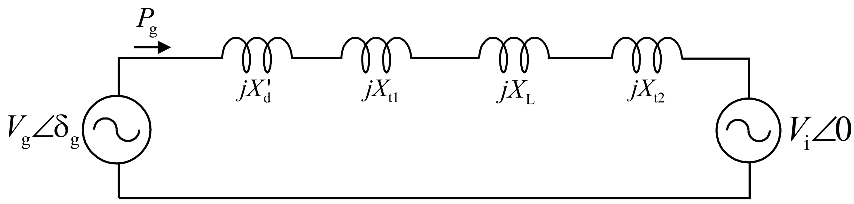

Fig. 2.2 Equivalent circuit of a single-machine infinite-bus system with the classical model of the synchronous generator.

$$\frac{d}{dt}\begin{bmatrix}\Delta\omega_\mathrm{g}\\ \Delta\delta_\mathrm{g}\end{bmatrix}=\begin{bmatrix}-K_\mathrm{Dm}/2H_\mathrm{g} & -K_\mathrm{Se}/2H_\mathrm{g}\\ \omega_0 & 0\end{bmatrix}\begin{bmatrix}\Delta\omega_\mathrm{g}\\ \Delta\delta_\mathrm{g}\end{bmatrix}+\begin{bmatrix}1/2H_\mathrm{g}\\ 0\end{bmatrix}\Delta T_\mathrm{m} \tag{2.7}$$

where $\Delta\omega_\mathrm{g}$ and $\Delta\delta_\mathrm{g}$represent variation of the generator speed and angle around the steady-state values ω_0 and $\delta_{\mathrm{g}0}$, respectively. The synchronizing torque coefficient K_Se is given by

$$K_\mathrm{Se}=\frac{dT_\mathrm{g}}{d\delta_\mathrm{g}}=\frac{V_\mathrm{g}V_\mathrm{i}\cos(\delta_{\mathrm{g}0})}{X} \tag{2.8}$$

The model in (2.7) can be used to analyze the nature of electromechanical dynamics in the power system as well as in the design of controllers.

2.4.2 Stability of a simplified power system

To analyze the small-signal stability of the simplified system, the poles of the dynamic model in (2.7) are calculated as

$$-\varsigma\omega_\mathrm{n}\pm\omega_\mathrm{n}\sqrt{\varsigma^2-1}$$

where the damping ratio (ς) and the natural frequency of the system (ω_n) are given by

$$\varsigma=\frac{K_\mathrm{Dm}}{\sqrt{8\omega_0 H_\mathrm{g}K_\mathrm{Se}}}\quad,\quad \omega_\mathrm{n}=\sqrt{\frac{\omega_0 K_\mathrm{Se}}{2H_\mathrm{g}}} \tag{2.9}$$

If $\varsigma\geq 1$, both poles become real and negative which implies that the system in (2.7) is stable around the steady-state operating point and characterized by a non-oscillatory decaying response for $\Delta\omega_\mathrm{g}$ and $\Delta\delta_\mathrm{g}$. The larger the damping ratio, the faster the decay. If $0<\varsigma<1$, the poles become complex conjugates that represent a decaying oscillatory mode. This is usually the case in a power system and the electromechanical oscillation frequency in this case is given by the imaginary part of the poles. Finally $\varsigma<0$ results in the poles to have positive real parts which corresponds to an unstable system.

The small-signal analysis is used to study the stability of the system around an operating point for small disturbances. In addition, the transient stability of the system following a large disturbance should be investigated. This is instead achieved using the well-known equal-area criterion for the simplified system in Fig. 2.1 [35]. For this system, consider an initial steady-state power transfer of $P_{\mathrm{g0}} = P_{\mathrm{m}}$ from the generator to the infinite bus. Figure 2.3 shows an example of its power angle curve before, during and after a disturbance. A lower power output during the fault results in that the generator accelerates and increases its rotor angle. When the fault is removed, the machine will start to decelerate as the power output is higher than the mechanical power input. But the generator angle δ_{g} keeps increasing until the kinetic energy gained during acceleration is totally balanced by the kinetic energy lost during deceleration, in this case at δ_3, where area ABCD = area DEFG. This implies that stability of the system in the first swing (the interval δ_0 to δ_3, where the generator angle is increasing) depends on whether the available deceleration area DEFH of the post-fault system is greater than the acceleration area ABCD during the fault. If the available deceleration area is higher, the system will be first swing stable and the generator angle starts to decrease at δ_3.

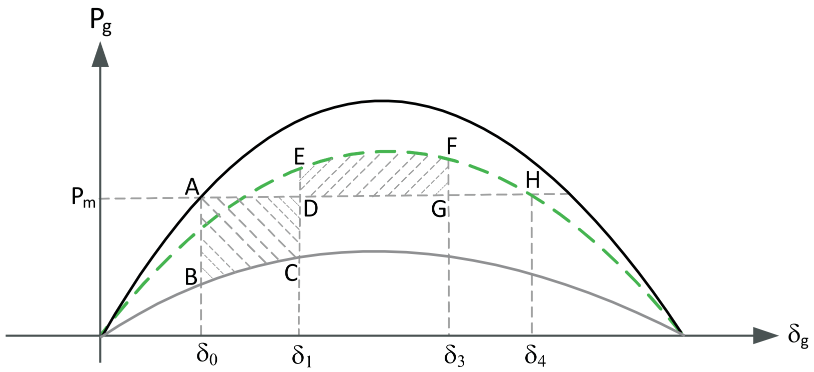

Fig. 2.3 Power angle curve for single-machine infinite-bus system before (black), during (gray solid) and after (dashed) fault.

As an example, the single-machine infinite-bus system in Fig. 2.2 is simulated to study its transient stability for two fault clearing times, t_{c}, and machine inertias. When the fault clearing time is increased beyond the critical value $t_{\mathrm{c,cri}}$, the available deceleration area will be smaller than the acceleration area during fault leading to loss of synchronism of the generator. This is shown with a continuous increase of the rotor angle in Fig. 2.4 (gray dashed curve). In the case of a fault clearing time lower than the critical value (black dashed curve), the system remains in synchronism. A test is repeated for the same system assuming a higher inertia of the synchronous generator and a similar fault clearing time. The higher inertia of the generator results in smaller swings in the angle (black solid curve) and therefore a higher stability margin than the first case (black dashed curve). If the mechanical damping in this last example is included, the rotor angle swings will converge to the steady-state value of the post-fault system.

2.4.3 Stability enhancement methods

Considering the simplified system in Fig. 2.1, two stability issues can be raised. The first is the ability of the generator to remain in synchronism with the infinite bus after a disturbance. This is the transient stability of the system and has been explained using the equal-area criterion in the previous section. The second is the small-signal stability of the system when the system

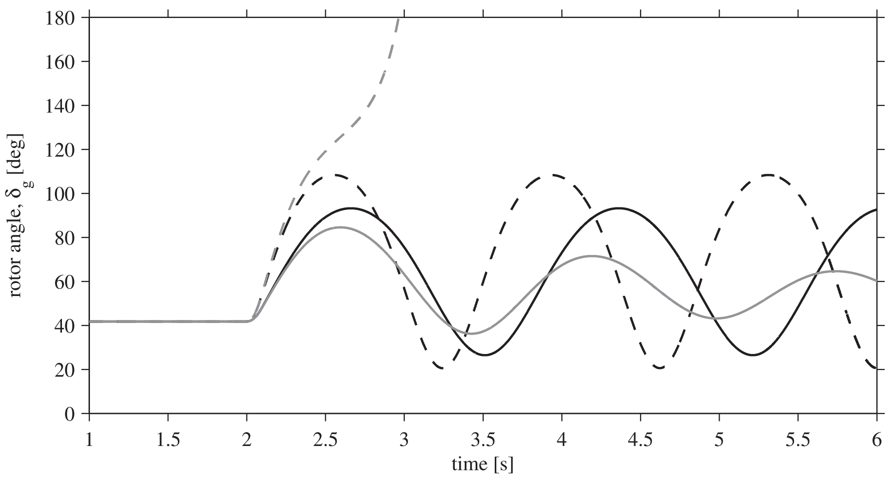

Fig. 2.4 Rotor angle variation of the generator following a three-phase fault for a fault clearing time $t_\mathrm{c} = t_\mathrm{c1} > t_\mathrm{c,cri}$ (gray dashed), $t_\mathrm{c} = t_\mathrm{c2} < t_\mathrm{c,cri}$ (black dashed), $t_\mathrm{c} = t_\mathrm{c2}$ and higher inertia with no mechanical damping (black solid) and with mechanical damping (gray solid).

remains in synchronism following a disturbance. As an example, a stable and damped system following a disturbance is shown in Fig. 2.4 (see gray solid curve). This system is transiently stable after the disturbance with positive damping of the subsequent oscillations. Although the stability of this specific case is achieved from the generator system, the purpose of this work is to design stability enhancement functions from controllable devices. Among the improvements added to the power system include increasing the transient stability margin of the power system and providing power oscillation damping.

Transient Stability Enhancement (TSE)

Consider the steady-state operating point A in Fig. 2.3. A disturbance in the system could cause the operating point to move away from the steady-state point and as a result changes the output power of the generator. From the dynamics of the generator in (2.5) and output power of the generator as in (2.6), it can be understood that the tendency of the generator is to swing back to the steady-state operating point. In other words, the synchronizing torque component that increases with the angle of the generator is responsible for the generator to remain in synchronism with the infinite bus. The higher the synchronizing torque coefficient as in (2.8), the more transiently stable the system becomes. An example for this is at lower steady-state power transfer, where the system has higher synchronizing torque coefficient. The synchronizing torque coefficient becomes lower as the system is heavily loaded and increasing the transient stability of the system is necessary. This can be achieved by controlling the FACTS devices in such a way that the generator torque output (T_g) varies in a similar way as the synchronizing torque component

$$\Delta T_\mathrm{g} = K_\mathrm{TSE} \Delta \delta_\mathrm{g} \tag{2.10}$$

where the constant $K_\mathrm{TSE} > 0$ is the synchronizing torque coefficient provided by the controllable device. In addition, as described from the example in Fig. 2.4, the transient stability of the system also depends on the inertia constant of the machine. It is shown that increasing the inertia constant reduces the maximum angle swing of the generator and hence increases its stability. Therefore, adding more inertia to the system from controllable devices can also indirectly increase the transient stability of the system.

Power Oscillation Damping (POD)

When the system is transiently stable after a disturbance, the tendency of the oscillations to die out depends on the amount of damping in the system. One such component comes from the mechanical damping as described in the previous section, where the torque output varies with the speed variation of the generator. From FACTS, a damping component can also be added to the system by controlling the device in such a way that the generator torque output (T_{g}) varies in phase with the speed variation as

$$\Delta T_{\mathrm{g}} = K_{\mathrm{POD}} \Delta \omega_{\mathrm{g}} \tag{2.11}$$

where the constant $K_{\mathrm{POD}} > 0$ is the damping torque coefficient provided from the controllable device. When both the TSE and POD controllers are implemented in the system, it should be noted that the TSE control algorithm is applied first to ensure the transient stability of the system and the POD control algorithm follows to damp the subsequent oscillations.

2.5 Conclusions

In this chapter, a simplified model of a single-machine infinite-bus system has been presented to describe the nature of power system dynamics. Using the simplified model and with the aid of the equal-area criterion, the transient stability of the system has been described. Moreover, the model of power system loads and controllable devices that impact the dynamics of the power system has been briefly described. To ensure the stability of a power system, different enhancement functions can be applied from power electronic equipped controllable devices [1][26]. Using the simplified model in Fig. 2.2, the application of FACTS controllers for this purpose will be described in the next chapter.

Chapter 3

FACTS controllers in the power system

3.1 Introduction

The use of various FACTS controllers, both series- and shunt-connected, for transmission system application will be briefly discussed in this chapter. The focus will be on power oscillation damping and transient stability enhancement using reactive power compensation. Moreover, the application of energy storage equipped power electronic converters as well as multiple FACTS devices for power system stability enhancement will be described.

3.2 Application of FACTS in the transmission system

Transmission lines are inductive at the rated frequency (50/60 Hz). This results in a voltage drop over the line that limits the maximum power transfer capability of the transmission system. By using reactive power compensation, the loading of the transmission line can be increased close to its thermal limit with sufficient stability margin. This can be achieved by using fixed reactive power compensation, such as series capacitors, or controlled variable reactive power compensation. The advantage with controlled variable compensation is that it counteracts system or load changes and disturbances. FACTS controllers can provide controlled reactive power compensation to the power system for voltage control, power flow control, power oscillation damping and transient stability enhancement [1]. The application of FACTS controllers for power system stability enhancement will be described in this section.

3.2.1 Series-connected FACTS controllers

As already described in Section 2.4, the power transfer capability of long transmission lines depends on the reactive impedance of the line. By using a series capacitor, the reactive impedance of the line can be reduced, thus increasing the transmittable power in the transmission system [36]. Fixed capacitors provide a constant series impedance ($-jX_c$) and makes the transmission line virtually shorter. This leads to an increase of the transient stability of the power system. When needed, a controlled variable impedance can be obtained by using series-connected FACTS controllers such as the Thyristor-Controlled Seried Capacitor (TCSC) and Static Synchronous Series Compensator (SSSC). This gives the advantage of power flow control and power oscillation damping that cannot be achieved when using uncontrolled compensation. Figure 3.1 shows the schematics of the available series-connected reactive power compensators.

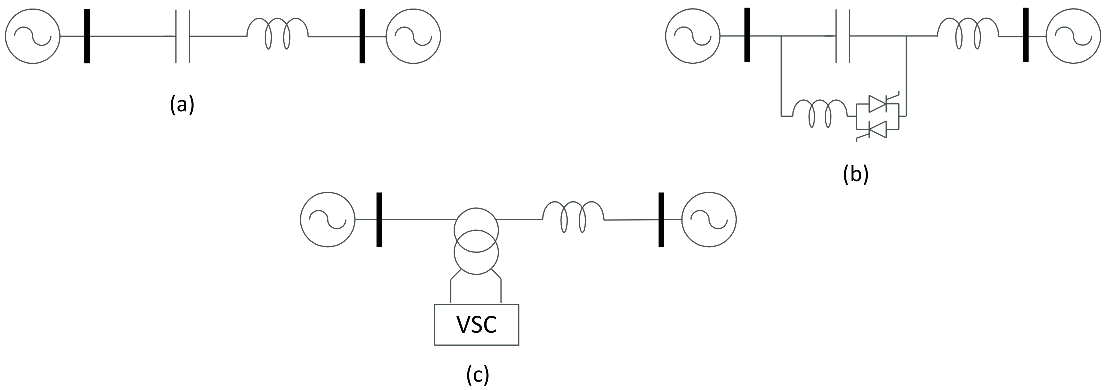

Fig. 3.1 Series-connected reactive power compensators; (a) Fixed series capacitor, (b) Thyristor-controlled Series Capacitor (TCSC), (c) Static Synchronous Series Compensator (SSSC).

Stability enhancement

To describe the increase in system stability by series-connected reactive power compensation, the system in Fig. 2.2 is considered. If the steady-state equivalent impedance of the compensator is denoted by $-jX_c$, the power transfer along the line is expressed as

$$P_{\mathrm{g}} = \frac{V_{\mathrm{g}} V_{\mathrm{i}} \sin(\delta_{\mathrm{g}})}{X - X_{\mathrm{c}}} \tag{3.1}$$

Figure 3.2 shows an example of the effect of a fixed series compensation ($X_{\mathrm{c}} = 0.2X$) on the power-angle curve. The transient stability margin for a given fault clearing time (at δ_1 in this case) is increased from area GFH for the uncompensated line (see Fig. 2.3) to area $\mathrm{G_1F_1H_1}$ for the compensated line. With the compensated system, the first swing of the generator angle ends at a lower angle (δ_2 in the figure) than the uncompensated system (δ_3), with area DEFG = area $\mathrm{DE_1F_1G_1}$ representing the deceleration area for the two cases.

To see the effect of fixed compensation on power oscillation damping, the variation of the generator active power can be calculated as

$$\Delta P_{\mathrm{g}} \approx \frac{\partial P_{\mathrm{g}}}{\partial \delta_{\mathrm{g}}} \Delta\delta_{\mathrm{g}} + \frac{\partial P_{\mathrm{g}}}{\partial X_{\mathrm{c}}} \Delta X_{\mathrm{c}} = \frac{V_{\mathrm{g}} V_{\mathrm{i}} \cos(\delta_{\mathrm{g0}})}{X - X_{\mathrm{c}}} \Delta\delta_{\mathrm{g}} + \frac{V_{\mathrm{g}} V_{\mathrm{i}} \sin(\delta_{\mathrm{g0}})}{(X - X_{\mathrm{c}})^2} \Delta X_{\mathrm{c}} \tag{3.2}$$

The electromechanical equation describing the single-machine infinite-bus system with fixed series compensation ($\Delta X_{\mathrm{c}} = 0$) becomes

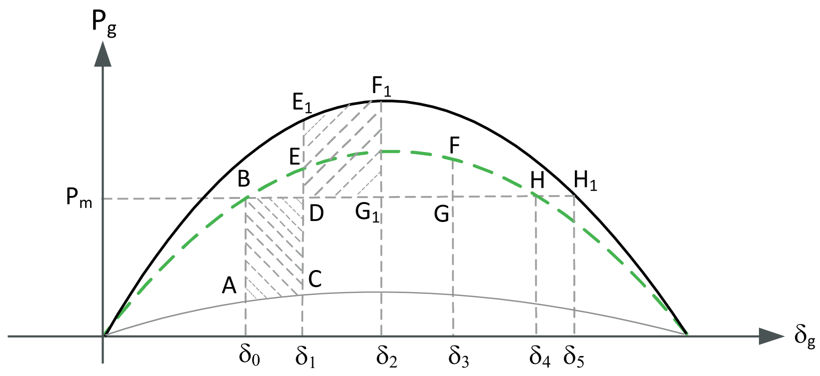

Fig. 3.2 power-angle curve for post-fault system with (black) and without (dashed) series reactive power compensation; Gray: power-angle curve during fault.

$$\frac{d}{dt}\begin{bmatrix}\Delta\omega \\ \Delta\delta_{\mathrm{g}}\end{bmatrix} = \begin{bmatrix} 0 & -K_{\mathrm{Se1}}/2H_{\mathrm{g}} \\ \omega_0 & 0 \end{bmatrix}\begin{bmatrix}\Delta\omega \\ \Delta\delta_{\mathrm{g}}\end{bmatrix} + \begin{bmatrix} 1/2H_{\mathrm{g}} \\ 0 \end{bmatrix}\Delta T_{\mathrm{mg}} \tag{3.3}$$

where the synchronizing torque coefficient K_{Se1} is given by

$$K_{\mathrm{Se1}} = \frac{V_{\mathrm{g}}V_{\mathrm{i}}\cos(\delta_{\mathrm{g0}})}{X - X_{\mathrm{c}}}$$

For simplicity, the damping in the mechanical system is neglected ($K_{\mathrm{Dm}} = 0$). It is clear from (3.3) that no additional damping to the system is provided by fixed series compensation. But, the synchronizing torque coefficient K_{se1} is increased for the compensated system compared to the uncompensated case. Hence, fixed compensation provides a transient stability enhancement for the first swing of the generator according to the discussion in Section 2.4.3. On the other hand, the generator output power should be controlled to vary in response to the speed variation of the generator to provide power oscillation damping. This can be achieved by controlling the series compensation level X_c using FACTS controllers such as the TCSC as [37]

$$\Delta X_{\mathrm{c}} \approx D_{\mathrm{c}\omega}\Delta\omega_{\mathrm{g}} \tag{3.4}$$

where $D_{\mathrm{c}\omega}$ represents a gain to control the variation of X_{c} with respect to speed variation of the generator. The electromechanical equation describing the single-machine infinite-bus system with a controlled compensation as in (3.4) becomes

$$\frac{d}{dt}\begin{bmatrix}\Delta\omega \\ \Delta\delta_{\mathrm{g}}\end{bmatrix} = \begin{bmatrix} -K_{\mathrm{De1}}/2H_{\mathrm{g}} & -K_{\mathrm{Se,c}}/2H_{\mathrm{g}} \\ \omega_0 & 0 \end{bmatrix}\begin{bmatrix}\Delta\omega \\ \Delta\delta_{\mathrm{g}}\end{bmatrix} + \begin{bmatrix} 1/2H_{\mathrm{g}} \\ 0 \end{bmatrix}\Delta T_{\mathrm{mg}} \tag{3.5}$$

where the damping torque coefficient K_{De1}, provided by the controlled series compensation and the synchronizing torque coefficient, $K_{\mathrm{Se,c}}$ due to the steady-state compensation (X_{c0}) are given by

$$K_{\mathrm{De1}} = \frac{V_{\mathrm{g}} V_{\mathrm{i}} \sin(\delta_{\mathrm{g0}})}{(X - X_{\mathrm{c0}})^2} D_{\mathrm{c}\omega}, \qquad K_{\mathrm{Se,c}} = \frac{V_{\mathrm{g}} V_{\mathrm{i}} \cos(\delta_{\mathrm{g0}})}{X - X_{\mathrm{c0}}}$$

It is shown in this case that power oscillation damping is achieved by varying the series impedance X_{c} around steady-state value according to (3.4). On the other hand, the transient stability of the system can be increased by maintaining an adequate value of the fixed series compensation, X_{c0}. It has been shown in (3.3) that transient stability enhancement can be achieved by using fixed series compensation. In order to maximize the use of series compensation for transient stability enhancement, the series impedance can also be controlled around the steady-state value as

$$\Delta X_{\mathrm{c}} \approx D_{\mathrm{c}\delta} \Delta\delta_{\mathrm{g}} \tag{3.6}$$

where $D_{\mathrm{c}\delta}$ represents a gain to control the variation of X_{c} with respect to the angle deviation of the generator. In this case, the synchronizing torque coefficient $K_{\mathrm{Se,v1}}$, which comprises of the contribution from the steady-state operating point and the controlled compensation, becomes

$$K_{\mathrm{Se,c1}} = \frac{V_{\mathrm{g}} V_{\mathrm{i}} \cos(\delta_{\mathrm{g0}})}{X - X_{\mathrm{c0}}} + \frac{V_{\mathrm{g}} V_{\mathrm{i}} \sin(\delta_{\mathrm{g0}})}{(X - X_{\mathrm{c0}})^2} D_{\mathrm{c}\delta}$$

It is possible to observe from the discussion that the series-connected FACTS controllers provide an effective way for power flow control and system stability enhancement by controlling the transmission line series impedance. One drawback associated with these devices is the complicated protection system required to deal with large short-circuit currents. Moreover, due to the intrinsic nature of series compensation, the market is dominated by fixed compensators (fixed series capacitors); it is only in specific applications that controllable series-connected FACTS are implemented.

3.2.2 Shunt-connected FACTS controllers

Shunt compensation is commonly used to maintain the voltage at various connection points of the transmission system. This helps to increase the transmittable power and hence improve system stability. Depending on the system loading, the voltage profile along the transmission line can be controlled using controlled compensation by shunt-connected FACTS controllers such as Thyristor-Controlled Reactor (TCR), Static Var Compensator (SVC) and Static Synchronous Compensator (STATCOM) [1]. The schematics of these devices is shown in Fig. 3.3.

Stability enhancement

The system in Fig. 2.2 is considered with a shunt compensator connected at the electrical midpoint of the line to show the impact of reactive power compensation on system stability. If the transmission end voltages are assumed equal ($V_{\mathrm{g}} = V_{\mathrm{i}}$), Figure 3.4 shows the voltage profile along the transmission line when the midpoint voltage is controlled such that $V_{\mathrm{m}} = V_{\mathrm{i}}$.

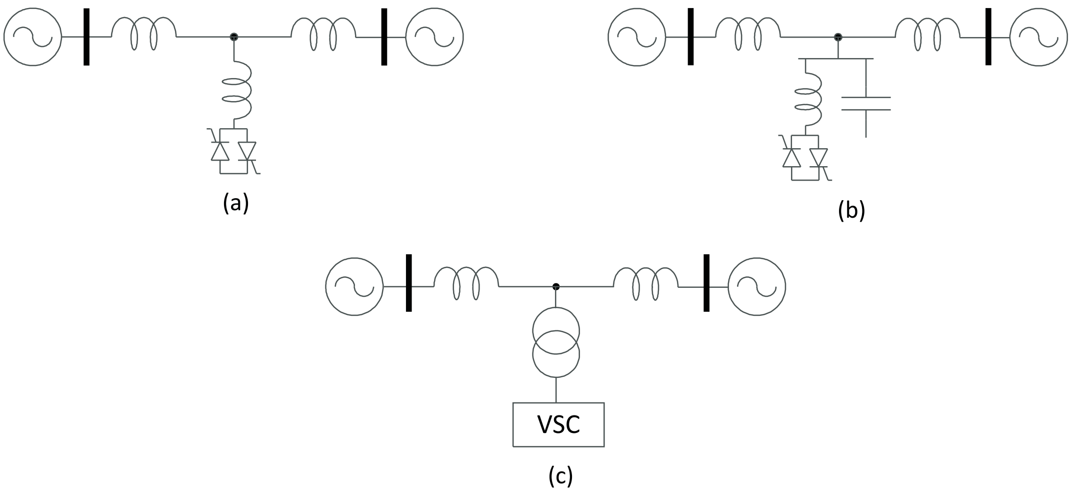

Fig. 3.3 Shunt-connected reactive power compensators; (a) Thyristor-controlled reactor (TCR), (b) Static Var Compensator (SVC), (c) Static Synchronous Compensator (SVC).

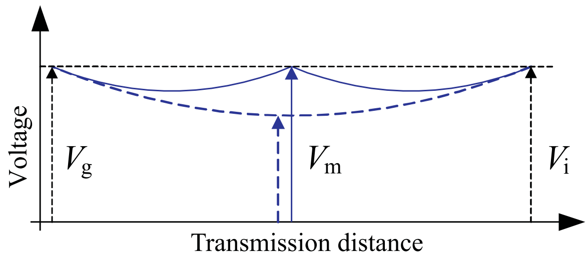

Fig. 3.4 Voltage profile along transmission line with midpoint shunt reactive power compensation (solid) and no compensation (dashed).

By controlling the PCC voltage, the power transfer over a line can be increased leading also to an increase in the transient stability. For the example in Fig. 3.4, the power flow along the transmission line is given by

$$P_{\mathrm{g}} = 2\frac{V_{\mathrm{m}}V_{\mathrm{i}}\sin(\frac{\delta_{\mathrm{g}}}{2})}{X} \tag{3.7}$$

For this particular case, the power-angle curve for the system is shown in Fig. 3.5. The increase in stability margin for a given fault clearing time is clearly shown in the figure. With the compensated system, the first swing of the generator angle ends at a lower angle (δ_2) than the uncompensated system (δ_3), with area DEFG = area $\mathrm{DE_1F_1G_1}$ representing the deceleration area for the two cases.

To see the effect of controlling the PCC voltage to a constant value on power oscillation damping, the variation of the generator power output for constant voltage control is calculated as

$$\Delta P_{\mathrm{g}} \approx \frac{\partial P_{\mathrm{g}}}{\partial \delta_{\mathrm{g}}}\Delta\delta_{\mathrm{g}} + \frac{\partial P_{\mathrm{g}}}{\partial V_{\mathrm{m}}}\Delta V_{\mathrm{m}} = \frac{V_{\mathrm{m0}}V_{\mathrm{i}}\cos(\delta_{\mathrm{g0}}/2)}{X}\Delta\delta_{\mathrm{g}} + \frac{2V_{\mathrm{i}}\sin(\delta_{\mathrm{g0}}/2)}{X}\Delta V_{\mathrm{m}} \tag{3.8}$$

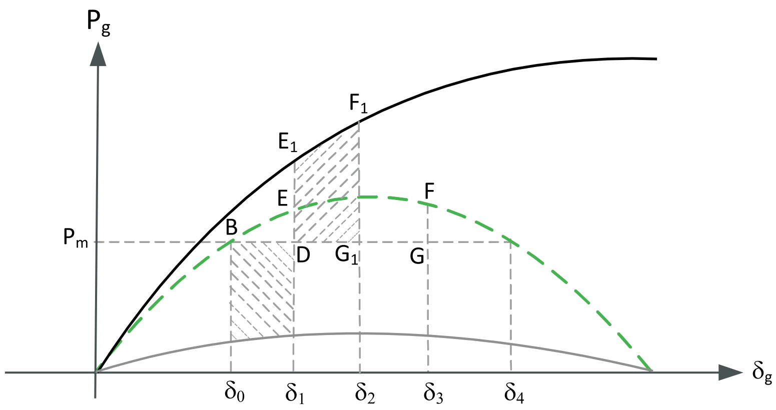

Fig. 3.5 power-angle curve for post-fault system with (black) and without (dashed) midpoint shunt reactive power compensation; Gray solid: power-angle curve during fault.

The electromechanical equation describing the single-machine infinite-bus system with constant voltage control ($\Delta V_\mathrm{m} = 0$) becomes

$$\frac{d}{dt}\begin{bmatrix}\Delta\omega \\ \Delta\delta_\mathrm{g}\end{bmatrix} = \begin{bmatrix}0 & -K_\mathrm{Se2}/2H_\mathrm{g} \\ \omega_0 & 0\end{bmatrix}\begin{bmatrix}\Delta\omega \\ \Delta\delta_\mathrm{g}\end{bmatrix} + \begin{bmatrix}1/2H_\mathrm{g} \\ 0\end{bmatrix}\Delta T_\mathrm{mg} \tag{3.9}$$

where the synchronizing torque coefficient K_Se2 is given by (3.10). For comparison, the synchronizing torque coefficient K_Se for the uncompensated system is given by (3.11).

$$K_\mathrm{Se2} = \frac{V_\mathrm{m} V_\mathrm{i} \cos(\delta_\mathrm{g0}/2)}{X} \tag{3.10}$$

$$K_\mathrm{Se} = \frac{V_\mathrm{g} V_\mathrm{i} \cos(\delta_\mathrm{g0})}{X} \tag{3.11}$$

Again, the damping provided by the mechanical system is neglected. It is clear from (3.9) that no damping is provided when the shunt compensation is controlled to keep the voltage constant. The synchronizing torque coefficient is increased for the compensated system compared to the uncompensated one ($K_\mathrm{se2} > K_\mathrm{se}$), hence increasing the transient stability of the system. In order to provide power oscillation damping to the system, the shunt-connected compensator should be controlled to modulate the voltage magnitude at the connection point. This is achieved by controlling ΔV_m linearly with the generator speed variation as

$$\Delta V_\mathrm{m} \approx D_{\mathrm{v}\omega} \Delta\omega_\mathrm{g} \tag{3.12}$$

where $D_{\mathrm{v}\omega}$ represents a gain to control the variation of V_m. Controlling the voltage magnitude as in (3.12) around the steady-state value (V_m0), the electromechanical equation describing the single-machine infinite-bus system becomes

$$\frac{d}{dt}\begin{bmatrix}\Delta\omega\\ \Delta\delta_{\mathrm{g}}\end{bmatrix}=\begin{bmatrix}-K_{\mathrm{De2}}/2H_{\mathrm{g}} & -K_{\mathrm{Se,v}}/2H_{\mathrm{g}}\\ \omega_0 & 0\end{bmatrix}\begin{bmatrix}\Delta\omega\\ \Delta\delta_{\mathrm{g}}\end{bmatrix}+\begin{bmatrix}1/2H_{\mathrm{g}}\\ 0\end{bmatrix}\Delta T_{\mathrm{mg}} \tag{3.13}$$

where the damping torque coefficient, K_{De2} provided by the controlled shunt compensation and the synchronizing torque coefficient, $K_{\mathrm{Se,v}}$ due to the steady-state compensation are given by

$$K_{\mathrm{De2}}=\frac{2V_{\mathrm{i}}\sin(\delta_{\mathrm{g0}}/2)}{X}D_{\mathrm{v}\omega},\qquad K_{\mathrm{Se,v}}=\frac{V_{\mathrm{m0}}V_{\mathrm{i}}\cos(\delta_{\mathrm{g0}}/2)}{X}$$

It is shown in this case that power oscillation damping is achieved by modulating the PCC voltage around the steady-state value according to (3.12). On the other hand, the transient stability of the system can be increased by boosting the voltage V_{m0}. It has been shown in (3.9) that transient stability enhancement can be achieved by controlling the voltage at the connection point constant. In order to maximize the use of shunt-compensation for transient stability enhancement, the voltage magnitude at the connection point can also be varied around the steady-state value as

$$\Delta V_{\mathrm{m}}\approx D_{\mathrm{v}\delta}\Delta\delta_{\mathrm{g}} \tag{3.14}$$

where $D_{\mathrm{v}\delta}$ represents a gain to control the variation of V_{m} with respect to the generator angle deviation. In this case, the synchronizing torque coefficient $K_{\mathrm{Se,v1}}$, which comprises of the contribution from the steady-state operating point and the controlled compensation becomes

$$K_{\mathrm{Se,v1}}=\frac{V_{\mathrm{m0}}V_{\mathrm{i}}\cos(\delta_{\mathrm{g0}}/2)}{X}+\frac{2V_{\mathrm{i}}\sin(\delta_{\mathrm{g0}}/2)}{X}D_{\mathrm{v}\delta}$$

If the TSE controller is implemented in the FACTS device according to (3.14), it should be emphasized that the POD controller in (3.12) will be started at the end of the TSE operation as described in Section 2.4.3.

3.3 Energy storage equipped shunt-connected STATCOM

As mentioned earlier, FACTS controllers are designed to exchange only reactive power with the network in steady-state. Stability enhancement by shunt-connected reactive power compensation is achieved by controlling the PCC voltage magnitude in order to affect the power flow over the line and consequently the power output of the generation units. Using the active power injection capability of the E-STATCOM, a more flexible control of the power system is possible. In this work, the active power injection capability of the E-STATCOM is obtained from a dedicated energy storage incorporated in the converter. Observe that the functionalities described and proposed here can also be implemented in other kinds of “controllable active power sources” connected to the power system, such as wind, solar and other distributed generation units [18][38]. These energy sources use some power electronics in their structure and a control method to provide POD and TSE using active power injection can be included. The availability of active power in the controllable devices also provides the possibility of adding more inertia to the power system by controlling the device in a similar fashion to a synchronous machine.

3.4 Multiple FACTS devices

The use of various FACTS devices for power system stability enhancement has been described in the previous sections. When multiple devices exist in the power system, the control method for each compensator should not lead to undesired interactions. For this reason, each device can be coordinately designed for example to maximize the damping of a particular oscillation mode of interest [28][30]. In this work, multiple compensators will also be considered and each device will be designed independently. The performance of the control method when multiple controllable devices are used together is investigated.

3.5 Stability enhancement controller for FACTS

As described in Section 2.4.3 and demonstrated in Section 3.2 using a simplified power system, stability enhancement can be achieved with a proper control of FACTS devices. In these examples, the speed and angle variation of the generator ($\Delta\omega_{\mathrm{g}}$, $\Delta\delta_{\mathrm{g}}$) are assumed to be known at the compensator location to implement the control algorithms. In an actual installation, this can be achieved through a remote measurement of the generator speed or angle variation, which could be both difficult and expensive. A simpler solution would be to estimate the required physical quantities of the generator from local signals such as the power flow over a line, the PCC voltage magnitude or the grid frequency.

Using the system in Fig. 2.2, the classical control approach for stability enhancement using FACTS devices will be described as an example. For this purpose, the angle and speed deviation of the generator should be estimated from local measurements to implement the TSE and POD controllers, respectively. As a local measurement signal, consider the total power flow over the line given by

$$P_{\mathrm{g}} = \frac{V_{\mathrm{g}} V_{\mathrm{i}} \sin(\delta_{\mathrm{g}})}{X} \tag{3.15}$$

Following a power system disturbance, the total power flow will comprise of the steady-state power (P_{g0}) and an additional component caused by the electromechanical dynamics (ΔP_{g}). If we consider small-signal changes, the angle and speed deviation of the generator can be estimated from the measured power as

$$\begin{aligned} \Delta P_{\mathrm{g}} &\approx \tfrac{V_{\mathrm{g}} V_{\mathrm{i}} \cos(\delta_{\mathrm{g0}})}{X} \Delta\delta_{\mathrm{g}} = K_{\delta} \Delta\delta_{\mathrm{g}} \\ \tfrac{dP_{\mathrm{g}}}{dt} &\approx \tfrac{V_{\mathrm{g}} V_{\mathrm{i}} \cos(\delta_{\mathrm{g0}})}{X} \Delta\omega_{\mathrm{g}} = K_{\omega} \Delta\omega_{\mathrm{g}} \end{aligned} \tag{3.16}$$

where the constants K_δ and K_ω relate the angle and speed deviation of the generator with the estimated signals, ΔP_{g} and $\frac{dP_{\mathrm{g}}}{dt}$, respectively. Extracting the estimated signals is conventionally done using a combination of filters. For example, ΔP_{g} can be estimated by removing the average component from the total measured power signal using a washout filter. On the other hand, $\frac{dP_{\mathrm{g}}}{dt}$ can be estimated by removing the average component from the measured power signal and providing a phase-shift of $90°$ at the expected oscillation frequency to represent the derivative action. For this purpose, the setup similar to the one in Fig. 3.6 can be used. With this approach, the washout filter is used to remove the power average whereas a low-pass filter is used to remove high frequency components. The required phase compensation at the frequency of interest is then provided by a number of lead-lag filters as indicated in the figure.

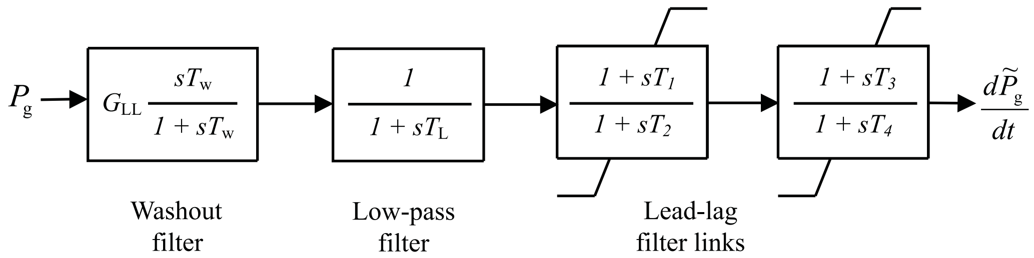

Fig. 3.6 Conventional filter setup to create a damping control input signal.

For the simplified system considered in this section, using the estimated quantities for $\Delta\delta_{\mathrm{g}}$ and $\Delta\omega_{\mathrm{g}}$ in place of the actual generator angle and speed deviation, the TSE and POD controllers for FACTS devices can be obtained. For a larger and interconnected system, various frequency components exist and each component should be separated and appropriate phase-shift must be applied. Depending on the input signal used for estimation, the power system configuration and the correlation between the controlled parameter of the FACTS device and the active power output of the generators, the required phase-shift for each frequency component can be obtained through eigenvalue analysis of the power system configuration including the FACTS controller [29].

In contrast with its simple design and implementation, the arrangement in Fig. 3.6 presents a number of drawbacks. As first, the filter links must be designed for a particular oscillation frequency and the required phase-shift will be provided only at that particular frequency. This reduces the dynamic performance of the POD controller during system parameter changes. In addition, the cut-off frequency of the washout filter to remove the average component should be well below the power oscillation frequency and this limits the speed to obtain the required estimates. Finally, in a system where there are more than one oscillation frequency components, the setup is not convenient to provide the required phase-shift for the various frequency components. To overcome these drawbacks, an estimation method based on a modified RLS algorithm is proposed in this work. This method will be described in Chapter 4 and its application for POD controller design in shunt-connected FACTS devices will be shown in Chapter 6. Note that the design method can be equally applied for series-connected FACS, HVDC or other controllable power system devices.

3.6 Conclusions

In this chapter, a brief overview of series- and shunt-connected FACTS controllers for power system stability enhancement has been carried out. The impact of the controllers on the active power transfer over a transmission line as well as on the system stability have been discussed. Furthermore, the need for auxiliary controllers to provide additional transient stability enhancement and power oscillation damping to the power system has been addressed. As pointed out, the classical stability enhancement controllers are mainly based on the use of several filtering stages connected in cascade. The drawbacks of this approach has been described and a need for a better estimation method has been highlighted. With the proposed method, which will be described in the next chapter, accurate estimation of the phase and amplitude of the various frequency components can be achieved. By using the estimated frequency components of interest, an effective stability enhancement controller that minimize the use of active and reactive power injection can be designed.

Chapter 4

Signal estimation techniques

4.1 Introduction

In the previous chapter, a description of a conventional filter setup for the design of POD controller for FACTS devices has been given. The drawbacks of this method in an actual installation have been briefly described and the need for a better estimation algorithm has been highlighted. In this chapter, an estimation algorithm based on the use of filters will be described first. Then, the proposed signal estimation method, based on an RLS algorithm, will be developed. Even if the proposed algorithm can be applied for estimation of various signal components [39], the focus will be on estimation of low-frequency electromechanical oscillations. Estimation of harmonics and sequence components in the power system will also be discussed.

4.2 Estimation methods

As explained in Section 3.5, a series of washout and lead-lag filter links connected in cascade as in Fig. 3.6 can be used to estimate oscillatory components for POD controller design in FACTS devices. To overcome the drawbacks of this method, an estimation method based on a combination of low-pass filters (LPF) is proposed in [6]. Although this method presents a better steady-state and dynamic performance as compared to the system in Fig. 3.6, its speed of response is tightly dependent on the frequency of the power oscillations. For this problem, a modified RLS-based estimation algorithm is proposed in this work.

To investigate the effectiveness of the considered estimation algorithms, a system consisting of a synchronous generator connected to an infinite bus through a transmission system as in Fig 4.1 is considered. As an example, a three-phase line fault is applied to this system at $t = 20$ s with a subsequent line disconnection to clear the fault after 100 ms. This results in a low-frequency oscillation in the transmitted active power as shown in Fig. 4.2.

The purpose of the estimation method is to extract the oscillatory component of the input power signal for POD controller design. For this particular case, the generator output power (p), which is used as input for the estimation algorithm can be modeled as the sum of an average (P_0) and

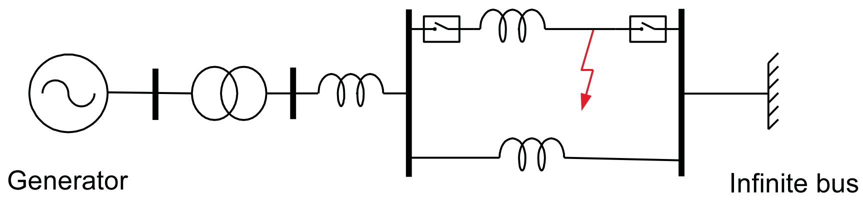

Fig. 4.1 A simple power system to model low-frequency power oscillation.

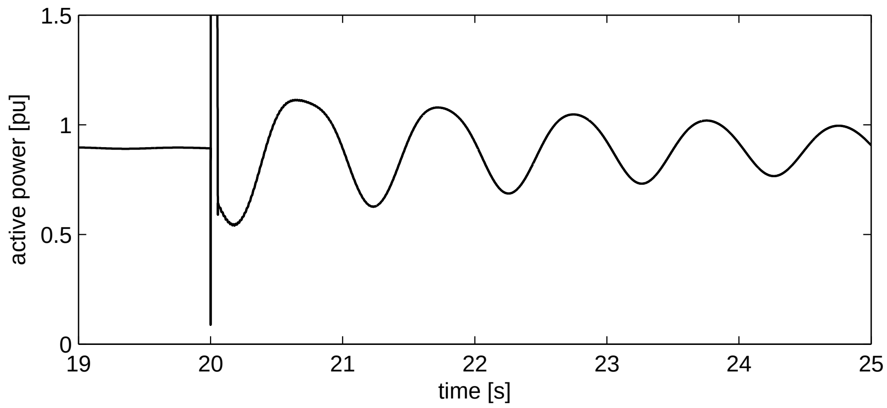

Fig. 4.2 Transmitted active power from the generator. Fault occurred at 20 s and cleared after 100 ms.

oscillatory component (P_{osc}) as

$$p(t) = P_0(t) + P_{\text{osc}}(t) = P_0(t) + P_{\text{ph}}(t)\cos[\omega_{\text{osc}}t + \varphi(t)] \tag{4.1}$$

The oscillatory component, P_{osc} is expressed in terms of its amplitude (P_{ph}), frequency (ω_{osc}) and phase (φ). Observe that even if the specific application to power oscillations are considered in this section, the analysis is valid in the generic case of signal estimation. In this section, design of cascade filter links will be described first and the limitations of the method will be addressed with an example application. A better estimation method based on a combination of LPF and RLS will then be described when used for estimation of low-frequency power oscillation components. The limitation of the LPF-based method when fast estimation is needed will be shown. Further improvements to the RLS-based method to increase its dynamic performance will be described in the next section.

4.2.1 Cascade filter links

The conventional way to generate damping signals is using a filter setup as described in Fig. 3.6. In this section, the design of the filter link parameters will be described and the problems associated with the method will be addressed. Assume that we want to estimate the oscillatory part of the input signal model in (4.1). This is achieved by removing the average part using the washout filter, whereas the high-frequency components are attenuated by the low-pass filter. The required gain and phase at the oscillation frequency of interest is provided using the gain

(G_{LL}) and time constants of the lead-lag filter links. The transfer function H_{LL} of this estimation algorithm can be described as

$$H_{\mathrm{LL}}(s) = G_{\mathrm{LL}} \left[\frac{sT_{\mathrm{w}}}{1+sT_{\mathrm{w}}}\right] \left[\frac{1}{1+sT_{\mathrm{L}}}\right] \left[\frac{1+sT_1}{1+sT_2}\right] \left[\frac{1+sT_3}{1+sT_4}\right] \tag{4.2}$$

To be able to remove the average component without affecting the low-frequency oscillatory component, the time constant for the washout filter, T_{w} is usually chosen in the range of 5 - 10 s. The large time constant results in a slow removal of the average component from the required estimated signal. On the other hand, the time constant of the low-pass filter, T_{L} is usually chosen in the range of 0.1 s to attenuate the high-frequency components. The value is chosen to make a cut-off frequency much higher than the low-frequency oscillation. The time constant of the lead-lag filter links, T_1, T_2, T_3 and T_4 are chosen based on the phase compensation required at the oscillation frequency of interest. The amplitude of the transfer function at the oscillation frequency can be adjusted by the gain, G_{LL}. Depending on the total phase compensation (φ_{comp}) required from the lead-lag filter links and considering a maximum phase compensation of $60°$ from each link, the number of lead-lag filter links can be decided [40].

Assuming that the transfer function (H_{LL}) is required to provide a gain of A_{LL} and phase of φ_{LL} at the oscillation frequency (ω_{osc}), the parameters of the lead-lag filter links can be calculated from the following equations as

$$\begin{gathered}
A_{\mathrm{LL}} = G_{\mathrm{LL}} \left| \frac{j\omega_{\mathrm{osc}}T_{\mathrm{w}}}{1+j\omega_{\mathrm{osc}}T_{\mathrm{w}}} \frac{1}{1+j\omega_{\mathrm{osc}}T_{\mathrm{L}}} \left(\frac{1+j\omega_{\mathrm{osc}}T_1}{1+j\omega_{\mathrm{osc}}T_2}\right) \left(\frac{1+j\omega_{\mathrm{osc}}T_3}{1+j\omega_{\mathrm{osc}}T_4}\right) \right| \\
\varphi_{\mathrm{LL}} = \varphi_{\mathrm{comp}} - \tan^{-1}[\omega_{\mathrm{osc}}T_{\mathrm{L}}] - \tan^{-1}[\omega_{\mathrm{osc}}T_{\mathrm{w}}] + \pi/2 \\
\gamma_{\mathrm{T1}} = \frac{T_1}{T_2} = \frac{1+\sin(\varphi_{\mathrm{comp1}})}{1-\sin(\varphi_{\mathrm{comp1}})} \quad , \quad \gamma_{\mathrm{T2}} = \frac{T_3}{T_4} = \frac{1+\sin(\varphi_{\mathrm{comp2}})}{1-\sin(\varphi_{\mathrm{comp2}})} \\
T_1 = \frac{\sqrt{\gamma_{\mathrm{T1}}}}{\omega_{\mathrm{osc}}} \quad , \quad T_2 = \frac{1}{\sqrt{\gamma_{\mathrm{T1}}}\omega_{\mathrm{osc}}} \quad , \quad T_3 = \frac{\sqrt{\gamma_{\mathrm{T2}}}}{\omega_{\mathrm{osc}}} \quad , \quad T_4 = \frac{1}{\sqrt{\gamma_{\mathrm{T2}}}\omega_{\mathrm{osc}}}
\end{gathered} \tag{4.3}$$

where φ_{comp1} and φ_{comp2} represents the phase compensation from the first and second lead-lag filter links, respectively. As an example, the signal in (4.1) is assumed to contain an average part and a 1 Hz oscillatory component. The filter in (4.2) is designed to extract the oscillatory part with a gain of 1 p.u. and a phase-shift of $0°$. Choosing the time constant for the washout and low-pass filters as $T_{\mathrm{w}} = 10$ s and $T_{\mathrm{L}} = 0.1$ s, the remaining parameters of the transfer function H_{LL} are calculated as $T_1 = 0.2826$ s, $T_2 = 0.0896$ s, $T_3 = T_4 = 0$ and $G_{\mathrm{LL}} = 0.6651$. In this example, the required phase compensation ($\varphi_{\mathrm{comp}} < 60°$) can be achieved only using one lead-lag filter. As shown in the bode diagram of the transfer function for these choice of parameters in Fig. 4.3, the wide band around the estimated frequency component results in a non-selective estimation. The problem will be evident when a nearby oscillatory component exists in the input signal and accurate estimation of the frequency component of interest (with high attenuation of the undesired frequency component) is necessary. Moreover, designing a filter to provide the correct amplitude and phase for more than one oscillation frequency component is difficult to achieve. For this reason, a better estimation technique is necessary and will be described next.

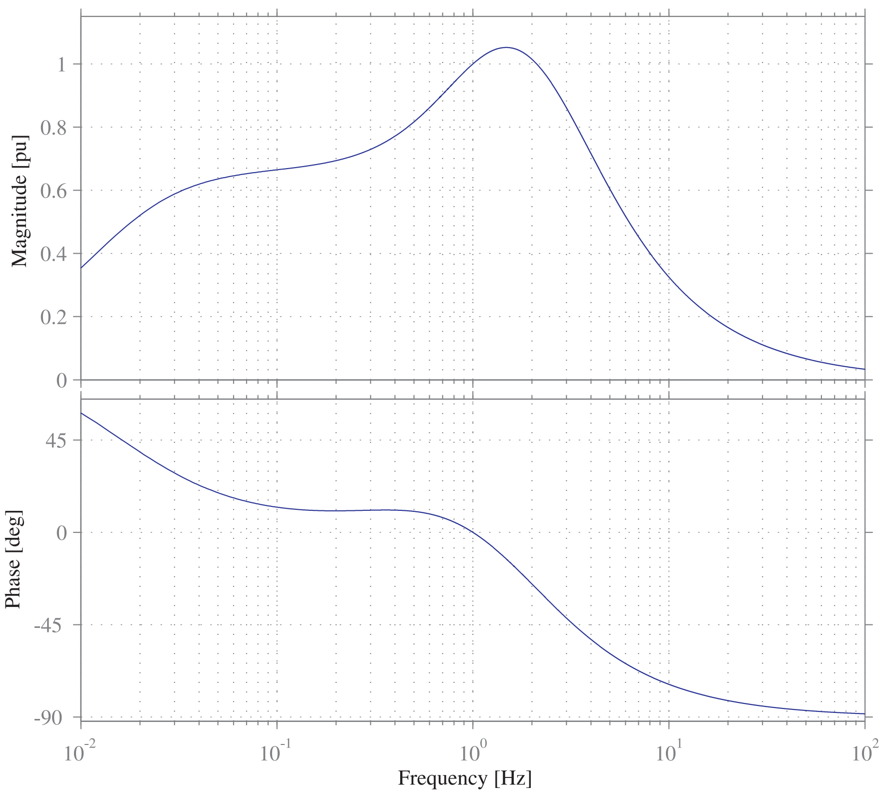

Fig. 4.3 Bode diagram for the cascade links transfer function ($H_{\mathrm{LL}}(s)$) from $p(t)$ to $\tilde{P}_{\mathrm{osc}}(t)$.

4.2.2 Low-pass Filter (LPF) based method

Unlike the method in the previous section, the estimation method described in this section enables a selective estimation of amplitude and phase of one or more oscillatory components with high attenuation at undesired frequency components. Considering the active power in (4.1) as an input signal and denoting $\underline{P}_{\mathrm{ph}} = P_{\mathrm{ph}} e^{j\varphi}$ as the complex phasor of the oscillatory component and $\theta_{\mathrm{osc}}(t) = \omega_{\mathrm{osc}} t$ as the oscillation angle, the input power signal can be expressed as

$$p(t) = P_0(t) + \mathrm{Real}\left[\underline{\mathrm{P}}_{\mathrm{ph}}(\mathrm{t})\mathrm{e}^{\mathrm{j}\theta_{\mathrm{osc}}(\mathrm{t})}\right] = \mathrm{P}_0(\mathrm{t}) + \frac{1}{2}\underline{\mathrm{P}}_{\mathrm{ph}}(\mathrm{t})\mathrm{e}^{\mathrm{j}\theta_{\mathrm{osc}}(\mathrm{t})} + \frac{1}{2}\underline{\mathrm{P}}^*_{\mathrm{ph}}(\mathrm{t})\mathrm{e}^{-\mathrm{j}\theta_{\mathrm{osc}}(\mathrm{t})} \tag{4.4}$$

The expression in (4.4) separates the input signal into three frequency components (having characteristic frequencies $0, \omega_{\mathrm{osc}}$, and $-\omega_{\mathrm{osc}}$), where the average P_0 and the phasor $\underline{P}_{\mathrm{ph}}$ are slowly varying signals. By rearranging (4.4) and applying low-pass filtering, the estimate for the average $\tilde{P}_0$, the phasor $\tilde{\underline{P}}_{\mathrm{ph}}$ and the oscillatory component $\tilde{P}_{\mathrm{osc}}$ can be extracted from the input signal as [6]

$$\tilde{P}_0(t) = H_0\{p(t) - \tilde{P}_{\mathrm{osc}}(t)\} \tag{4.5}$$

$$\tilde{\underline{P}}_{\mathrm{ph}}(t) = H_{\mathrm{ph}}\{[2p(t) - 2\tilde{P}_0(t) - \tilde{\underline{P}}^*_{\mathrm{ph}}(t)e^{-j\theta_{\mathrm{osc}}(t)}]e^{-j\theta_{\mathrm{osc}}(t)}\} \tag{4.6}$$

$$\tilde{P}_{\text{osc}}(t) = \frac{1}{2}\tilde{\underline{P}}_{\text{ph}}(t)e^{j\theta_{\text{osc}}(t)} + \frac{1}{2}\tilde{\underline{P}}^{*}_{\text{ph}}(t)e^{-j\theta_{\text{osc}}(t)} \tag{4.7}$$

where H_0 and H_{ph} represent the transfer function of the low-pass filters to extract the average and the phasor component, respectively. The block diagram describing this method is shown in Fig. 4.4. For the various notations, a signal or parameter $\tilde{x}$ represents an estimate of the actual value x.

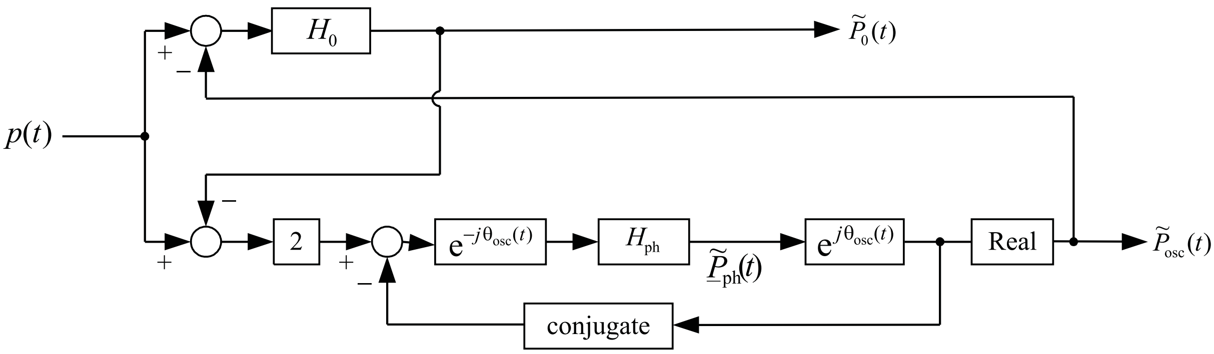

Fig. 4.4 Block diagram of the LPF-based estimation algorithm.

In order to evaluate the dynamic performance of the LPF-based estimation algorithm, a first order low-pass filter with cut-off frequency α_{LPF} is used for the filters in (4.5) - (4.6) as

$$H_0(s) = H_{\text{ph}}(s) = \frac{\alpha_{\text{LPF}}}{s + \alpha_{\text{LPF}}} \tag{4.8}$$

To separate the average and oscillatory components, it is necessary that the cut-off frequency, α_{LPF} is smaller than the oscillation frequency ω_{osc}. The dynamic performance of the LPF-based method is a function of the cut-off frequency. By increasing the magnitude of α_{LPF}, a faster estimation can be obtained at the cost of its frequency selectivity. To observe this, the algorithm in (4.5) - (4.7) is expressed in state space form as [36]

$$\frac{d}{dt}\begin{bmatrix} \tilde{P}_0 \\ \tilde{P}_{\text{osc}} \\ \tilde{P}_{\beta} \end{bmatrix} = \begin{bmatrix} -\alpha_{\text{LPF}} & -\alpha_{\text{LPF}} & 0 \\ -2\alpha_{\text{LPF}} & -2\alpha_{\text{LPF}} & -\omega_{\text{osc}} \\ 0 & \omega_{\text{osc}} & 0 \end{bmatrix} \begin{bmatrix} \tilde{P}_0 \\ \tilde{P}_{\text{osc}} \\ \tilde{P}_{\beta} \end{bmatrix} + \begin{bmatrix} \alpha_{\text{LPF}} \\ 2\alpha_{\text{LPF}} \\ 0 \end{bmatrix} p(t) \tag{4.9}$$

where $\tilde{P}_{\beta}$ is a signal orthogonal to the oscillatory component $\tilde{P}_{\text{osc}}$. From (4.9), the dynamic response of the LPF-based method can be investigated. As before, the signal $p(t)$ is assumed to contain an average and a 1 Hz oscillatory component. The cut-off frequency α_{LPF} is then varied from 0.01 to 1 Hz in steps of 0.05 Hz to see the estimator's performance. The movement of the poles for the transfer function from the input (p) to the estimate of the oscillatory component ($\tilde{P}_{\text{osc}}$) is shown in Fig. 4.5. As clearly seen from the figure, the angular position of the poles from the imaginary axis starts to decrease for $\alpha_{\text{LPF}} > 0.4\omega_{\text{osc}}$ (marked as gray cross for clarity) indicating that its dynamic performance starts to deteriorate. It is here recommended to set the bandwidth of the filter one decade smaller than the frequency component to be estimated (for the specific case, α_{LPF} = 0.628 rad/s).

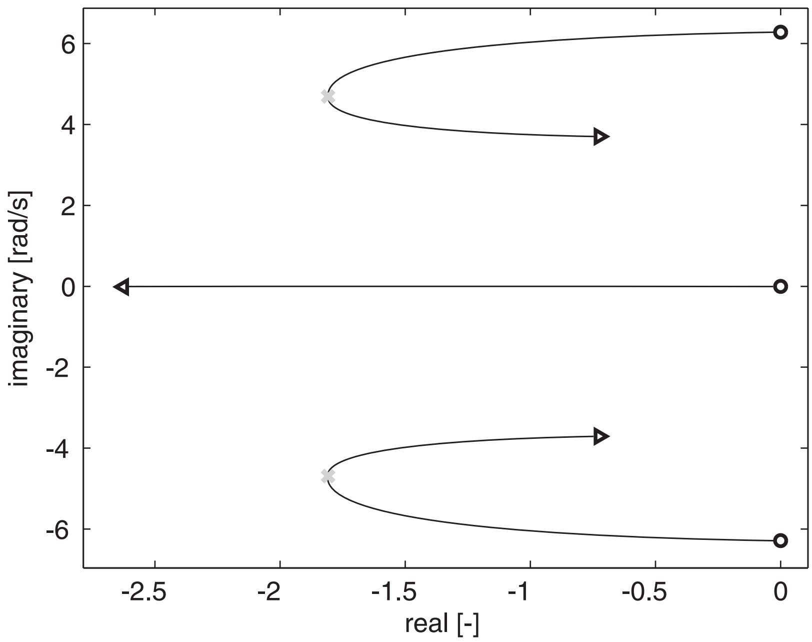

Fig. 4.5 Movement of poles for the transfer function from $p(t)$ to $\tilde{P}_{\text{osc}}(t)$ as α_{LPF} varies from 0.01 to 1 Hz in steps of 0.05 Hz; Poles start at '$\circ$' and move toward '$\triangleright$'.

4.2.3 Recursive Least Square (RLS) based method

A Recursive Least Square (RLS) algorithm is a time-domain approach (an adaptive filter in frequency domain) used to estimate signals based on a given model of the investigated system. Consider a generic input signal (either real or complex) y, modeled as the sum of its estimate $\tilde{y}$ and the estimation error d as in (4.10)

$$y(k) = \tilde{y}(k) + d(k) = \mathbf{\Phi}(k)\tilde{\mathbf{h}}(k-1) + d(k) \tag{4.10}$$

where $\tilde{\mathbf{h}}$ is the estimated state vector and $\mathbf{\Phi}$ is named the observation matrix that depends on the model of the signal. An update of the estimation state vector $\tilde{\mathbf{h}}$ is developed using the RLS algorithm in discrete time as

$$\tilde{\mathbf{h}}(k) = \tilde{\mathbf{h}}(k-1) + \mathbf{G}(k)\left[y(k) - \mathbf{\Phi}(k)\tilde{\mathbf{h}}(k-1)\right] \tag{4.11}$$

The gain matrix $\mathbf{G}$ is given by

$$\mathbf{G}(k) = \frac{\mathbf{R}(k-1)\mathbf{\Phi}^T(k)}{\lambda + \mathbf{\Phi}(k)\mathbf{R}(k-1)\mathbf{\Phi}^T(k)} \tag{4.12}$$

with the covariance matrix $\mathbf{R}$ expressed as

$$\mathbf{R}(k) = [\mathbf{I} - \mathbf{G}(k)\mathbf{\Phi}(k)]\,\mathbf{R}(k-1)/\lambda \tag{4.13}$$

The term λ is named forgetting factor and **I** is an identity matrix. As it can be seen in (4.11) - (4.13), the algorithm is performed recursively starting from an initial invertible matrix $\mathbf{R}(0)$ and initial state vector $\tilde{\mathbf{h}}(0)$ [41]. The RLS algorithm minimizes the cost function ξ defined as

$$\xi(k) = \sum_{n=0}^{k} |d(n)|^2 \lambda^{k-n} \tag{4.14}$$

In steady-state, the estimation speed of the RLS algorithm in rad/s is related to the sampling time (T_s) and the forgetting factor as

$$\alpha_\mathrm{RLS} = \frac{1-\lambda}{T_\mathrm{s}} \tag{4.15}$$

where α_RLS is the bandwidth of the estimator. Depending on the speed of estimation required, the forgetting factor can be chosen accordingly. For a constant forgetting factor, the matrices in (4.12) - (4.13) converge to their steady-state values depending on the observation matrix $\mathbf{\Phi}$ and the estimation speed will be decided by the value of the forgetting factor according to (4.15).

Using the same input signal $p(t)$ as in (4.1), the model of the input signal can be expressed as

$$p(t) = P_0(t) + P_d \cos(\theta_\mathrm{osc}(t)) - P_q \sin(\theta_\mathrm{osc}(t)) \tag{4.16}$$

where

$$P_d = P_\mathrm{ph}(t)\cos(\varphi), \quad P_q = P_\mathrm{ph}(t)\sin(\varphi) \tag{4.17}$$

For estimation of low-frequency power oscillation, the RLS algorithm in (4.10) - (4.13) can be easily applied by choosing $\tilde{\mathbf{h}}$ and $\mathbf{\Phi}$ as

$$\tilde{\mathbf{h}}(k) = \left[\begin{array}{ccc} \tilde{P}_0(k) & \tilde{P}_\mathrm{d}(k) & \tilde{P}_\mathrm{q}(k) \end{array}\right]^\mathrm{T} \tag{4.18}$$

$$\mathbf{\Phi}(k) = \left[\begin{array}{ccc} 1 & \cos(\theta_\mathrm{osc}(k)) & -\sin(\theta_\mathrm{osc}(k)) \end{array}\right] \tag{4.19}$$

From the estimated state vector $\tilde{\mathbf{h}}$, the oscillatory component estimate ($\tilde{P}_\mathrm{osc}$) can be obtained as

$$\tilde{P}_\mathrm{osc}(k) = \tilde{P}_\mathrm{ph}(k)\cos(\theta_\mathrm{osc}(k) + \tilde{\varphi}(k)) \tag{4.20}$$

where the amplitude and phase estimates of the oscillatory component are expressed as

$$\tilde{P}_\mathrm{ph}(k) = \sqrt{\left[\tilde{P}_\mathrm{d}(k)\right]^2 + \left[\tilde{P}_\mathrm{q}(k)\right]^2}, \qquad \tilde{\varphi}(k) = \tan^{-1}\left[\frac{\tilde{P}_\mathrm{q}(k)}{\tilde{P}_\mathrm{d}(k)}\right] \tag{4.21}$$

Note that once the RLS algorithm has converged to steady-state, it becomes a linear and time invariant system. Thus, the steady-state model of the RLS estimator will be derived and its performance will be compared with the LPF-based method. For this, the algorithm in (4.10) - (4.20) in steady-state can be expressed in state-space form as

$$\frac{d}{dt}\begin{bmatrix} \tilde{P}_0 \\ \tilde{P}_{\text{osc}} \\ \tilde{P}_\beta \end{bmatrix} = \begin{bmatrix} -\alpha_0 & -\alpha_0 & 0 \\ -2\alpha_{\text{a}} & -2\alpha_{\text{a}} & -\omega_{\text{osc}} \\ -\alpha_{\text{b}} & -\alpha_{\text{b}} + \omega_{\text{osc}} & 0 \end{bmatrix} \begin{bmatrix} \tilde{P}_0 \\ \tilde{P}_{\text{osc}} \\ \tilde{P}_\beta \end{bmatrix} + \begin{bmatrix} \alpha_0 \\ 2\alpha_{\text{a}} \\ \alpha_{\text{b}} \end{bmatrix} p(t) \tag{4.22}$$

with $\xi = \alpha_{\text{RLS}}/\omega_{\text{osc}}$, the constants α_0, α_{a} and α_{b} are given by

$$\alpha_0 = \alpha_{\text{RLS}}(1+\xi^2), \qquad \alpha_{\text{a}} = (1-\frac{\xi^2}{2})\alpha_{\text{RLS}}, \qquad \alpha_{\text{b}} = -3\xi\alpha_{\text{RLS}}$$

From (4.22), the dynamic response of the RLS-based method can be investigated. Considering the same signal $p(t)$, α_{RLS} is varied from 0.01 to 1 Hz in steps of 0.05 Hz to see the estimator's performance. The movement of the poles for the transfer function from the input ($p(t)$) to the estimate of the oscillatory component ($\tilde{P}_{\text{osc}}(t)$) is shown in Fig. 4.6. As clearly seen from the figure, the angular position of the poles from the imaginary axis increases continuously regardless of the value of α_{RLS} unlike the case for the LPF-based method. This indicates that the speed of response of the RLS-based method increase with higher value of α_{RLS} (or correspondingly lower value of λ).

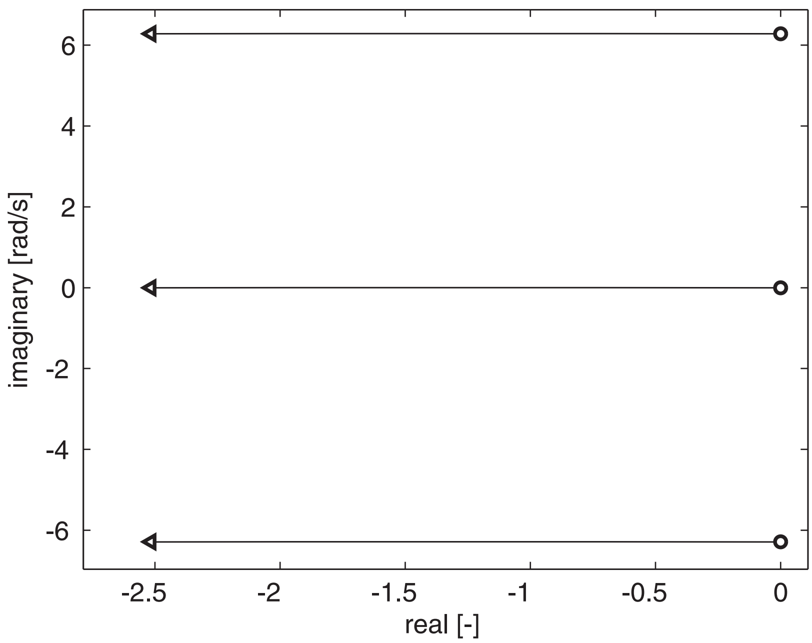

Fig. 4.6 Movement of poles for the transfer function from $p(t)$ to $\tilde{P}_{\text{osc}}(t)$ as α_{RLS} varies from 0.01 to 1 Hz in steps of 0.05 Hz; Poles start at '$\circ$' and move toward '$\triangleright$'.

When low bandwidth in the estimation (i.e. for $\alpha_{\text{RLS}} = \alpha_{\text{LPF}} << \omega_{\text{osc}}$) is acceptable, the two methods present similar dynamic performance. This can be seen from the state-space models where (4.22) is reduced to (4.9). If fast estimation is needed, the LPF-based method presents poor dynamic performance unlike the RLS-based method. Therefore, the RLS algorithm can be used to obtain faster estimation during rapid changes of the input signal and hence will be the preferred method in this work.

Even if faster estimation is obtained using RLS algorithm with small value of λ, its frequency selectivity should be investigated. For this purpose, the bode diagram of the transfer function from the input $p(t)$ to the average ($\tilde{P}_0$) and oscillatory ($\tilde{P}_{\mathrm{osc}}$) estimates are shown in Fig. 4.7. For all the cases, the bode diagram presents a 1 pu gain and $0°$ phase at the required frequency and a gain of 0 pu at the unwanted oscillation frequency. However, when increasing the estimation speed (decreasing λ), the frequency selectivity of the algorithm reduces. This means that using the conventional RLS algorithm, the estimation speed should be compromised to achieve good frequency selectivity and vise versa. For this reason, a modification to the algorithm is necessary to achieve fast estimation speed with only little penalty on the frequency selectivity.

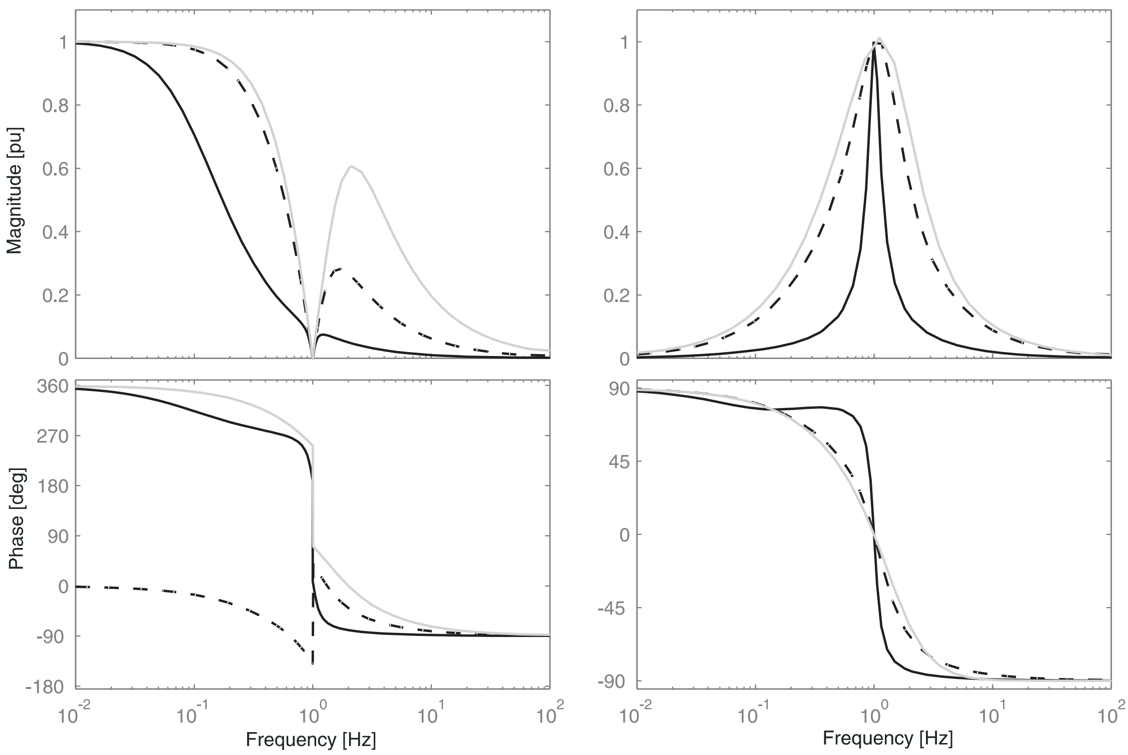

Fig. 4.7 Bode diagram for the transfer function from $p(t)$ to $\tilde{P}_0(t)$ (left) and $p(t)$ to $\tilde{P}_{\mathrm{osc}}(t)$ (right); Forgetting factor with $\alpha_{\mathrm{RLS}} = 0.1$ Hz (black solid), $\alpha_{\mathrm{RLS}} = 0.5$ Hz (black dashed) and $\alpha_{\mathrm{RLS}} = 1.0$ Hz (gray solid).

4.3 Improved RLS-based method

As already described in the previous section, the conventional RLS-based method with fixed forgetting factor λ will eventually converge to steady-state and its estimation speed cannot be changed during fast transients. Moreover, its performance in steady-state highly depends on knowledge of system parameters expressed in the observation matrix $\mathbf{\Phi}$. This calls for modifications in the conventional RLS algorithm that enables fast estimation during transients without compromising its frequency selectivity in steady-state as well as adaptation to input signal parameter changes.

4.3.1 Variable forgetting factor

In the conventional RLS-based method, a large forgetting factor results in low estimation speed with high frequency selectivity. Likewise, a small value of the forgetting factor results in the estimator to be fast but less selective [42]. Therefore, to achieve fast estimation when a change occurs in the input signal, the gain matrix of the RLS algorithm $\mathbf{G}$ in (4.12) must be increased for a short time. This can be done by resetting the covariance matrix $\mathbf{R}$ to a high value [41][43]. In this method, the covariance matrix to be used for the reset is chosen by trial and error and has to be selected case by case. Moreover, the behavior of the estimator response during transient is difficult to predict. An alternative solution is to use a variable forgetting factor as proposed in this work. With this approach, λ is varied in a controlled way depending on the input and this helps to know the behavior of the estimator's response during transient and steady-state.

When the RLS algorithm is in steady-state, its bandwidth is determined by the steady-state forgetting factor (λ_{ss}) according to (4.15). If a fast change is detected in the input (i.e. if the absolute error $|d(k)|$ in (4.10) exceeds a pre-defined threshold d_{th}), λ can be modified to a smaller value, here denoted as "transient forgetting factor (λ_{tr})". Thus, by using the properties of the step response for a high-pass filter, λ will be slowly increased back to its steady-state value λ_{ss} in order to guarantee the selectivity of the algorithm. The parameters λ_{ss}, λ_{tr} as well as the time constant for the high-pass filter τ_{hp} determine the performance of the RLS algorithm in the transient conditions. Figure 4.8 shows the resetting method for the forgetting factor and its variation in time when a change is detected in the input signal.

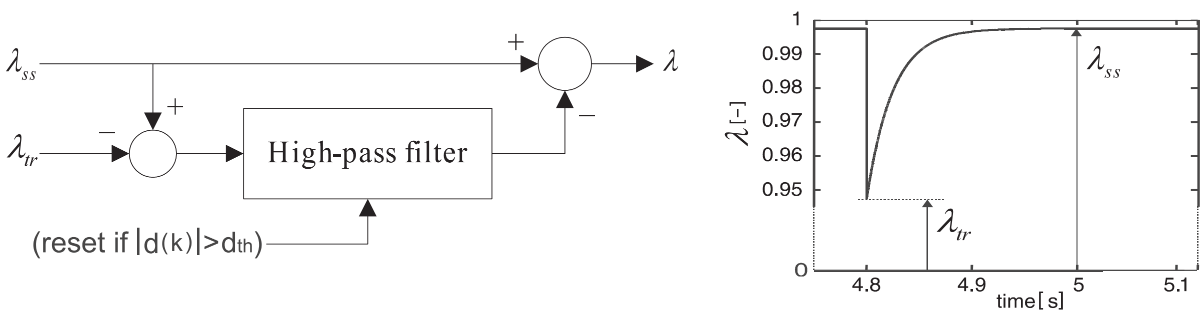

Fig. 4.8 Resetting method to vary the forgetting factor during transient. Left: Block diagram; Right: Variation of λ with τ_{hp} = 0.04 s.

Once the value of λ_{ss} is chosen based on the steady-state performance requirement of the algorithm, the value of λ_{tr} and τ_{hp} can be determined based on the required transient estimation speed. Evaluation of the performance of the algorithm for different choices of the parameters λ_{tr} and τ_{hp} will be made in this section using the example in Section 4.2. In this example, the input signal for the estimation algorithm was the transmitted active power $p(t)$, which consists of an average term (P_0) and a 1 Hz oscillatory components (P_{osc}). The model in (4.11) - (4.13) has been used for the estimation with a variable forgetting factor. The aim of the estimator is to quickly separate these two signal components accurately in the presence of noise.

During steady-state operations, the bandwidth of the RLS is set to a low value, meaning that the forgetting factor will be close to unity. For an oscillating frequency of 1 Hz, the steady-state forgetting factor is set equal to $\lambda = \lambda_{\mathrm{ss}} = 0.9995$, corresponding to a bandwidth of 0.4 Hz for a sampling time T_{s} = 0.2 ms according to (4.15). This gives the performance of the estimator to be selective, less sensitive to noise and at the same time adaptive to slow changes in the input signal. To evaluate the transient performance of the algorithm for different choices of the parameters λ_{tr} and τ_{hp}, two types of input signals (one noisy free and another one noisy) are considered. For each input, the settling time for the estimator as a function of λ_{tr} and τ_{hp} is shown in Fig. 4.9. With T_{s} = 0.2 ms and λ_{ss} = 0.9995, the transient bandwidth of the estimator, α_{tr} is varied between 5 and 100 Hz in steps of 5 Hz, while τ_{hp} is varied between 5 and 100 ms in steps of 5 ms. The transient forgetting factor, λ_{tr} is calculated using α_{tr} (expressed in rad/s) from expression (4.15).

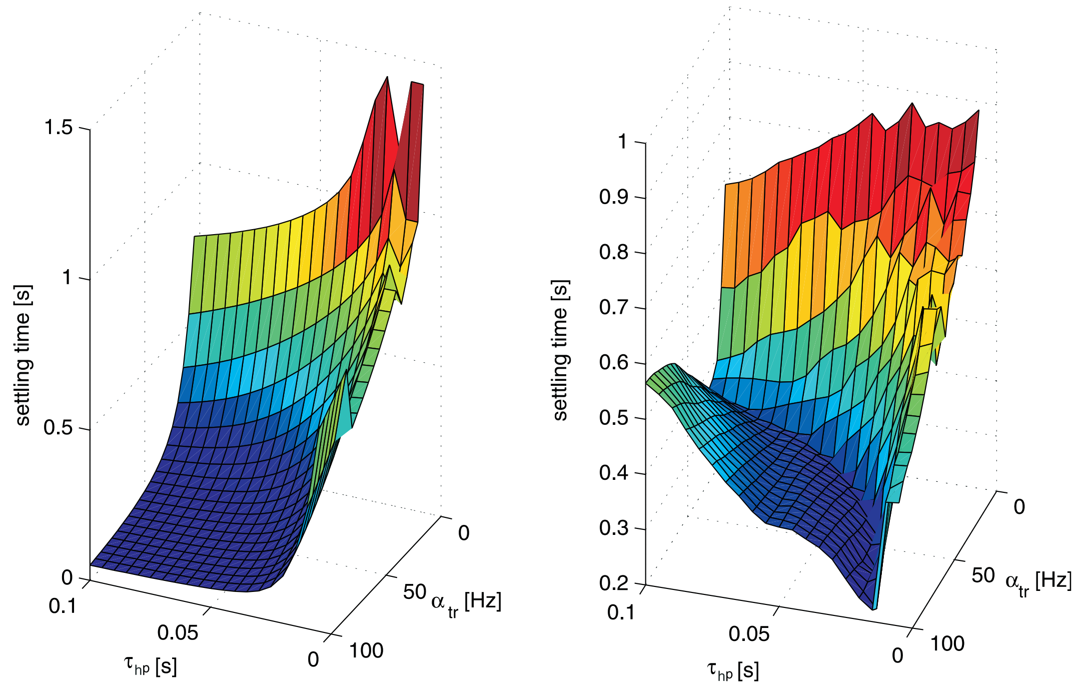

Fig. 4.9 Transient estimation speed for a step change in the input using variable forgetting factor. Left: ideal input signal; Right: input signal with 20 dB noise-to-signal ratio.

As it can be seen in Fig. 4.9, higher α_{tr} and higher τ_{hp} results in faster response in the case of noise free input signal. When noise is included in the input signal, the estimation speed starts to decrease beyond some values of α_{tr} and τ_{hp}. This is due to the estimators tendency to follow the noise, leading to an increase of the settling time. The value that gives a compromised response time for both signals lies in the middle. Depending on the required estimation speed and noise rejection performance, an appropriate value for λ_{tr} and τ_{hp} can be chosen. For this application, a value of $\lambda_{\mathrm{tr}} = 0.8995$ corresponding to $\alpha_{\mathrm{tr}} = 80$ Hz and $\tau_{\mathrm{hp}} = 0.04$ s have been selected.

4.3.2 Frequency adaptation

The RLS algorithm described in Section 4.2.3 relies on the information in the observation matrix $\mathbf{\Phi}$ to correctly estimate the signal components. The observation matrix $\mathbf{\Phi}$, which contains information about the model of the signal according to (4.10), usually assumes some system parameters. When these parameters change, the performance of the algorithm will be affected and an updating mechanism for the signal model is important. For example, to estimate the oscillatory component P_{osc} from the measured input signal p using the RLS algorithm in (4.16) - (4.20), the oscillation frequency ω_{osc} should be known. Any change in the system, resulting in a different oscillation frequency, will affect the steady-state performance of the RLS algorithm. To overcome the problem, the RLS algorithm is further improved by implementing a frequency adaptation mechanism. Using the same example and parameter selection as in Section 4.3.1, the steady-state frequency characteristic of the estimator's transfer function from the input to the average and oscillatory component is shown in Fig. 4.10. The transfer functions have 1 pu gain and $0°$ phase-shift at the estimated frequency component and 0 pu gain at the other frequency component in the model. This results in a correct extraction of the average and oscillatory components in steady-state for accurate knowledge of the oscillation frequency.

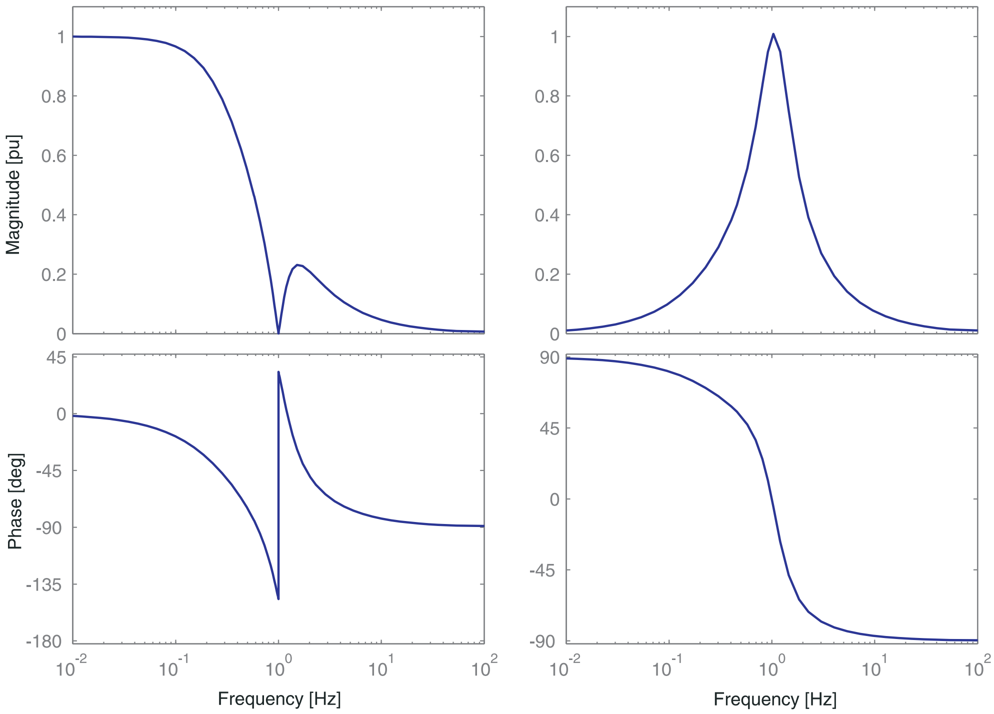

Fig. 4.10 Bode diagram of the steady-state RLS-based estimator transfer function. Left: from $p(t)$ to $\tilde{P}_0(t)$; Right: from $p(t)$ to $\tilde{P}_{\text{osc}}(t)$.

If the frequency content of the input is not accurately known, the estimator will give rise to a phase and amplitude error in the estimated quantities. Note that a correct estimation of the phase of the oscillatory component is a crucial point in applications like POD. Using the information in the phase estimate $\tilde{\varphi}$, the true oscillation frequency can be tracked by using a frequency estimator as the one in Fig. 4.11.

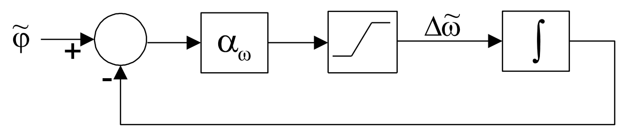

Fig. 4.11 Block diagram for updating the oscillation frequency.

The corrective term $\Delta\tilde{\omega}$ is limited and fed back to the RLS algorithm to update the oscillation frequency $\tilde{\omega}_{\text{osc}}$ as

$$\tilde{\omega}_{\text{osc}} = \omega_{\text{osc0}} + \Delta\tilde{\omega} \tag{4.23}$$

The term ω_{osc0} represents the initial assumed oscillation frequency and the transfer function from the estimated phase ($\tilde{\varphi}$) to the estimated change in frequency ($\Delta\tilde{\omega}$) is given by

$$\frac{\Delta\tilde{\omega}}{\tilde{\varphi}} = \frac{\alpha_\omega s}{\alpha_\omega + s} \tag{4.24}$$

If the initial assumed oscillation frequency is correct, the estimated average and phasor components $[\tilde{P}_0, \tilde{P}_d, \tilde{P}_q]$ will be constants or slowly varying quantities. Correspondingly, the estimated phase $\tilde{\varphi}$ will be a constant value resulting $\Delta\tilde{\omega} = 0$ in steady-state. However, if a change in the true oscillation frequency $\Delta\omega$ occurs, the estimates $[\tilde{P}_0, \tilde{P}_d, \tilde{P}_q]$ will contain a disturbance term at the true oscillatory frequency in addition to a slowly varying quantity. This is due to the fact that the estimator's transfer function cannot have zero gain at the true oscillation frequency for the estimates ($[\tilde{P}_0, \tilde{P}_d, \tilde{P}_q]$) due to wrong assumption of the initial oscillation frequency. Similarly, the estimate $\tilde{P}_{\text{osc}}$ will have an amplitude and phase error. If A_ω and φ_ω represent the gain and phase of the estimator's transfer function at the true oscillation frequency respectively, the oscillatory estimate in steady-state can be expressed as

$$\tilde{P}_{\text{osc}}(t) = A_\omega P_{\text{ph}} \cos(\omega_{\text{osc}} t + \varphi + \varphi_\omega) = \tilde{P}_{\text{ph}}(t) \cos(\omega_{\text{osc0}} t + \tilde{\varphi}(t)) \tag{4.25}$$

The terms P_{ph}, φ and ω_{osc} represent the true amplitude, phase and frequency of the oscillatory component, respectively. As it can be seen in (4.25), the frequency of the oscillation is preserved in the estimate. The idea here is to estimate the corrective term $\Delta\tilde{\omega}$ from the estimated phasors ($\tilde{P}_d, \tilde{P}_{\text{q}}$). From (4.25) and using the definition in (4.20) and (4.21), the phase estimate $\tilde{\varphi}$ can be expressed as

$$\tilde{\varphi}(t) = \tan^{-1}\left[\frac{\tilde{P}_q(t)}{\tilde{P}_d(t)}\right] \approx (\Delta\omega + d_\omega)t \tag{4.26}$$

The disturbance term at the true oscillation frequency in the estimates ($\tilde{P}_d, \tilde{P}_q$) results in a disturbance d_ω in the phase estimate $\varphi(t)$ at twice the true oscillation frequency. As it can be seen from (4.26), the phase estimate is a function the frequency error $\Delta\omega$ and this has to be extracted. If the disturbance term d_ω is neglected, the transfer function from the actual frequency error $\Delta\omega$ to the estimated frequency error $\Delta\tilde{\omega}$ can be expressed as

$$\frac{\Delta\tilde{\omega}}{\Delta\omega} \approx \frac{\alpha_\omega}{s+\alpha_\omega} \tag{4.27}$$

Using (4.27), the bandwidth of the frequency controller (α_ω) can be chosen. To be able to filter the disturbance term, the bandwidth should be set below the oscillation frequency. For an assumed oscillation frequency ω_{osc0}, choosing $\alpha_\omega = 0.2\omega_{\text{osc0}}$ gives the frequency correction controller a cut-off frequency of a decade below the frequency of the disturbance term d_ω.

4.3.3 Multiple oscillatory components

The investigated RLS estimator has been derived under the assumption of a single oscillatory frequency component in the input signal. Assuming that the input signal p contains N oscillatory components, (4.1) must be modified as

$$p(t) = P_0(t) + \sum_{i=1}^{N} P_{\text{osc},i} = P_0(t) + \sum_{i=1}^{N} P_{\text{ph},i}(t)\cos\left[\omega_{\text{osc},i}t + \varphi_i(t)\right] \tag{4.28}$$

where the i^{th} oscillatory component, $P_{\text{osc},i}$ (with $i = 1, ..., N$) is expressed in terms of its amplitude ($P_{\text{ph},i}$), frequency ($\omega_{\text{osc},i}$) and phase (φ_i). Using the model in (4.28), the RLS algorithm described in the previous sections (including variable forgetting factor and frequency adaptation for each considered oscillatory component) can be modified as described in Fig. 4.12.

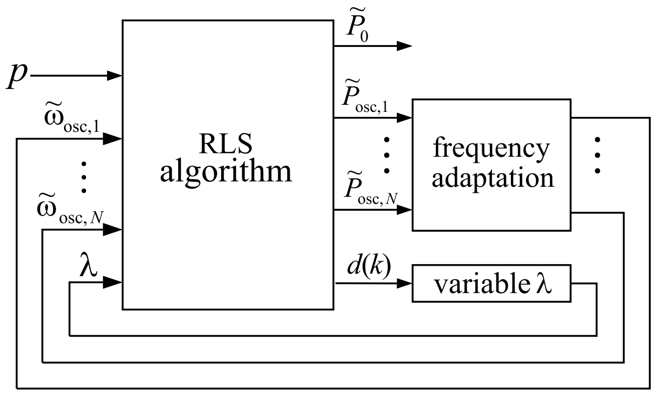

Fig. 4.12 Block diagram of the modified RLS estimator for multiple oscillatory components.

As an example, the input signal p is assumed to be comprised of an average component and two oscillatory components with frequency $\omega_{\text{osc},1}$ and $\omega_{\text{osc},2}$, respectively. Hence, the RLS algorithm in (4.10) - (4.13) can be easily applied by choosing the state vector, $\tilde{\mathbf{h}}$ as

$$\tilde{\mathbf{h}} = [\ \tilde{P}_0 \quad \tilde{P}_{d,1} \quad \tilde{P}_{q,1} \quad \tilde{P}_{d,2} \quad \tilde{P}_{q,2}\ ]^{\text{T}} \tag{4.29}$$

where the phasor components, $\tilde{P}_{d,i}$ and $\tilde{P}_{q,i}$ with $i = [1, 2]$ are defined as

$$\tilde{P}_{d,i} = \tilde{P}_{\text{ph},i}\cos(\theta_{\text{osc},i}), \qquad \tilde{P}_{q,i} = \tilde{P}_{\text{ph},i}\sin(\theta_{\text{osc},i}) \tag{4.30}$$

Defining the oscillation angles ($\theta_{\text{osc},1} = \omega_{\text{osc},1}t$ and $\theta_{\text{osc},2} = \omega_{\text{osc},2}t$), the covariance matrix ($\mathbf{\Phi}$) for the algorithm is similarly modified as

$$\mathbf{\Phi} = \begin{bmatrix} 1 & \cos(\theta_{\text{osc},1}) & -\sin(\theta_{\text{osc},1}) & \cos(\theta_{\text{osc},2}) & -\sin(\theta_{\text{osc},2}) \end{bmatrix} \tag{4.31}$$

From the estimated state vector $\tilde{\mathbf{h}}$, the oscillatory component estimates ($\tilde{P}_{\text{osc},1}$ and $\tilde{P}_{\text{osc},2}$) can be obtained as

$$\tilde{P}_{\text{osc},1} = \tilde{P}_{d,1}\cos(\theta_{\text{osc},1}) - \tilde{P}_{q,1}\sin(\theta_{\text{osc},1}), \quad \tilde{P}_{\text{osc},2} = \tilde{P}_{d,2}\cos(\theta_{\text{osc},2}) - \tilde{P}_{q,2}\sin(\theta_{\text{osc},2}) \tag{4.32}$$

As described earlier, the RLS algorithm becomes linear and time invariant in steady-state. Thus, the steady-state model of the RLS estimator in (4.28) - (4.32) can be expressed in state-space form as

$$\frac{d}{dt}\begin{bmatrix} \tilde{P}_0 \\ \tilde{P}_{\text{osc},1} \\ \tilde{P}_{\beta,1} \\ \tilde{P}_{\text{osc},2} \\ \tilde{P}_{\beta,2} \end{bmatrix} = \begin{bmatrix} -\alpha_{0,1} & -\alpha_{0,1} & 0 & -\alpha_{0,1} & 0 \\ -\alpha_{\text{a},1} & -\alpha_{\text{a},1} & -\omega_{\text{osc},1} & -\alpha_{\text{a},1} & 0 \\ -\alpha_{\text{b},1} & -\alpha_{\text{b},1} + \omega_{\text{osc},1} & 0 & -\alpha_{\text{b},1} & 0 \\ -\alpha_{\text{a},2} & -\alpha_{\text{a},2} & 0 & -\alpha_{\text{a},2} & -\omega_{\text{osc},2} \\ -\alpha_{\text{b},2} & -\alpha_{\text{b},2} & 0 & -\alpha_{\text{b},2} + \omega_{\text{osc},2} & 0 \end{bmatrix} \cdots$$
$$\begin{bmatrix} \tilde{P}_0 \\ \tilde{P}_{\text{osc},1} \\ \tilde{P}_{\beta,1} \\ \tilde{P}_{\text{osc},2} \\ \tilde{P}_{\beta,2} \end{bmatrix} + \begin{bmatrix} \alpha_{0,1} \\ \alpha_{\text{a},1} \\ \alpha_{\text{b},1} \\ \alpha_{\text{a},2} \\ \alpha_{\text{b},2} \end{bmatrix} p(t) \tag{4.33}$$

where $\tilde{P}_{\beta,1}$ and $\tilde{P}_{\beta,2}$ represent signals components orthogonal to the oscillatory components $\tilde{P}_{\text{osc},1}$ and $\tilde{P}_{\text{osc},2}$, respectively. Using the steady-state RLS estimator bandwidth α_{RLS} and the oscillation frequencies $\omega_{\text{osc},1}$ and $\omega_{\text{osc},2}$, the constants are given by

$$\alpha_{0,1} = \frac{\alpha_{\text{RLS}}(\alpha_{\text{RLS}}^2+\omega_{\text{osc},1}^2)(\alpha_{\text{RLS}}^2+\omega_{\text{osc},2}^2)}{\omega_{\text{osc},1}^2\omega_{\text{osc},2}^2}$$

$$\alpha_{a,1} = \frac{\alpha_{\text{RLS}}\left[\alpha_{\text{RLS}}^4+2\omega_{\text{osc},1}^2(\omega_{\text{osc},1}^2-\omega_{\text{osc},2}^2)+\alpha_{\text{RLS}}^2(\omega_{\text{osc},2}^2-9\omega_{\text{osc},1}^2)\right]}{\omega_{\text{osc},1}^4-\omega_{\text{osc},1}^2\omega_{\text{osc},2}^2}$$

$$\alpha_{b,1} = \frac{\alpha_{\text{RLS}}^2(5\alpha_{\text{RLS}}^2-7\omega_{\text{osc},1}^2+3\omega_{\text{osc},2}^2)}{\omega_{\text{osc},1}^3-\omega_{\text{osc},1}\omega_{\text{osc},2}^2}$$

$$\alpha_{a,2} = \frac{\alpha_{\text{RLS}}\left[\alpha_{\text{RLS}}^4+2\omega_{\text{osc},2}^2(\omega_{\text{osc},2}^2-\omega_{\text{osc},1}^2)+\alpha_{\text{RLS}}^2(\omega_{\text{osc},1}^2-9\omega_{\text{osc},2}^2)\right]}{\omega_{\text{osc},2}^4-\omega_{\text{osc},1}^2\omega_{\text{osc},2}^2}$$

$$\alpha_{b,2} = \frac{\alpha_{\text{RLS}}^2(5\alpha_{\text{RLS}}^2-7\omega_{\text{osc},2}^2+3\omega_{\text{osc},1}^2)}{\omega_{\text{osc},2}^3-\omega_{\text{osc},1}^2\omega_{\text{osc},2}}$$

For selective estimation of the various frequency components, the steady-state bandwidth of the estimator is calculated from the smallest frequency gap in the input signal. As an example, consider the same signal $p(t)$ with an average component, a 1 Hz and 1.7 Hz oscillatory components. The smallest frequency gap in the input signal is 0.7 Hz that exists between the two oscillatory components. Hence the steady-state bandwidth is calculated as 40% of the minimum frequecy gap as $\alpha_{\mathrm{RLS}} = 0.28$ Hz. Using this bandwidth, the bode diagram of the RLS algorithm to estimatate the average and oscillatory components is shown in Fig. 4.13 where a selective and accurate extraction of each frequency component can be achieved.

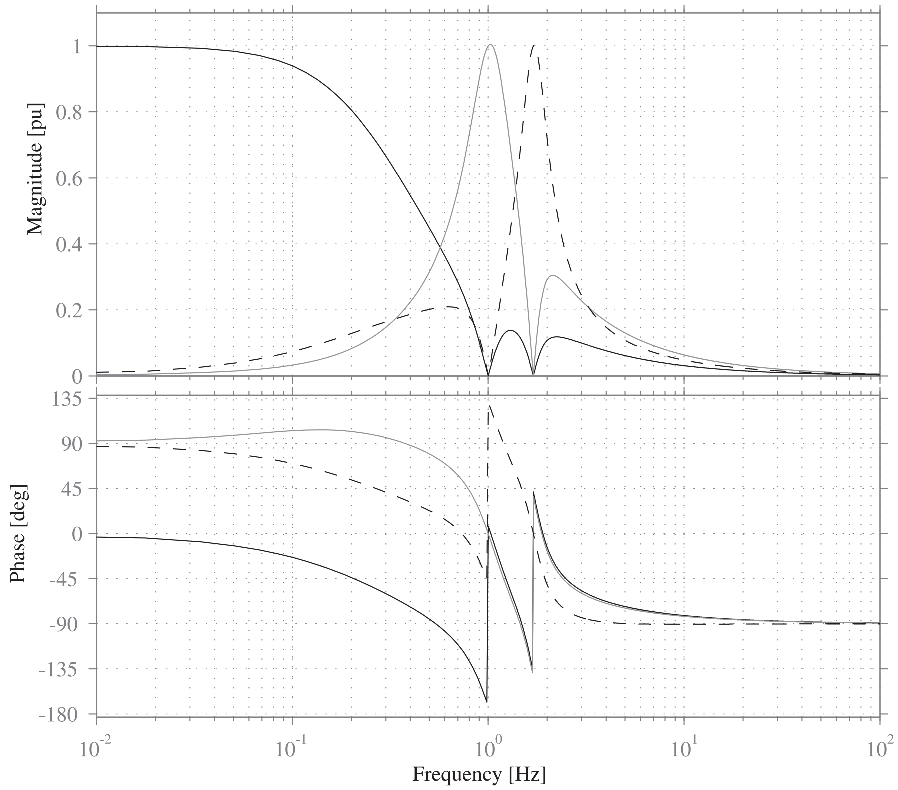

Fig. 4.13 Bode diagram for the transfer function from $p(t)$ to $\tilde{P}_0(t)$ (black solid), $p(t)$ to $\tilde{P}_{\text{osc},1}(t)$ (gray solid) and $p(t)$ to $\tilde{P}_{\text{osc},2}(t)$ (black dashed).

4.4 Application examples on signal estimation

In this section, application examples for signal estimation using the improved RLS-based method will be described.

4.4.1 Low-frequency electromechanical oscillations

To evaluate the performance of the improved RLS-based method for estimation of low-frequency electromechanical oscillations, simulation results are presented here for both ideal and disturbed conditions.

Single-oscillation mode in ideal conditions

The first test is made using an input signal as the one depicted in Fig. 4.14. As shown in the figure, the input signal is initially constituted by a 1 pu dc component only. At $t = 3$ s, the average component is stepped down to 0.7 pu and an additional oscillatory component having characteristic frequency of 1 Hz is added to the input. Figure 4.15 shows the estimated average and oscillatory component of the input signal (in amplitude and phase) for different choices of the forgetting factor λ when using the conventional RLS algorithm. In this simulation, three λ values of λ = 0.9995 (black solid), λ = 0.9987 (gray solid) and λ = 0.9975 (black dashed) that correspond to a steady-state bandwidth of 0.4 Hz, 1.0 Hz, and 2.0 Hz, respectively, are considered.

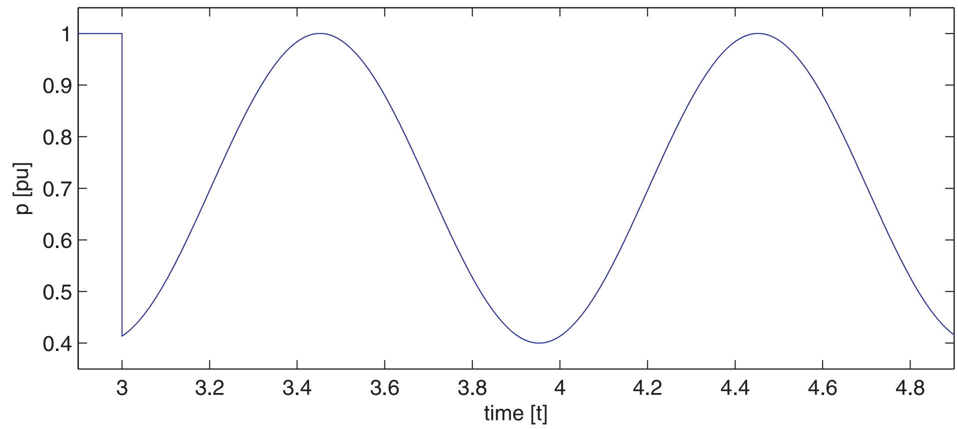

Fig. 4.14 Input signal for simulation.

As the results in Fig. 4.15 show, by using the conventional RLS with a fixed forgetting factor, it is not possible to achieve both estimation speed and frequency selectivity. As the forgetting factor is reduced, estimation speed will be improved whereas the selectivity is reduced and vise versa. This can be improved by using a variable forgetting factor as described in Section 4.3.1. Figure 4.16 shows the performance of the improved RLS method with the estimator parameters chosen as ($\lambda_{ss} = 0.9995, \lambda_{tr} = 0.8995$ and $\tau_{hp} = 0.04$ s for T_s = 0.2 ms). As it can be seen from the results in Figs. 4.15 and 4.16, the improved RLS-based method gives a fast estimation with a better frequency selectivity than the conventional RLS (See Fig. 4.15).

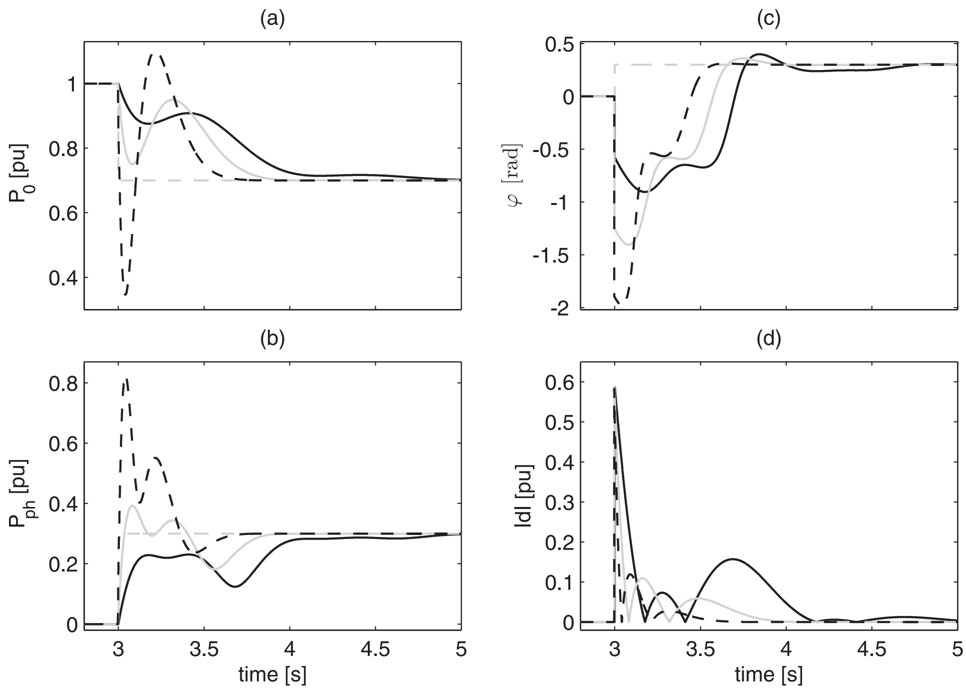

Fig. 4.15 Estimate for the average (plot a), amplitude (plot b), phase (plot c) and estimation error (plot d) by conventional RLS with forgetting factor $\lambda = 0.9995$ (black solid), $\lambda = 0.9987$ (gray solid), $\lambda = 0.9975$ (black dashed), input signals (gray dashed); the actual oscillation frequency is used in the simulation.

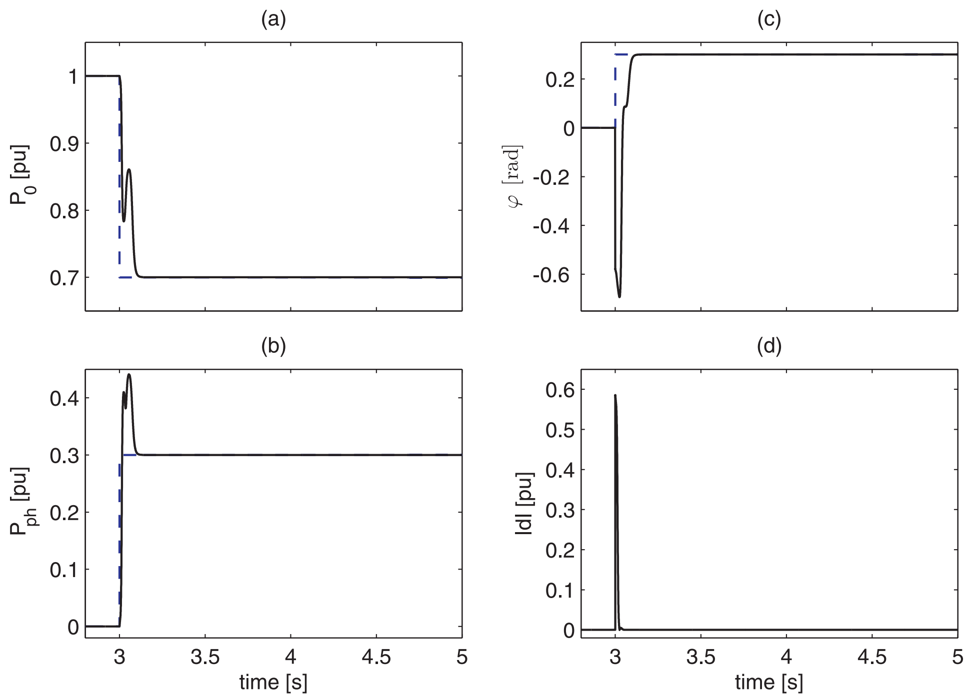

Fig. 4.16 Estimate for the average (plot a), amplitude (plot b), phase (plot c) and estimation error (plot d) using the improved RLS method ($\lambda_{\mathrm{ss}} = 0.9995, \lambda_{\mathrm{tr}} = 0.8995$ and $\tau_{\mathrm{hp}} = 0.04$ s); dashed: inputs, solid: estimates; the actual oscillation frequency is used in the simulation.

Multiple-oscillation modes in disturbed conditions

A second simulation is performed using a more realistic input signal with multiple oscillatory modes in the presence of measurement noise and a modeling error. The input signal represents the measured power on a line in a simplified three-area power system (to be discussed in Chapter 6), where two oscillatory components with a frequency of 1 Hz and 1.7 Hz are excited due to a three-phase short-circuit fault in the system. A 5 Hz frequency component not included in the signal model (with its amplitude selected as 20% of the 1.7 Hz oscillatory component) and a measurement noise (with a signal to noise ratio of 20 dB) are added as disturbences in the measured input signal to test the filtering performance of the algorithm against undesired frequency components. The resulting signal, shown in Fig. 4.17, is used as an input for the estimator. The aim of the estimation algorithm is to extract the desired frequency components (the two oscillatory modes in this case) in spite of the measurement noise and undesired low-frequency component in the input signal.

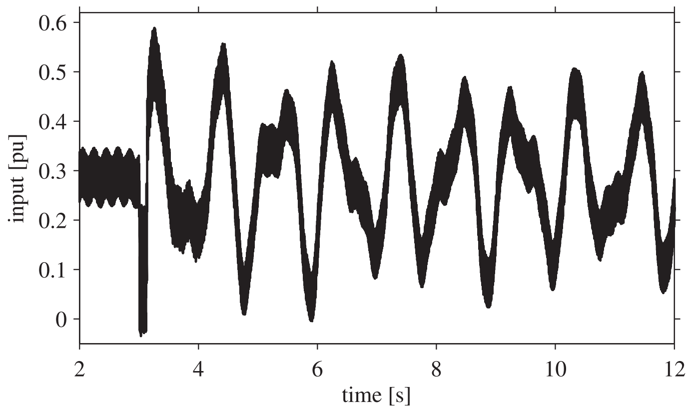

Fig. 4.17 Input signal with two oscillatory modes for simulation.

To appreciate the advantages of the improved algorithm with variable forgetting factor, the performance of two conventional RLS algorithms with fixed forgetting factor is also included. The parameters for the variation of the forgetting factor are chosen as $\lambda_{\text{ss}} = 0.9997$, $\lambda_{\text{tr}} = 0.9497$ and $\tau_{\text{hp}} = 0.03$ s. For the conventional RLS algorithm, a value of $\lambda = 0.9997$ and $\lambda = 0.9975$ which corresponds to a steady-state bandwidth of 0.2 Hz and 2 Hz, respectively, are considered. The performance of the estimators to extract the oscillatory components is shown in Figs. 4.18 - 4.19. The conventional RLS algorithm with higher λ is characterized by a slow transient response and good steady-state filtering (see gray curves in Fig. 4.18). On the other hand, the conventional RLS algorithm with lower λ improves the transient response, where the steady-state filtering performance is compromised as it can be observed in the estimates (see gray curves in Fig. 4.19). By using the proposed algorithm with variable λ, a fast transient response without reducing the steady-state filtering performance is achieved (see black curves in Figs. 4.18 - 4.19). It can also be seen from the obtained results that the measurement noise and the non-desired 5 Hz oscillation component are effectively filtered by the estimation algorithm.

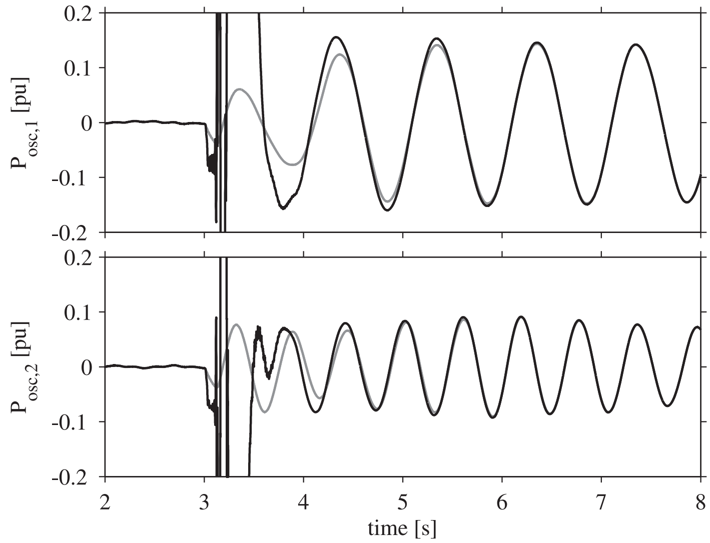

Fig. 4.18 Estimation of first (top) and second (bottom) oscillatory components using RLS algorithm with variable λ (black) and fixed forgetting factor, $\lambda = 0.9997$ (gray).

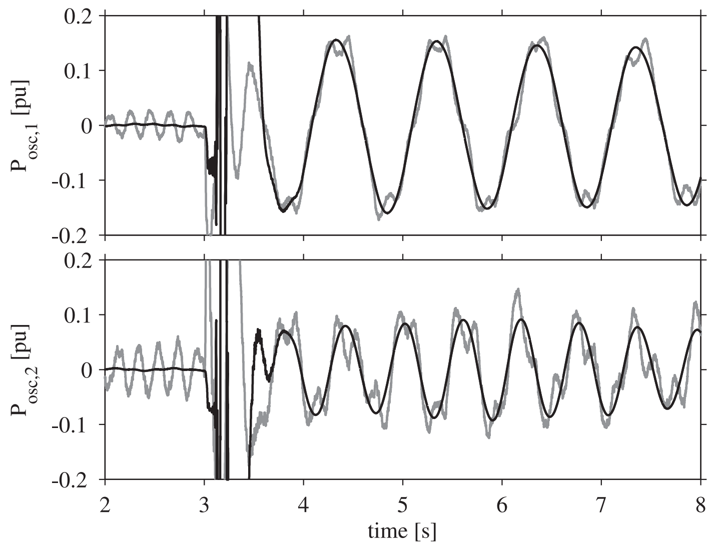

Fig. 4.19 Estimation of first (top) and second (bottom) oscillatory components using RLS algorithm with variable λ (black) and fixed forgetting factor, $\lambda = 0.9975$ (gray).

A final set of simulations is performed considering an input signal like the one depicted in Fig. 4.17. For this simulation, it is assumed that the power oscillation shown in Fig. 4.17 is damped by a shunt-connected FACTS controller installed in the power system. The aim of this simulation is to investigate the dynamic performance of the proposed estimator when the characteristic parameters of the input signal such as its amplitude, phase and frequency change in time due to POD action. Moreover, the initial oscillation frequencies are assumed to be 0.7 Hz and 2.0 Hz, which represents an error of ± 0.3 Hz from the actual values to test the frequency adaptation mechanism. For comparison, the performance of the improved RLS algorithm (i.e., with variable λ and a frequency adaptation) together with the conventional RLS algorithm (i.e. a fixed forgetting factor, $\lambda = 0.9997$ and without frequency adaptation) is presented.

The variation of λ and estimation of the oscillation frequencies for the improved RLS algorithm is shown in Fig. 4.20, whereas the performance of the conventional and improved RLS algorithms is presented in Fig. 4.21. Observing the results from the conventional RLS algorithm, the estimation is not selective as indicated by the existence of more than one frequency component in the estimate of each oscillatory component (see plot (a) in Fig. 4.21). The slow and inaccurate estimation can be noticed from the mismatch between the input signal and its estimate (see plot (b) in Fig. 4.21). On the other hand, the improved RLS algorithm (see plots (c) and (d) in Fig. 4.21) provides accurate estimation of the desired oscillatory modes despite the presence of disturbances, modeling error and changes in the parameters of the input signal.

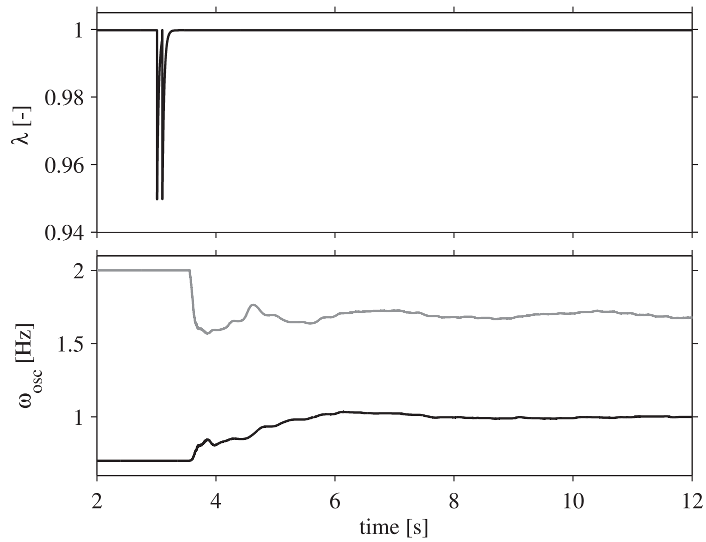

Fig. 4.20 Variation of parameters of improved RLS algorithm; Top: variation of forgetting factor; Bottom: estimate of the first oscillation frequency (black) and second oscillation frequency (gray).

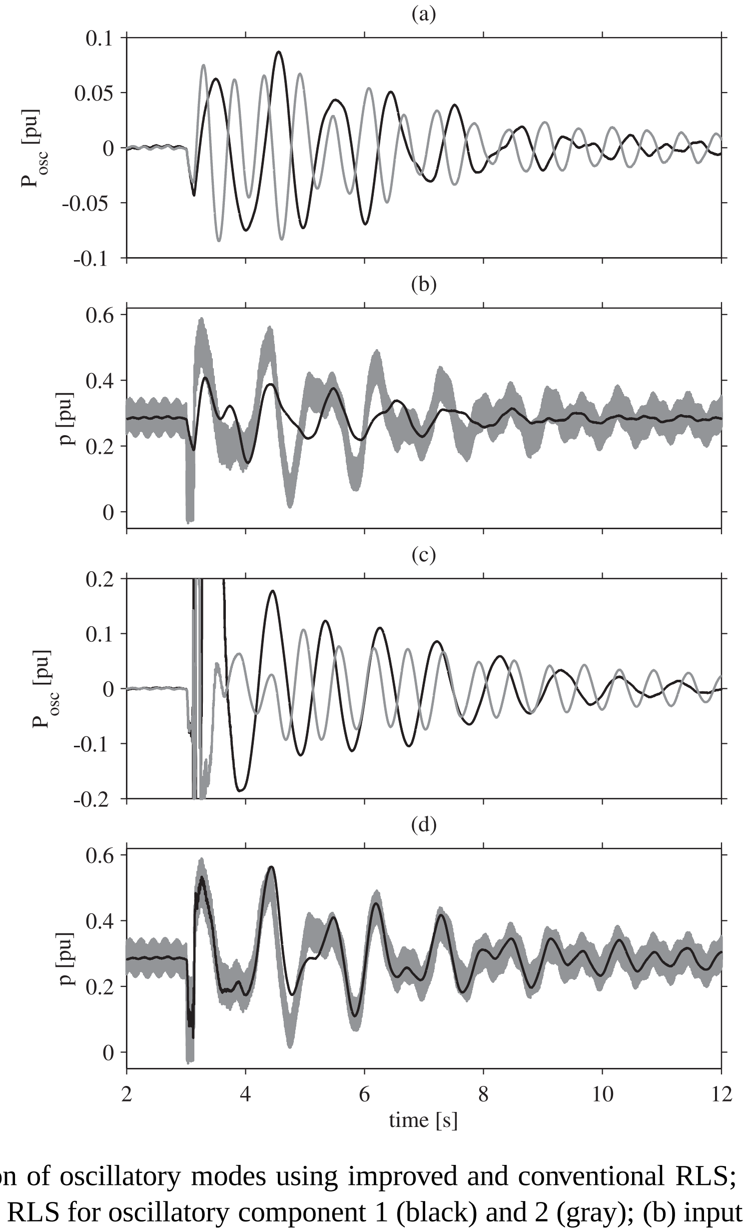

Fig. 4.21 Estimation of oscillatory modes using improved and conventional RLS; (a) estimate by conventional RLS for oscillatory component 1 (black) and 2 (gray); (b) input signal (gray) and its estimate by conventional RLS (black);(c) estimate by improved RLS for oscillatory component 1 (black) and 2 (gray); (d) input signal (gray) and its estimate by improved RLS (black);.

4.4.2 Sequence and harmonic components

In this section, estimation of harmonic and sequence components in a three-phase system using the improved RLS-based algorithm will be described. When the grid voltage is unbalanced (for example, due to unbalanced loads or unbalanced faults), a 50 Hz negative-sequence component exists in the grid voltage and a fast estimation algorithm is needed to separate the negative-sequence component for control or synchronization purposes [44][45]. Assuming that the zero-sequence component in the measured signal can be neglected, the complex grid voltage $\underline{e}_{\mathrm{g}}^{\alpha\beta}$ in the stationary $\alpha\beta$ coordinate system can be written as the sum of its positive- and negative-sequence components as

$$\underline{e}_{\mathrm{g}}^{\alpha\beta}(t) = \underline{E}_{\mathrm{p}}(t)e^{j\theta_{\mathrm{g}}(t)} + \underline{E}_{\mathrm{n}}(t)e^{-j\theta_{\mathrm{g}}(t)} \tag{4.34}$$

Calling the grid frequency ω with $\theta_{\mathrm{g}}(t) = \omega t$, $\underline{E}_{\mathrm{p}}$ and $\underline{E}_{\mathrm{n}}$ are the positive- and negative-sequence component phasors, respectively. Therefore, the model in (4.35) can be used to set up an RLS algorithm as described in Section 4.2.3 (including the modifications in Section 4.3) to estimate the positive and negative-sequence components. For this particular case, the state vector to be estimated and the observation matrix are given as in (4.36) and (4.37), where the updates are performed recursively as in (4.11) - (4.13).

$$\underline{e}_{\mathrm{g}}^{\alpha\beta}(k) = \underline{\tilde{E}}_{\mathrm{p}}(k)e^{j\tilde{\theta}_{\mathrm{g}}(k)} + \underline{\tilde{E}}_{\mathrm{n}}(k)e^{-j\tilde{\theta}_{\mathrm{g}}(k)} + \underline{d}(k) = \mathbf{\Phi}(k)\tilde{\mathbf{h}}(k-1) + \underline{d}(k) \tag{4.35}$$

$$\tilde{\mathbf{h}}(k) = \begin{bmatrix} \underline{\tilde{E}}_{\mathrm{p}}(k) & \underline{\tilde{E}}_{\mathrm{n}}(k) \end{bmatrix}^{\mathrm{T}} \tag{4.36}$$

$$\mathbf{\Phi}(k) = \begin{bmatrix} e^{j\tilde{\theta}_{\mathrm{g}}(k)} & e^{-j\tilde{\theta}_{\mathrm{g}}(k)} \end{bmatrix} \tag{4.37}$$

For a constant grid frequency with nominal value $\omega = \omega_{\mathrm{N}}$, the estimator's steady-state frequency response is shown in Fig. 4.22 (left) for the positive-sequence component, where a gain of 1 pu and a phase of $0°$ is achieved at the estimated frequency component ω_{N}. Similarly, for the negative-sequence component, a gain of 1 pu and a phase of $0°$ is achieved at the desired frequency $-\omega_{\mathrm{N}}$. A typical example, where the sequence estimation can be used is in a phase locked loop (PLL). The PLL estimates the phase of the positive-sequence grid voltage θ_{g} [46][47]. The block diagram for this application is shown in Fig. 4.22 (plot b), where the frequency output of the PLL can be fed back to the sequence estimator to make the sequence estimator frequency adaptive.

Consider now the case of a distorted grid voltage. Each harmonic component appears at a frequency $n\omega$ where n represents the harmonic order, and its sign depends on whether the harmonic is a positive or negative-sequence component. In general, the model of the grid voltage $\underline{e}_{\mathrm{g}}^{\alpha\beta}$ is given by [48]

$$\underline{e}_{\mathrm{g}}^{\alpha\beta}(t) = \underline{E}_{1}(t)e^{j\theta_{\mathrm{g}}(t)} + \sum_{i=1}^{N} \underline{E}_{n_i}(t)e^{jn_i\theta_{\mathrm{g}}(t)} \tag{4.38}$$

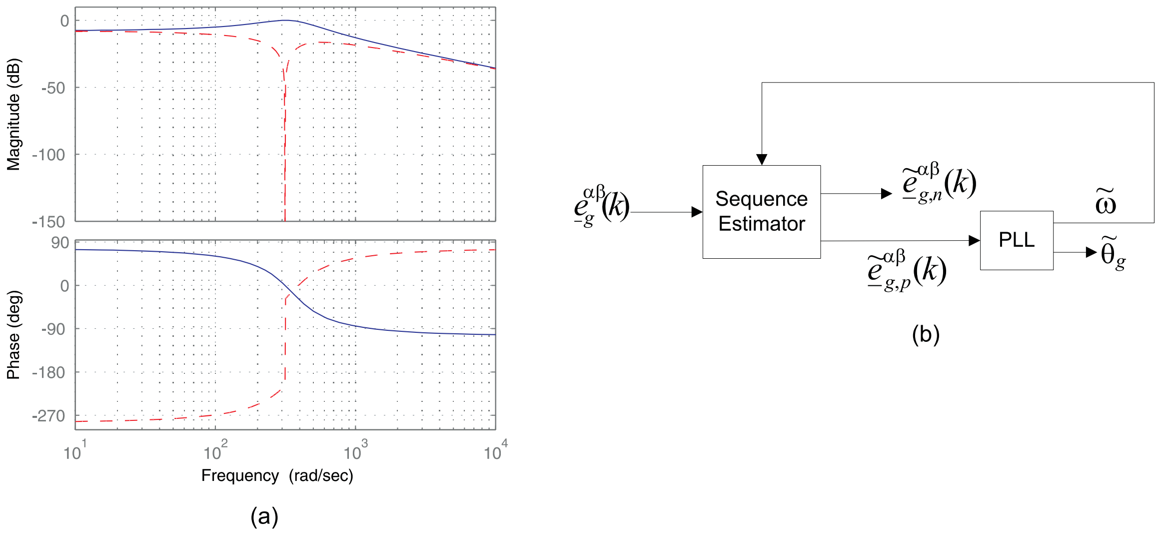

Fig. 4.22 Sequence estimation (a) Bode diagram for positive-sequence component estimation; response for the positive frequency (solid), response for the negative frequency (dashed); (b) Block diagram of RLS-based sequence estimator with a PLL for synchronization and frequency adaptation of the sequence estimator.

where $\underline{E}_{n_i}$ represents the $n_{\mathrm{i}}^{\mathrm{th}}$ harmonic phasor and $\underline{E}_1$ is the fundamental frequency phasor. The RLS algorithm as described in Section 4.2.3 can be set up from the model in (4.39) where the state vector and observation matrix are given by (4.40) and (4.41).

$$\underline{e}_{\mathrm{g}}^{\alpha\beta}(k) = \underline{\tilde{E}}_1(k)e^{j\tilde{\theta}_{\mathrm{g}}(k)} + \sum_{i=1}^{N} \underline{\tilde{E}}_{n_i}(k)e^{jn_i\tilde{\theta}_{\mathrm{g}}(k)} + \underline{d}(k) = \mathbf{\Phi}(k)\mathbf{h}(k-1) + \underline{d}(k) \tag{4.39}$$

$$\tilde{\mathbf{h}}(k) = \begin{bmatrix} \underline{\tilde{E}}_1(k) & \underline{\tilde{E}}_{n_1}(k) & \dots & \underline{\tilde{E}}_{n_N}(k) \end{bmatrix}^{\mathrm{T}} \tag{4.40}$$

$$\mathbf{\Phi}(k) = \begin{bmatrix} e^{j\tilde{\theta}_{\mathrm{g}}(k)} & e^{jn_1\tilde{\theta}_{\mathrm{g}}(k)} & \dots & e^{jn_N\tilde{\theta}_{\mathrm{g}}(k)} \end{bmatrix} \tag{4.41}$$

For a balanced three-phase system, each harmonic component will appear as either positive or negative-sequence component in (4.38). For an unbalanced case, both positive and negative-sequence components could exist for each harmonic order (including harmonic orders at multiple of three) and the model in (4.38) should take that into consideration. When needed, the dc component which is typically present in the measured signals can also be estimated by including a zero-frequency component in the model.

As the same grid angle is used in both the sequence and harmonic estimation algorithms, the PLL structure used in Fig. 4.22 (right) can be used to realize a frequency adaptive estimator. The model in (4.34) - (4.37) can be obtained from (4.38) - (4.41) by setting n_i to -1 and 0 for $i = 1$ and $i \neq 1$, respectively. To find the parameters of the estimator, the frequency content of the input signal and the required estimation speed should be considered. For this particular application, with a sampling time $T_s = 0.2$ ms, the steady-state forgetting factor $\lambda_{\mathrm{ss}} = 0.9686$

corresponding to a bandwidth of 25 Hz is chosen. For fast transient performance, the transient forgetting factor $\lambda_{\text{tr}} = 0.6859$ corresponding to $\alpha_{\text{tr}} = 250$ Hz and $\tau_{\text{hp}} = 0.01$ s have been selected.

To evaluate the performance of the improved RLS-based method for estimation of sequence components, an unbalanced fault with a phase jump is applied to a three-phase grid voltage and the estimator's performance is shown in Fig. 4.23. As the results indicate, the sequence components are estimated quickly and properly following the fault, which verifies the validity of the estimator. The simulation is repeated to estimate harmonic components. In this case, a 0.15 pu 5^{th} order harmonic component and a 0.1 pu 7^{th} order harmonic component are applied to the three-phase voltage at 0.02 s and again the effectiveness of the estimator can be observed from the results in Fig. 4.24.

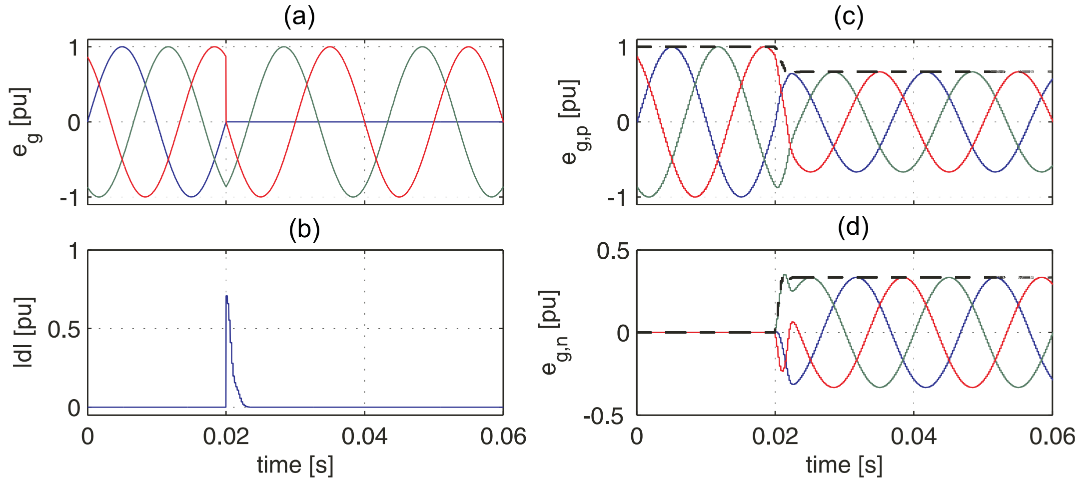

Fig. 4.23 Sequence estimation for unbalanced fault with phase jump; (a) grid voltage, (b) estimation error, (c) positive-sequence component and (d) negative-sequence component. Dashed: Magnitude of sequence component phasor.

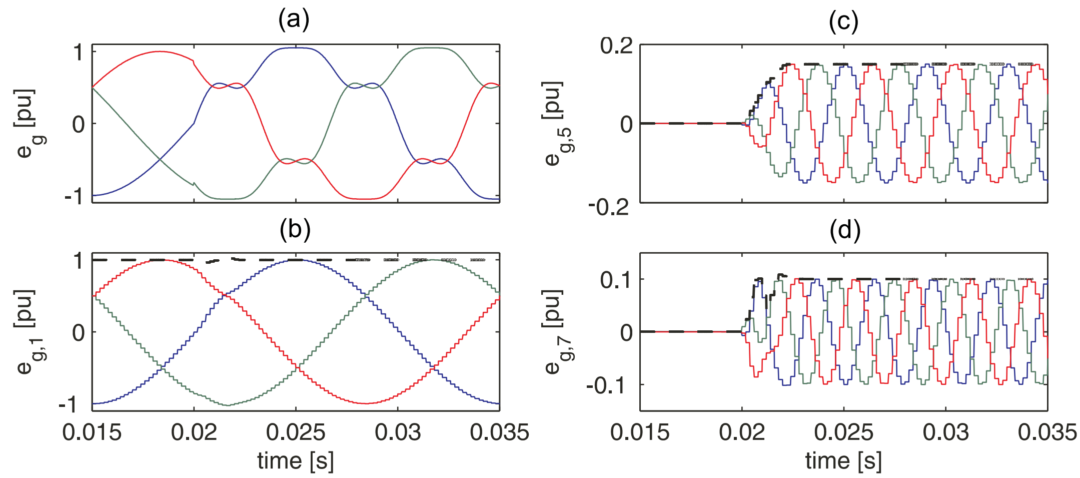

Fig. 4.24 Harmonic estimation in distorted three-phase voltage; (a) grid voltage, (b) fundamental component, (c) 5^{th} order harmonic component and (d) 7^{th} order harmonic component. Dashed: Magnitude of harmonic component phasor.

4.5 Experimental Verification

To validate the results obtained via simulation for the improved RLS-based estimator, experimental tests have been performed in the Power System Laboratory at the Department of Energy and Environment at Chalmers University of Technology. In this section, a description of the laboratory setup will be shown and experimental results on estimation of low-frequency oscillations, sequence and harmonic components will be presented.

4.5.1 Laboratory setup

Two separate laboratory setups are used for the tests in this section. The schematic of the first setup to test estimation of low-frequency power oscillations is shown in Fig. 4.25, while Fig. 4.26 shows a photo of the actual setup. The system consists of a 75 kVA, 400 V synchronous generator connected to a stiff AC grid through a transmission line model. Faults can be applied to the transmission system using the contactor (CT) to create low-frequency electromechanical oscillations in the power output of the synchronous generator. The transmission line model is a down-scaled version of an actual Swedish 400 kV transmission system with the model rated 400 V, 50 Hz. The model consists of six identical Π sections, each constituted by a series inductor L_{n} of 2.05 mH and two shunt capacitors C_{n} of $46\ \mu$F, and represents a model of a portion of 150 km of the actual line. A picture of the generator system, which models an accurate model of the Harsprånget hydro power plant situated by the Lule river in northern Sweden, is shown in Fig. 4.26. The synchronous generator is driven by an 85 kW DC motor. A flywheel is coupled to the shaft between the DC motor and the generator to give the model similar mechanical behavior as the actual power plant [49].

The schematic of the second setup to test estimation of sequence and harmonic components is shown in Fig. 4.27. In this case, the AC grid is connected to a 9 kW three-phase resistor

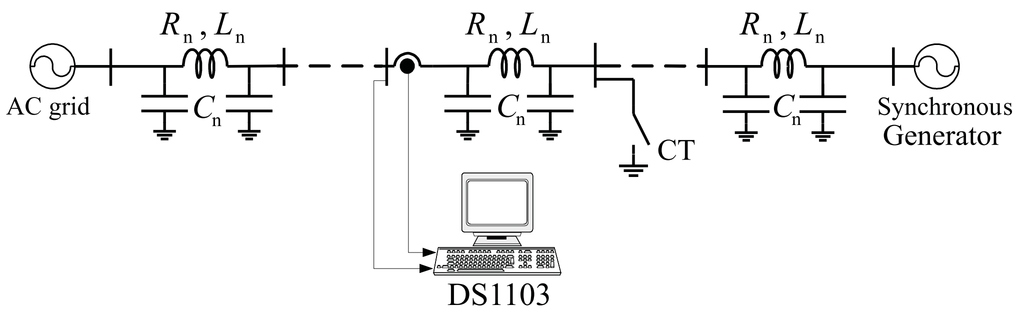

Fig. 4.25 Single line diagram of the laboratory setup for estimation of low-frequency oscillations.

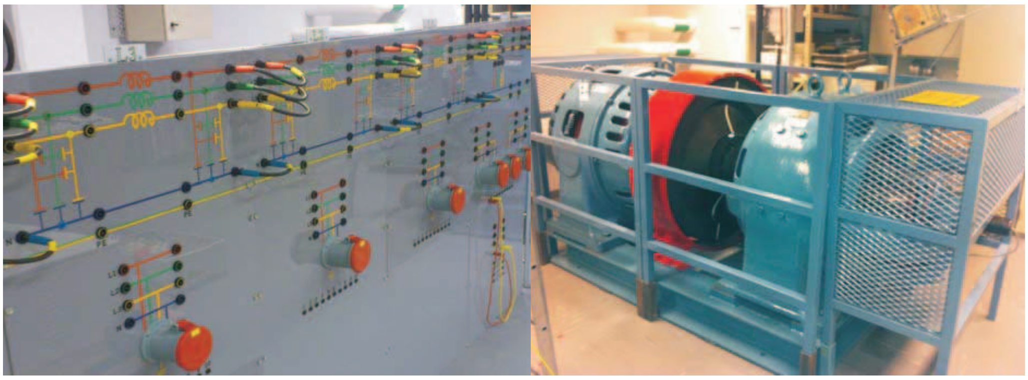

Fig. 4.26 Photo of the laboratory setup consisting of the analog transmission line model (left) and the generator system (right).

(denoted as "Load 3" in the figure) through the transmission line model. Different voltage dips at the measurement point can be generated by controlling the contactor CT2 and the value of the Load 2 impedance for each phase. Furthermore, a non-linear load constituted by a $10\ \Omega$ resistor (denoted as "Load 1") connected to the mains through a diode rectifier ($L_{\mathrm{d}} = 300$ mH, $C_{\mathrm{d}} = 300\ \mu$F) can be inserted by closing the contactor CT1. The investigated RLS algorithm is implemented in a control computer with a dSpace 1103 board [50], which can be programmed using C-code or Matlab/Simulink.

4.5.2 Estimation of low-frequency power oscillations

In order to create a power oscillation in the system, a three-phase fault has been applied in the middle of the transmission line with a fault clearing time of 250 ms using the contactor CT in Fig. 4.25. The measured output active power from the generator $p(t)$, as shown in Fig. 4.28, is then used as an input to estimate the low-frequency electromechanical oscillation component that occurs in the transmitted power following the fault. As shown in Fig. 4.28, the measured signal contains noise and high frequency harmonics to test the robustness of the estimator in disturbed conditions. The actual oscillation frequency of the measured signal in Fig. 4.28 is close to 0.42 Hz. This low oscillation frequency highlights the importance of the adopted method, since the classical approaches (using lead-lag filter links or low-pass filters, see Fig. 3.6 and Fig. 4.4) would require low bandwidth, resulting in a reduction in the estimation speed. The

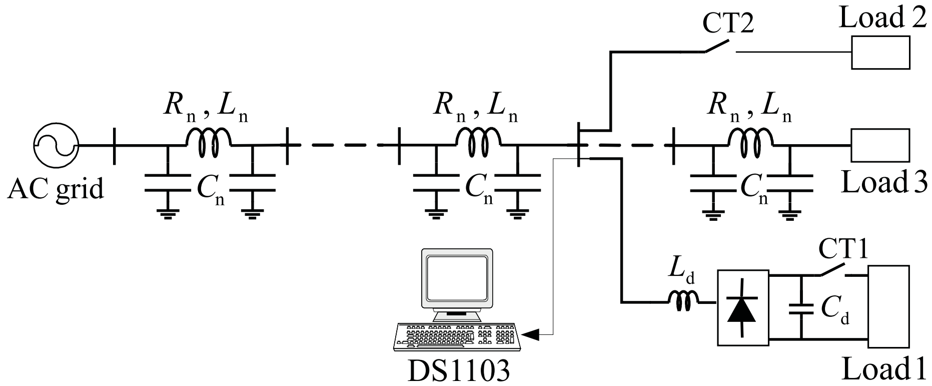

Fig. 4.27 Single line diagram of the laboratory setup for sequence and harmonic estimation.

parameters for the improved RLS algorithm are chosen based on the discussion in Section 4.3.

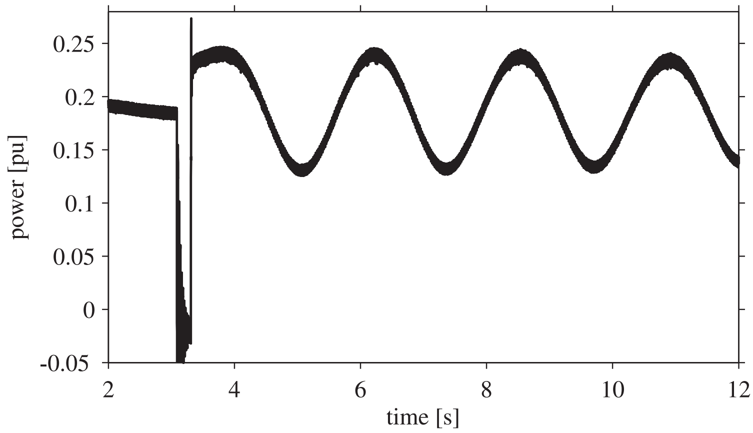

Fig. 4.28 Measured transmitted active power from the generator. A three-phase Fault is applied and cleared after 250 ms.

The improved RLS algorithm as described in Section 4.3 uses a variable forgetting factor and a frequency adaptation mechanism. When both are used together, the variation of λ and adaptation of the oscillation frequency from the initially assumed value of 0.80 Hz is shown in Fig. 4.29. In order to appreciate the impact of each feature, two separate tests are made. The first test is a comparison of the RLS algorithm with fixed forgetting factor and variable forgetting factor (see Fig. 4.29 for variation of λ), where the actual oscillation frequency is used in the estimation. Figure 4.30 shows the dynamic performance of the two estimators. As the results in the figure show, the estimation with variable forgetting factor is very fast immediately after fault clearing. As expected, the use of fixed forgetting factor works in the same way as the LPF-based method, where the speed of estimation is limited by the oscillation frequency. This can be seen by comparing the estimated signals with the input signal in Fig. 4.30.

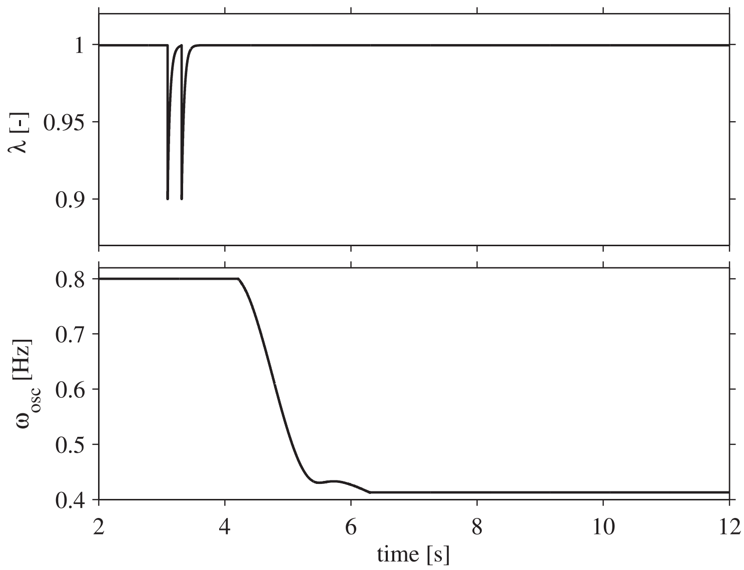

Fig. 4.29 Improved RLS-based estimator; Variation of forgetting factor λ (top) and estimate of oscillation frequency $\tilde{\omega}_{\mathrm{osc}}$ (bottom).

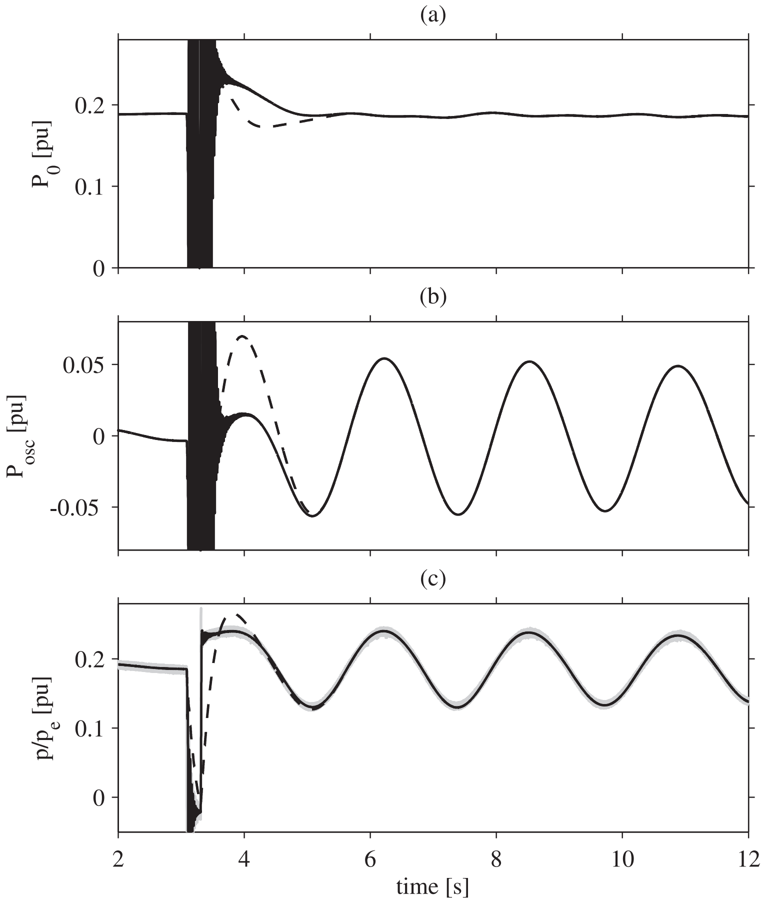

Fig. 4.30 Estimation with accurate knowledge of oscillation frequency; (a) estimate of average component with fixed λ (black dashed) and variable λ (black solid); (b) estimate of oscillatory component with fixed λ (black dashed) and variable λ (black solid); (c) input signal p (gray), estimated signal p_{e} with fixed λ (black dashed) and with variable λ (black solid).

The test is repeated with an initially assumed oscillation frequency of 0.80 Hz while the true value in the measured signal is close to 0.42 Hz. The performance of the improved RLS algorithm with and without frequency adaptation is shown in Fig. 4.31. As the results in the figure show, the algorithm quickly estimates the different frequency components in both cases (see plot c). The fast transient estimation is followed by the steady-state estimation, where the oscillation frequency is updated using the frequency adaption mechanism described in Section 4.3.2 (see Fig. 4.29 for the oscillation frequency update). This corrects the oscillation in the estimate of the average component and any amplitude and phase error in the estimate of the oscillatory component (see plot a and plot b) resulting from wrong assumption of the oscillation frequency. Note that a correct estimation of the phase of the oscillatory component is a crucial point in applications like POD. When the frequency adaptation is used, a proper estimation is achieved.

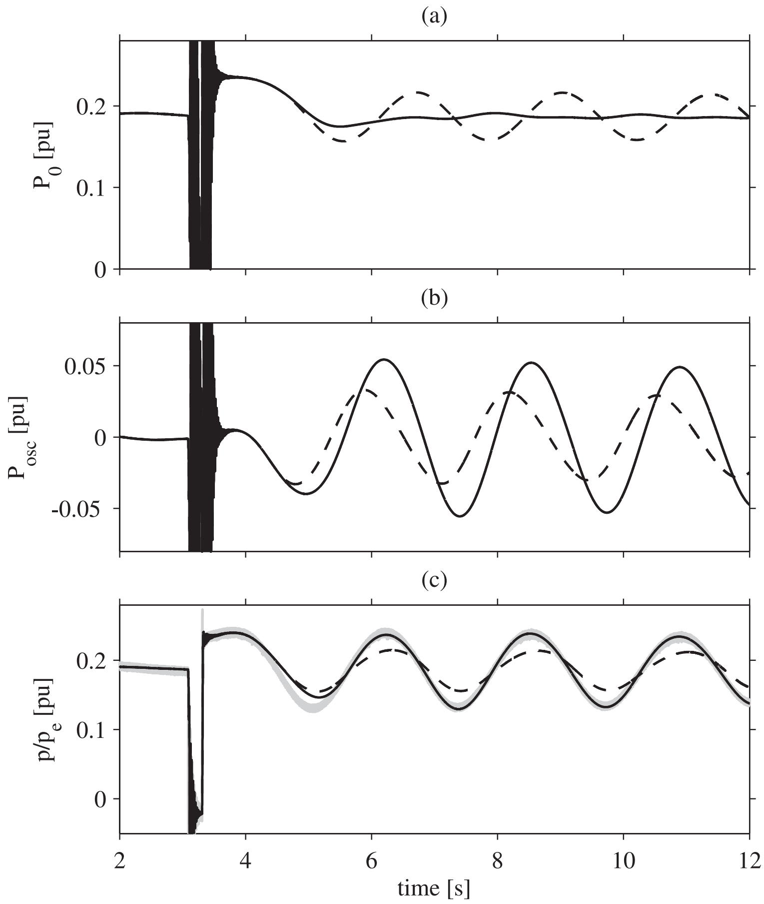

Fig. 4.31 Estimation with variable λ and 90% error in assumed oscillation frequency; (a) estimate of average component without frequency adaptation (black dashed) and with frequency adaptation (black solid); (b) estimate of oscillatory component without frequency adaptation (black dashed) and with frequency adaptation (black solid); (c) input signal p (gray) and estimated signal p_{e} without frequency adaptation (black dashed) and with frequency adaptation (black solid).

4.5.3 Estimation of sequence and harmonic components

Using the setup in Fig. 4.27, a first experiment has been carried out in case of unbalanced voltage dips with the diode rectifier load disconnected from the grid. To create the dip, CT2 in Fig. 4.27 has been closed for phase a only at $t = 0.02$ s. The resistance value for Load 2 is set to $0.01\ \Omega$. The grid voltage at the measurement point is depicted in Fig. 4.32 (top plot). As shown, due to the sudden insertion of the additional load, the phase a voltage is almost zero after closing CT2. The three-phase voltage is used as input to the estimator. Observe that even if the grid frequency does not change significantly during the test, a PLL has been implemented to track the grid frequency from the estimate of the positive-sequence fundamental voltage (see Fig. 4.32, bottom plot).

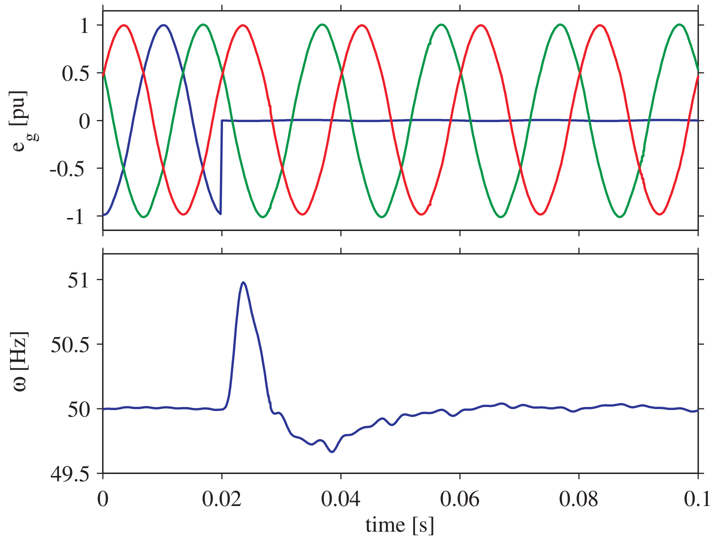

Fig. 4.32 A three-phase grid voltage input signal for the RLS estimator (top plot) and estimate of grid frequency from PLL (bottom plot).

With the same choice of parameters as in Section 4.4.2, the performance of the RLS algorithm to estimate sequence components from the measured grid voltage e_g are shown in Fig. 4.33. The effectiveness of the proposed algorithm in estimating the sequence voltage components can be easily seen from the figure, where the estimation error quickly converges close to zero in about 0.0025 s.

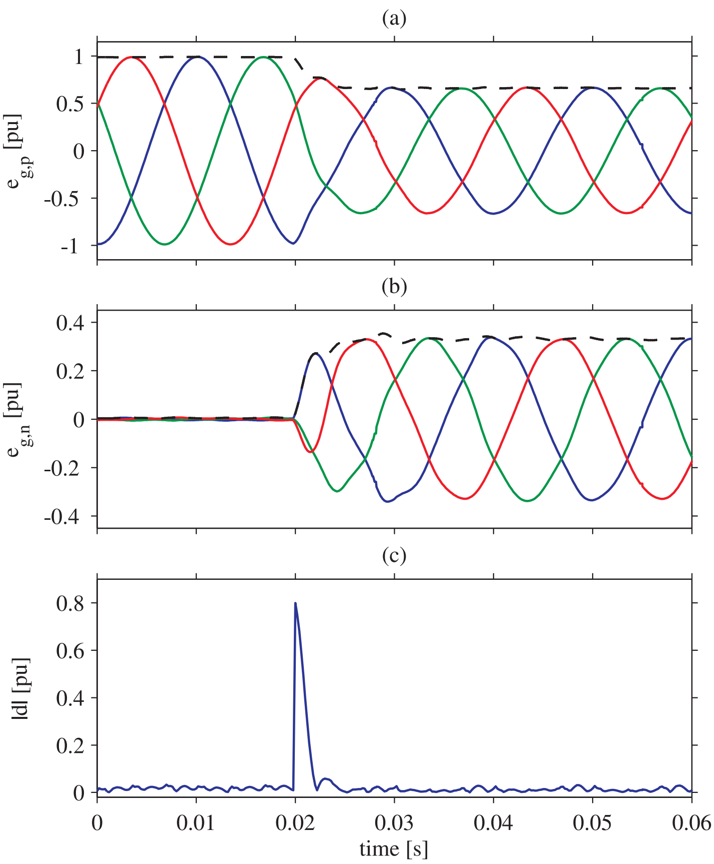

Fig. 4.33 Sequence estimation in three-phase system using the proposed method; (a) positive-sequence component (b) negative-sequence component (c) estimation error; Dashed curves represent magnitude of sequence component phasors.

A similar test is then performed by also applying a step in the harmonic content of the measured grid voltage by closing CT1 in Fig. 4.27. At the same time, a balanced three-phase voltage dip with an associated phase-angle jump is applied by closing contactor CT2 with a Load 2 resistance of $8.9\ \Omega$. The resulting voltage waveforms are depicted in Fig. 4.34 (top plot). The same figure also shows the estimated fundamental component, 5^{th} harmonic and the estimation error. Here, the RLS algorithm is used to estimate only the 5^{th} and 7^{th} order harmonic components in the measured signal. As shown in the figure, the fast estimation of the algorithm is shown by a rapid reduction of the estimation error following the dip. The small oscillations visible in the steady-state estimation error are due to the harmonic components not included in the model. Observe that the transient in the estimated 5^{th} harmonic component after the closing of CT1 is due to the dynamics associated with the dc capacitor of the diode rectifier.

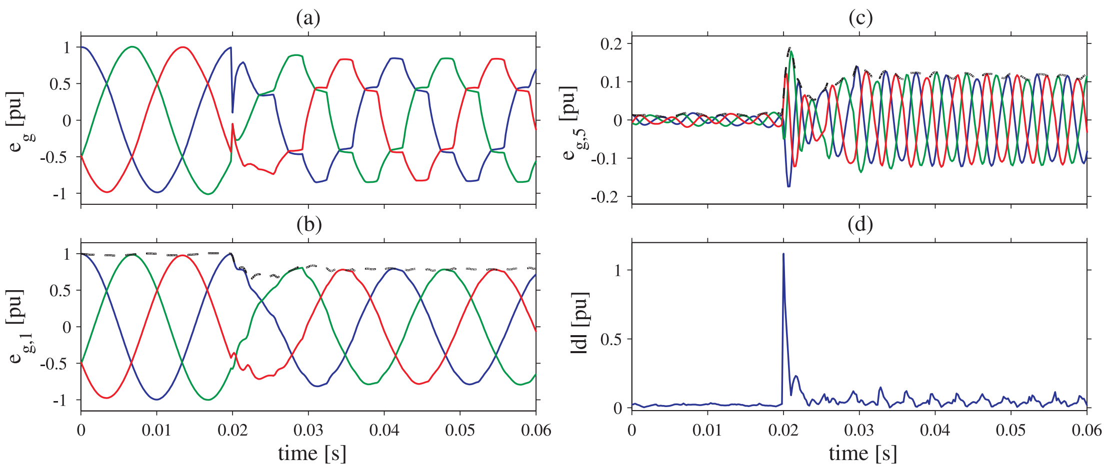

Fig. 4.34 Harmonic estimation in distorted three-phase voltage; (a) A three-phase grid voltage input signal for the estimator (b) fundamental component, (c) 5^{th} order harmonic component (d) estimation error; dashed curves represent magnitude of estimated phasors.

4.6 Conclusions

In this chapter, an estimation algorithm based on an improved RLS algorithm has been described in detail. First, a LPF-based estimation algorithm has been described and compared with a conventional RLS-based estimator. The problem of the LPF-based method when high speed of response is required has been highlighted. To obtain a fast estimator with good frequency selectivity, the RLS algorithm has been modified using variable forgetting factor and frequency adaptation. With this method, a fast and selective estimation performance of the algorithm has been obtained. The application of the algorithm has been shown for estimation of low-frequency electromechanical oscillations as well as estimation of harmonic and sequence components both in simulation and experiment. The results in this chapter will be applied for controller design in the coming chapters. Estimation of harmonics and sequence components will be used to design a current controller for converters that operate in distorted grids in Chapter 5, whereas the estimation of low-frequency power oscillations will be used for design of a POD controller in Chapter 6.

Chapter 5

Overall controller for shunt-connected VSC with energy storage

5.1 Introduction

In this chapter, the overall control structure for the E-STATCOM connected to a three-phase grid will be described. First, a cascade control system, based on an inner vector-current controller and various outer-control loops will be derived and analyzed. Modification to the current controller to deal with disturbances from harmonics and unbalanced grid conditions will be discussed. Secondly, an alternative control approach for the E-STATCOM to mimic the behavior of a synchronous machine will be described. The performance of each control structure will be validated through simulation and experimental verification.

5.2 System layout

The main circuit scheme of a two-level Voltage Source Converter (VSC) with energy storage connected to a grid through an L-filter having inductance L_{f} and resistance R_{f} is shown in Fig. 5.1. The grid is represented by its Thevenin equivalent with voltages at the connection point $e_{\mathrm{ga}}(t)$, $e_{\mathrm{gb}}(t)$ and $e_{\mathrm{gc}}(t)$. The grid inductance and resistance are denoted by L_{g} and R_{g}, respectively. The VSC injects three-phase currents denoted by $i_{\mathrm{fa}}(t)$, $i_{\mathrm{fb}}(t)$, $i_{\mathrm{fc}}(t)$ to the grid.

The valves in the phase-legs of the VSC (usually Insulated Gate Bipolar Transistors, IGBTs) are controlled by the switching signals $sw_{\mathrm{a}}(t)$, $sw_{\mathrm{b}}(t)$ and $sw_{\mathrm{c}}(t)$. The DC-link voltage is denoted by $u_{\mathrm{dc}}(t)$. When $sw_{\mathrm{a}}(t)$ is equal to 1, the upper valve in phase a is turned on while the lower valve in the same leg is off. Therefore, the potential $u_{\mathrm{ca}}(t)$ is equal to half of the DC-link voltage, $u_{\mathrm{dc}}(t)/2$. Similarly, when the switching signal is equal to -1, the upper valve is off and the lower one is on and, thus, $u_{\mathrm{ca}}(t)$ is equal to $-u_{\mathrm{dc}}(t)/2$. To obtain the switching signals for the VSC, Pulse Width Modulation technique (PWM) has been adopted [51]. An energy storage is connected on the DC side of the converter to give the VSC the capability of injecting active power.

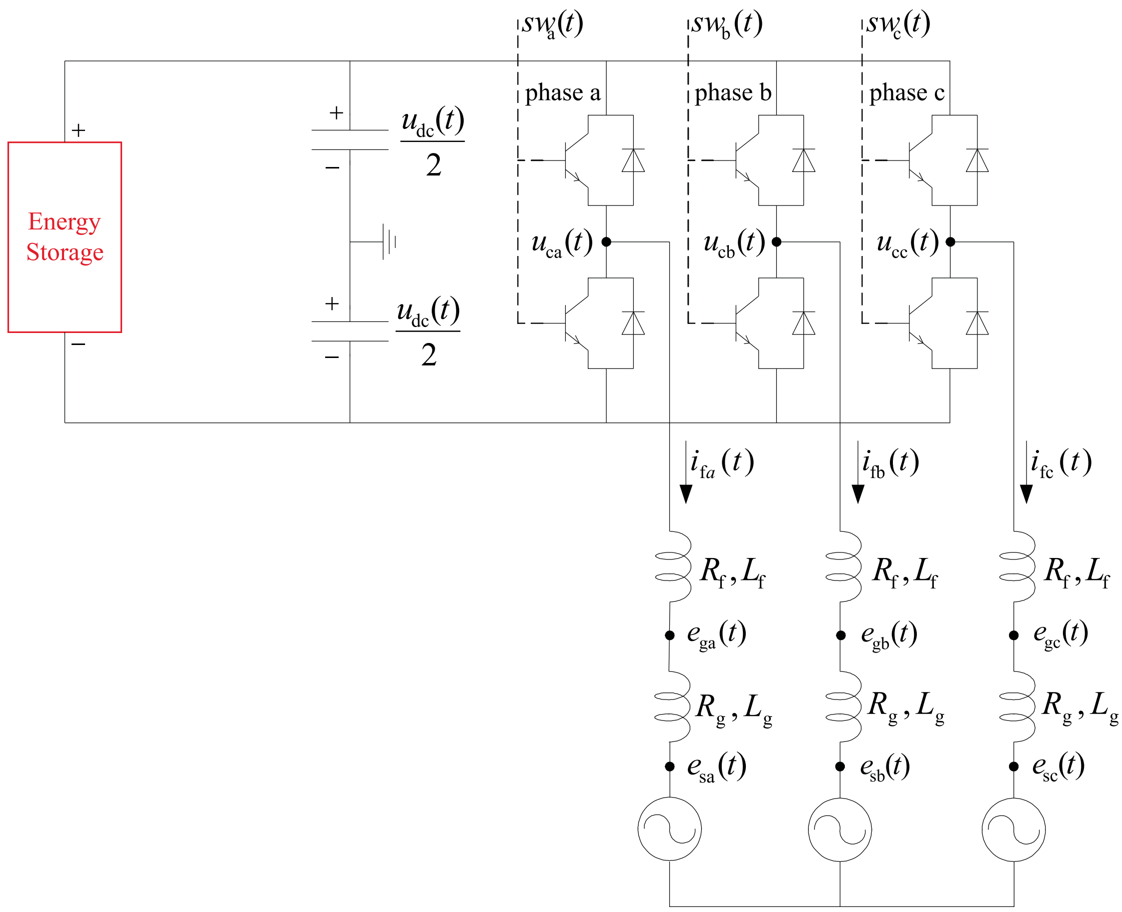

Fig. 5.1 Main circuit of three-phase two-level E-STATCOM connected to the grid.

5.3 Classical cascade controller

The most common control structure for a VSC consists of an inner vector-current controller and different outer-control loops. This structure is named *classical cascade controller* hereafter and the overall control block diagram is shown in Fig. 5.2. In this scheme, a Phase-Locked Loop (PLL) is used to track the grid voltage angle, θ_g for coordinate transformation [47]. See Appendix A for the adopted transformation from three-phase to $\alpha\beta$ and $\alpha\beta$ to dq reference-frames and vise versa.

Outputs from the control system are the PWM signals sw_a, sw_b and sw_c. To generate these signals, the following will be performed.

1. Various signals such as the grid voltages, filter currents, DC-link voltage and active power flow in the transmission system (P_{tran}) are measured and sampled at a rate of $1/T_s$, where T_s is the sampling time.

2. After coordinate transformation, the reference currents input to the current controller are calculated in the different outer control blocks. The converter voltage reference, which is

the output of the current controller, will then be converted from the rotating dq-coordinate system to the stationary $\alpha\beta$-coordinate using the transformation angle $\theta_{\mathrm{g}}(k) + \Delta\theta$, where $\Delta\theta = 1.5\omega_{\mathrm{N}}T_{\mathrm{s}}$ is a compensation angle (calculated using the nominal grid frequency, ω_{N}) to take into account the half sample delay introduced by the discretization of the measured quantities and one sample delay introduced by the computation time delay [52].

3. From the three-phase converter voltage references (u^*_{ca}, u^*_{cb}, u^*_{cc}), the duty-cycles are calculated in the PWM block and the switching pulses are sent to the VSC valves.

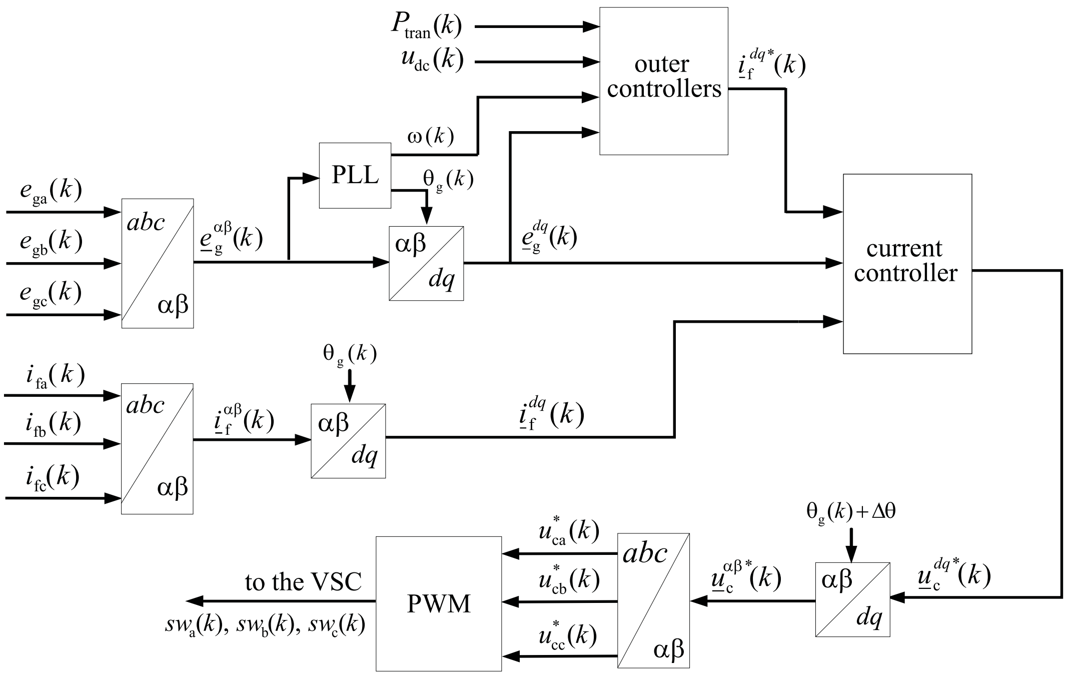

Fig. 5.2 Overall block diagram of the classical cascaded controller for E-STATCOM.

5.3.1 Vector-current controller

A number of control strategies for grid-connected Voltage Source Converter (VSC) are available in the literature [53][54][55]. Among the different methods, a synchronous-frame Proportional-Integral (PI) current control, designed using the internal model control approach, has the advantage of simple implementation and robust performance in ideal-grid conditions [56]. This method is used in this work to design the current controller for the E-STATCOM.

For a VSC connected to a grid with voltage e_{g} at the connection point though a filter with inductance L_{f} and resistance R_{f} as in Fig. 5.3, the filter current i_{f} dynamics are expressed in the stationary $\alpha\beta$ reference-frame as

$$L_{\mathrm{f}}\frac{d}{dt}\underline{i}_{\mathrm{f}}^{\alpha\beta}(t) = \underline{u}_{\mathrm{c}}^{\alpha\beta}(t) - \underline{e}_{\mathrm{g}}^{\alpha\beta}(t) - R_{\mathrm{f}}\underline{i}_{\mathrm{f}}^{\alpha\beta}(t) \tag{5.1}$$

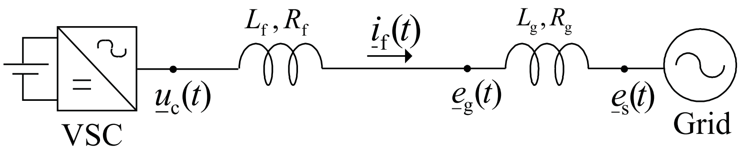

Fig. 5.3 Single line diagram of a VSC connected to a grid through a filter.

where u_c is the converter output voltage. By using the grid voltage angle θ_g, the expression in (5.1) can be rewritten in the synchronous dq reference-frame as

$$L_f \frac{d}{dt}\underline{i}_f^{dq}(t) = \underline{u}_c^{dq}(t) - \underline{e}_g^{dq}(t) - j\omega_N L_f \underline{i}_f^{dq}(t) - R_f \underline{i}_f^{dq}(t) \tag{5.2}$$

where $\omega_N = d\theta_g(t)/dt$ represents the nominal grid frequency. If the PLL is synchronized with the grid voltage vector, the d and q components of the current represent the active and reactive currents injected to the grid, respectively. The purpose of the current controller is to independently control these currents. For the dynamical model in (5.2), using the internal model control approach [55][56], the PI current controller in continuous time is given by

$$\begin{aligned}\underline{u}_c^{dq*}(t) = \underline{e}_g^{dq}(t) + j\hat{\omega}_N \hat{L}_f \underline{i}_f^{dq}(t) + \alpha_{cc}\hat{L}_f\left(\underline{i}_f^{dq*}(t) - \underline{i}_f^{dq}(t)\right) \quad + \\ \alpha_{cc}\hat{R}_f \int_0^t \left(\underline{i}_f^{dq*}(\tau) - \underline{i}_f^{dq}(\tau)\right) d\tau\end{aligned} \tag{5.3}$$

where α_{cc} represents the desired closed-loop bandwidth of the current controller. Using the estimate of the filter inductance and resistance, the proportional and integral gains of the PI controller are given by $\alpha_{cc}\hat{L}_f$ and $\alpha_{cc}\hat{R}_f$, respectively. The cross-coupling between the d and q filter currents is easily compensated in steady-state. A feed-forward of the grid voltage is also included for a good dynamic performance of the controller. In the notations, the superscript "*" denotes a reference signal.

In ideal grid conditions with perfect cancellation of the cross-coupling term and treating the VSC as a linear amplifier ($u_c = u_c^*$), the closed-loop transfer function from reference to actual signal results in a first-order low-pass filter with a cut-off frequency α_{cc} as

$$\begin{bmatrix} \underline{i}_f^d(s) \\ \underline{i}_f^q(s) \end{bmatrix} = \begin{bmatrix} \frac{\alpha_{cc}}{s+\alpha_{cc}} & 0 \\ 0 & \frac{\alpha_{cc}}{s+\alpha_{cc}} \end{bmatrix} \begin{bmatrix} \underline{i}_f^{d*}(s) \\ \underline{i}_f^{q*}(s) \end{bmatrix} \tag{5.4}$$

For real-time implementation, the controller in (5.3) is expressed in discrete time using Euler's forward approximation as

$$\begin{aligned}\underline{u}_c^{dq*}(k) = \underline{e}_g^{dq}(k) + j\hat{\omega}_N \hat{L}_f \underline{i}_f^{dq}(k) + \alpha_{cc}\hat{L}_f\left(\underline{i}_f^{dq*}(k) - \underline{i}_f^{dq}(k)\right) \quad + \\ \alpha_{cc}\hat{R}_f T_s \sum_{n=0}^{k} \left(\underline{i}_f^{dq*}(n) - \underline{i}_f^{dq}(n)\right)\end{aligned} \tag{5.5}$$

Although effective to derive the controller parameters, the desired closed-loop transfer function in (5.4) is difficult to obtain in an actual system due to inaccurate knowledge of filter parameters, converter voltage saturation and time delays [52]. In particular, delays due to discretization and computational time have a major impact on the system dynamic performance when the VSC is connected to a distorted or an unbalanced grid. A brief description of how to mitigate these problems will be described in the following.

Inaccurate knowledge of system parameters

To deal with system parameter variations and disturbances, active damping can be included to the controller in (5.5) [55]. This involves calculating the controller parameters assuming a fictitious resistance (or active damping term, R_a) in the system. This will impact the value of the total system resistance which is equal to $R_\mathrm{f} + R_\mathrm{a}$. The effect of additional resistance R_a will then be compensated in the feed-forward term as

$$\begin{aligned}\underline{u}_\mathrm{c}^{dq*}(k) = \underline{e}_\mathrm{g}^{dq}(k) + \left(j\hat{\omega}_\mathrm{N}\hat{L}_\mathrm{f} - R_\mathrm{a}\right)\underline{i}_\mathrm{f}^{dq}(k) + \alpha_\mathrm{cc}\hat{L}_\mathrm{f}\left(\underline{i}_\mathrm{f}^{dq*}(k) - \underline{i}_\mathrm{f}^{dq}(k)\right) \quad + \\ \alpha_\mathrm{cc}\left(\hat{R}_\mathrm{f} + R_\mathrm{a}\right)T_\mathrm{s}\sum_{n=0}^{k}\left(\underline{i}_\mathrm{f}^{dq*}(n) - \underline{i}_\mathrm{f}^{dq}(n)\right)\end{aligned} \tag{5.6}$$

The value of the active damping term should be selected carefully. Even if a higher value would provide larger damping to system disturbances, the increase of the integral gain might lead to instabilities when used in discrete controllers with non-negligible time delays. Guidelines on selection of the active damping term can be found in [55].

Converter voltage saturation

The magnitude of the reference voltage for the converter must be limited based on the available DC-link voltage magnitude. When the magnitude of the calculated reference voltage in (5.6) $|\underline{u}_\mathrm{c}^{dq*}|$ is higher than the maximum converter voltage ($U_\mathrm{c,max}$), the converter cannot provide the required reference voltage. When this happens, the integrator in the controller will not be able to force the error to zero and this leads to an integration windup. To avoid this, the integral action should be stopped during saturation or an anti-windup function should be added [57][56]. In this work, the later is used, where the input to the integral gain is modified through back calculation. With the anti-windup function, the current controller is given by

$$\begin{aligned}\underline{u}_\mathrm{c}^{dq*}(k) = \underline{e}_\mathrm{g}^{dq}(k) + \left(j\hat{\omega}_\mathrm{N}\hat{L}_\mathrm{f} - R_\mathrm{a}\right)\underline{i}_\mathrm{f}^{dq}(k) + \alpha_\mathrm{cc}\hat{L}_\mathrm{f}\left(\underline{i}_\mathrm{f}^{dq*}(k) - \underline{i}_\mathrm{f}^{dq}(k)\right) \quad + \\ \alpha_\mathrm{cc}\left(\hat{R}_\mathrm{f} + R_\mathrm{a}\right)T_\mathrm{s}\sum_{n=0}^{k}\left(\underline{i}_\mathrm{f}^{dq*}(n) - \underline{i}_\mathrm{f}^{dq}(n) + \underline{i}_{\mathrm{err}(n)}^{dq}\right)\end{aligned} \tag{5.7}$$

where the additional error input to the integral gain, $\underline{i}_\mathrm{err}^{dq}$ and the limited converter voltage, $\underline{u}_\mathrm{c,lim}^{dq*}$ are given by

$$\underline{i}_\mathrm{err}^{dq}(k) = \frac{1}{\alpha_\mathrm{cc}\hat{L}_\mathrm{f}}\left(\underline{u}_\mathrm{c,lim}^{dq*}(k) - \underline{u}_\mathrm{c}^{dq*}(k)\right)$$

$$\underline{u}_{\mathrm{c,lim}}^{dq*}(k) = \frac{\underline{u}_{\mathrm{c}}^{dq*}(k)}{|\underline{u}_{\mathrm{c}}^{dq*}(k)|} \min\left\{\left|\underline{u}_{\mathrm{c}}^{dq*}(k)\right|, U_{\mathrm{c,max}}\right\}$$

Grid voltage harmonics and unbalance

The current controller in (5.7) works as designed in ideal grid conditions where the feed-forward term provides a perfect voltage compensation. However, problems arise in the presence of harmonics or unbalances in the grid voltage. Due to the delays in the discretization and computational time in the control system, a phase-shift exists between the actual and feed-forwarded grid voltage. This phase-shift is properly compensated only for the fundamental voltage component using the transformation angle $\theta_{\mathrm{g}} + \Delta\theta$ in Fig. 5.2. In the presence of harmonics in the measured voltage $\underline{e}_{\mathrm{g}}$, this leads to a harmonic current flow between the VSC and the grid. Using the estimation method for sequence and harmonic components in Section 4.4.2, the basic current controller can be modified to deal with disturbances from harmonics or unbalanced grid conditions.

Direct feed-forwarding of the grid voltage as in (5.7) and providing an angle compensation of $\Delta\theta = 1.5\omega_{\mathrm{N}}T_{\mathrm{s}}$ for transforming the converter reference voltage to the stationary $\alpha\beta$ coordinate will not reproduce the grid voltage accurately in the case of harmonic disturbances and unbalanced grid conditions. This is due to the fact that the harmonic components rotate with a frequency different from the fundamental. In addition, the negative-sequence components rotate in opposite direction to the positive-sequence components. Therefore, the harmonic and negative-sequence components should be estimated and the angle compensation should be applied accordingly. For example, if the grid voltage e_{g} contains harmonic orders 5^{th}, 7^{th}, 11^{th}, 13^{th} and a negative-sequence component at fundamental frequency due to unbalanced voltages, the grid voltage vector can be expressed in dq coordinate as

$$\begin{aligned}\underline{e}_{\mathrm{g}}^{dq}(k) = {} & \underline{E}_1(k) + \underline{E}_{-1}(k)e^{-j2\theta_{\mathrm{g}}(k)} + \underline{E}_5(k)e^{-j6\theta_{\mathrm{g}}(k)} + \underline{E}_7(k)e^{j6\theta_{\mathrm{g}}(k)} \quad + \\ & \underline{E}_{11}(k)e^{-j12\theta_{\mathrm{g}}(k)} + \underline{E}_{13}(k)e^{j12\theta_{\mathrm{g}}(k)}\end{aligned} \tag{5.8}$$

where $\underline{E}_5$, $\underline{E}_7$, $\underline{E}_{11}$ and $\underline{E}_{13}$ represent slowly varying harmonic voltage phasors. $\underline{E}_1$ and $\underline{E}_{-1}$ are the positive and negative-sequence component voltage phasors at fundamental frequency, respectively. Using the model in (5.8), the voltage phasors are estimated using the improved RLS-based estimator described in Chapter 4. Note that the use of the fundamental positive-sequence component, $\underline{E}_1$ in the PLL structure helps to avoid the impact of harmonics or any negative-sequence component in the grid voltage on the estimated angle.

To compensate for disturbances from harmonics and unbalanced grid voltage conditions in the case of a strong grid ($L_{\mathrm{g}} << L_{\mathrm{f}}$ in Fig. 5.3), the feed-forwarded voltage in (5.7) is modified as

$$\underline{\tilde{e}}_{\mathrm{g}}^{dq}(k) = \mathbf{\Phi}_{\mathrm{c}}(k)\underline{\tilde{\mathbf{E}}}(k) \tag{5.9}$$

where the matrices $\mathbf{\Phi}_{\mathrm{c}}$ and $\tilde{\mathbf{E}}$ are defined by

$$\mathbf{\Phi}_{\mathrm{c}}(k) = [\ 1 \quad e^{-j2(\tilde{\theta}_{\mathrm{g}}(k)+\Delta\theta)} \quad e^{-j6(\tilde{\theta}_{\mathrm{g}}(k)+\Delta\theta)} \quad e^{j6(\tilde{\theta}_{\mathrm{g}}(k)+\Delta\theta)} \quad e^{-j12(\tilde{\theta}_{\mathrm{g}}(k)+\Delta\theta)} \quad e^{j12(\tilde{\theta}_{\mathrm{g}}(k)+\Delta\theta)} \ ]$$

$$\underline{\tilde{\mathbf{E}}}(k) = [\ \underline{\tilde{E}}_1(k) \quad \underline{\tilde{E}}_{-1}(k) \quad \underline{\tilde{E}}_5(k) \quad \underline{\tilde{E}}_7(k) \quad \underline{\tilde{E}}_{11}(k) \quad \underline{\tilde{E}}_{13}(k) \ ]^{\mathrm{T}}$$

On the other hand, for a weak connection point, where the grid voltage dynamics are affected by the current injection from the VSC, a closed-loop control of the current may be required. For this, the harmonic current phasors are estimated from the model of the filter current given by

$$\begin{aligned} \underline{i}_{\mathrm{f}}^{dq}(k) = \underline{I}_1(k) + \underline{I}_{-1}(k)e^{-j2\theta_{\mathrm{g}}(k)} + \underline{I}_5(k)e^{-j6\theta_{\mathrm{g}}(k)} + \underline{I}_7(k)e^{j6\theta_{\mathrm{g}}(k)} \quad + \\ \underline{I}_{11}(k)e^{-j12\theta_{\mathrm{g}}(k)} + \underline{I}_{13}(k)e^{j12\theta_{\mathrm{g}}(k)} \end{aligned} \tag{5.10}$$

where $\underline{I}_5$, $\underline{I}_7$, $\underline{I}_{11}$ and $\underline{I}_{13}$ represent slowly varying harmonic current phasors. The terms $\underline{I}_1$ and $\underline{I}_{-1}$ are the positive and negative-sequence component current phasors at fundamental frequency, respectively. Using the estimated current phasors, a PI controller can be used to control the disturbances to zero. In this case, (5.9) will be modified to

$$\underline{\tilde{e}}_{\mathrm{g}}^{dq}(k) = \mathbf{\Phi}_{\mathrm{c}}(k)\left[\underline{\tilde{\mathbf{E}}}(k) - \left(\alpha_{\mathrm{hc}}\hat{L}_{\mathrm{f}} + R_{\mathrm{ha}}\right)\underline{\tilde{\mathbf{I}}}_{\mathrm{h}}(k) - \alpha_{\mathrm{hc}}\left(\hat{R}_{\mathrm{f}} + R_{\mathrm{ha}}\right)T_{\mathrm{s}}\sum_{n=0}^{k}\underline{\tilde{\mathbf{I}}}_{\mathrm{h}}(n)\right] \tag{5.11}$$

with the harmonic phasor $\underline{\tilde{\mathbf{I}}}_{\mathrm{h}}$ defined by

$$\underline{\tilde{\mathbf{I}}}_{\mathrm{h}}(k) = [\ 0 \quad \underline{\tilde{I}}_{-1}(k) \quad \underline{\tilde{I}}_5(k) \quad \underline{\tilde{I}}_7(k) \quad \underline{\tilde{I}}_{11}(k) \quad \underline{\tilde{I}}_{13}(k) \ ]^{\mathrm{T}}$$

The term α_{hc} represents the bandwidth of the closed-loop harmonic compensator and R_{ha} is a small active damping term. As the harmonics can be treated as steady-state quantities, the harmonic compensator bandwidth α_{hc} is chosen much lower than the fundamental current controller bandwidth, α_{cc}. This choice of bandwidth also helps in the sense that the harmonic compensator will not affect the current controller performance at fundamental frequency. Including the harmonic compensation, where the feed-forward of the grid voltage $\underline{\tilde{e}}_{\mathrm{g}}^{dq}(k)$ is expressed by (5.11), the controller in (5.7) is modified as

$$\begin{aligned} \underline{u}_{\mathrm{c}}^{dq*}(k) = \underline{\tilde{e}}_{\mathrm{g}}^{dq}(k) + \left(j\hat{\omega}_{\mathrm{N}}\hat{L}_{\mathrm{f}} - R_{\mathrm{a}}\right)\underline{i}_{\mathrm{f}}^{dq}(k) + \gamma_{\mathrm{cc}}\hat{L}_{\mathrm{f}}\left(\underline{i}_{\mathrm{f}}^{dq*}(k) - \underline{i}_{\mathrm{f}}^{dq}(k)\right) \quad + \\ \gamma_{\mathrm{cc}}\left(\hat{R}_{\mathrm{f}} + R_{\mathrm{a}}\right)T_{\mathrm{s}}\sum_{n=0}^{k}\left(\underline{i}_{\mathrm{f}}^{dq*}(n) - \underline{i}_{\mathrm{f}}^{dq}(n) + \underline{i}_{\mathrm{err}}^{dq}(n)\right) \end{aligned} \tag{5.12}$$

The modification made to the current controller enables a zero harmonic or negative-sequence current injection from the converter using a simple PI controller avoiding the need for resonant controllers [58][59] or adopting multiple reference-frames [60][61]. For reference purpose in later sections, the controller in (5.7) with a direct feed-forward of the grid voltage is named the *conventional current controller* whereas the current controller with the harmonic compensation included in the feed-forward term as in (5.12) is named the *harmonic compensated current controller*.

5.3.2 Phase-Locked Loop (PLL)

For synchronization purpose in grid-connected VSCs, a PLL that tracks the phase of the positive-sequence voltage vector is typically employed. The PLL should be robust against harmonics, grid voltage unbalances and faults [44][46]. When fast synchronization is not needed, good harmonic rejection from the PLL can be achieved by choosing a low bandwidth. For accurate synchronization against grid voltage unbalances, the sequence estimation method described in Section 4.4.2 and implemented in the dq reference frame can be used. The block diagram of the PLL with the sequence estimation in the dq-coordinate system is shown in Fig. 5.4.

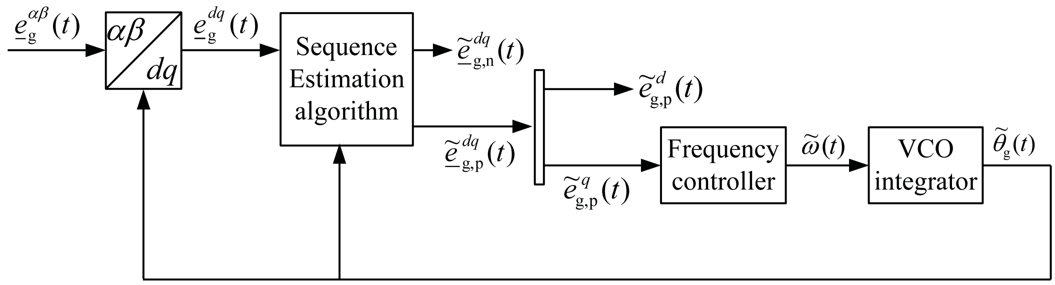

Fig. 5.4 Block diagram of PLL.

For a voltage-oriented coordinate system, the PLL controller tries to force the imaginary part of the positive-sequence voltage $\underline{\tilde{e}}_{\mathrm{g,p}}^{dq}$ to zero. Therefore, the imaginary part ($\tilde{e}_{\mathrm{g,p}}^{q}$) normalized to the grid voltage is used as an angle error (ε_θ) to setup the update of the grid frequency (ω) and grid angle (θ_{g}) as

$$\begin{aligned} \tilde{\omega}(k+1) &= \tilde{\omega}(k) + K_{\mathrm{i}} T_{\mathrm{s}} \varepsilon_\theta(k) \\ \tilde{\theta}_{\mathrm{g}}(k+1) &= \tilde{\theta}_{\mathrm{g}}(k) + T_{\mathrm{s}}\tilde{\omega}(k) + K_{\mathrm{p}} T_{\mathrm{s}} \varepsilon_\theta(k) \end{aligned} \tag{5.13}$$

With α_{PLL} representing the PLL bandwidth, the controller parameters are calculated as [47]

$$\varepsilon_\theta(k) = \tilde{e}_{\mathrm{g,p}}^{q}(k) \Big/ \left|\underline{\tilde{e}}_{\mathrm{g,p}}^{dq}(k)\right| \quad , \qquad K_{\mathrm{p}} = 2\alpha_{\mathrm{PLL}} \quad , \qquad K_{\mathrm{i}} = \alpha_{\mathrm{PLL}}^2$$

The selection of the bandwidth of the PLL is a trade of between harmonic rejection and speed of response. When the sequence estimation is included in the PLL, it provides a 0 pu gain at the negative-sequence component and a smaller gain at harmonic frequencies. Hence, the bandwidth of the PLL can be increased. For this application, the parameters of the PLL are chosen to have a bandwidth of 31.4 rad/s. Figure 5.5 shows a simulation of the PLL response to a sudden phase-angle jump and single-phase fault. As shown in the figure, the impact of an unbalanced fault in the PLL performance is mitigated by using the sequence estimator.

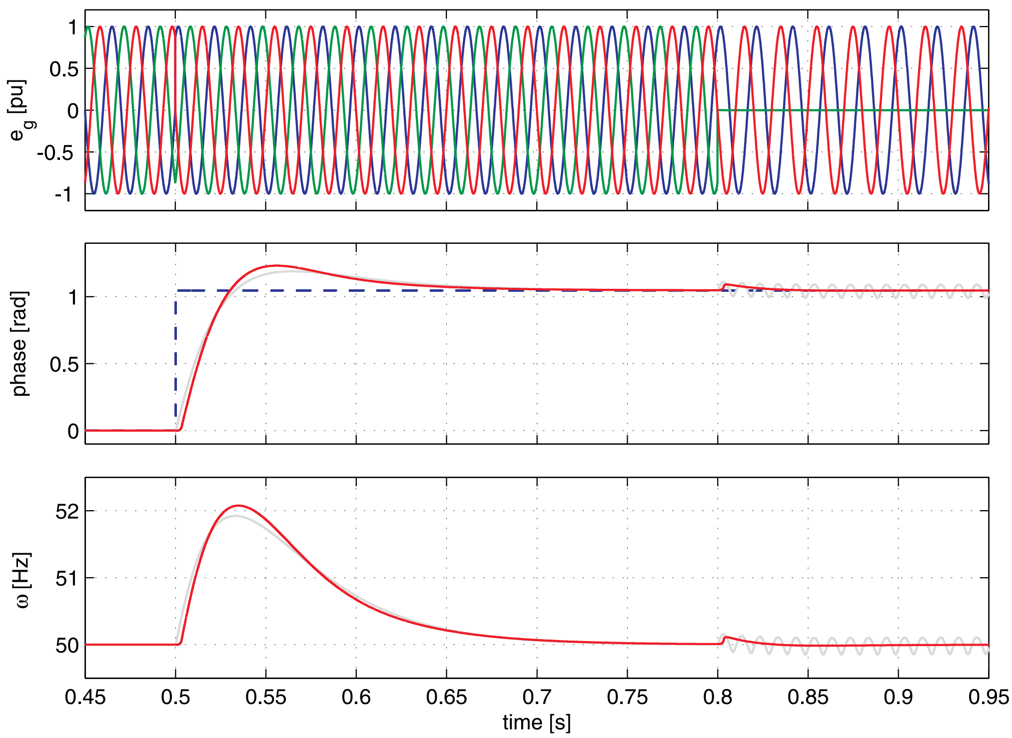

Fig. 5.5 Phase and frequency response of PLL for a sudden phase angle jump at 0.5 s and single-phase fault at 0.8 s; Top: three-phase grid voltage; Middle: Phase angle jump (dashed), PLL phase estimate with no sequence estimation (gray) and with sequence estimation (red); Bottom: PLL grid frequency estimate with no sequence estimation (gray) and with sequence estimation (red).

5.3.3 Outer control loops

As shown in Fig. 5.2, the current reference input to the current controller is calculated through outer control loops. The speed of these controllers is typically selected to be much slower than the inner current control loop to guarantee stability. For this reason, the current controller can be considered infinitely fast when designing the parameters of the outer control loops.

DC-link voltage controller

When operating the VSC, the DC-link voltage should be controlled within allowable limits of the nominal value. If only reactive power injection is used, the DC-link voltage control can be achieved by controlling the active current reference and drawing a small active power from the AC grid [62]. If an energy storage is mounted on the DC side of the VSC, the control of the DC-link voltage also depends on the control of the energy source [20]. Among the energy storage devices that can be integrated to the VSC are components such as capacitors, supercapacitors, batteries and superconducting magnetic coil [14][63][64]. The modeling of the energy storage is outside the focus of this work and will not be considered here. For the performed simulations, a constant DC voltage source is assumed to be connected to the DC-link of the VSC. On the other hand, a DC generator with controlled output voltage is considered for the experimental setup and this will act as the energy storage device. For this reason, a DC-link voltage controller is not implemented.

AC voltage controller

To control the magnitude of the voltage at the connection point, an AC voltage controller using reactive power injection is used. Injection of reactive current at PCC results in a change of the voltage magnitude E_{g} due to the variation of the voltage drop over the steady-state impedance of the system at the connection point X_{pcc} [62]. To derive the controller parameters, a simplified block diagram of an AC voltage controller with droop control as in Fig. 5.6 is considered as an example. The signal E_{g0} represents the steady-state voltage at PCC. If the injected capacitive current to the grid is assumed to be a positive reactive current, the change in voltage magnitude would be negative and hence the system is represented by a gain of $-X_{\mathrm{pcc}}$.

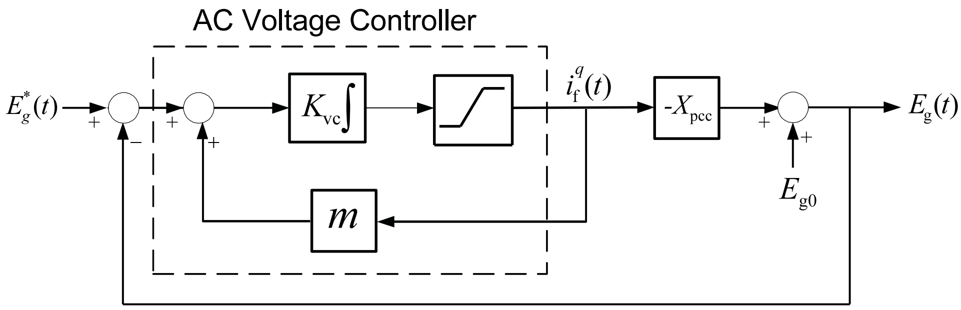

Fig. 5.6 Simplified Block diagram of an AC voltage controller.

Using small-signal variations, the transfer function (G_{vc}) from the change in voltage reference ($\Delta E_{\mathrm{g}}^{*}$) to the change in PCC voltage magnitude (ΔE_{g}) is given by

$$G_{\mathrm{vc}}(s) = \frac{\Delta E_{\mathrm{g}}(s)}{\Delta E_{\mathrm{g}}^{*}(s)} = \frac{-K_{\mathrm{vc}} X_{\mathrm{pcc}}}{s - K_{\mathrm{vc}}\left(X_{\mathrm{pcc}} + m\right)} \tag{5.14}$$

where K_{vc} is the integral gain and m is a droop constant. For perfect voltage control, the droop must be set to zero. To obtain a voltage controller bandwidth of α_{vc}, assuming perfect knowledge of the system impedance X_{pcc} and no droop, the integral gain is calculated as

$$K_{\mathrm{vc}} = -\alpha_{\mathrm{vc}} \Big/ \hat{X}_{\mathrm{pcc}} \tag{5.15}$$

The actual bandwidth of the voltage controller depends on the system impedance and the parameter K_{vc} is usually calculated assuming the largest value of X_{pcc} corresponding to the smallest short-circuit power at the PCC [1]. The reactive current reference for AC voltage control in the linear region is by

$$i_{\mathrm{f}}^{q*}(k+1) = i_{\mathrm{f}}^{q*}(k) + K_{\mathrm{vc}} T_{\mathrm{s}} \left(E_{\mathrm{g}}^{*}(k) - E_{\mathrm{g}}(k) + m i_{\mathrm{f}}^{q}(k)\right) \tag{5.16}$$

If the reference reactive current is beyond the reactive current limit, controlling the PCC voltage to the reference value cannot be guaranteed.

POD and TSE controllers

As explained in Chapter 3, stability enhancement functions such as Power Oscillation Damping (POD) and Transient Stability Enhancement (TSE) can be achieved by controlling FACTS devices in response to power system disturbances. When an E-STATCOM with the cascade control structure in Fig. 5.2 is used for this purpose, the required reference currents for the inner current controller are generated by the POD and TSE controllers. A detail derivation of the POD and TSE controllers will be carried out in the next chapter. Note that the total current references from the outer-control loops should be limited based on the rating of the E-STATCOM before passing to the current controller.

5.4 Virtual machine controller

In the previous section, the classical cascade control structure for the E- ESTATCOM has been discussed. An alternative strategy is to control the E-STATCOM so that the compensator mimics the dynamic behavior of a synchronous generator [22]. This control scheme is here named *virtual machine controller*. Unlike the vector-current controller structure, no dedicated PLL is required in this control method [65][66]. With the active power injection capability of the E-STATCOM, the mechanical behavior of an actual machine can be implemented in the control algorithm. For the specific application, this method allows a direct control of the inertia and damping that can be added to the power system [21]. As described in Chapter 2, the added inertia and damping can increase the stability of the power system. After developing the control method in this section, a discussion of how the stability of the power system can be enhanced will be made in the next chapter.

The main circuit scheme of a two-level E-STATCOM connected to a grid through an L-filter has been described in Section 5.2. The same device is considered here and the control block diagram is shown in Fig. 5.7. The various signals such as the grid voltages, filter currents, DC-link voltage and transmitted power are measured and sampled at a rate $1/T_\mathrm{s}$. The control system then generates the converter reference voltage, $\underline{u}_\mathrm{c}^{\alpha\beta*}$, from which the PWM signals sw_a, sw_b and sw_c will be calculated similar to the case in Fig. 5.2. The detail of the algorithm for generating $\underline{u}_\mathrm{c}^{\alpha\beta*}$ from the input signals will be developed in the following.

The detail of a synchronous generator model varies greatly depending on the type of study to be investigated and the classical model of a synchronous generator has been adopted in Chapter 2 to study power system stability. Similarly, the simplified model will be emulated through control implementation of an E-STATCOM in this section. The classical generator model consists of an internal generator voltage (V_g) and dynamic rotor angle (δ_g) behind a transient impedance (X'_d) as explained in Section 2.2.1. From a physical point of view, these quantities are similar to

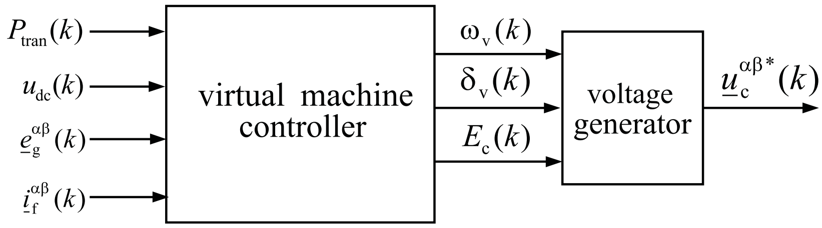

Fig. 5.7 Overall block diagram of the virtual machine controller for E-STATCOM.

the converter voltage magnitude (E_{c}), the converter voltage angle (δ_{v}) and the filter impedance (X_{f}), respectively. The actual mechanical speed and rotor angle dynamics of the generator (ω_{g}, δ_{g}) are emulated in the control of the E-STATCOM using the equation of motion as in (2.1) to generate their virtual counterparts (ω_{v}, δ_{v}). The magnitude of the internal voltage of the actual generator can be controlled through the excitation system to provide auxiliary functions such as terminal voltage control, reactive power control and damping by PSS. These functionalities can be similarly replicated in the virtual machine control algorithm by manipulating the magnitude of the converter voltage, E_{c}. Note that the subscript "v" in the various parameter definitions in this section indicates that the described quantity is related to the virtual machine.

In an actual synchronous generator, the active and reactive power exchange of the machine with the connected grid is controlled through variation of the rotor angle and internal voltage magnitude, respectively. Using the same principle, the active and reactive power control of the virtual machine will be described.

5.4.1 Active power controller

The electromechanical dynamics in the actual machine are expressed through the equation of motion as described in Chapter 2 for the classical synchronous generator model. In the virtual machine model, this is expressed similarly as

$$\begin{gathered} 2H_{\mathrm{v}}\frac{d\omega_{\mathrm{v}}}{dt} = P_{\mathrm{ref}} - P_{\mathrm{inj}} - K_{\mathrm{Dv}}\omega_{\mathrm{v}} \\ \frac{d\delta_{\mathrm{v}}}{dt} = \omega_0\omega_{\mathrm{v}} - \omega_0 \end{gathered} \tag{5.17}$$

The angle δ_{v} represents the angular position of the converter voltage vector with respect to a reference frame synchronized with the grid and rotating at a constant frequency of ω_0 in steady-state. P_{ref} and P_{inj} represent the reference and actual active power output from the converter, respectively. Note that the reference active power of the virtual machine controller is similar to the input mechanical torque for the actual machine. Finally, K_{Dv} represents a damping coefficient added in the model to mimic the behavior of the mechanical damping term in the actual machine. However, this term does not lead to losses as in the case of the actual machine and the value can be adjusted to get as much damping as needed in the emulated generator system.

Using the equation of motion in (5.17) and the network power flow equation, the active power control of the virtual machine can be derived. The expression for the injected power from the converter, P_{inj}, depends on the converter voltage output and the parameters of the transmission network. Considering the system in Fig. 5.3 and neglecting the losses in the filter reactor, the steady-state power injected from the converter can be expressed as

$$P_{\mathrm{inj}} = \frac{E_{\mathrm{c}} E_{\mathrm{g}} \sin(\delta_{\mathrm{v}})}{X_{\mathrm{f}}} \tag{5.18}$$

where E_{g} is the magnitude of the grid voltage and the virtual angle, δ_{v} represents the angle difference between the converter voltage ($\underline{u}_{\mathrm{c}}^{\alpha\beta}$) and the grid voltage ($\underline{e}_{\mathrm{g}}^{\alpha\beta}$). To study the small-signal oscillations around steady-state operating points, a linear model of the system can be obtained as

$$\frac{d}{dt}\begin{bmatrix} \Delta\omega_{\mathrm{v}} \\ \Delta\delta_{\mathrm{v}} \end{bmatrix} = \begin{bmatrix} -K_{\mathrm{Dv}}/2H_{\mathrm{v}} & -K_{\mathrm{Sv}}/2H_{\mathrm{v}} \\ \omega_0 & 0 \end{bmatrix} \begin{bmatrix} \Delta\omega_{\mathrm{v}} \\ \Delta\delta_{\mathrm{v}} \end{bmatrix} + \begin{bmatrix} 1/2H_{\mathrm{g}} \\ 0 \end{bmatrix} \Delta P_{\mathrm{ref}} \tag{5.19}$$

where ω_0 represents the nominal frequency of the grid and the synchronizing torque coefficient, K_{Sv} is given by

$$K_{\mathrm{Sv}} = \frac{dP_{\mathrm{inj}}}{d\delta_{\mathrm{v}}} = \frac{E_{\mathrm{c}} E_{\mathrm{g}} \cos(\delta_{\mathrm{v0}})}{X_{\mathrm{f}}}$$

where δ_{v0} is the steady-state virtual angle. Note that the model in (5.19) assumes a stiff grid and the magnitude of the converter voltage is kept constant to emulate the synchronous generator in the classical model. From (5.18) and (5.19), the transfer function from the reference to actual active power from the converter is given by

$$\frac{\Delta P_{\mathrm{inj}}}{\Delta P_{\mathrm{ref}}} = \frac{\frac{\omega_0 K_{\mathrm{Sv}}}{2H_{\mathrm{v}}}}{s^2 + \frac{K_{\mathrm{Dv}}}{2H_{\mathrm{v}}} s + \frac{\omega_0 K_{\mathrm{Sv}}}{2H_{\mathrm{v}}}} = \frac{\omega_{\mathrm{n}}^2}{s^2 + 2\varsigma\omega_{\mathrm{n}} s + \omega_{\mathrm{n}}^2} \tag{5.20}$$

where ς and ω_{n} are the damping ratio and natural frequency of the system in (5.20), respectively. Using these definitions, the poles of the transfer function for the active power controller are given by

$$-\varsigma\omega_{\mathrm{n}} \pm \omega_{\mathrm{n}}\sqrt{\varsigma^2 - 1}$$

Based on the dynamic behavior required from the emulated generator, various parameters can be determined using the relation

$$\frac{K_{\mathrm{Dv}}}{4H_{\mathrm{v}}} = \varsigma\omega_{\mathrm{n}} \quad , \quad \frac{\omega_0 K_{\mathrm{Sv}}}{2H_{\mathrm{v}}} = \omega_{\mathrm{n}}^2 \tag{5.21}$$

The damping ratio should be chosen to be positive in order to get a positive damping to the system. If $0 < \varsigma < 1$, the poles become complex conjugates, representing a decaying oscillatory mode. The oscillation frequency in this case is given by the imaginary part of the poles and the system is characterized by an overshoot for a step in the reference active power. If $\varsigma \geq 1$, the poles become real and negative and this results in non-oscillatory damped response. When the damping ration is equal to 1, the system in (5.20) results in double real poles at $-\omega_{\mathrm{n}}$. Increasing ς above 1 will result two real poles at $(-\varsigma+\sqrt{\varsigma^2-1})\omega_{\mathrm{n}}$ and $(-\varsigma-\sqrt{\varsigma^2-1})\omega_{\mathrm{n}}$. In this case, the smaller pole, $(-\varsigma+\sqrt{\varsigma^2-1})\omega_{\mathrm{n}}$ decides the overall dynamic response of the system. For this reason, $\varsigma=1$ can be chosen to maximize the dynamic response of the active power controller and this reduces the transfer function in (5.20) to

$$\frac{\Delta P_{\mathrm{inj}}}{\Delta P_{\mathrm{ref}}}=\frac{\omega_{\mathrm{n}}^2}{(s+\omega_{\mathrm{n}})^2} \tag{5.22}$$

Once the damping ratio is chosen, the selection of the natural frequency depends on the required dynamic response from the system. However, it can be understood from (5.21) and (5.22) that the value of the virtual inertia to be implemented directly affects the speed of the controller. Depending on the specific application of the compensator in the power system, the value of the virtual inertia can be chosen [22].

5.4.2 Reactive power controller

The reactive power injected into the grid from the converter (Q_{inj}) can be controlled by manipulating the magnitude of the converter voltage, E_{c}. For this purpose, consider the steady-state reactive power injection from the converter

$$Q_{\mathrm{inj}}=\frac{E_{\mathrm{g}}\left[E_{\mathrm{c}}\cos(\delta_{\mathrm{v}})-E_{\mathrm{g}}\right]}{X_{\mathrm{f}}} \tag{5.23}$$

Assuming a stiff grid as before and using (5.23), the change in reactive power injection into the grid is directly affected by the change in the converter voltage magnitude. If the parameters and operating points of the system are accurately known, the steady-state reference reactive power can be achieved by changing the converter voltage magnitude in open-loop fashion according to the relation in (5.23). However, a closed-loop controller is required to guarantee reference tracking for varying operation points. Hence, an example of a reactive power controller is given by

$$E_{\mathrm{c}}(t)=K_{\mathrm{Qc}}\int_0^t(Q_{\mathrm{ref}}-Q_{\mathrm{inj}})\,d\tau \tag{5.24}$$

Using small-signal variations, the transfer function from the change in reactive power reference to the injected reactive power is given by

$$\frac{\Delta Q_{\mathrm{inj}}}{\Delta Q_{\mathrm{ref}}}=\frac{\alpha_{\mathrm{Qc}}}{s+\alpha_{\mathrm{Qc}}} \tag{5.25}$$

where α_{Qc} is the bandwidth of the reactive power controller. To achieve the required bandwidth, the integral gain K_{Qc} is calculated using the relation

$$\alpha_{\mathrm{Qc}} = \frac{K_{\mathrm{Qc}} E_{\mathrm{g}} \cos(\delta_{\mathrm{v0}})}{\hat{X}_{\mathrm{f}}}$$

Using the virtual angle (δ_{v}), converter voltage magnitude (E_{c}) and the steady-state grid frequency (ω_0), the reference converter voltage ouput ($\underline{u}_{\mathrm{c}}^{\alpha\beta *}$) to realize the virtual machine controller is given by

$$\underline{u}_{\mathrm{c}}^{\alpha\beta *}(t) = E_{\mathrm{c}} e^{j(\omega_0 t + \delta_{\mathrm{v}})} \tag{5.26}$$

5.4.3 Converter current limitation

The control method described so far in this section calculates the converter reference voltage based on the active and reactive power references and the converter current will be decided by the power flow equations, as shown in (5.18) and (5.23). However, a current higher than the rating of the converter might flow during transient conditions and a mechanism to limit the current should be available in the control algorithm. In the conventional cascade controller, this is straight forward as the current reference to the inner current controller can be easily limited. Hence, one way to apply the current limitation in the virtual machine controller is to setup a current controller that runs in parallel and works only when the current from the converter is above the current limit [66]. Assume that the current controller in the dq-reference frame for this purpose is given by

$$\underline{u}_{\mathrm{c}}^{dq*}(t) = \underline{e}_{\mathrm{g}}^{dq}(t) + j\hat{X}_{\mathrm{f}} \underline{i}_{\mathrm{f}}^{dq}(t) + \alpha_{\mathrm{cc}} \hat{L}_{\mathrm{f}} \left[\underline{i}_{\mathrm{f}}^{dq*}(t) - \underline{i}_{\mathrm{f}}^{dq}(t) \right] \tag{5.27}$$

where α_{cc} represents the required bandwidth of the controller. Unlike the implementation of the virtual machine controller, the controller in (5.27) needs a reference current input. If we assume that the virtual machine controller in (5.26) and the current controller in (5.27) result in the same converter voltage under normal conditions, the rule for the required reference current to apply the current limitation can be derived as [66]

$$\underline{i}_{\mathrm{f}}^{dq*} = \frac{E_{\mathrm{c}} e^{j(\omega_0 t + \delta_{\mathrm{v}} - \theta_{\mathrm{g}})} - \underline{e}_{\mathrm{g}}^{dq} + (\alpha_{\mathrm{cc}} \hat{L}_{\mathrm{f}} - j\hat{X}_{\mathrm{f}}) \underline{i}_{\mathrm{f}}^{dq}}{\alpha_{\mathrm{cc}} \hat{L}_{\mathrm{f}}} \tag{5.28}$$

where θ_{g} is the angle from a PLL synchronized with the grid voltage. Hence, a current limitation can be applied to the reference current in (5.28) when this becomes higher that its rated value. In this case, the converter voltage using the limited reference current ($\underline{i}_{\mathrm{f,lim}}^{dq*}$) is given by

$$\underline{u}_{\mathrm{c}}^{\alpha\beta *}(t) = \left(\underline{e}_{\mathrm{g}}^{dq}(t) + j\hat{X}_{\mathrm{f}} \underline{i}_{\mathrm{f}}^{dq}(t) + \alpha_{\mathrm{cc}} \hat{L}_{\mathrm{f}} \left[\underline{i}_{\mathrm{f,lim}}^{dq*}(t) - \underline{i}_{\mathrm{f}}^{dq}(t) \right] \right) e^{j\theta_{\mathrm{g}}} \tag{5.29}$$

Note that the current limitation algorithm is used only when the calculated reference currents are beyond the current limit of the converter. In this case, the converter voltage calculation switches smoothly from (5.26) to (5.29). During this current limitation interval, the demanded converter voltage to enable the converter to work as a virtual machine cannot be guaranteed and the maximum current injection is instead prioritized.

5.4.4 Auxiliary control loops

The main control blocks in the virtual machine controller described so far are the active and reactive power controllers. Based on the reference active and reactive powers, the control algorithm tries to change the virtual angle and converter voltage magnitude in an effort for the converter power outputs to follow the references. The reference powers can be set in different ways based on the requirement from the converter. Therefore, the various functions that are required from the implemented virtual machine can be added to the main active and reactive power controllers through additional auxiliary control loops and this will be briefly described in the following.

AC voltage controller

The terminal voltage of an actual generator can be controlled through variation of the field current from the excitation system. The variation of the excitation system in turn changes the magnitude of the internal voltage so that the reactive power flow from the generator varies to control the terminal voltage. In the virtual machine controller, this can be similarly implemented by varying the magnitude of the converter voltage, E_{c}. As described in Section 5.4.2, reactive power control has been achieved by varying the converter voltage magnitude. Assume that the AC voltage controller is implemented in the virtual machine controller instead of the reactive power controller and the connection grid is represented by its Thevenin's equivalent with voltage ($\underline{E}_{\mathrm{th}}$) behind an impedance ($X_{\mathrm{th}}$) in steady-state. With the converter connected to the grid though a filter with reactance X_{f} as described in Fig. 5.3, the grid voltage magnitude (E_{g}) in steady-state is given by

$$E_{\mathrm{g}} = \sqrt{X_{\mathrm{th}}^2 E_{\mathrm{c}}^2 + X_{\mathrm{f}}^2 E_{\mathrm{th}}^2 + 2X_{\mathrm{f}} X_{\mathrm{th}} E_{\mathrm{c}} E_{\mathrm{th}} \cos(\delta_{\mathrm{ct}})} \Big/ (X_{\mathrm{f}} + X_{\mathrm{th}}) \tag{5.30}$$

where δ_{ct} is the angle difference between the converter voltage and the Thevenin equivalent voltage. It can be understood from (5.30) that the grid voltage magnitude can be controlled by changing the magnitude of the converter voltage. Hence, a control algorithm that ensures reference tracking in steady-state can be given by

$$E_{\mathrm{c}}(t) = K_{\mathrm{vc}} \int_0^t \left(E_{\mathrm{g}}^* - E_{\mathrm{g}}\right) d\tau \tag{5.31}$$

where E_{g}^* is the reference grid voltage. Based on the steady-state operating point and parameters of the grid, the value of the integral gain, K_{vc} can be selected to achieve the required bandwidth of the AC voltage controller.

POD and TSE controllers

To achieve POD and TSE functions, the active and reactive power from the VSC should be controlled in response to power system disturbances. This can be achieved by modulating the reference active and reactive power references in the virtual machine controller similar to the discussion in Section 5.3.3, where the reference currents are modulated instead. With respect to the use of reactive power, the AC voltage controller could be used instead of the reactive power controller in Section 5.4.2. In this case, the required POD and TSE functions can be achieved by proper control of the reference AC voltage.

5.5 Simulation verification

The performance of the two control strategies for the E-STATCOM, the classical cascade controller and the virtual machine controller, will be investigated via simulation in this section. Considering an ideal and a distorted grid, the performance of the conventional current controller and the harmonic compensated current controller will also be compared.

5.5.1 Vector-current controller performance

To test the performance of the current controller, the system and controller parameters are given in Table 5.1. In the simulation, a constant DC-link voltage is assumed and PWM is used to generate the switching patterns for the VSC valves. The switching frequency f_s is equal to the sampling frequency and is set to 5 kHz.

TABLE 5.1. SYSTEM AND CONTROLLER PARAMETERS

Grid voltage	400 V = 1 pu
Grid current	40 A = 1 pu
Grid frequency	50 Hz
DC-link voltage	650 V
Filter inductance, L_f	2 mH
Filter resistance, R_f	6.2 mΩ
Current controller bandwidth, α_cc	2500 rad/s
Active damping, R_a	0.0502 Ω
Harmonic compensation bandwidth, α_hc	628.3 rad/s
Active damping for harmonic compensation, R_ha	0.0625 Ω

First, the conventional current controller in (5.7) is simulated and Fig. 5.8 shows the dynamic current response for a step in the fundamental reference dq current with an ideal grid (no harmonic distortion) and a distorted grid. For the distorted grid, the harmonic magnitudes in pu of 0.015, 0.01, 0.002 and 0.002 for the 5^{th}, 7^{th}, 11^{th} and 13^{th} order harmonics, respectively, are considered. The harmonic content is chosen to be of the same order of magnitude as the ones in the measured grid voltage in the actual laboratory setup to be shown in the next section. For

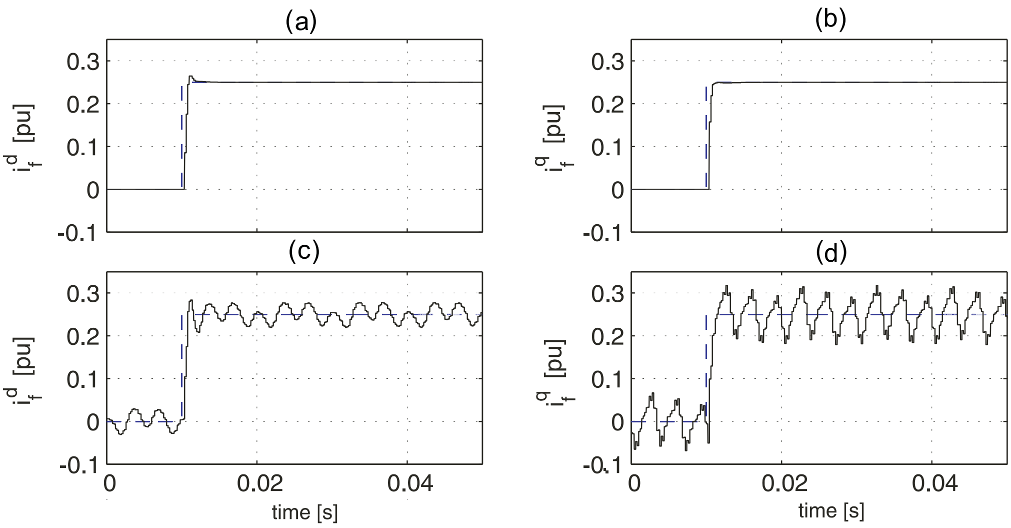

Fig. 5.8 Simulated conventional current controller response for d-component (left) and q-component (right); (a, b) ideal grid and discrete controller, (c, d) distorted grid and discrete controller; reference current (dashed) and actual current (solid).

the ideal grid, the discrete controller works as expected (Fig. 5.8 plots a, b) with the required bandwidth. The small overshoot observed in the current response is due to the delay resulting from the discrete controller. In case of distorted grid, the injected currents will be affected by low-order harmonics (Fig. 5.8 plots c, d). To show that this problem exists only in the discrete controller, where a significant time delay exists, the conventional controller in (5.7) has been implemented in continuous time instead using the same distorted grid and the results are shown in Fig. 5.9. The continuous controller works as expected without any harmonic current injection to the grid due to the absence of time delays in the control implementation.

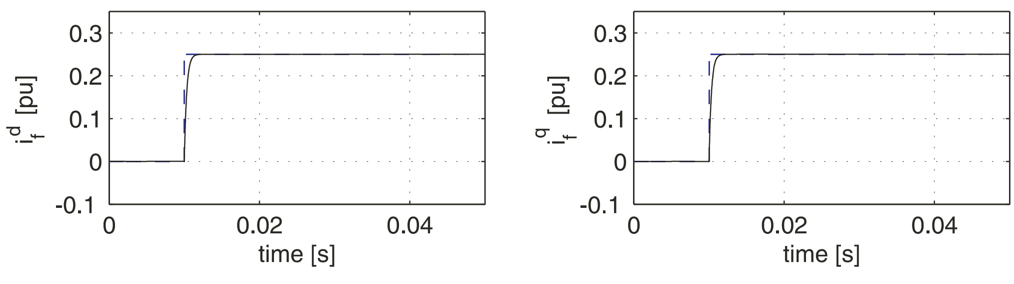

Fig. 5.9 Simulated conventional current controller response for d-component (left) and q-component (right) with distorted grid and continuous controller; reference current (dashed) and actual current (solid).

To evaluate the performance of the harmonic compensated current controller in (5.12), the same grid as in the previous case which is distorted by 5^{th}, 7^{th}, 11^{th} and 13^{th} order harmonics has been considered. Figure 5.10 shows the dynamic performance of the two controller structures. As shown in the figure, the harmonic compensated controller performs similar to the conventional current controller on the fundamental current components. On the other hand, the harmonic current components injected to the grid are controlled to zero with in half the fundamental period in the case of the harmonic compensated current controller. Similarly, to evaluate the impact of unbalanced grid, a three-phase voltage with magnitudes of phase a, phase b and phase c set to 0.7 pu, 1 pu and 1 pu, respectively, is considered. A step in the reference dq current is applied at 0.04 s and Fig. 5.11 shows the dynamic performance of the conventional and harmonic compensated current controllers. Again, the steady-state negative-sequence current injection into the grid is avoided with the harmonic compensated current controller, which verifies the validity of the control method.

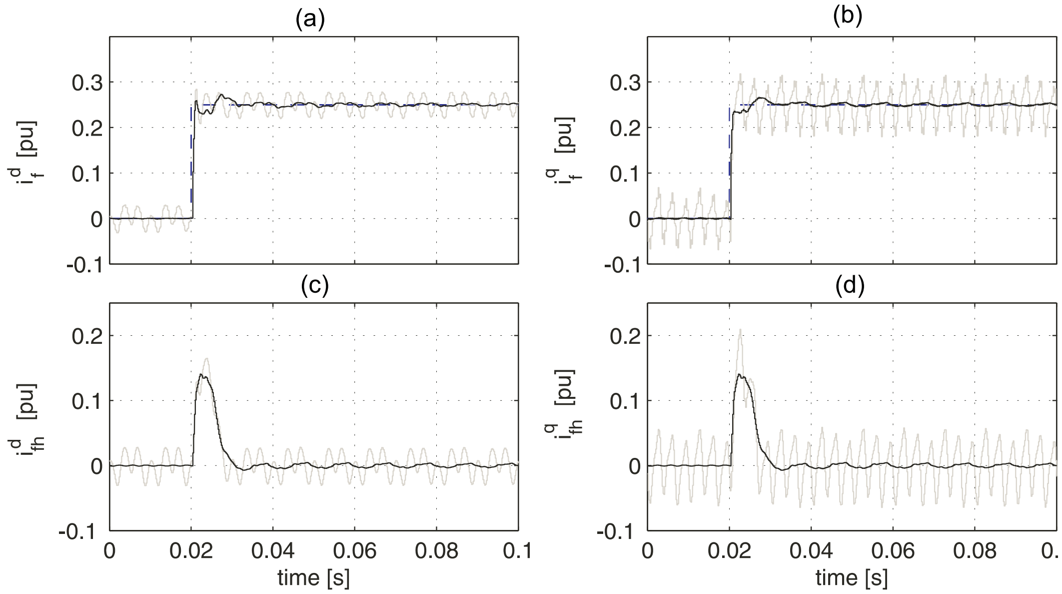

Fig. 5.10 Simulated current controller response with conventional current controller (gray solid) and harmonic compensated current controller (black solid). (a) d-component current, (b) q-component current , (c) d-component harmonic current and (d) q-component harmonic current; reference current (dashed) and actual current (solid).

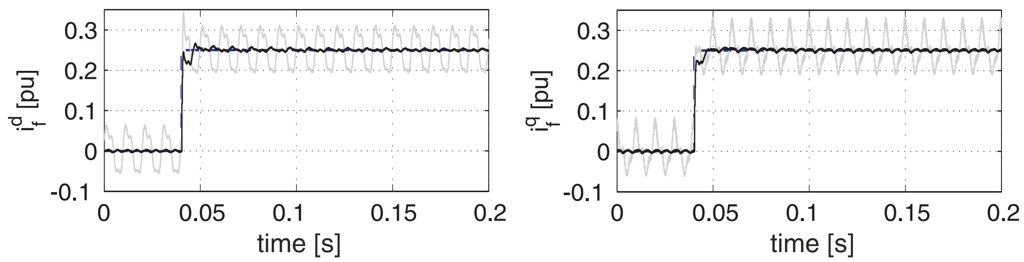

Fig. 5.11 Simulated current controller response for d-component (left) and q-component (right) for unbalanced grid; conventional current controller (gray solid) and harmonic compensated current controller (black solid); reference current (dashed) and actual current (solid).

5.5.2 Virtual machine controller performance

Considering a converter connected to a strong grid, the performance of the virtual machine controller described in Section 5.4 will be verified via simulation in this section. For this, the parameters of the system are set similar to the one in Table 5.1. A constant DC-link voltage is assumed and a PWM scheme with a switching frequency of 5 kHz is used for the converter control similar to the discussion in Section 5.5.1 .

Before testing the dynamic performance of the virtual machine controller for a step in the active and reactive power reference, the converter should be synchronized to the grid similar to the case in an actual synchronous machine. This is achieved by using a vector current controller and a PLL. Once the converter is connected to the grid with zero current injection, the grid frequency and angle outputs from the PLL will be used to initialize the speed and angle of the virtual machine controller, respectively.

The first test involves designing a virtual machine controller according to the description in Section 5.4 to verify if the design requirements are met in a time-domain simulation. For this purpose, a damping ratio of 0.1 and a natural frequency of 12.6 rad/s are chosen for the active power controller, which yields $K_{\mathrm{Dv}} = 17$ and $H_{\mathrm{v}} = 3.38$ s. For the reactive power controller, the integrator gain is chosen as $K_{\mathrm{Qc}} = 18.5$ to get a bandwidth of $\alpha_{\mathrm{Qc}} = 62.8$ rad/s. For this choice of parameters, the dynamic performance of the virtual machine controller for a step in the active and reactive power reference is shown in Fig. 5.12. As it can be observed from the results, active and reactive power control are achieved with the desired design requirements through variation of the virtual angle and converter voltage magnitude, respectively.

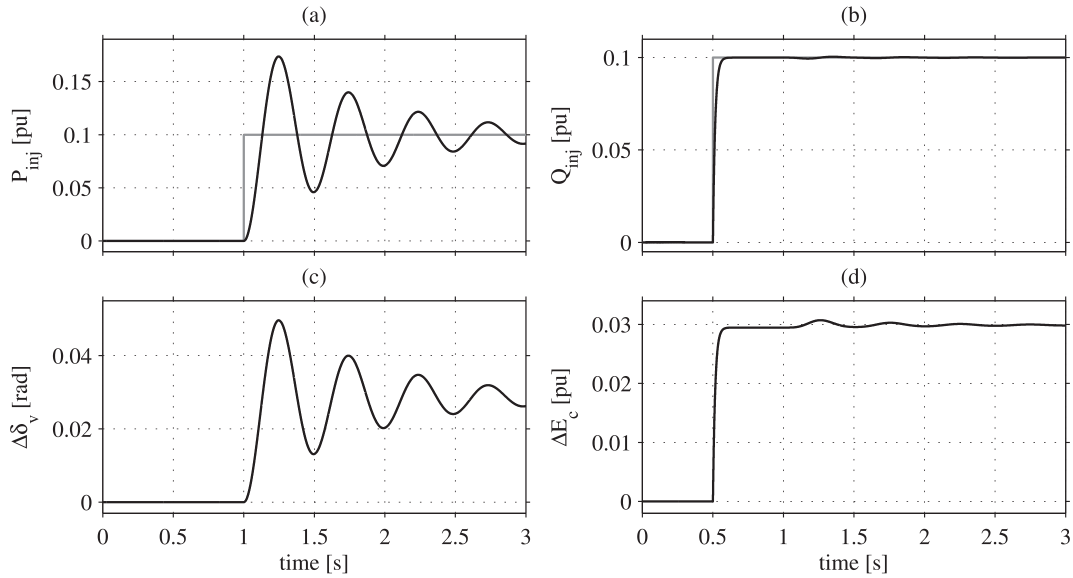

Fig. 5.12 Dynamic performance of the virtual machine controller; (a) reference (gray) and actual (black) injected active power; (b) reference (gray) and actual (black) injected reactive power; (c) virtual angle deviation; (d) change in converter voltage magnitude.

As shown in the results in Fig. 5.12, the active and reactive power controllers work with a reasonably small coupling between them. Hence with zero reactive power injection, the impact of various parameters such as K_{Dv} and H_{v} on the dynamic performance of the active power controller will be investigated next. The first set of tests is performed using a natural frequency of $\omega_{\mathrm{n}} = 12.6$ and three different values of the damping coefficient, $K_{\mathrm{Dv}} = [67.9, 118.8, 169.8]$ corresponding to a damping ratio of $\varsigma = [0.4, 0.7, 1.0]$, respectively. The test is repeated using a damping ratio of $\varsigma = 1.0$ and three different values of the virtual inertia, $H_{\mathrm{v}} = [3.38, 0.54, 0.14]$ corresponding to a natural frequency of $\omega_{\mathrm{n}} = [12.6, 31.4, 62.8]$, respectively. The dynamic response of the active power controller for the various cases when a step in the reference active power is applied at 0.5 s is shown in Fig. 5.13.

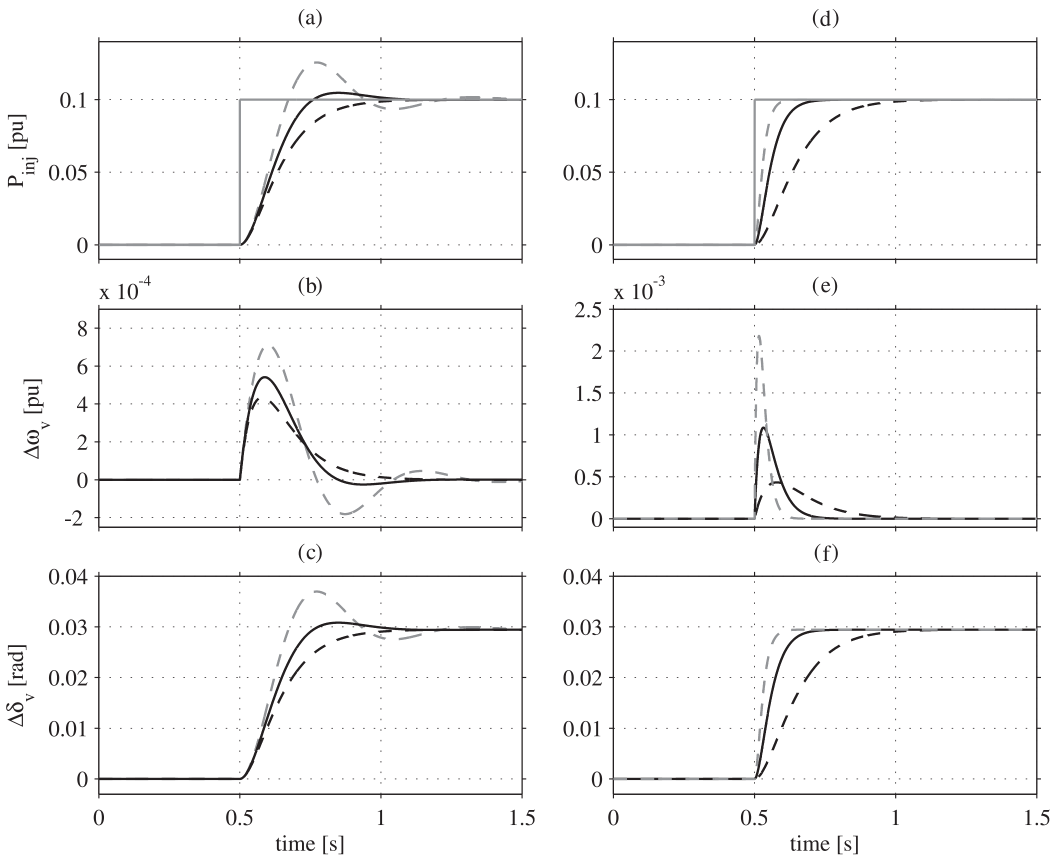

Fig. 5.13 Impact of parameters on the active power controller; Injected active power (plot a), virtual speed deviation (plot b) and virtual angle deviation (plot c) with $\omega_{\mathrm{n}} = 12.6$ and $\varsigma = 0.4$ (gray dashed), $\varsigma = 0.7$ (black solid) and $\varsigma = 1.0$ (black dashed); Injected active power (plot d), virtual speed deviation (plot e) and virtual angle deviation (plot f) with $\varsigma = 1.0$ and $\omega_{\mathrm{n}} = 12.6$ (black dashed), $\omega_{\mathrm{n}} = 31.4$ (black solid) and $\omega_{\mathrm{n}} = 62.8$ (gray dashed); Gray solid curves represent the injected active power reference.

As the results in Fig. 5.13 show, a higher damping ratio gives a well damped response. By choosing a damping ratio close to 1, an overshoot in the response of the injected active power can be avoided. On the other hand, the choice of the natural frequency is a compromise between response speed and emulated inertia. A higher choice of the natural frequency, correspondingly a lower virtual inertia, results in a faster response. However, this could be a disadvantage if the purpose of the converter is to provide some inertia support to the power system. Based on the requirement from the converter, the controller parameters can be selected.

A final test is made to investigate the performance of the virtual machine controller versus the classical cascade controller. For this purpose, the active power controller parameters are chosen as $\varsigma = 1.0$ and $\omega_{\mathrm{n}} = 62.8$ rad/s whereas the bandwidth of the reactive power controller is chosen as $\alpha_{\mathrm{Qc}} = 62.8$ rad/s for the virtual machine controller. For comparison, an integral outer loop active and reactive power controller that gives a bandwidth of 62.8 rad/s is selected for the classical cascade controller. The dynamic performance of the two controllers for a step in the active and reactive power reference is shown in Fig. 5.14.

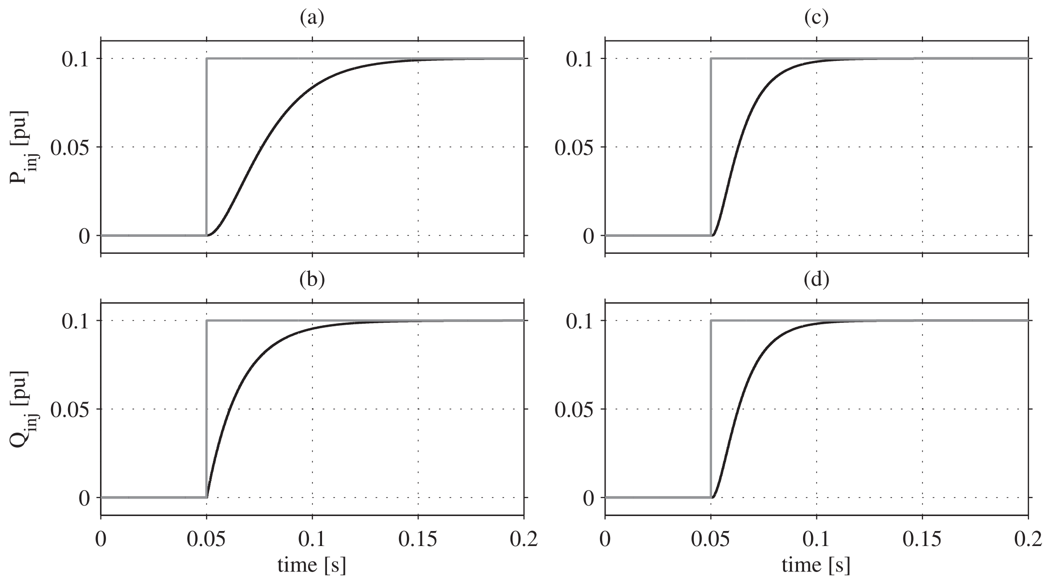

Fig. 5.14 Comparison of the virtual machine controller versus the classical cascade controller; Injected active power (plot a) and reactive power (plot b) using virtual machine controller; Injected active power (plot c) and reactive power (plot d) using classical cascade controller; Gray curves represent reference power and black curves represent actual power.

The results in Fig. 5.14 show that the two control structures provide the required power reference tracking based on the design requirement. However, the virtual machine controller is slightly slower for this choice of parameters, due to the fact that the active power controller in (5.22) is a second-order system unlike the classical cascade controller, which is characterized by a first-order transfer function. If a similar performance as the classical cascade controller is required from the virtual machine controller, it can be achieved by adjusting the parameters H_{v} and K_{Dv}. One advantage with the classical cascade controller is that a reliable control of the converter current is possible during fast transients such as power system faults. On the other hand, the virtual machine controller has the capability of providing inertia support to the power system, where the added inertia value (H_{v}) can be calculated directly.

5.6 Experimental Verification

The obtained simulation results have been verified experimentally in the laboratory. A description of the setup together with the experimental results will be presented in this section.

5.6.1 Laboratory setup

A single line diagram of the actual laboratory setup for the tests in this section is shown in Fig. 5.15. The setup consists of a VSC system connected to an AC grid. The grid voltage e_g contains about 0.015 pu 5^{th} and 7^{th} order harmonics among others as shown in Fig. 5.16, where the FFT of the phase-to-ground voltage (phase a) is depicted.

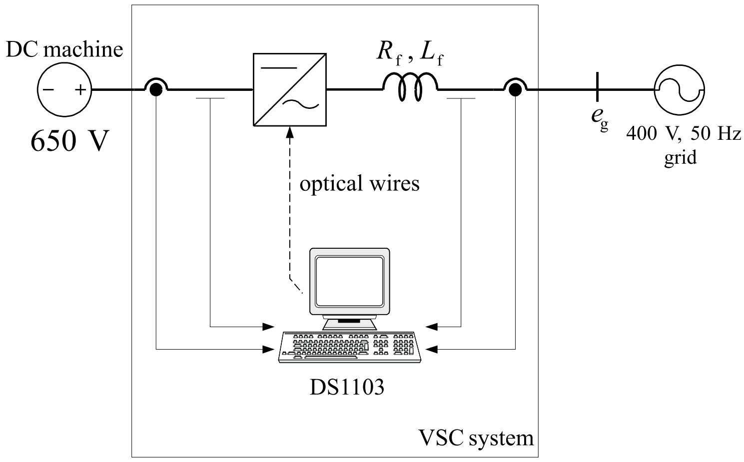

Fig. 5.15 Single line diagram of the laboratory setup.

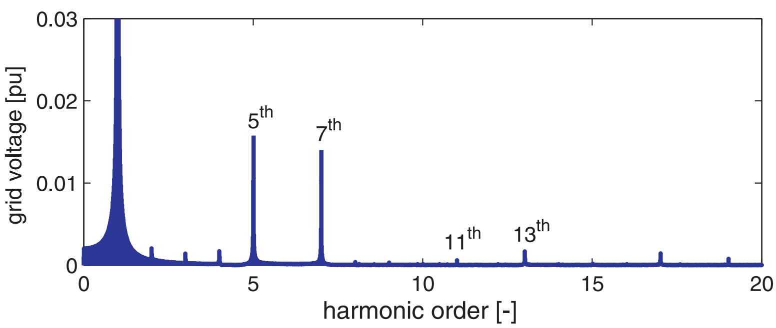

Fig. 5.16 FFT of measured phase-to-ground grid voltage.

The VSC system consists of a two-level converter connected to the AC grid though an L-filter. The parameters of the laboratory setup together with the controller parameters are the same as the ones in the simulation in Section 5.5. The VSC is controlled from a computer with a dSpace 1103 board [50]. The DC-link of the VSC is connected to a DC machine rated 700 V and 60 A, which gives the VSC active power injection capability. The terminal voltage of the DC machine is controlled to a constant value of 650 V and this has been used for all the tests. Moreover, PWM with a switching frequency of 5 kHz is used to generate the pulses for the VSC valves.

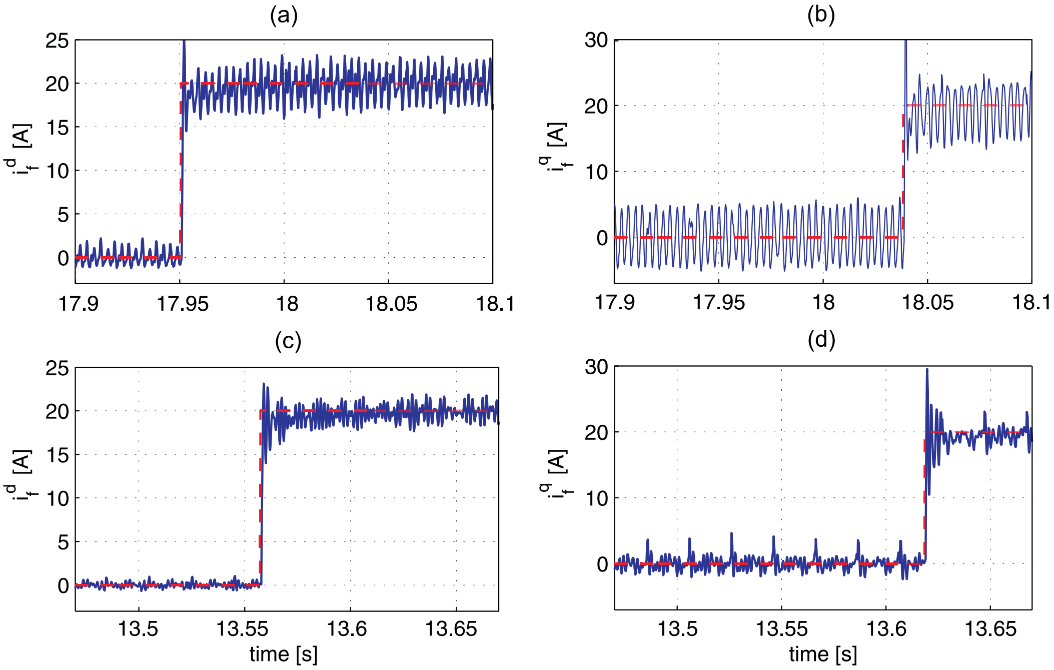

Fig. 5.17 Dynamic performance of vector-current controller for a step in current reference (dashed curves); conventional current controller response for d-component current (plot a) and q-component current (plot b); harmonic compensated current controller response for d-component current (plot c) and q-component current (plot d).

5.6.2 Experimental results on vector-current controller

With the set up as in Fig. 5.15, the conventional and harmonic compensated current controllers are tested and the dynamic performance of the two controllers for a step in the dq current reference is shown in Figs. 5.17 and 5.18. The harmonic compensated current controller has been designed to set the 5^{th} and 7^{th} order current harmonics injected to the grid to zero. From the FFT in Fig. 5.16, it can be observed that the grid contains other harmonics in addition to the considered ones. Therefore, to see the impact of the harmonic compensation on the 5^{th} and 7^{th} order harmonic components, the FFT of the current response in Fig. 5.18 for phase a is shown in Fig. 5.19. As it can be seen from the results, the harmonic compensated current controller successfully removes the 5^{th} and 7^{th} order harmonic current injection to the grid.

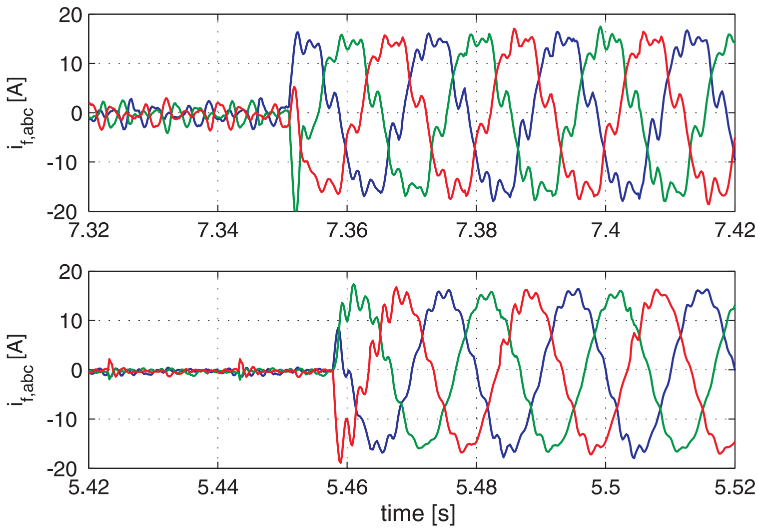

Fig. 5.18 Three-phase current controller response with conventional current controller (top) and harmonic compensated current controller (bottom).

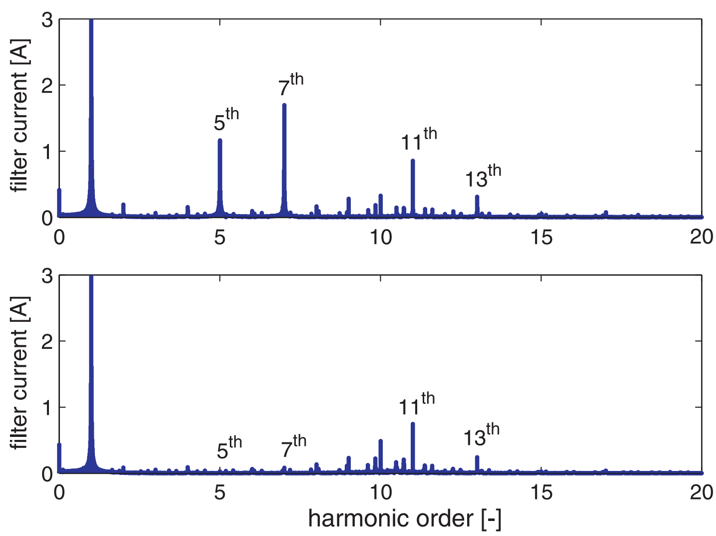

Fig. 5.19 FFT for phase a filter current when conventional current controller used (top) and harmonic compensated current controller used (bottom).

5.6.3 Experimental results on virtual machine controller

With the laboratory setup as in Fig. 5.15 and the parameters of the system as described in Table 5.1, the performance of the virtual machine controller for various parameter choices will be verified in this section. First, the response of the controller for a change in the reference active and reactive power is tested. For this test, a virtual inertia of $H_{\mathrm{v}} = 3.38$ and a virtual damping constant of $K_{\mathrm{Dv}} = 67.9$ corresponding to a natural frequency of 12.6 rad/s and a damping ratio of 0.4 for accurate system parameters are chosen for the active power controller. Similarly, the integrator gain is chosen as $K_{\mathrm{Qc}} = 18.5$ corresponding to a bandwidth of $\alpha_{\mathrm{Qc}} = 62.8$ rad/s for the reactive power controller. For this choice of parameters, the dynamic performance of the virtual machine controller is shown in Fig. 5.20. It can be observed from the results that the measured active and reactive powers follow the references based on the design.

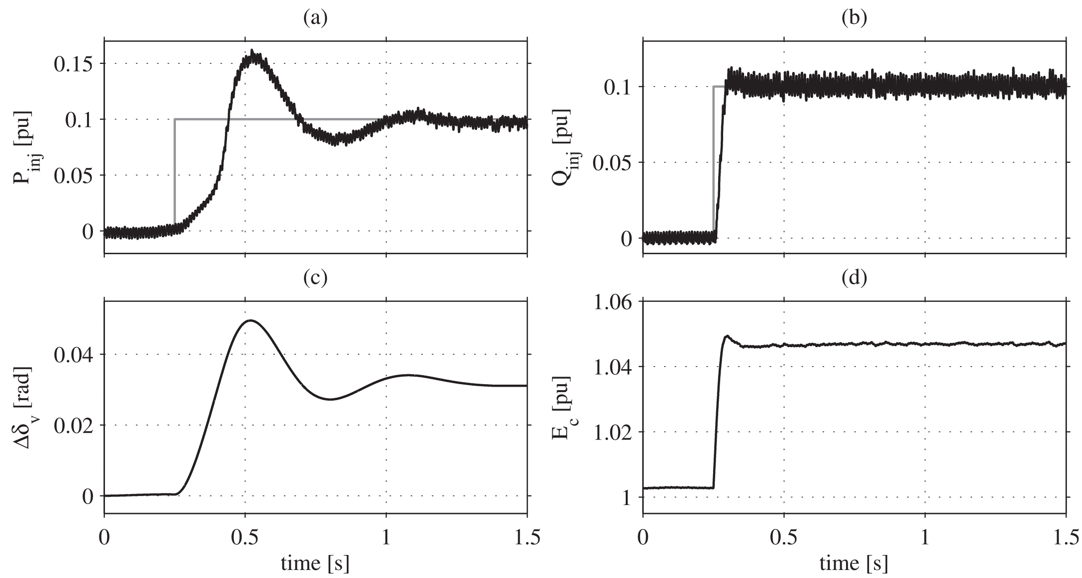

Fig. 5.20 Dynamic performance of the virtual machine controller; (a) reference (gray) and actual (black) injected active power; (b) reference (gray) and actual (black) injected reactive power; (c) virtual angle deviation; (d) converter voltage magnitude; Gray solid curves represent reference active and reactive power.

With zero reactive power injection, the impact of the control parameters K_{Dv} and H_{v} on the dynamic performance of the active power controller will be investigated next. For three different choice of the parameters, the dynamic response of the active power controller for a step in the reference active power is shown in Fig. 5.21. As the results indicate, the damping in the active power response of the implemented virtual machine model increases with a higher choice of the parameter K_{Dv}. On the other hand, a higher choice of the virtual inertia results in a slower response. This means that any additional inertia added to the system from the converter is achieved at a cost of reduced speed of response.

A final test is made to investigate the performance of the virtual machine controller versus the classical cascade controller. For this purpose, the active power controller parameters are chosen as $K_{\mathrm{Dv}} = 33.95$ and $H_{\mathrm{v}} = 0.14$ corresponding to a damping ratio of $\varsigma = 1.0$ and natural

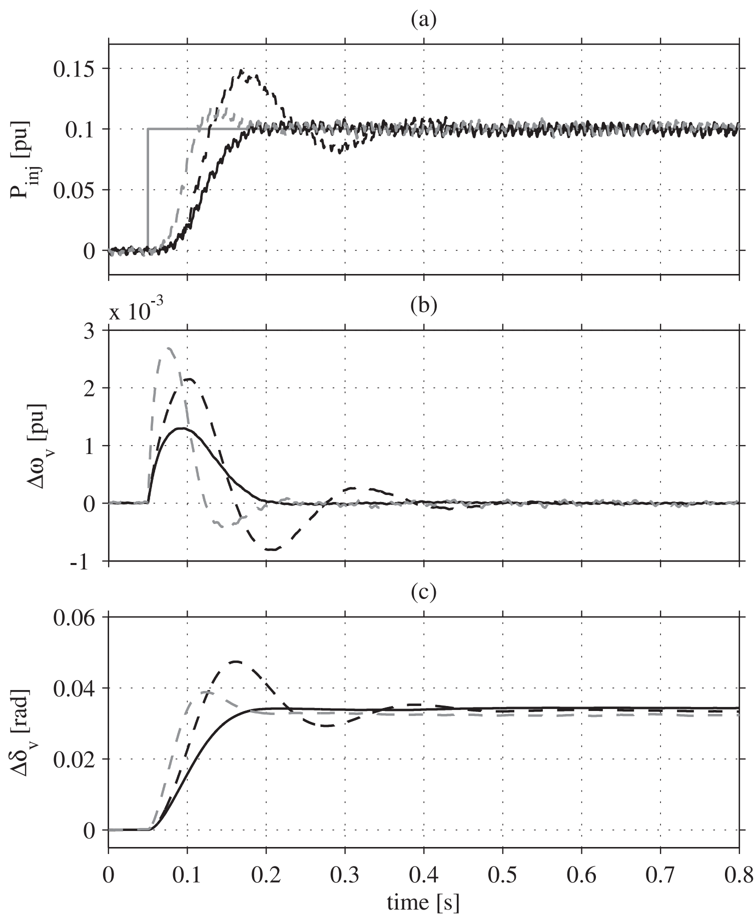

Fig. 5.21 Impact of parameters on the active power controller; Injected active power (plot a), virtual speed deviation (plot b) and virtual angle deviation (plot c) with $H_{\mathrm{v}} = 0.54$ and $K_{\mathrm{Dv}} = 33.95$ (black dashed), $H_{\mathrm{v}} = 0.54$ and $K_{\mathrm{Dv}} = 67.9$ (black solid) and $H_{\mathrm{v}} = 0.14$ and $K_{\mathrm{Dv}} = 33.95$ (gray dashed); Gray solid curve represents reference active power.

frequency of $\omega_{\mathrm{n}} = 62.8$ rad/s for accurate system parameters. The bandwidth of the reactive power controller is chosen as $\alpha_{\mathrm{Qc}} = 62.8$ rad/s for the virtual machine controller. The gray solid curves in plot (a) and (b) in Fig. 5.22 represent the performance of the virtual machine controller for this choice of parameters. The reactive power controller performs similar to the simulation result in Fig. 5.14. On the other hand, the active power controller is characterized by an overshoot unlike the simulation results in Fig. 5.14. This is due to inaccuracies in the estimated parameters of the system resulting in the actual damping ratio to be less than 1. To avoid the overshoot, the damping term is increased to $K_{\mathrm{Dv}} = 67.9$ and the test is repeated. The black solid curves in plot (a) and (b) in Fig. 5.22 represent the performance of the virtual machine controller for the new choice of parameters. In this case, both the active and reactive power controllers perform similar to a first-order system with no overshoot. For a fair comparison, an integral outer loop active and reactive power controller that gives a bandwidth of 62.8 rad/s is selected for the classical cascade controller and its dynamic performance is shown in Fig. 5.22 (plots (c) and (d)). It can be observed that the performance of the classical cascade controller is similar to the simulation results obtained in Fig. 5.14. In the classical cascade controller, the fast inner current controller helps to mitigate the impact of system parameter error and grid harmonics on the dynamic response of the power controllers.

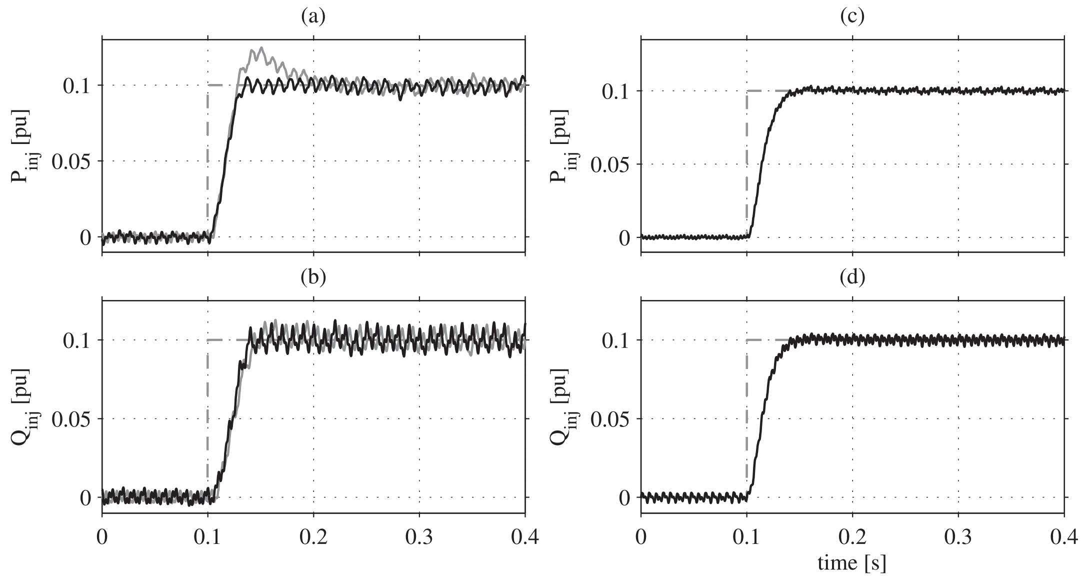

Fig. 5.22 Comparison of the virtual machine controller versus the classical cascade controller; Injected active power (plot a) and reactive power (plot b) using virtual machine controller with $K_{\mathrm{Dv}} = 33.95$ (gray solid) and $K_{\mathrm{Dv}} = 67.9$ (black); Injected active power (plot c) and reactive power (plot d) using classical cascade controller; Dashed curves represent reference power and solid curves represent actual power.

By adjusting the parameters of the virtual machine controller, a similar performance to the classical cascade controller can be achieved without the need for an inner vector-current controller and the use of a PLL (see black curves in Fig. 5.22). However, the use of a current controller and a PLL is necessary during fast transients like fault conditions where converter current needs to be limited. The experimental results in this section verify the validity of the virtual machine controller as described in Sections 5.4 and 5.5.2.

5.7 Conclusions

The overall control approach for the E-STATCOM has been described in this chapter. First, a classical cascade controller that uses an inner vector-current controller has been derived. Modifications to the inner current controller to deal with grid-harmonics disturbances has been proposed. Next, an approach to control the E-STATCOM like a synchronous machine has been described. The performance of both control methods has been verified and compared through simulation and experimental results. A detail description of the auxiliary control loops using the two approaches for POD and TSE will be discussed in the next chapter.

Chapter 6

Control of E-STATCOM for power system stability enhancement

6.1 Introduction

In the previous chapter, the overall control strategy for the E-STATCOM has been discussed. A detailed description of the outer control loops for stability enhancement such as POD and TSE will be made in this chapter. Starting from a simple two-machine model of a power system, the impact of active and reactive power injection on the output power of the generators will be carried out and control strategies for system stability enhancement will be derived.

6.2 System modeling for controller design

A simplified power system model, as the one depicted in Fig. 6.1, is used to study the performance of the E-STATCOM on the power system dynamics. The investigated system approximates an aggregate model of a two-area power system, where each area is represented by a synchronous generator [37]. The E-STATCOM is assumed to be connected at arbitrary points along the transmission line for analysis purposes. Even if the E-STATCOM can be connected at one specific point in the transmission line, a different connection point can be seen as a change in system configuration between the two areas, for instance, following a fault and a subsequent disconnection of one of the parallel transmission lines.

As discussed in Section 2.2.1, the synchronous generators are modeled as voltage sources of constant magnitude ($V_{\mathrm{g1}}, V_{\mathrm{g2}}$) and dynamic rotor angles ($\delta_{\mathrm{g1}}, \delta_{\mathrm{g2}}$) behind a transient impedance ($X'_{\mathrm{d1}}, X'_{\mathrm{d2}}$). The generators are connected through a transformer and a transmission line. Since the frequency of the generators does not change significantly and the electrical transients extinguish quickly for the investigated transient stability studies, it can be assumed that the system is in steady-state from an electrical point of view, meaning that the transformers and transmission lines can be represented by their reactance values (X_{t1}, X_{t2}, X_{L1} and X_{L2}) [26], where the resistance values are ignored for simpler analytical expressions. As shown in Section 2.4, if

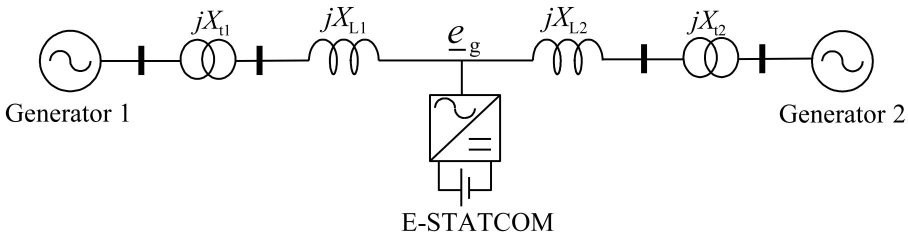

Fig. 6.1 Simplified two-machine system with E-STATCOM.

the mechanical damping in the generators is neglected, the overall damping for the investigated system is equal to zero. Therefore, the model is appropriate to allow a conservative approach of the impact of the E-STATCOM when used for stability studies. For analysis purpose, the electrical connection point of the converter along the transmission line is expressed as a function of the parameter a as

$$a = \frac{X_1}{X_1 + X_2} \tag{6.1}$$

where,

$$X_1 = X'_{\mathrm{d1}} + X_{\mathrm{t1}} + X_{\mathrm{L1}} \quad , \quad X_2 = X'_{\mathrm{d2}} + X_{\mathrm{t2}} + X_{\mathrm{L2}}$$

To derive the system stability enhancement control algorithms in the following sections, it is assumed that the control of the E-STATCOM consists of an outer control loop and an inner current control loop as described in Chapter 5. The outer control loop, which can be a DC-link voltage, AC voltage or POD/TSE controller, sets the reference current for the inner current controller. The control algorithm is implemented in the dq-reference frame where a Phase-Locked Loop (PLL) is used to track the grid-voltage angle θ_{g} from the grid-voltage vector, $\underline{e}_{\mathrm{g}}$. By synchronizing the PLL with the grid-voltage vector, the d- and q-components of the injected current (i_{f}^{d} and i_{f}^{q}) control the injected active and reactive power, respectively. It is assumed that the outer control loop is a POD/TSE controller and the injected active and reactive powers are zero in steady-state. When designing a cascade controller, the speed of the outer control loop is typically selected to be much slower than the inner one to guarantee stability. This means that the current controll can be considered infinitely fast when designing the parameters of the outer controller loop. Therefore, the E-STATCOM can be modeled as a controlled ideal current source, as depicted in the equivalent circuit in Fig. 6.2, for analysis purpose.

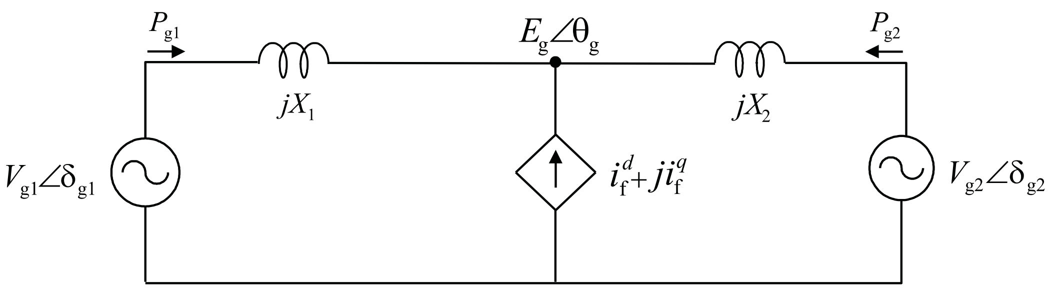

Fig. 6.2 Equivalent circuit for two-machine system with E-STATCOM.

The level of stability enhancement provided by the compensator depends on how much the active power output from the generators is changed by the injected current i_{f}. For the system in Fig. 6.2, the change in active power output from the generators due to injected active and reactive power from the E-STATCOM is calculated as

$$\Delta P_{\mathrm{g1,P}} \approx -\Gamma_{\mathrm{P}} P_{\mathrm{inj}} \tag{6.2}$$

$$\Delta P_{\mathrm{g2,P}} \approx -(1-\Gamma_{\mathrm{P}}) P_{\mathrm{inj}} \tag{6.3}$$

$$\Delta P_{\mathrm{g1,Q}} \approx \left[\frac{V_{\mathrm{g1}} V_{\mathrm{g2}} \sin(\delta_{\mathrm{g10}} - \delta_{\mathrm{g20}}) a(1-a)}{E_{\mathrm{g0}}^2}\right] Q_{\mathrm{inj}} \tag{6.4}$$

$$\Delta P_{\mathrm{g2,Q}} \approx -\left[\frac{V_{\mathrm{g1}} V_{\mathrm{g2}} \sin(\delta_{\mathrm{g10}} - \delta_{\mathrm{g20}}) a(1-a)}{E_{\mathrm{g0}}^2}\right] Q_{\mathrm{inj}} \tag{6.5}$$

where $(\Delta P_{\mathrm{g1,P}}, \Delta P_{\mathrm{g2,P}})$ and $(\Delta P_{\mathrm{g1,Q}}, \Delta P_{\mathrm{g2,Q}})$ represent the change in active power from the corresponding generators due to injected active power (P_{inj}) and reactive power (Q_{inj}), respectively. The constant Γ_{P}, P_{inj} and Q_{inj} are given by

$$\Gamma_{\mathrm{P}} = \frac{V_{\mathrm{g1}}^2 (1-a)^2 + V_{\mathrm{g1}} V_{\mathrm{g2}} \cos(\delta_{\mathrm{g10}} - \delta_{\mathrm{g20}}) a(1-a)}{E_{\mathrm{g0}}^2} \tag{6.6}$$

$$P_{\mathrm{inj}} \approx E_{\mathrm{g0}} i_{\mathrm{f}}^{d} \tag{6.7}$$

$$Q_{\mathrm{inj}} \approx -E_{\mathrm{g0}} i_{\mathrm{f}}^{q} \tag{6.8}$$

The initial steady-state PCC voltage magnitude (E_{g0}) and generator rotor angles ($\delta_{\mathrm{g10}}, \delta_{\mathrm{g20}}$) correspond to the operating point, where the converter is in idle mode. It can be seen from (6.2) - (6.8) that the change in active power output from the generators, for a given active and reactive power injection from the E-STATCOM, depends on the location of the converter a as well as on the amount of injected power (P_{inj}, Q_{inj}). As indicated from (6.4) and (6.5), the effect of reactive power injection depends on the magnitude and direction of the transmitted power from the generators. From observation of the impact of active and reactive power injection on the power output of the generators, the POD and TSE controllers for E-STATCOM will be derived in the next sections.

6.3 Power Oscillation Damping (POD) controller

The derivation of the POD controller from locally measured signals such as the PCC voltage magnitude (E_{g}), PCC voltage phase (θ_{g}) and power transfer between the two areas (P_{tran}) will be made in this section. Using the simplified two-machine system as described in the previous section, a stability analysis of the control method will also be performed.

6.3.1 Derivation of control input signals

As described in Section 2.4.3 for a single-machine infinite-bus system, the active power output of the generator should be modulated in proportion to the speed variation to provide damping. However, the generator speed is not easily available at the compensator location and this requires deriving a control input signal that provides an estimate of the speed variation of the generator. Using the estimate of the speed variation, the outputs of the compensator (i.e., the current references in the case of E-STATCOM) can be controlled to modulate the active power output of the generator. Observing (6.2) - (6.5) for the simplified system in Fig. 6.1, it can also be understood that the impact of injected active and reactive power on the generator active power output highly depends on the parameter a, i.e. on the location of the E-STATCOM. Hence, it would be beneficial if the derived control input signal to estimate the speed variation of the generators contains information on the location of the compensator.

Consider the system in Fig. 6.2, where the E-STATCOM is in idle mode. The variation of various local signals at different E-STATCOM connection points using the dynamic generator rotor angles (δ_{g1}, δ_{g2}) is given by

$$E_{\mathrm{g}} = \sqrt{[(1-a)V_{\mathrm{g1}}]^2 + [aV_{\mathrm{g2}}]^2 + 2a(1-a)V_{\mathrm{g1}}V_{\mathrm{g2}}\cos(\delta_{\mathrm{g1}} - \delta_{\mathrm{g2}})} \tag{6.9}$$

$$\theta_{\mathrm{g}} = \delta_{\mathrm{g2}} + \tan^{-1}\left[\frac{(1-a)V_{\mathrm{g1}}\sin(\delta_{\mathrm{g1}} - \delta_{\mathrm{g2}})}{(1-a)V_{\mathrm{g1}}\cos(\delta_{\mathrm{g1}} - \delta_{\mathrm{g2}}) + aV_{\mathrm{g2}}}\right] \tag{6.10}$$

$$P_{\mathrm{tran}} = \frac{V_{\mathrm{g1}}V_{\mathrm{g2}}\sin(\delta_{\mathrm{g1}} - \delta_{\mathrm{g2}})}{X_1 + X_2} \tag{6.11}$$

From small-signal point of view and under the assumption that the PCC voltage magnitude along the line E_{g} does not change much, the derivative of the PCC voltage magnitude, phase and transmitted active power are given by

$$\frac{dE_{\mathrm{g}}}{dt} \approx -\left\{\frac{a(1-a)V_{\mathrm{g1}}V_{\mathrm{g2}}\sin(\delta_{\mathrm{g10}} - \delta_{\mathrm{g20}})}{E_{\mathrm{g0}}}\right\}\omega_0\left[\Delta\omega_{\mathrm{g1}} - \Delta\omega_{\mathrm{g2}}\right] \tag{6.12}$$

$$\frac{d\theta_{\mathrm{g}}}{dt} \approx \Gamma_{\mathrm{P}}\omega_0\Delta\omega_{\mathrm{g1}} + (1-\Gamma_{\mathrm{P}})\omega_0\Delta\omega_{\mathrm{g2}} \tag{6.13}$$

$$\frac{dP_{\mathrm{tran}}}{dt} \approx \left\{\frac{V_{\mathrm{g1}}V_{\mathrm{g2}}\cos(\delta_{\mathrm{g10}} - \delta_{\mathrm{g20}})}{X_1 + X_2}\right\}\omega_0\left[\Delta\omega_{\mathrm{g1}} - \Delta\omega_{\mathrm{g2}}\right] \tag{6.14}$$

where the constant Γ_{P} has been defined in the previous section and the steady-state system frequency is represented by ω_0. From the equation of motion in (2.5), the speed deviation of each generator ($\Delta\omega_{\mathrm{g1}}$ and $\Delta\omega_{\mathrm{g2}}$) is inversely proportional to the inertia constant of the corresponding generator (H_{g1} and H_{g2}) and the derivative of the PCC voltage phase can be estimated from the speed deviation between the generators as

$$\begin{aligned}\frac{d\theta_{\mathrm{g}}}{dt} &\approx \frac{H_{\mathrm{g1}}H_{\mathrm{g2}}}{H_{\mathrm{g1}}+H_{\mathrm{g2}}}\left\{\Gamma_{\mathrm{P}}\omega_0\frac{[\Delta\omega_{\mathrm{g1}}-\Delta\omega_{\mathrm{g2}}]}{H_{\mathrm{g1}}}+(1-\Gamma_{\mathrm{P}})\omega_0\frac{[\Delta\omega_{\mathrm{g2}}-\Delta\omega_{\mathrm{g1}}]}{H_{\mathrm{g2}}}\right\} \\ &\approx \frac{H_{\mathrm{g1}}H_{\mathrm{g2}}}{H_{\mathrm{g1}}+H_{\mathrm{g2}}}\left\{\frac{\Gamma_{\mathrm{P}}}{H_{\mathrm{g1}}}-\frac{1-\Gamma_{\mathrm{P}}}{H_{\mathrm{g2}}}\right\}\omega_0\left[\Delta\omega_{\mathrm{g1}}-\Delta\omega_{\mathrm{g2}}\right]\end{aligned} \tag{6.15}$$

The derivative of the PCC voltage magnitude, phase and transmitted active power are all dependent on the speed deviation between the generators and are candidates as control input signals. Moreover, the derivative of the PCC voltage magnitude and phase contains information on the location of E-STATCOM and this information can be exploited in the POD controller design. For the two-machine system in Fig. 6.2, the stability of the system depends on the damping provided on the speed deviation between the two generators, $\Delta\omega_{\mathrm{g12}} = \Delta\omega_{\mathrm{g1}} - \Delta\omega_{\mathrm{g2}}$. Therefore, the impact of active and reactive power injection on the dynamics of $\Delta\omega_{\mathrm{g12}}$ should be investigated to select the appropriate control input signals for POD. For discussion purposes, the mass-scaled electrical location of the compensator from Generator 1 (a_{M}) is defined by

$$a_{\mathrm{M}} = \frac{H_{\mathrm{g1}}(1-\Gamma_{\mathrm{P}})}{H_{\mathrm{g1}}(1-\Gamma_{\mathrm{P}})+H_{\mathrm{g2}}\Gamma_{\mathrm{P}}} \tag{6.16}$$

The definition for a_{M} is chosen in such a way that it will be close to the electrical location of the compensator, a defined in (6.1), when the inertia constant of the two generators is the same.

If the use of active power injection for POD is considered for the system in Fig. 6.2, its impact on the dynamics of $\Delta\omega_{\mathrm{g12}}$ using the equation of motion in (2.5) is given by

$$\frac{d\Delta\omega_{\mathrm{g12}}}{dt} = \frac{-\Delta P_{\mathrm{g1,P}}}{2H_{\mathrm{g1}}} + \frac{\Delta P_{\mathrm{g2,P}}}{2H_{\mathrm{g2}}} = \left\{\frac{\Gamma_{\mathrm{P}}}{2H_{\mathrm{g1}}}-\frac{1-\Gamma_{\mathrm{P}}}{2H_{\mathrm{g2}}}\right\}E_{\mathrm{g0}}i_{\mathrm{f}}^{d} \tag{6.17}$$

To provide damping to the system regardless of the location of the compensator, the POD control law for the active power injection is chosen as

$$i_{\mathrm{f}}^{d} = K_{\mathrm{P}}\frac{d\theta_{\mathrm{g}}}{dt} \tag{6.18}$$

where the constant K_{P} is a proportional gain whose magnitude affects the level of damping. Using the control law in (6.18), the dynamics of the speed deviation between the generators becomes

$$\frac{d\Delta\omega_{\mathrm{g12}}}{dt} = K_{\mathrm{P}}\frac{E_{\mathrm{g0}}H_{\mathrm{g1}}H_{\mathrm{g2}}}{2(H_{\mathrm{g1}}+H_{\mathrm{g2}})}\left[\frac{\Gamma_{\mathrm{P}}}{H_{\mathrm{g1}}}-\frac{1-\Gamma_{\mathrm{P}}}{H_{\mathrm{g2}}}\right]^2\omega_0\Delta\omega_{\mathrm{g12}} \tag{6.19}$$

By choosing the gain $K_{\mathrm{P}} < 0$, positive damping can be provided. Choosing the derivative of the PCC voltage phase as the control input signal also has the advantage of maximizing the effectiveness of active power injection for POD. Observe that when the compensator is close to the mass-scaled electrical midpoint of the line (i.e, $a_{\mathrm{M}} \approx 0.5$), the damping provided is zero as shown by (6.17) irrespective of the magnitude of active power injection. However, the use of $d\theta_{\mathrm{g}}/dt$ as a control input signal ensures that the injected active power is also zero at that location. Moving away from the mass-scaled electrical midpoint, the impact of active power injection for POD increases and at the same time the magnitude of $d\theta_{\mathrm{g}}/dt$ increases.

Similarly, the impact of reactive power injection on the dynamics of $\Delta\omega_{\mathrm{g12}}$ is given by

$$\begin{aligned}\frac{d\Delta\omega_{\mathrm{g12}}}{dt} &= \frac{-\Delta P_{\mathrm{g1,Q}}}{2H_{\mathrm{g1}}} + \frac{\Delta P_{\mathrm{g2,Q}}}{2H_{\mathrm{g2}}} \\ &= \left\{\frac{V_{\mathrm{g1}}V_{\mathrm{g2}}\sin(\delta_{\mathrm{g10}}-\delta_{\mathrm{g20}})a(1-a)}{E_{\mathrm{g0}}^2}\right\}\left\{\frac{1}{2H_{\mathrm{g1}}}+\frac{1}{2H_{\mathrm{g2}}}\right\}E_{\mathrm{g0}}i_{\mathrm{f}}^q\end{aligned} \tag{6.20}$$

The POD control law for the reactive power injection is chosen as

$$i_{\mathrm{f}}^q = K_{\mathrm{Q}}\frac{dP_{\mathrm{tran}}}{dt} \tag{6.21}$$

where the constant K_{Q} is a proportional gain whose magnitude affects the level of damping. Using the control law in (6.21), the dynamics of the speed deviation between the generators becomes

$$\frac{d\Delta\omega_{\mathrm{g12}}}{dt} = K_{\mathrm{Q}}\left[\frac{\Gamma_{\mathrm{Q}}}{2H_{\mathrm{g1}}}+\frac{\Gamma_{\mathrm{Q}}}{2H_{\mathrm{g2}}}\right]\omega_0\Delta\omega_{\mathrm{g12}} \tag{6.22}$$

where the constant Γ_{Q} is given by

$$\Gamma_{\mathrm{Q}} = \frac{[V_{\mathrm{g1}}V_{\mathrm{g2}}]^2\sin\left(2[\delta_{\mathrm{g10}}-\delta_{\mathrm{g20}}]\right)a(1-a)}{2E_{\mathrm{g0}}(X_1+X_2)} \tag{6.23}$$

By choosing the gain K_{Q} to have opposite sign to the constant Γ_{Q}, positive damping can be provided. The damping provided to the system due to reactive power injection is maximum at the electrical midpoint of the line (i.e. $a = 0.5$) and minimum at the generator terminals (i.e. $a = 0$ and $a = 1$). As it can be observed from (6.12) and (6.20), the derivative of the PCC voltage magnitude can be an alternative control input signal for reactive power injection. Unlike the derivative of the transmitted active power, the derivative of the PCC voltage magnitude depends on the location of the compensator and this can help to minimize the injection of reactive power at the generator terminals. However, the dependency of dE_{g}/dt on the voltage controller offered either by the considered compensator or other compensators installed in the vicinity makes it not suitable to provide the required information about the speed variation of the generators. On the other hand, dP_{tran}/dt provides a better information about the speed variation between the generators and has been chosen as the control input signal for reactive power injection.

Even if the analysis so far has been made for a two-machine system, it can be easily reduced to a single-machine infinite-bus system by setting $H_{\mathrm{g2}} \approx \infty$. In this case, injection of active or reactive power will not provide any damping when the compensator is connected at the infinite bus ($a = 1$ and $a_{\mathrm{M}} = 0.5$). Maximum damping by active and reactive power will be provided at the generator terminal ($a = a_{\mathrm{M}} = 0$) and electrical midpoint of the line ($a = 0.5$), respectively.

6.3.2 Estimation of control input signals

As described in Section 3.5, the derivative action as in (6.18) and (6.21) cannot be used directly in actual applications. Instead, using a fast, accurate and adaptive estimation of the critical power oscillation frequency component as described in Chapter 4, an effective power oscillation damping for various power system operating points and E-STATCOM locations can be achieved. For the reasons described previously, the derivative of the PCC-voltage phase and transmitted power should be estimated for controlling the active and reactive power injection, respectively. The aim of the algorithm is therefore to estimate the signal components that consist of only the low-frequency electromechanical oscillation in the measured signals, θ_{g} and P_{tran}.

By using a PLL with bandwidth much higher than the frequency of the electromechanical oscillations, the derivative of the PCC-voltage phase can be obtained from the change in frequency estimate of the PLL ($\Delta\tilde{\omega}_{\mathrm{g}} = d\theta_{\mathrm{g}}/dt$). Therefore, the low-frequency electromechanical oscillation component can be extracted directly from the frequency estimate of the PLL. On the other hand, the derivative of transmitted power is estimated by extracting the low-frequency electromechanical oscillation component from the measured signal, P_{tran} and then applying a phase shift of $\pi/2$ to the estimated oscillation frequency component. While this is valid for the system in Fig. 6.2, it should be noted that the phase-shift applied to the estimated oscillatory component should be tuned based on the selected control input signal, the power system configuration and the correlation between injected active and reactive power with the active power output of the generators.

From the estimated control input signals, $\tilde{\omega}_{\mathrm{g,osc}} = d\tilde{\theta}_{\mathrm{g,osc}}/dt$ and $d\tilde{P}_{\mathrm{tran,osc}}/dt$, which contain only a particular oscillation-frequency component, the reference injected active and reactive current components (i_{f}^{d*}, i_{f}^{q*}) from the E-STATCOM can be calculated to setup the POD controller as in Fig. 6.3. The terms K_{P} and K_{Q}, as defined in the previous section, represent the proportional controller gains for the active and reactive current components, respectively.

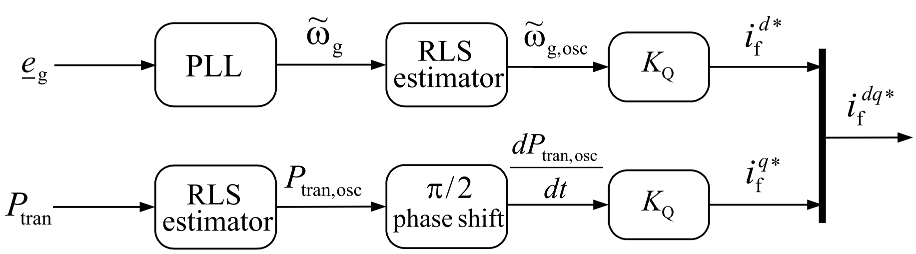

Fig. 6.3 Block diagram of the POD controller.

6.3.3 Stability analysis

The mathematical model of the system in Fig. 6.2 is developed in this section to investigate the performance of the POD controller using active and reactive power injection. Each generator will be represented by the classical model and the E-STATCOM is modeled as a controlled ideal current source as described in Section 6.2. To reduce the order of the system for simplicity of the analysis, the RLS estimator in the POD control structure in Fig. 6.3 is assumed ideal and the injected currents are calculated as

$$i_{\mathrm{f}}^{\mathrm{d}} \approx K_{\mathrm{P}}\omega_0 \left[\Gamma_{\mathrm{P}}\Delta\omega_{\mathrm{g1}} + (1-\Gamma_{\mathrm{P}})\Delta\omega_{\mathrm{g2}}\right] \tag{6.24}$$

$$i_{\mathrm{f}}^{\mathrm{q}} \approx K_{\mathrm{Q}}\omega_0 \left\{\frac{V_{\mathrm{g1}}V_{\mathrm{g2}}\cos(\delta_{\mathrm{g10}}-\delta_{\mathrm{g20}})}{X_1+X_2}\right\}\left[\Delta\omega_{\mathrm{g1}} - \Delta\omega_{\mathrm{g2}}\right] \tag{6.25}$$

Linearizing around an initial steady-state operating point, the small-signal dynamic model of the two-machine system with the E-STATCOM in per unit is developed as

$$\frac{d}{dt}\begin{bmatrix}\Delta\omega_{\mathrm{g1}}\\ \Delta\delta_{\mathrm{g12}}\\ \Delta\omega_{\mathrm{g2}}\end{bmatrix} = \begin{bmatrix}\beta_{11} & \beta_{12} & \beta_{13}\\ \omega_0 & 0 & -\omega_0\\ \beta_{31} & \beta_{32} & \beta_{33}\end{bmatrix}\begin{bmatrix}\Delta\omega_{\mathrm{g1}}\\ \Delta\delta_{\mathrm{g12}}\\ \Delta\omega_{\mathrm{g2}}\end{bmatrix} + \begin{bmatrix}\frac{1}{2H_{\mathrm{g1}}} & 0\\ 0 & 0\\ 0 & \frac{1}{2H_{\mathrm{g2}}}\end{bmatrix}\begin{bmatrix}\Delta T_{\mathrm{m1}}\\ \Delta T_{\mathrm{m2}}\end{bmatrix} \tag{6.26}$$

where $\Delta\delta_{\mathrm{g12}} = \Delta\delta_{\mathrm{g1}} - \Delta\delta_{\mathrm{g2}}$ represents the rotor-angle difference between the two generators and other signals have been defined previously. Assuming no mechanical damping and the initial steady-state speed of the generators set to ω_0, the constants are derived as

$$\begin{bmatrix}\beta_{11} & \beta_{31}\\ \beta_{12} & \beta_{32}\\ \beta_{13} & \beta_{33}\end{bmatrix} = \begin{bmatrix}\frac{\omega_0(K_{\mathrm{P}}E_{\mathrm{g0}}\Gamma_{\mathrm{P}}^2+K_{\mathrm{Q}}\Gamma_{\mathrm{Q}})}{2H_{\mathrm{g1}}} & \frac{\omega_0(K_{\mathrm{P}}E_{\mathrm{g0}}\Gamma_{\mathrm{P}}(1-\Gamma_{\mathrm{P}})-K_{\mathrm{Q}}\Gamma_{\mathrm{Q}})}{2H_{\mathrm{g2}}}\\ -\frac{V_{\mathrm{g1}}V_{\mathrm{g2}}\cos(\delta_{\mathrm{g10}}-\delta_{\mathrm{g20}})}{2H_{\mathrm{g1}}(X_1+X_2)} & \frac{V_{\mathrm{g1}}V_{\mathrm{g2}}\cos(\delta_{\mathrm{g10}}-\delta_{\mathrm{g20}})}{2H_{\mathrm{g2}}(X_1+X_2)}\\ \frac{\omega_0(K_{\mathrm{P}}E_{\mathrm{g0}}\Gamma_{\mathrm{P}}(1-\Gamma_{\mathrm{P}})-K_{\mathrm{Q}}\Gamma_{\mathrm{Q}})}{2H_{\mathrm{g1}}} & \frac{\omega_0(K_{\mathrm{P}}E_{\mathrm{g0}}(1-\Gamma_{\mathrm{P}})^2+K_{\mathrm{Q}}\Gamma_{\mathrm{Q}})}{2H_{\mathrm{g2}}}\end{bmatrix} \tag{6.27}$$

The terms β_{12} and β_{32} represent the synchronizing torque coefficients resulting from the selected operating point and the contribution of the E-STATCOM to these terms is zero. The terms β_{11} and β_{33} determine the damping torque coefficient provided by the E-STATCOM with respect to the change in speed of the respective generator. To provide positive damping, β_{11} and β_{33} should be negative. For this, the sign of K_{P} should be negative and the sign of K_{Q} should be chosen based on the sign of Γ_{Q}, similar to the discussion in Section 6.3.1. For a transmitted power from Generator 1 to Generator 2, Γ_{Q} will be positive and the sign of K_{Q} should be negative. For a transmitted power in the other direction, the sign of K_{Q} should be opposite. The terms β_{13} and β_{31} are the cross coupling terms between the two generator speed variations.

Application example

As an example for the analysis in this section, a hypothetical 20/230 kV, 900 MVA transmission system similar to the one in Fig. 6.1 with a total series reactance of 1.665 pu and inertia constant of the generators $H_{\rm g1} = H_{\rm g2} = 6.5$ s is considered. The leakage reactance of the transformers and transient impedance of the generators are 0.15 pu and 0.3 pu, respectively. The movement of the poles for the system as a function of the E-STATCOM location is shown in Fig. 6.4. With the described control strategy, the injected active power is zero at the mass-scaled electrical midpoint of the line (in this case $a_{\rm M} = a = 0.5$). At this point, the impact of active power on damping is negligible and the control method avoids unnecessary use of active power injection. Moving away from the midpoint of the line, the damping by active power injection increases. On the other hand, the damping by reactive power injection is maximum at the electrical midpoint of the line ($a = 0.5$) and decreases when moving towards the generator terminals. By combining both active and reactive power injection, a more uniform damping along the line can be obtained.

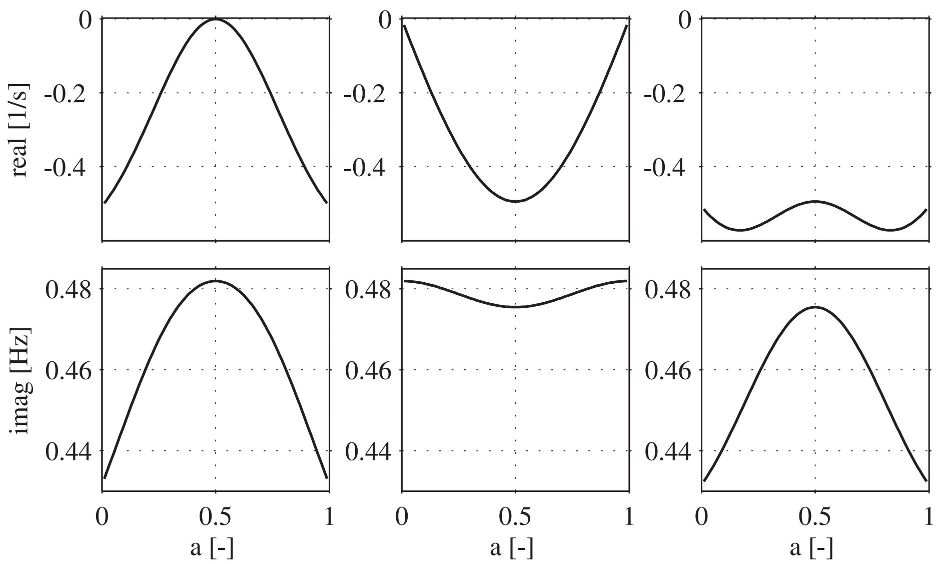

Fig. 6.4 Real and imaginary part of the complex conjugate poles vs. position; Left: active power injection, Middle: reactive power injection and Right: active and reactive power injection. [$K_{\rm P} = -0.08$, $K_{\rm Q} = -0.34$, $P_{\rm tran} = 0.444$ pu].

A single-machine infinite-bus system is a special case of two-machine system with $H_{\rm g2} >> H_{\rm g1}$ ($d\Delta\omega_{\rm g2}/dt \approx 0$). Figure 6.5 shows the effect of the E-STATCOM on damping at different locations for different transmitted active powers. As the results show, damping by reactive power is effective at the middle of the line and damping by active power is effective at the Generator 1 terminal. No damping is provided at the infinite bus (Generator 2 terminal) and injected active power is zero at this location, similar to the discussion in Section 6.3.1. Finally, the amount of transmitted power highly affects the damping by reactive power injection, whereas its impact on the damping by active power injection is negligible.

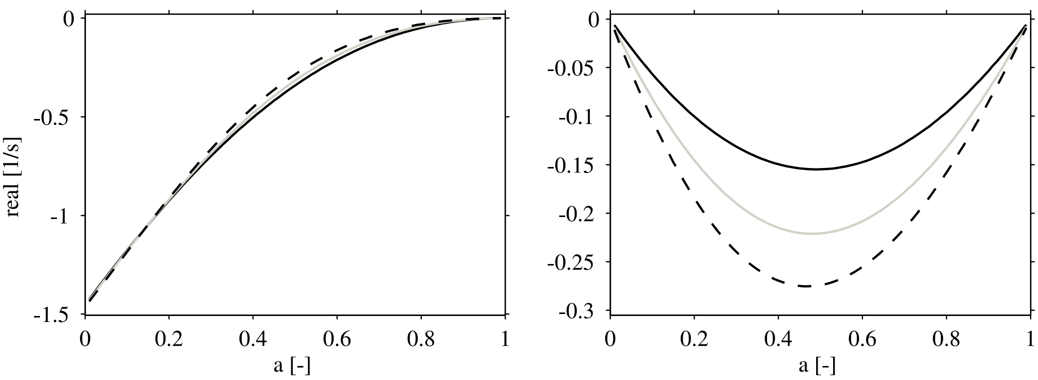

Fig. 6.5 Movement of real part of the poles for a single-machine infinite-bus system with position of E-STATCOM for three transmitted power P_{tran} values. Black dashed: $P_{\text{tran}} = 0.444$ pu, Gray solid: $P_{\text{tran}} = 0.333$ pu, Black solid: $P_{\text{tran}} = 0.222$ pu. Left: active power injection for POD with $K_{\text{P}} = -0.1$, Right: reactive power injection with $K_{\text{Q}} = -0.2$.

6.4 Impact of load characteristics on POD

The POD controller developed in Section 6.3 considers a simplified two-area power system as in Fig. 6.1, where each area is represented with a synchronous generator. Even if the simplified system is assumed for the purpose of control design, the performance of the POD controller should be investigated in a power system that includes loads and multiple generators. In this section, the impact of various load characteristics on the POD performance by E-STATCOM will be addressed. For the intended study, the system in Fig. 6.6 is considered, where the voltage phasor at the load location is given by $V_{\text{L}}\angle\delta_{\text{L}}$. The active and reactive power of the load, P_{L} and Q_{L}, are modeled separately using the expressions in (2.4).

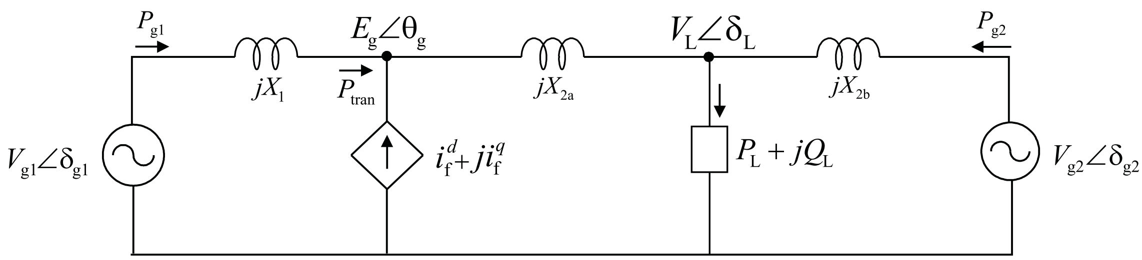

Fig. 6.6 Equivalent circuit for two-machine system with E-STATCOM.

With the various signals as defined in Fig. 6.6, the relative location of the load from Generator 1 is expressed as a function of the parameter a_{L} as

$$a_{\text{L}} = \frac{X_1 + X_{2\text{a}}}{X_1 + X_{2\text{a}} + X_{2\text{b}}} \tag{6.28}$$

Again, the POD performance of the E-STATCOM depends on how the power output of the generators are modulated by the injected active and reactive powers. This is in turn affected by the characteristic of the loads. Hence, the change in active power output from the generators due to injected active and reactive power from the E-STATCOM for the system in Fig. 6.6 is recalculated as

$$\begin{bmatrix} \Delta P_{\mathrm{g1,P}}/P_{\mathrm{inj}} & \Delta P_{\mathrm{g2,P}}/P_{\mathrm{inj}} \\ \Delta P_{\mathrm{g1,Q}}/Q_{\mathrm{inj}} & \Delta P_{\mathrm{g2,Q}}/Q_{\mathrm{inj}} \end{bmatrix} = \begin{bmatrix} K_{\mathrm{g1,P}} & K_{\mathrm{g2,P}} \\ K_{\mathrm{g1,Q}} & K_{\mathrm{g2,Q}} \end{bmatrix} = \mathbf{\Psi}_{\mathrm{LE}}\mathbf{A}_{\mathrm{m}}^{-1}\mathbf{B}_{\mathrm{m}} + \mathbf{D}_{\mathrm{m}} \tag{6.29}$$

The parameters $K_{\mathrm{g1,P}}$, $K_{\mathrm{g2,P}}$ and $K_{\mathrm{g1,Q}}$, $K_{\mathrm{g1,Q}}$ indicate the effectiveness of active and reactive power injection in modulating the power output of the generators and hence are useful quantities to characterize the impact of the connected load on damping performance. The matrices $\mathbf{\Psi}_{\mathrm{LE}}$, $\mathbf{A}_{\mathrm{m}}$, $\mathbf{B}_{\mathrm{m}}$ and $\mathbf{D}_{\mathrm{m}}$ are given by

$$\begin{aligned}
\mathbf{\Psi}_{\mathrm{LE}} &= \begin{bmatrix} -\cos(\delta_{\mathrm{L0}} - \theta_{\mathrm{g0}}) & \sin(\delta_{\mathrm{L0}} - \theta_{\mathrm{g0}}) \\ \sin(\delta_{\mathrm{L0}} - \theta_{\mathrm{g0}}) & \cos(\delta_{\mathrm{L0}} - \theta_{\mathrm{g0}}) \end{bmatrix} \\
\mathbf{A}_{\mathrm{m}} &= \tfrac{(a_{\mathrm{L}}-1)X_{\mathrm{tot}}}{aV_{\mathrm{L0}}^2} \begin{bmatrix} \frac{V_{\mathrm{L0}}^2}{(a_{\mathrm{L}}-1)X_{\mathrm{tot}}} - a_{\mathrm{L}}Q_{\mathrm{L0}} & -a_{\mathrm{L}}P_{\mathrm{L0}} \\ a_{\mathrm{L}}\left(\sum_{\mathrm{i=1}}^{3} m_{\mathrm{i}}p_{\mathrm{i}} - 1\right)P_{\mathrm{L0}} & \frac{V_{\mathrm{L0}}^2}{(a_{\mathrm{L}}-1)X_{\mathrm{tot}}} - a_{\mathrm{L}}\left(\sum_{\mathrm{i=1}}^{3} n_{\mathrm{i}}q_{\mathrm{i}} - 1\right)Q_{\mathrm{L0}} \end{bmatrix} \\
\mathbf{B}_{\mathrm{m}} &= \tfrac{1}{E_{\mathrm{g0}}} \begin{bmatrix} (1/a_{\mathrm{L}} - 1)V_{\mathrm{g1}}\cos(\delta_{\mathrm{g10}} - \delta_{\mathrm{L0}}) & V_{\mathrm{g2}}\cos(\delta_{\mathrm{g20}} - \delta_{\mathrm{L0}}) \\ (1/a_{\mathrm{L}} - 1)V_{\mathrm{g1}}\sin(\delta_{\mathrm{g10}} - \delta_{\mathrm{L0}}) & V_{\mathrm{g2}}\sin(\delta_{\mathrm{g20}} - \delta_{\mathrm{L0}}) \end{bmatrix} \\
\mathbf{D}_{\mathrm{m}} &= \left(\tfrac{a}{a_{\mathrm{L}}} - 1\right)\tfrac{V_{\mathrm{g1}}}{E_{\mathrm{g0}}} \begin{bmatrix} \cos(\delta_{\mathrm{g10}} - \theta_{\mathrm{g0}}) & 0 \\ -\sin(\delta_{\mathrm{g10}} - \theta_{\mathrm{g0}}) & 0 \end{bmatrix}
\end{aligned} \tag{6.30}$$

Similarly, the control input signals are recalculated using the model in Fig. 6.6 as

$$\begin{bmatrix} d\theta_{\mathrm{g}}/dt \\ dP_{\mathrm{tran}}/dt \end{bmatrix} = \omega_0 \begin{bmatrix} \Gamma_{\theta_{\mathrm{g}}} & 1 - \Gamma_{\theta_{\mathrm{g}}} \\ \Gamma_{P_{\mathrm{tran}}} & \Gamma_{P_{\mathrm{tran}}} \end{bmatrix} \begin{bmatrix} \Delta\omega_{\mathrm{g1}} \\ \Delta\omega_{\mathrm{g2}} \end{bmatrix} \tag{6.31}$$

where the constants $\Gamma_{\theta_{\mathrm{g}}}$, $\Gamma_{P_{\mathrm{tran}}}$ and the matrices $\mathbf{G}_{\mathrm{m}}$ and $\mathbf{C}_{\mathrm{m}}$ are given by

$$
\begin{bmatrix} \Gamma_{\theta_{\mathrm{g}}} \\ \\ \Gamma_{P_{\mathrm{tran}}} \end{bmatrix} = \begin{bmatrix} 1 - \frac{a V_{\mathrm{L0}} \cos(\theta_{\mathrm{g0}} - \delta_{\mathrm{L0}})}{a_{\mathrm{L}} E_{\mathrm{g0}}} \\ \\ \frac{V_{\mathrm{g1}} V_{\mathrm{L0}} \cos(\delta_{\mathrm{g10}} - \delta_{\mathrm{L0}})}{a_{\mathrm{L}} X_{\mathrm{tot}}} \end{bmatrix} + \mathbf{G}_{\mathrm{m}} \mathbf{C}_{\mathrm{m}}^{-1} \begin{bmatrix} \frac{V_{\mathrm{g1}} \cos(\delta_{\mathrm{g10}} - \delta_{\mathrm{L0}})}{a_{\mathrm{L}} X_{\mathrm{tot}}} \\ \\ \frac{V_{\mathrm{g1}} \sin(\delta_{\mathrm{g10}} - \delta_{\mathrm{L0}})}{a_{\mathrm{L}} X_{\mathrm{tot}}} \end{bmatrix}
$$

$$
\mathbf{G}_{\mathrm{m}} = \begin{bmatrix} \frac{a \sin(\delta_{\mathrm{L0}} - \theta_{\mathrm{g0}})}{a_{\mathrm{L}} E_{\mathrm{g0}}} & \frac{a V_{\mathrm{L0}} \cos(\delta_{\mathrm{L0}} - \theta_{\mathrm{g0}})}{a_{\mathrm{L}} E_{\mathrm{g0}}} \\ \\ \frac{V_{\mathrm{g1}} \sin(\delta_{\mathrm{g10}} - \delta_{\mathrm{L0}})}{a_{\mathrm{L}} X_{\mathrm{tot}}} & -\frac{V_{\mathrm{g1}} V_{\mathrm{L0}} \cos(\delta_{\mathrm{g10}} - \delta_{\mathrm{L0}})}{a_{\mathrm{L}} X_{\mathrm{tot}}} \end{bmatrix} \tag{6.32}
$$

$$
\mathbf{C}_{\mathrm{m}} = \begin{bmatrix} \frac{\left(\sum_{\mathrm{i}=1}^{3} m_{\mathrm{i}} p_{\mathrm{i}} - 1\right) P_{\mathrm{L0}}}{V_{\mathrm{L0}}^2} & \frac{V_{\mathrm{g1}} \cos(\delta_{\mathrm{g10}} - \delta_{\mathrm{L0}})}{a_{\mathrm{L}} X_{\mathrm{tot}}} + \frac{V_{\mathrm{g2}} \cos(\delta_{\mathrm{g20}} - \delta_{\mathrm{L0}})}{(1 - a_{\mathrm{L}}) X_{\mathrm{tot}}} \\ \\ -\frac{\left(\sum_{\mathrm{i}=1}^{3} n_{\mathrm{i}} q_{\mathrm{i}} - 1\right) Q_{\mathrm{L0}}}{V_{\mathrm{L0}}^2} - \frac{1}{a_{\mathrm{L}}(1 - a_{\mathrm{L}}) X_{\mathrm{tot}}} & \frac{V_{\mathrm{g1}} \sin(\delta_{\mathrm{g10}} - \delta_{\mathrm{L0}})}{a_{\mathrm{L}} X_{\mathrm{tot}}} + \frac{V_{\mathrm{g2}} \sin(\delta_{\mathrm{g20}} - \delta_{\mathrm{L0}})}{(1 - a_{\mathrm{L}}) X_{\mathrm{tot}}} \end{bmatrix}
$$

The parameters $\Gamma_{\theta_{\mathrm{g}}}$ and $\Gamma_{P_{\mathrm{tran}}}$ represent how the control input signals depend on the speed variation of the generators. Note that the various steady-state quantities in (6.30) and (6.32), as defined in the previous section, correspond to the initial operating point, where the E-STATCOM is in idle mode (zero current injection).

Using a simplified 20/230 kV, 900 MVA power system similar to the one in Fig. 6.6, the impact of different static load characteristics on the performance of the POD controller described in Section 6.3 is investigated. The total reactance of the transmission system is set to 1.17 pu whereas the leakage reactance of the transformers and transient impedance of the generators is 0.15 pu and 0.3 pu, respectively. The inertia constant of the generators is assumed equal $H_{\mathrm{g1}} = H_{\mathrm{g2}} = 6.5$ s for a better understanding of the oscillation between the two areas. An initial power transfer $P_{\mathrm{tran}} = 0.4$ pu from Generator 1 to the load area is considered for the investigated cases.

6.4.1 Impact of steady-state load magnitude

A static load consisting of equal proportion of constant power, constant current and constant impedance loads with a power factor of 0.9 and connected at a position $a_{\mathrm{L}} = 0.91$ is considered. The gains of the POD controllers are chosen as $K_{\mathrm{P}} = -0.1$ and $K_{\mathrm{Q}} = -0.2$.

The movement of poles for the dynamic model of the system in Fig. 6.6 with a change in the location of the E-STATCOM is shown in Fig. 6.7. As the results show, the impact of the load on the level of damping to the system is significant when reactive power injection is used for POD and the magnitude of load is high. For this particular example, it can also be observed that the POD controllers described in Section 6.3 works as intended in the presence of a load in the power system model.

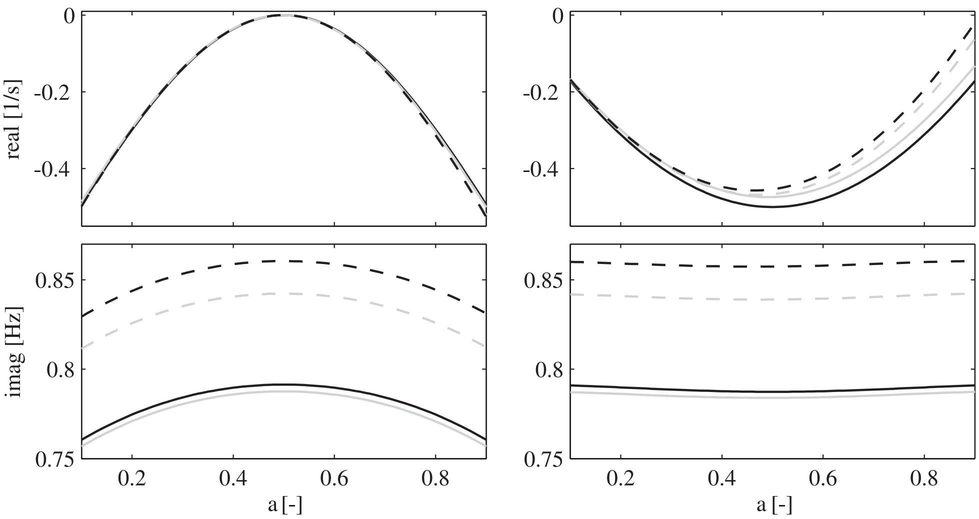

Fig. 6.7 Real and imaginary part of the complex conjugate poles vs. position of E-STATCOM a with active power injection (left) and reactive power injection (right) for POD; Active power of load, $P_{\mathrm{L0}} = 0.8$ pu (black dashed), 0.6 pu (gray dashed), 0.2 pu (gray solid) and no load connected (black solid).

6.4.2 Impact of load type and location

Choosing the total load magnitude of $P_{\mathrm{L0}} = 0.8$ pu and power factor of 0.9, the test in the previous section is repeated for 12 different load types as shown in Table 6.1 [26]. The composition of the load types is selected as $p_{\mathrm{i}} = q_{\mathrm{i}} = 1/3$ for i=[1,2,3] and the E-STATCOM is connected at $a = 0.19$ for the tests.

TABLE 6.1. DIFFERENT STATIC LOAD TYPES FOR ANALYSIS

Load type	Description	m_1, m_2, m_3	n_1, n_2, n_3
0	Constant power load	0, 0, 0	0, 0, 0
1	Constant current load	1, 1, 1	1, 1, 1
2	Constant impedance load	2, 2, 2	2, 2, 2
3	Mixed constant power, constant current and constant impedance load	0, 1, 2	0, 1, 2
4	Exponential load	0.5, 1.5, 2.5	0.5, 1.5, 2.5
5	Water heaters, ovens, deep fryer	2, 2, 2	0, 0, 0
6	Refrigerator	0.77, 0.77, 0.77	2.5, 2.5, 2.5
7	Industrial motors	0.07, 0.07, 0.07	0.5, 0.5, 0.5
8	Fan motors	0.08, 0.08, 0.08	1.6, 1.6, 1.6
9	Arc furnaces	2.3, 2.3, 2.3	1.6, 1.6, 1.6
10	Mixed load 7, 8 and 9	0.07, 0.08, 2.3	0.5, 1.6, 1.6
11	Unloaded transformers	3.4, 3.4, 3.4	11.5, 11.5, 11.5

The movement of poles with a change in the location of the various load types is shown in Fig. 6.8. The results show that load characteristics close to that of “constant impedance” in the active power component of the load have the most impact on POD by active power injection.

On the other hand, load characteristics close to that of "constant power" in the active power component have the biggest influence on POD performance by reactive power injection. For the various load types, it can also be observed that the characteristic of load associated with the active power part is more significant than the reactive power part. Finally, it is shown that the impact of load type and location on POD is more significant when reactive power injection is used.

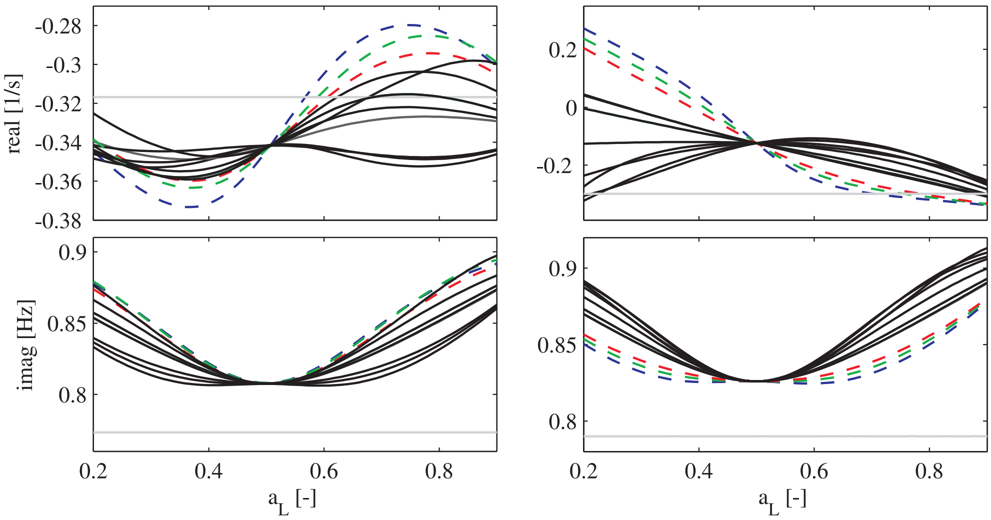

Fig. 6.8 Real and imaginary part of the complex conjugate poles vs. position of load a_{L}; left plots: active power injection for POD with load type 5 (blue dashed), 9 (green dashed) , 2 (red dashed) and black solid for all other load types; right plots: reactive power injection for POD with load type 0 (blue dashed), 7 (green dashed), 8 (red dashed) and black solid for all other load types; gray solid plots represent the case for no load connected.

As shown in the results in Fig. 6.8, the use of the POD controller for reactive power injection described in Section 6.3 could result in an unstable system (poles with positive real part) for some load types connected close to the compensator. To identify the cause of the instability in this case, the parameters for the controller input signals $[\Gamma_{\theta_{\mathrm{E}}}, \Gamma_{P_{\mathrm{tran}}}]$ and the parameters for the change in the generator power outputs $[K_{\mathrm{g1,P}}, K_{\mathrm{g2,P}}, K_{\mathrm{g1,Q}}, K_{\mathrm{g2,Q}}]$ for the most dominant loads (see colored and dashed curves in Fig.6.8) are shown in Fig. 6.9. The results indicate that the parameters $[\Gamma_{\theta_{\mathrm{g}}}, \Gamma_{P_{\mathrm{tran}}}]$ for the POD controller input signals do not change much as the location of the load is varied. On the other hand, the parameters for the change in the power output of the generators due to injection of reactive power $[K_{\mathrm{g1,Q}}, K_{\mathrm{g2,Q}}]$ are affected significantly both in magnitude and sign (see bottom right curves in Fig. 6.9) unlike the parameters for active power injection $[K_{\mathrm{g1,P}}, K_{\mathrm{g2,P}}]$ (see bottom left curves in Fig. 6.9). Therefore, the sign of the gain, K_{Q} in the POD controller by reactive power injection should be chosen carefully depending on the nature of the loads connected close to the compensator.

By adjusting the sign of the gain depending on the load location, a net positive damping is achieved as shown in Fig. 6.10 (see right plots) for all types of loads and at all locations. At the locations where $K_{\mathrm{g1,Q}} = K_{\mathrm{g2,Q}} \approx 0$, the action of the compensator is counteracted by the load characteristics and no damping can be provided. By setting the gain K_{Q} to zero in this case, unnecessary use of reactive power for POD can be avoided.

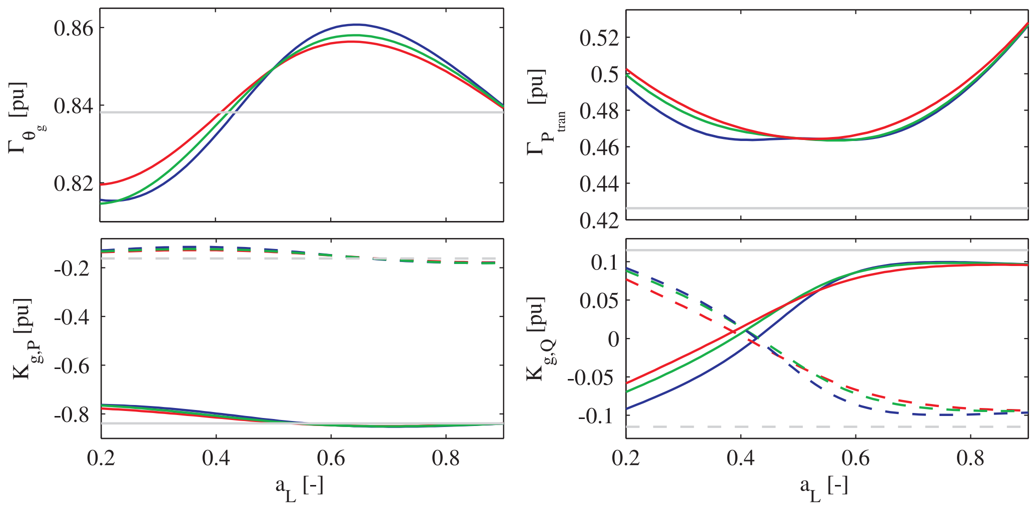

Fig. 6.9 Top plots: variation of parameters for input signals for POD [Γ_{θ_g}, $\Gamma_{P_{\text{tran}}}$]; bottom plots: variation of parameters [$K_{\text{g1,P}}$ (solid), $K_{\text{g2,P}}$ (dashed)] (left) and [$K_{\text{g1,Q}}$ (solid), $K_{\text{g2,Q}}$ (dashed)] (right); left plots: load type 5 (blue), 9 (green), 2 (red); right plots: load type 0 (blue), 7 (green), 8 (red); gray plots represent the case for no load connected.

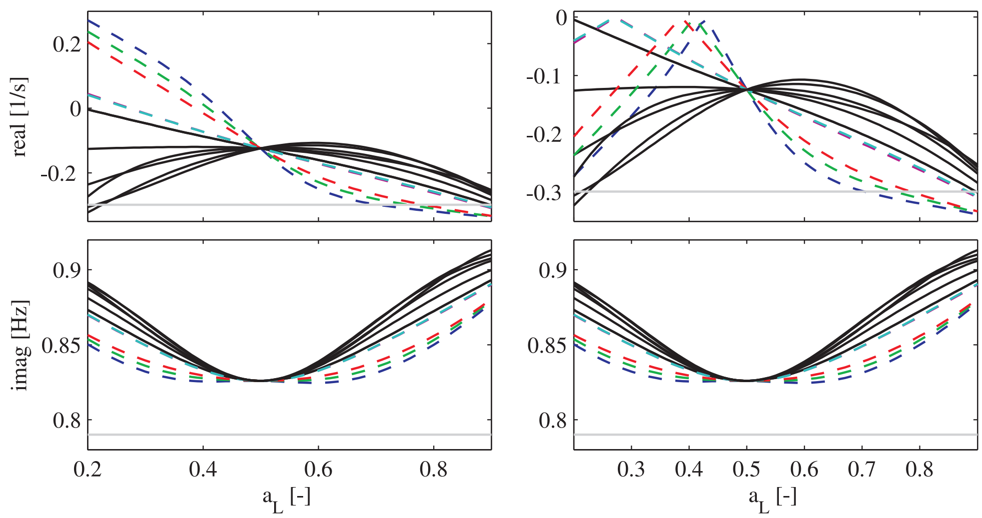

Fig. 6.10 Real and imaginary part of the complex conjugate poles vs. position of load a_{L}; left plots: reactive power injection for POD with a constant gain; right plots: reactive power injection for POD with a variable gain; dashed plots represent load type 0 (blue), 7 (green), 8 (red), 10 (cyan), 6 (violet) and black solid plots represent all other loads; gray solid plots represent the case for no load connected.

6.5 Impact of multiple-oscillation modes on POD

Depending on the power system configuration, its operating conditions and the nature of the disturbance, one or more oscillation modes can be excited in the system. The problem in this case could be that the action of the POD controller to damp a particular oscillation mode of interest might deteriorate the damping at other oscillation modes. In this section, the application of the POD controller described in Section 6.3 for independent damping of multiple-oscillation modes will be described. For this purpose, the two-area power system model in [26] is modified deliberately to obtain a simplified three-area power system model as in Fig. 6.11 with rating 20/230 kV, 900 MV. A disturbance in this system results in two oscillation modes and the purpose of the controller is to provide damping to each oscillation mode without affecting the damping of the other oscillation mode.

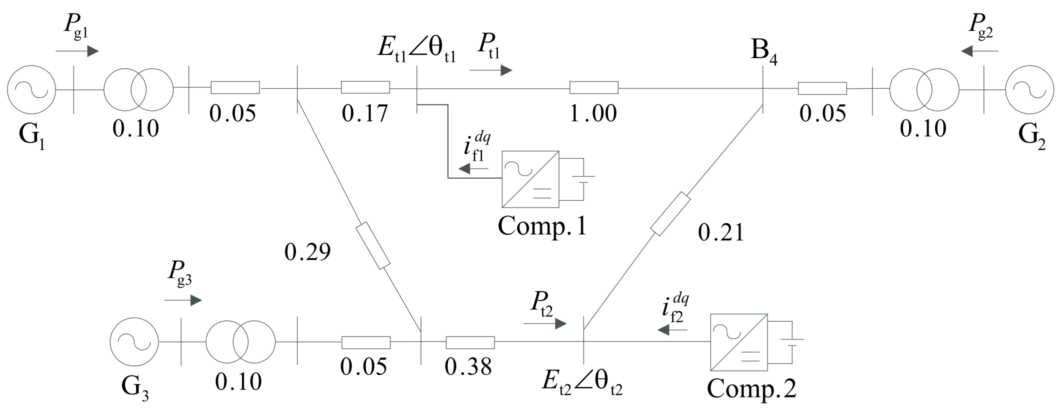

Fig. 6.11 A simplified three-area test system with two compensators.

The POD controller described so far has assumed a single compensator in the power system. However, independently designed multiple compensators can be used together without any problem of adverse interaction among themselves. To verify this, two compensators are considered in the system in Fig. 6.11. The power output of each generator (P_{gi}, with i = 1,2,3) and local voltage and power flow measurements at the compensator location ($E_{\text{ti}}\angle\theta_{\text{ti}}$, P_{ti}, with i = 1,2) are as indicated in the figure.

6.5.1 Multimode damping controller

The derivation of the multimode damping controller from the locally measured signals involves estimating the critical oscillation modes accurately in spite of uncertainties in the operating points and parameters of the power system using the modified RLS algorithm described in Section 4.3. Based on the power system configuration, the corresponding phase shift is added to each estimated mode to get the required damping signal component. By using the damping signals from each mode separately, the required active and reactive current references for POD are generated using a proportional controller similar to the discussion in Section 6.3.

For the system in Fig. 6.11, the block diagram of the control scheme for the first compensator is shown in Fig. 6.12, where the frequency estimate of the PLL (ω_{t1}) and the active power flow (P_{t1}) at the compensator location are used to set up the POD controller. For the investigated system, a phase shift of $0°$ and $90°$ have been used for the oscillatory mode estimates in ω_{t1} and P_{t1}, respectively. The control scheme for the second compensator is set up similarly using the locally measured signals, ω_{t2} and P_{t2}.

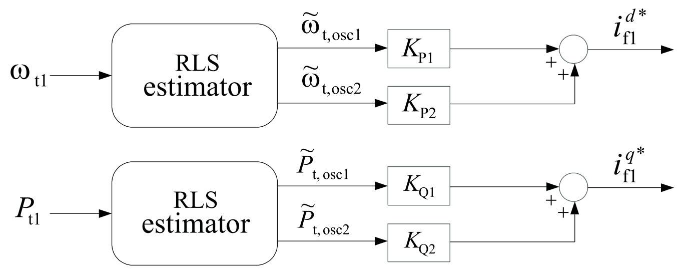

Fig. 6.12 Block diagram of the multimode POD controller for compensator 1.

By using the estimate of each oscillation mode in the multimode damping controller, the injected active and reactive power from the compensators will consist of only the frequency of the oscillation mode to be damped. This decouples the performance of the damping controller on the various modes. As each mode is a global variable in the system dynamics, the use of multiple compensators that are designed to damp a particular oscillation mode results in a net additive damping thus avoiding any negative interaction between the compensators.

6.5.2 Stability analysis

The dynamic model of the system in Fig. 6.11 is implemented to investigate the effectiveness of the independent multimode damping controller. While the full controller in Fig. 6.12 is nonlinear, a modal analysis of the whole system can be made by using the RLS algorithm in its steady-state form, similar to the one in (4.33). Thus, the whole system dynamic can be expressed as

$$\Delta\dot{\mathbf{x}} = \mathbf{A}_{\mathrm{G}}\Delta\mathbf{x} + \mathbf{B}_{\mathrm{G}}\Delta\mathbf{T} + \mathbf{B}_{\mathrm{C}}\Delta\mathbf{u} \tag{6.33}$$

where the state ($\Delta\mathbf{x}$), mechanical torque ($\Delta\mathbf{T}$) and control input ($\Delta\mathbf{u}$) vectors are given by

$$\Delta\mathbf{x} = \begin{bmatrix} \Delta\omega_{\mathrm{g1}} & \Delta\delta_{\mathrm{g1}} & \Delta\omega_{\mathrm{g2}} & \Delta\delta_{\mathrm{g2}} & \Delta\omega_{\mathrm{g3}} & \Delta\delta_{\mathrm{g3}} \end{bmatrix}^{\mathrm{T}}$$
$$\Delta\mathbf{T} = \begin{bmatrix} \Delta T_{\mathrm{m1}} & \Delta T_{\mathrm{m2}} & \Delta T_{\mathrm{m3}} \end{bmatrix}^{\mathrm{T}}$$
$$\Delta\mathbf{u} = \begin{bmatrix} i^{d}_{\mathrm{f1}} & i^{q}_{\mathrm{f1}} & i^{d}_{\mathrm{f2}} & i^{q}_{\mathrm{f2}} \end{bmatrix}^{\mathrm{T}}$$

The matrices $\mathbf{A}_{\mathrm{G}}$, $\mathbf{B}_{\mathrm{G}}$ and $\mathbf{B}_{\mathrm{C}}$ are calculated from the steady-state operating point and the injected currents are controlled as in Fig. 6.12. Using (6.33), the performance of the control method for independent damping of the oscillation modes for various cases will be investigated in the following.

As an example, the transient impedance of all generators is chosen to be 0.3 pu and a steady-state operating point with $P_{\mathrm{g1}} = 0.4$ pu, $P_{\mathrm{g2}} = -0.5$ pu, $P_{\mathrm{g3}} = 0.1$ pu; the terminal voltage for all the generators is set to 1 pu. The compensators are connected at two specific locations as shown in Fig. 6.11. The steady-state reactance of the transmission lines and leakage reactance of the transformers in pu are as shown in the figure. Choosing the inertia constant of the generators as $H_{\mathrm{g1}} = H_{\mathrm{g2}} = 6.5$ s and $H_{\mathrm{g3}} = 2.2$ s, a small-signal analysis around the selected operating point results in two oscillation modes with frequencies 0.98 Hz (mode 1) and 1.69 Hz (mode 2) when both compensators are in idle mode. The first mode involves mainly oscillation of Generator 1 against Generator 2, whereas the second mode involves oscillation of Generator 1 and 3 against Generator 2. The second oscillation mode is mainly caused by the mechanical behavior of Generator 3 and therefore the power output of the third generator will comprise mainly of this frequency.

The first test is made to investigate how the damping controller works when each compensator is used separately. The movement of the poles are plotted in Fig. 6.13 when the gains of the first compensator change from zero to [$K_{\mathrm{P1}} = K_{\mathrm{Q1}} = K_{\mathrm{P2}} = K_{\mathrm{Q2}} = -0.30$] whereas Fig. 6.14 shows the movement of poles when the gains of the second compensator change from zero to [$K_{\mathrm{P1}} = K_{\mathrm{Q1}} = -0.24$ and $K_{\mathrm{P2}} = K_{\mathrm{Q2}} = -0.10$]. The results show that controlling only mode 1 results in positive damping to mode 1 without affecting the damping of mode 2. Similarly, controlling only mode 2 results in positive damping to mode 2 without affecting the damping of mode 1. This confirms the validity of the controller to provide damping at the critical oscillation mode of interest without affecting the system damping at the other mode.

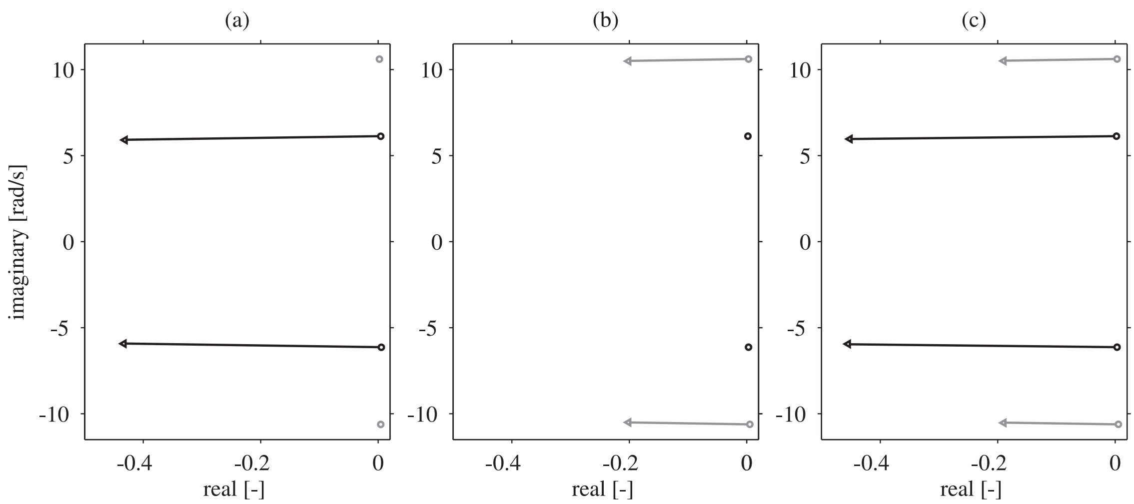

Fig. 6.13 Movement of oscillatory mode poles using compensator 1 when controlling mode 1 oscillation only (plot (a)), mode 2 oscillation only (plot (b)) and both modes (plot (c)); Black curves represent mode 1 poles and gray curves represent mode 2 poles; Poles start at '∘' and move toward '▷'.

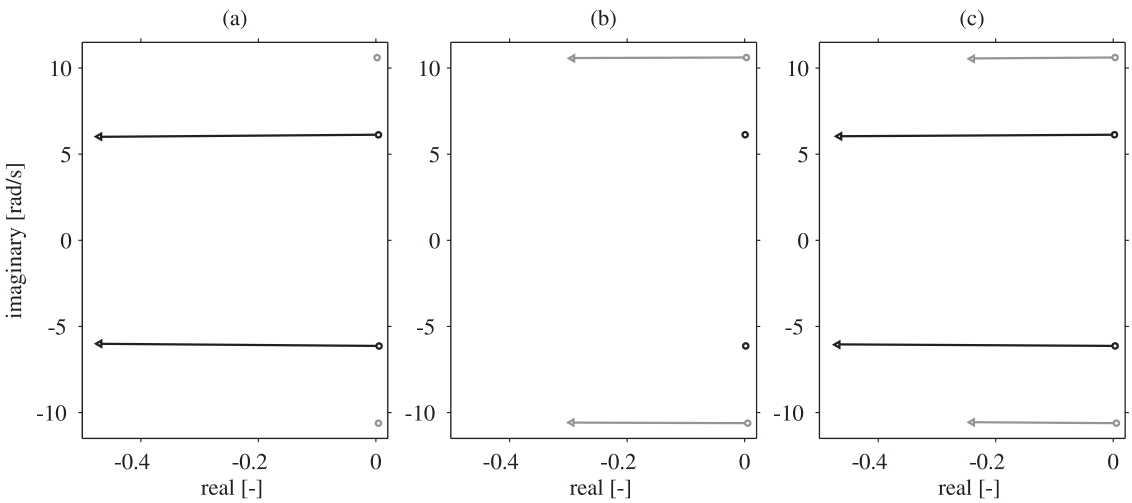

Fig. 6.14 Movement of oscillatory mode poles using compensator 2 when controlling mode 1 oscillation only (plot (a)), mode 2 oscillation only (plot (b)) and both modes (plot (c)); Black curves represent mode 1 poles and gray curves represent mode 2 poles; Poles start at '○' and move toward '▷'.

Even if the same control method is used for the two compensators and their gains are adjusted to obtain similar damping for the previous results, it should be observed that the impact of each compensator to damp a particular mode differs, depending on the observability and controllability of the oscillation mode at the compensator location. Another set of tests is made to investigate the damping performance of the controller when the two compensators are active at the same time with the compensator gains chosen similar to the results in Figs. 6.13 and 6.14. It is possible to see from the results in Fig. 6.15 that independent damping of each mode is achieved in this case as well. It is also possible to see that the action of the two compensators adds up in increasing the damping of the specific oscillation mode, i.e. the two compensators perform well when operating separately or together without any risk of negative interaction. With the proposed method and by using each compensator to control the mode where the observability and controllability of that mode is higher at the connection point, the use of multiple compensators can maximize the damping that can be provided to the system. In the case of active power use for POD, this could mean that the amount of total energy needed to damp an oscillation mode can be reduced by using distributed compensators.

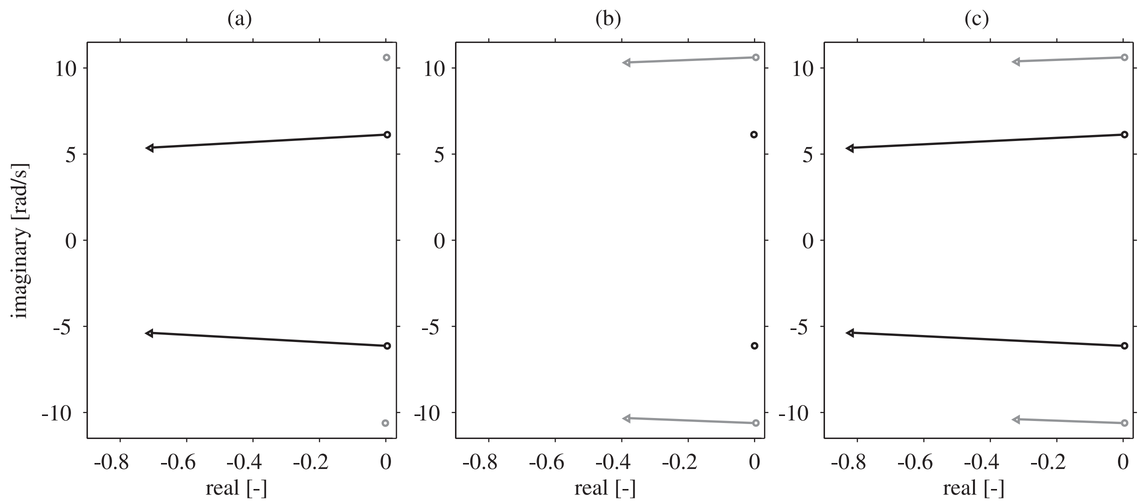

Fig. 6.15 Movement of oscillatory mode poles using compensator 1 and compensator 2 when controlling mode 1 oscillation only (plot (a)), mode 2 oscillation only (plot (b)) and both modes (plot (c)); Black curves represent mode 1 poles and gray curves represent mode 2 poles; Poles start at '○' and move toward '▷'.

Finally, the damping analysis is made assuming an error of 0.2 Hz in the mode frequencies considered in the control algorithm to represent a lack of full knowledge of the system parameters. For this, a mode frequency of 1.18 Hz and 1.89 Hz is assumed instead of the actual values of 0.98 Hz and 1.69 Hz for oscillation mode 1 and oscillation mode 2, respectively. The performance of the control method is summarized in Figs. 6.16 - 6.17 when using Compensator 2. In this case, the movement of the poles is plotted when the gains of Compensator 2 are changed from zero to [$K_{\mathrm{P1}} = K_{\mathrm{Q1}} = K_{\mathrm{P2}} = K_{\mathrm{Q2}} = -0.30$]. It can be observed by comparing the two figures that the damping performance of each mode is reduced and interactions between the modes arise that could lead to a negative damping of the uncontrolled mode as in Fig. 6.17 (plot (a) gray curves). To avoid this, a mode frequency adaptation mechanism as described in Fig. 4.12 in Section 4.3.3 is necessary and this will be verified in Section 7.2.2 using time-domain simulations.

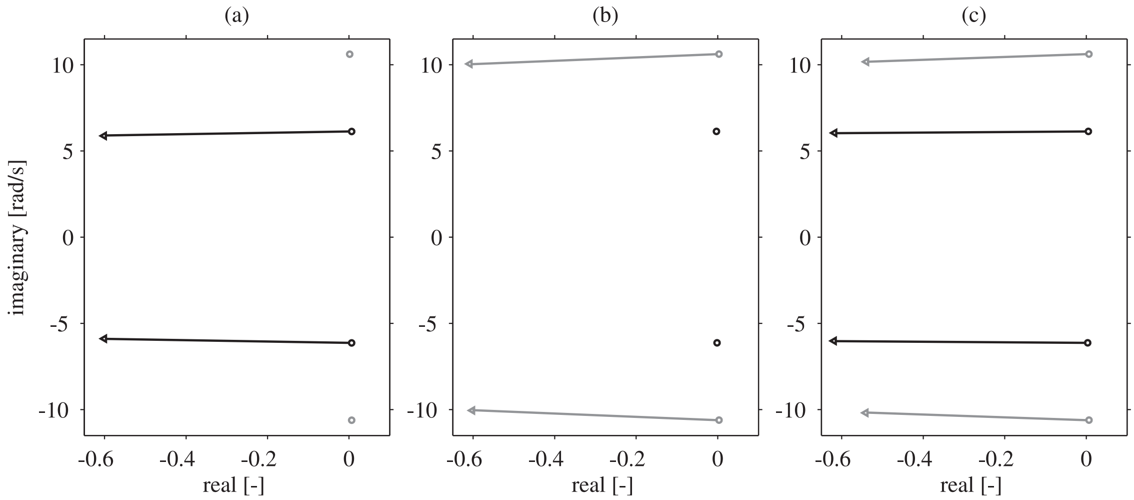

Fig. 6.16 Movement of oscillatory mode poles using compensator 2 and with accurate knowledge of mode frequencies when controlling mode 1 oscillation only (plot (a)), mode 2 oscillation only (plot (b)) and both modes (plot (c)); Black curves represent mode 1 poles and gray curves represent mode 2 poles; Poles start at '○' and move toward '▷'.

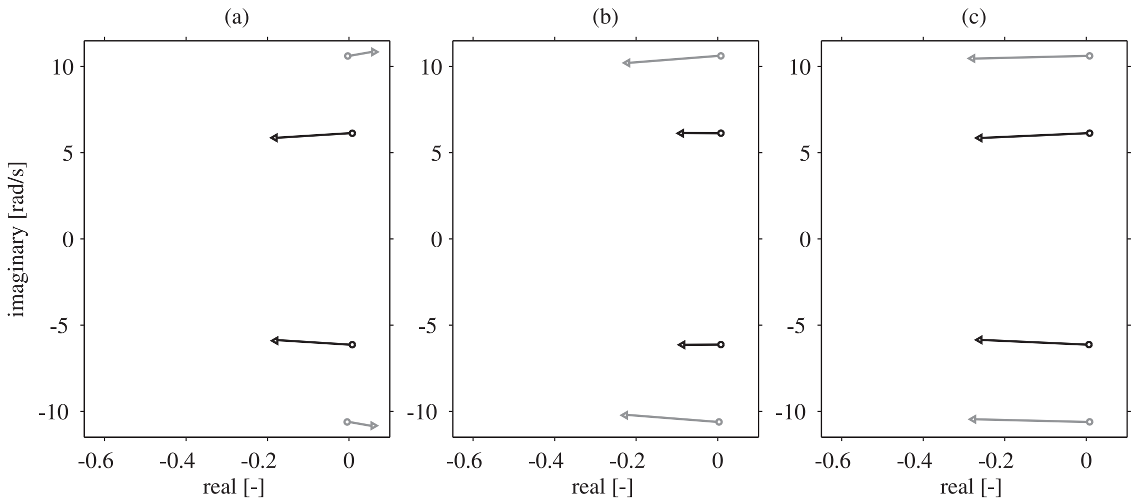

Fig. 6.17 Movement of oscillatory mode poles using compensator 2 and with inaccurate knowledge of mode frequencies when controlling mode 1 oscillation only (plot (a)), mode 2 oscillation only (plot (b)) and both modes (plot (c)); Black curves represent mode 1 poles and gray curves represent mode 2 poles; Poles start at '○' and move toward '▷'.

6.6 Transient Stability Enhancement (TSE)

Transient stability enhancement function is necessary to ensure secure operation of the power system following large disturbances, such as transmission line faults. Similar to the discussion in Chapter 2 for the single-machine infinite-bus system, the transient stability of a two-machine system can be described using the equal-area criterion, where the angle deviation between the machines is instead used. Considering the system in Fig. 6.1, the TSE control algorithm for the E-STATCOM will be described in this section.

6.6.1 Derivation of control input signals

When a change in the operating point of the system occurs due to a disturbance, the synchronizing torque component is responsible for the synchronous operation of the generators. Therefore, one way to increase the transient stability of the system in Fig. 6.1 is to control the E-STATCOM in such a way that the change in the power output of the generators (ΔP_{g1} and ΔP_{g2}) is proportional to the angle deviation as

$$\begin{aligned} \Delta P_{\mathrm{g1}} &= K_{\mathrm{syn1}}(\delta_{\mathrm{g1}} - \delta_{\mathrm{g2}}) \\ \Delta P_{\mathrm{g2}} &= K_{\mathrm{syn2}}(\delta_{\mathrm{g2}} - \delta_{\mathrm{g1}}) \end{aligned} \tag{6.34}$$

where the constants K_{syn1} and K_{syn2} represent the synchronizing torque coefficients provided by the compensator to Generator 1 and Generator 2, respectively. To implement (6.34), the impact of active and reactive power injection on the power output of the generators should be investigated first. Using the expressions (6.2) - (6.8), the change in the power output of the generators due to the injected reactive current (i_{f}^{q}) and active current (i_{f}^{d}) from the compensators can be described as

$$\begin{aligned} \Delta P_{\mathrm{g1}} &\approx -\left[\frac{V_{\mathrm{g1}}V_{\mathrm{g2}}\sin(\delta_{\mathrm{g10}}-\delta_{\mathrm{g20}})a(1-a)}{E_{\mathrm{g0}}}\right] i_{\mathrm{f}}^{q} - \Gamma_{\mathrm{P}} E_{\mathrm{g0}} i_{\mathrm{f}}^{d} \\ \Delta P_{\mathrm{g2}} &\approx \left[\frac{V_{\mathrm{g1}}V_{\mathrm{g2}}\sin(\delta_{\mathrm{g10}}-\delta_{\mathrm{g20}})a(1-a)}{E_{\mathrm{g0}}}\right] i_{\mathrm{f}}^{q} - \left[1-\Gamma_{\mathrm{P}}\right] E_{\mathrm{g0}} i_{\mathrm{f}}^{d} \end{aligned} \tag{6.35}$$

From (6.34) and (6.35), the control algorithm to increase the synchronizing torque component using reactive power injection for instance is given by

$$i_{\mathrm{f}}^{q} = -K_{\mathrm{Q,TSE}}(\delta_{\mathrm{g1}} - \delta_{\mathrm{g2}}) \tag{6.36}$$

where $K_{\mathrm{Q,TSE}}$ is a positive constant assuming that the steady-state active power transfer is from Generator 1 to Generator 2. The added synchronizing torque coefficient is given by

$$K_{\mathrm{syn1}} = K_{\mathrm{syn2}} = K_{\mathrm{Q,TSE}}\left[\frac{V_{\mathrm{g1}}V_{\mathrm{g2}}\sin(\delta_{\mathrm{g10}} - \delta_{\mathrm{g20}})a(1-a)}{E_{\mathrm{g0}}}\right] \tag{6.37}$$

Following a three-phase short-circuit fault, the angle deviation between the generators will be increasing and the control method in (6.36) increases the synchronizing torque component. This in turn increases the deceleration area of the system and hence the transient stability of the system is enhanced. However, the control method should be modified if the disturbance in the system instead results in the angle deviation between the generators, $\delta_{\mathrm{g12}} = \delta_{\mathrm{g1}} - \delta_{\mathrm{g2}}$ to decrease. In this case, the sign of the injected reactive current should be reversed to increase the stability of the system. Moreover, in order to maximize the survival of the system, it is better to use the the maximum reactive current limit (I^q_{max}) of the compensator according to (6.36). With this modifications, the TSE control algorithm for reactive power injection becomes

$$i^q_{\mathrm{f}} = \begin{cases} -I^q_{\mathrm{max}} & , \quad \text{when } \delta_{\mathrm{g12}} \text{ is increasing during the first swing} \\ \\ I^q_{\mathrm{max}} & , \quad \text{when } \delta_{\mathrm{g12}} \text{ is decreasing during the first swing} \end{cases} \tag{6.38}$$

Note that the TSE control should be applied only during the first swing of the generator angles and the POD function as described in the previous sections will follow the subsequent swings. Observing (6.34) and (6.35), it can be understood that the use of reactive current increases the synchronizing torque component for both generators for the system in Fig. 6.1. Hence, the same TSE control algorithm is applied at various locations of the compensator. On the other hand, the use of active current for TSE increases the synchronizing torque component for one generator and decreases the synchronizing torque component of the other generator. This means that the use of active power should be monitored depending on the location of the compensator. To provide an overall TSE function for the system, enhancing the stability of Generator 1 should be prioritized if the mass-scaled electrical location of the compensator, $a_{\mathrm{M}} < 0.5$. For this case, the TSE control algorithm using active power injection is given by

$$i^d_{\mathrm{f}} = \begin{cases} -I^d_{\mathrm{max}} & , \quad \text{when } \delta_{\mathrm{g12}} \text{ is increasing during the first swing} \\ \\ I^d_{\mathrm{max}} & , \quad \text{when } \delta_{\mathrm{g12}} \text{ is decreasing during the first swing} \end{cases} \tag{6.39}$$

where I^d_{max} is the maximum active current rating of the compensator. For the case $a_{\mathrm{M}} > 0.5$, enhancing the stability of Generator 2 should be prioritized and the control action in (6.39) should be reversed. Note that at the location $a_{\mathrm{M}} = 0.5$, TSE function cannot be provided using active power. It should be emphasized that the time interval, where the algorithm in (6.39) is applied during the first swing, depends on the amount of stored energy in the compensator. By using the enhancement functions as in (6.38) and (6.39), the power output between the two areas after fault clearing increases, which increases the deceleration area of the system. This increases the stability margin of the system.

6.6.2 Estimation of control input signals

To implement a stability enhancement function as described in (6.38) and (6.39), the nature of the angle deviation between the two generators is required. One way to obtain this is through remote measurements of the relative speed between the two generators. In this case, a positive relative speed between the generators indicates that the angle deviation, δ_{g12} is increasing, whereas a negative speed deviation indicates that δ_{g12} is decreasing. This information can be used to decide the control action in the TSE algorithm during the first swing. However, to implement the TSE algorithm using locally measured signals, an estimate of the rate of change of δ_{g12} is necessary. For this purpose, the PCC voltage magnitude (E_{g}) or the transmitted power between the generators (P_{tran}) can be two possible alternatives.

Using the expression for the PCC voltage magnitude in (6.9) for the uncompensated system in Fig. 6.1, the estimate for the derivative of the angle deviation between the generators ($d\tilde{\delta}_{\mathrm{g12}}/dt$) can be expressed as

$$\frac{d\tilde{\delta}_{\mathrm{g12}}}{dt} = -K\frac{dE_{\mathrm{g}}}{dt} = K\frac{a(1-a)V_{\mathrm{g1}}V_{\mathrm{g2}}\sin(\delta_{\mathrm{g12}})}{E_{\mathrm{g}}}\frac{d\delta_{\mathrm{g12}}}{dt} \tag{6.40}$$

By choosing a positive value for the constant K in the range $0 < \delta_{\mathrm{g12}} < \pi$, the estimate for the angle deviation between the generators can be obtained from the derivative of the PCC voltage magnitude. However, the PCC voltage magnitude is easily affected by the TSE control action. Alternatively, $d\tilde{\delta}_{\mathrm{g12}}/dt$ can be estimated using the expression in (6.11) as

$$\frac{d\tilde{\delta}_{\mathrm{g12}}}{dt} = K\frac{dP_{\mathrm{tran}}}{dt} = K\frac{V_{\mathrm{g1}}V_{\mathrm{g2}}\cos(\delta_{\mathrm{g12}})}{X_1+X_2}\frac{d\delta_{\mathrm{g12}}}{dt} \tag{6.41}$$

By choosing a positive value for the constant K in the range $0 < \delta_{\mathrm{g12}} < \pi/2$ and a negative value in the range $\pi/2 < \delta_{\mathrm{g12}} < \pi$, the estimate for the angle deviation between the generators can be obtained from the derivative of the transmitted power between the two areas. The problem in this case would be to know when the angle deviation between the generators is above $\pi/2$. Even if the use of local signals for TSE control are easier to implement, it is difficult to obtain a complete information about δ_{g12} and remote measurements are preferable to provide reliable information for the required TSE function.

As described previously, the TSE control is applied during the first swing of the generator angles and the POD control follows the subsequent swings. Using the estimated angle deviation ($d\tilde{\delta}_{\mathrm{g12}}/dt$), the TSE controller together with the POD controller using reactive power injection is summarized as

$$i_{\mathrm{f}}^{q*} = \begin{cases} -I_{\max}^{q}\mathrm{sign}\left\{\frac{d\tilde{\delta}_{\mathrm{g12}}}{dt}\right\} & , \text{ during the first swing} \\ \\ -I_{\max}^{q} \le K_{\mathrm{Q}}\frac{P_{\mathrm{tran,osc}}}{dt} \le I_{\max}^{q} & , \text{ after the first swing} \end{cases} \tag{6.42}$$

Note that the end of the first swing is indicated by a change in the sign of $d\tilde{\delta}_{\mathrm{g12}}/dt$ and the injection of the reactive current will follow the design of the POD controller as described in Section 6.3.2 in Fig. 6.3. Similarly, the TSE controller together with the POD controller using active power injection is summarized as

$$i_{\mathrm{f}}^{d*} = \begin{cases} -I_{\max}^{d}\mathrm{sign}\left\{(0.5-a_{\mathrm{M}})\frac{d\tilde{\delta}_{\mathrm{g12}}}{dt}\right\} & , \quad \text{during the first swing} \\ \\ -I_{\max}^{d} \leq K_{\mathrm{P}}\tilde{\omega}_{\mathrm{g,osc}} \leq I_{\max}^{d} & , \quad \text{after the first swing} \end{cases} \tag{6.43}$$

Note that the control in (6.43) takes the mass-scaled electrical location of the compensator, a_{M} into account. The challenge with the use of active power injection for TSE is the estimation of the mass-scaled electrical location of the compensator immediately after a system disturbance. Unlike the POD control which estimates control signals continuously to have knowledge of the state of the system, adapting the TSE control described in (6.42) and (6.43) to a large power system is a complicated task [7] due to the limited time available to estimate the various power system parameters following a power system disturbance.

Stability enhancement by virtual machine controller

The TSE and POD controllers described in (6.42) and (6.43) for the classical cascade controller calculates the reference currents, i_{f}^{d*} and i_{f}^{q*}, which act as inputs to the inner current control loop. As an inner current controller is not used in the virtual machine controller, the stability enhancement functions can instead be implemented by calculating the active and reactive power references from the reference currents as

$$\begin{aligned} P_{\mathrm{ref}} &= E_{\mathrm{g}} i_{\mathrm{f}}^{d*} \\ Q_{\mathrm{ref}} &= -E_{\mathrm{g}} i_{\mathrm{f}}^{q*} \end{aligned} \tag{6.44}$$

As defined previously, E_{g} represents the magnitude of the PCC voltage to which the PLL is synchronized and the reference currents, i_{f}^{d*} and i_{f}^{q*} are calculated from the TSE and POD controllers.

In the conventional cascade controller, the actual current follows its reference very quickly thanks to the high bandwidth of the current controller. In the virtual machine controller, the speed of the power controllers have an impact on the reference tracking capability and hence on the TSE and POD functions. Therefore, the bandwidth of the power controllers should be selected to be faster than the rate of change of the power references in (6.44), which are dependent on the electromechanical dynamics. As described in Section 5.4, the reactive power output of the virtual machine is controlled through variation of the converter voltage magnitude, E_{c}. Hence, the stability enhancement functions can also be implemented directly by varying E_{c} based on the expressions in (5.23) and (6.44).

Assuming that the bandwidth of the transfer function in the active power controller in the virtual machine implementation is fast enough to implement the TSE and POD functions, a similar stability enhancement to the power system as the classical cascade controller can be achieved. However, a difference is that an inertia can be added in the virtual machine implementation and this could help in increasing the stability of the power system. The amount of inertia to be added to the system is limited by the bandwidth requirement of the active power controller as described in Section 5.5.2. One advantage with the virtual machine implementation over the conventional cascade controller is that the added inertia to the power system could guarantee transient stability without the need for control input signals to implement the algorithm in (6.43). This will not however ensure that the available active power is used effectively to enhance the stability of the power system. During disturbances such as short-circuit faults, the current limitation in the virtual machine controller could be activated. In this case, it cannot be guaranteed that the reference power tracking is achieved and all the implemented inertia is added to the system.

6.6.3 Evaluation of TSE performance

As described in Section 6.2, the level of stability enhancement provided by the converter depends on how much the active power output from the generators is changed by the injected currents. This in turn depends on the location of the converter a, the power system configuration as well as the active and reactive power rating of the compensator. On the other hand, the TSE function from the available maximum current ratings for the system in Fig. 6.2 is described in (6.42) and (6.43). Considering the same power system configuration, evaluation of the TSE function during the first swing of the machines will be made in this section. This can be achieved by investigating how much the stability margin or power transfer capability of a transmission system increase for a given disturbance using active and reactive power injection.

For this analysis, the system in Fig. 6.2 with the second generator modeled as an infinite bus ($H_{\mathrm{g2}} = \infty$) is considered for simplicity. The increase in power transfer capability of the system without reducing its stability margin will then be investigated while using the TSE function at various locations in the power system. Assuming that the connection point of the converter is given by the parameter a as before, the output power of Generator 1 with a constant active or reactive current injection during TSE is derived as

$$\begin{aligned}
P_{\mathrm{g1,P}} &\approx \frac{V_{\mathrm{g1}}V_{\mathrm{g2}}\sin(\delta_{\mathrm{g1}}-\delta_{\mathrm{g2}})}{X_1+X_2} \pm \left[\frac{V_{\mathrm{g1}}^2(1-a)^2+V_{\mathrm{g1}}V_{\mathrm{g2}}\cos(\delta_{\mathrm{g1}}-\delta_{\mathrm{g2}})a(1-a)}{\sqrt{[(1-a)V_{\mathrm{g1}}]^2+[aV_{\mathrm{g2}}]^2+2a(1-a)V_{\mathrm{g1}}V_{\mathrm{g2}}\cos(\delta_{\mathrm{g1}}-\delta_{\mathrm{g2}})}}\right] I_{\max}^{d} \\
P_{\mathrm{g1,Q}} &\approx \frac{V_{\mathrm{g1}}V_{\mathrm{g2}}\sin(\delta_{\mathrm{g1}}-\delta_{\mathrm{g2}})}{X_1+X_2} \pm \left[\frac{V_{\mathrm{g1}}V_{\mathrm{g2}}\sin(\delta_{\mathrm{g1}}-\delta_{\mathrm{g2}})a(1-a)}{\sqrt{[(1-a)V_{\mathrm{g1}}]^2+[aV_{\mathrm{g2}}]^2+2a(1-a)V_{\mathrm{g1}}V_{\mathrm{g2}}\cos(\delta_{\mathrm{g1}}-\delta_{\mathrm{g2}})}}\right] I_{\max}^{q}
\end{aligned} \tag{6.45}$$

Consider that the system has a total series reactance of 1.5 pu with $V_{\mathrm{g1}} = V_{\mathrm{g2}} = 1$ pu and the connection point of the converter is $a = 0.3$. Using the expressions in (6.45), an example of the power-angle curve for the system during TSE operation (with the current rating chosen as $I_{\max}^{d} = I_{\max}^{q} = 0.1$ pu) is shown in Fig. 6.18.

If the generator is initially operating with an output power of 0.5 pu, the uncompensated system will have a maximum deceleration area of 0.159 pu as calculated from the power-angle curve. It is possible to observe that an increase in the transmitted power will reduce the available deceleration area and hence the stability margin of the system. As it can be seen from the same figure, the compensated system has more deceleration area for the same initial transmitted power. This means that the active power transfer capability of the system can be increased

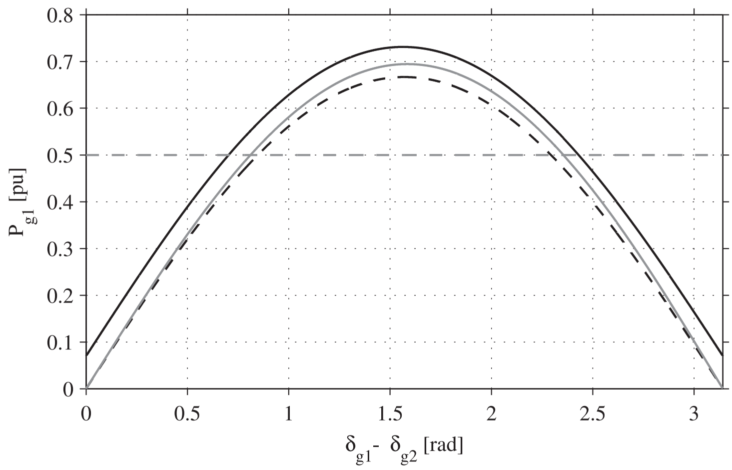

Fig. 6.18 power-angle curve without TSE (black dashed), TSE with constant active current injection (black solid), TSE with constant reactive current injection (gray solid) and initial transmitted power (gray dashed).

without reducing its stability margin by using a TSE controller. For the specific case in Fig. 6.18, it is found that the initial transmitted power can be increased to 0.561 pu and 0.526 pu without reducing the stability margin of the system when active and reactive power is used for TSE, respectively.

Figure 6.19 summarizes the current rating of the converter needed to increase the power transfer in Fig. 6.18 to 0.6 pu at various locations, without reducing the available deceleration area of the uncompensated system with initial transmitted power of 0.5 pu. As it can be seen from the results, the required active power rating to increase the power transfer capability reduces closer to the generator location. At the location $a = 0.1$, for example, the active current rating is 10% of the reactive current requirement to increase the power transfer by the same amount. On the other hand, the reactive power rating reduces when moving closer to the middle of the transmission line. By combining the use of both active and reactive power, it is possible to increase the power transfer capability of the system at various locations of the system.

Although the results in Fig. 6.19 give an idea of how much can be gained by using a TSE operation and the choice of active or reactive power depending on location of the compensator, it should be noted that the results are specific to the case studied and a similar evaluation should be made for other power system configurations in question.

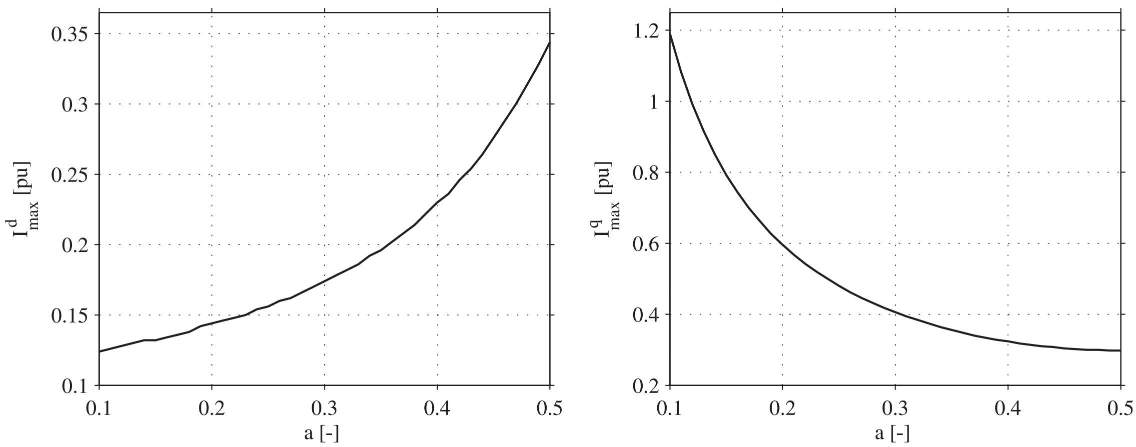

Fig. 6.19 Current rating requirement to increase power transfer capability at various locations; Left: active power for TSE and Right: reactive power for TSE.

6.7 Conclusions

A POD and TSE control algorithms have been derived in this chapter. For this, the signal estimation technique described in Chapter 4 has been used to design an adaptive POD controller. It has been shown that with proper selection of the local measurement signals together with the proposed estimation method, the use of active and reactive power for stability enhancement function can be maximized. Moreover, the impact of various loads and the use of multiple compensators on power system stability has been investigated. The use of the proposed control method has been shown to provide independent damping for multiple oscillation modes without any negative interaction among the compensators. The control methods derived in this section will be verified using various power system configurations in the next chapter.

Chapter 7

Verification of E-STATCOM control for power system stability enhancement

7.1 Introduction

A detailed description of the outer control loops for stability enhancement has been derived in the previous chapter. In this chapter, the dynamic performance of the stability enhancement controllers will be verified through simulations and experimental tests.

7.2 Simulation verification

In this section, the performance of the POD and TSE controllers will be evaluated for various power system configurations.

7.2.1 Two-area test system

In Section 6.3.3, a simplified aggregate model of a power system transferring power from one area to the other (see Fig. 6.1) has been used to describe the principle of power oscillation damping by active and reactive power injection. In this section, the POD controller described in Section 6.3 will be verified though time-domain simulations by using a two-area power system model as in Fig. 7.1. This simplified two-area four-machine model has been used to study the nature of inter-area power oscillations in [4]. The system represents a 20/230 kV, 900 MVA system (similar to the system in Fig. 6.1) and the parameters for the generator and transmission system together with the loading of the system are given in Appendix B.2. The system is initially operating in steady-state with a transmitted active power, $P_{\rm tran} = 400$ MW from area 1 to area 2.

A three-phase fault is applied to the system on one of the transmission lines between bus 7 and bus 8. The fault is cleared after 120 ms by disconnecting the faulted line. Due to the applied

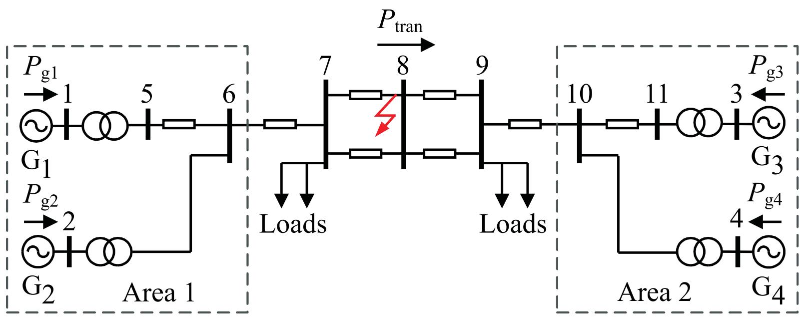

Fig. 7.1 Simplified two-area four-machine power system.

disturbance, a poorly damped oscillation is experienced in the system. Figure 7.2 shows the estimates of the control input signals for POD, while the performance of the E-STATCOM following the fault at three different locations is shown in Figs. 7.3 and 7.4. As described in the small-signal analysis for the two-machine system in Section 6.3.3, when moving closer to the generator units, a better damping is achieved by active power injection (see Fig. 7.3 black solid plots). With respect to reactive power injection, maximum damping action is provided when the E-STATCOM is connected close to the electrical midpoint of the line and the level of damping decreases when moving away from it (see Fig. 7.3 gray solid plots). Because of a good choice of signals for controlling both active and reactive power injection, effective power oscillation damping is provided by the E-STATCOM irrespective of its location in the line (see Fig. 7.3 black dashed plots). Observe that the gains, G_{P} and G_{Q} are chosen to obtain a damping ratio of 10% at bus 7 using active power injection and at bus 8 using reactive power injection. These are used for all the tests carried out in this section.

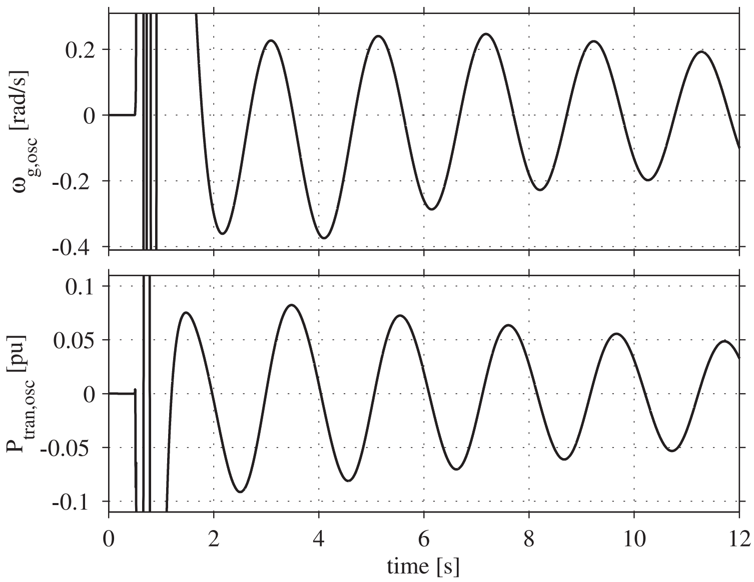

Fig. 7.2 Estimated control input signals for POD at bus 7 with P_{inj} (top) and with Q_{inj} (bottom).

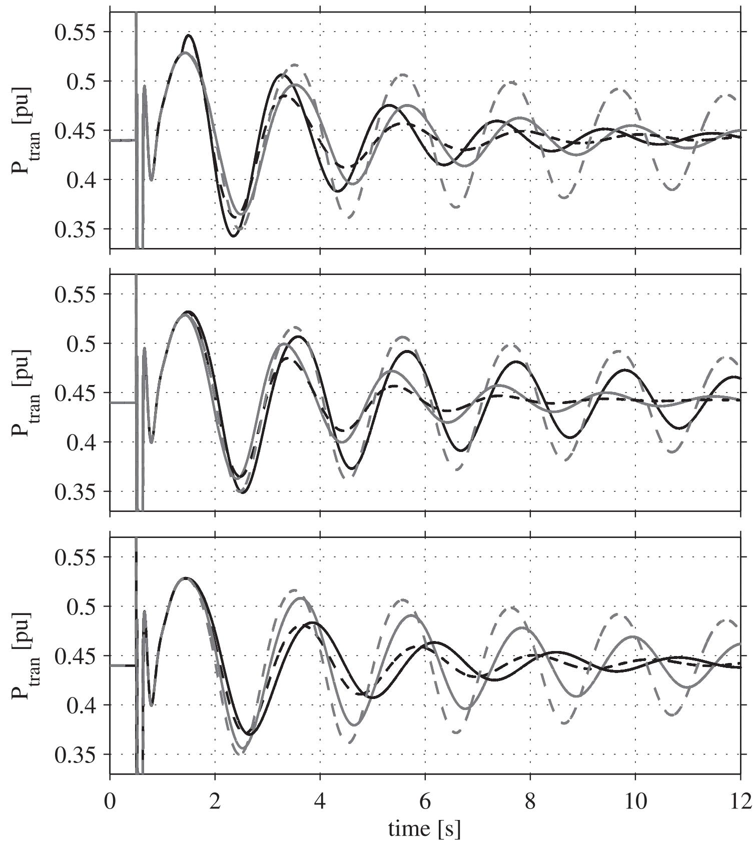

Fig. 7.3 Measured transmitted active power output following a three-phase fault with E-STATCOM connected at bus 7 (top), bus 8 (middle) and bus 9 (bottom). POD by P_{inj} only (black solid), Q_{inj} only (gray solid), both P_{inj}, Q_{inj} (black dashed) and no POD (gray dashed).

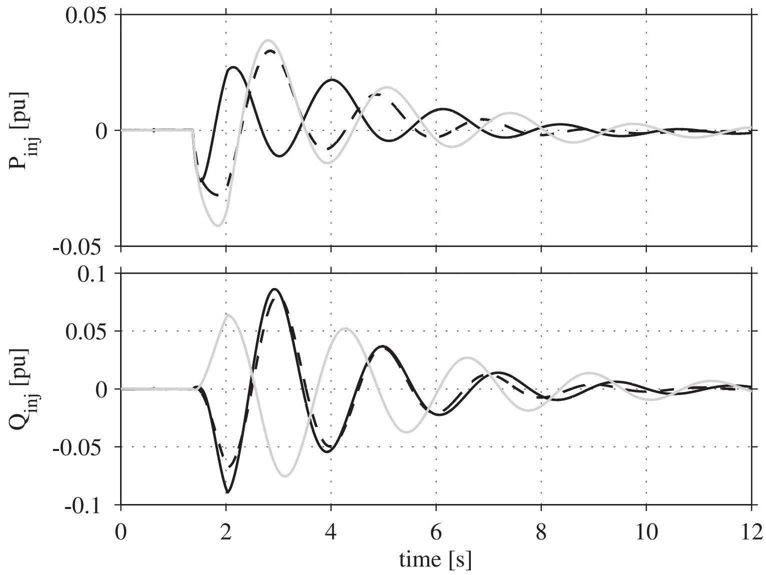

Fig. 7.4 Injected active and reactive power with E-STATCOM connected at bus 7 (black solid), bus 8 (black dashed) and bus 9 (gray solid). Active power injection (top); reactive power injection (bottom); both P_{inj} and Q_{inj} used for POD.

Even if reactive power injection is effective closer to the electrical midpoint of the line, the PCC voltage E_{g} will be highly affected to provide POD as shown in Fig. 7.5. The possibility of having active power injection both reduces the maximum PCC voltage swing and provides more damping action except when the E-STATCOM is close to the mass-scaled electrical midpoint of the line ($a_{\mathrm{M}} \approx 0.5$). Moreover, the use of active power is advantageous when the E-STATCOM is connected close to load locations, where the use of reactive power for POD will be affected by the voltage dependent characteristic of the loads (see bottom gray curve in Fig. 7.4 where the phase of injected reactive power has to be reversed to provide positive damping at bus 9).

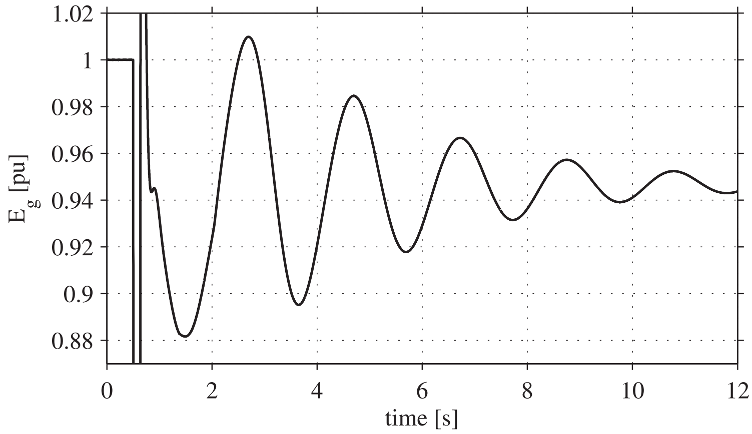

Fig. 7.5 PCC voltage at bus 8 when only Q_{inj} is used for POD.

The simulation results shown so far, have been carried out under the assumption of accurate knowledge of the oscillatory frequency in the estimated control input signals. As mentioned in Chapter 4, the improved RLS algorithm used in this work is frequency adaptive. To test the dynamic performance of the implemented controller with uncertainties in system parameters, a simulation is performed assuming inaccurate knowledge of the electromechanical oscillation frequency. Figure 7.6 shows the obtained simulation results when an error of 100% in the estimated oscillatory frequency is considered. The compensator is connected at bus 7 (see Fig. 7.1) and POD is achieved using both active and reactive power injection. The figure shows the dynamic performance of the system under frequency adaptation algorithm in the POD controller (black curves). To highlight the effectiveness of the proposed controller, the results that would be obtained without the frequency adaptation in the POD controller are also shown (gray curves). When the frequency adaptation is used, the update of the oscillation frequency is shown in Fig. 7.7. This enables the injection of active and reactive power with the correct phase thereby providing a better damping. The result highlights the advantage of the adopted POD controller over existing filtering solutions, where accurate knowledge of the oscillation frequncy is needed.

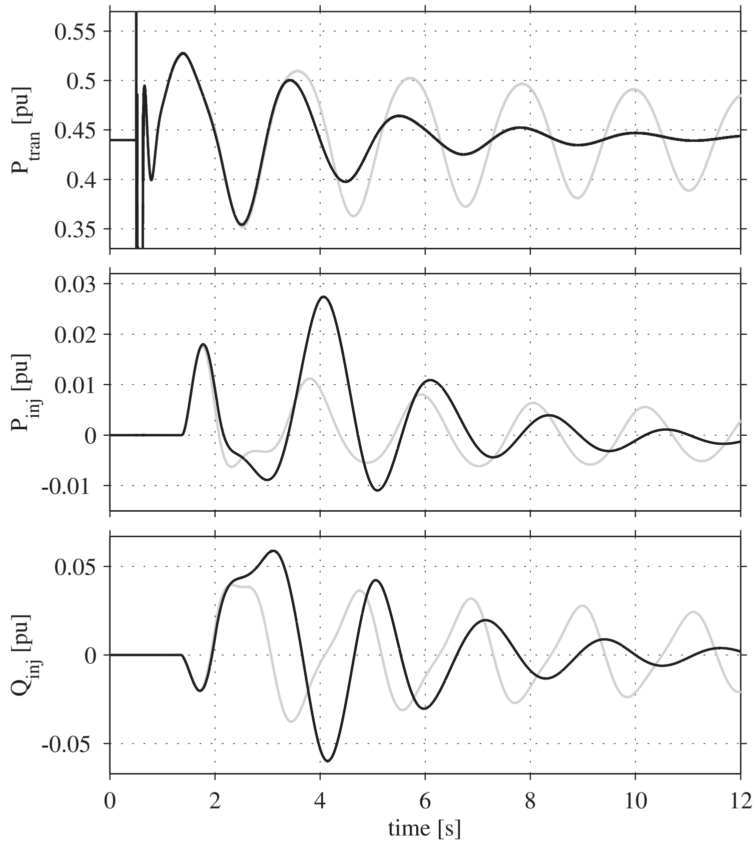

Fig. 7.6 Top: measured transmitted active power with frequency adaptation (black) and without frequency adaptation (gray); Middle: Injected active power with frequency adaptation (black) and without frequency adaptation (gray); Bottom: Injected reactive power with frequency adaptation (black) and without frequency adaptation (gray).

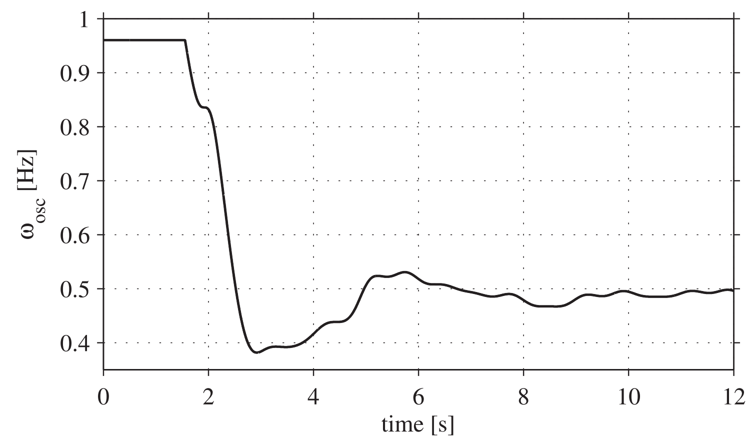

Fig. 7.7 Estimation of the actual oscillation frequency.

Another set of simulations is performed with a longer fault clearing time to test the TSE function described in Section 6.6. First, the critical fault clearing time of 420 ms is applied to the system and the transmitted power is shown in Fig. 7.8 (top figure). In the same figure, the estimate of the derivative of the angle deviation between Area 1 and Area 2 ($d\tilde{\delta}_{g12}/dt$), which is obtained using two PLLs placed at bus 6 and 10 in Fig. 7.1, is shown. The transmitted power stays around the steady-state value and the derivative of the angle deviation between the two areas remain around zero. This indicates that the system remains in synchronism with a sustained low-frequency oscillation. By monitoring $d\tilde{\delta}_{g12}/dt$ as described in the TSE control algorithm in (6.42) and (6.43), the performance of the TSE control will be validated.

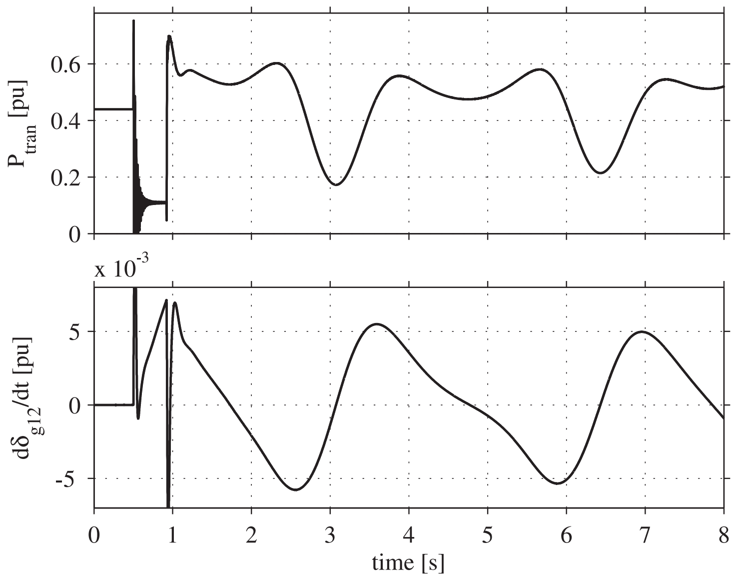

Fig. 7.8 Top: Transmitted power with E-STATCOM in idle mode for a 420 ms fault; Bottom: Estimate of the derivative of the angle deviation between Area 1 and Area 2 ($d\tilde{\delta}_{g12}/dt$).

With the TSE control activated for the E-STATCOM connected at bus 7, it has been found that the critical fault clearing time of the system can be increased by 30 ms when using a maximum reactive power injection of 0.10 pu. Similarly, the critical fault clearing time of the system can be further increased by 20 ms when using a maximum active power injection of 0.05 pu. By using both both active and reactive power injection, the fault clearing time can be increased by 50 ms. Figure 7.9 shows the performance of the TSE controller for an example case of a three-phase fault applied to the system in Fig. 7.1. The fault is applied close to bus 8 and cleared after 440 ms by disconnecting the faulted line. For this fault, it can be seen from the transmitted power (top curve) that the system loses synchronism when the compensator is in idle mode. In this case, the angle between the two areas keep increasing and the transmitted power no more stays with in the steady-state value unlike the case in Fig. 7.8. When the compensator is active, the stability of the system is guaranteed.

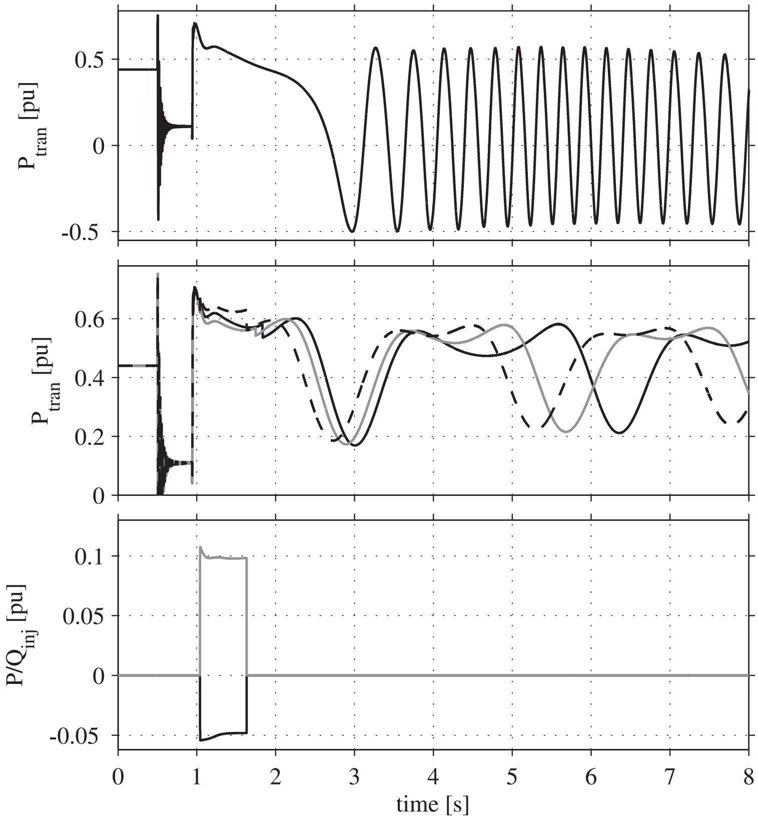

Fig. 7.9 TSE performance with E-STATCOM connected at bus 7; Top: no TSE, Middle: TSE by $P_{\rm inj}$ (black), TSE by $Q_{\rm inj}$ (gray) and TSE by $P_{\rm inj}$ & $Q_{\rm inj}$ (black dashed); Bottom: $P_{\rm inj}$ (black) and $Q_{\rm inj}$ (gray) when $P_{\rm inj}$ & $Q_{\rm inj}$ are used for TSE.

Observe that the POD function in the E-STATCOM control has been disabled for the simulation results depicted in Fig. 7.9. Even if the TSE function keeps the stability of the system, the POD function should also be used to provide damping to the system. Figure 7.10 shows the performance of the TSE and POD controllers together for a similar 440 ms fault applied to the system. Observe from the figure that the larger fault clearing time results in the E-STATCOM to hit the current limit even during the POD action. Immediately after fault clearing, the TSE function will be active during the first swing of the generators. By the end of the first swing, which is indicated by a change in the sign of the control input signal ($d\tilde{\delta}_{12}/dt$), the POD function follows.

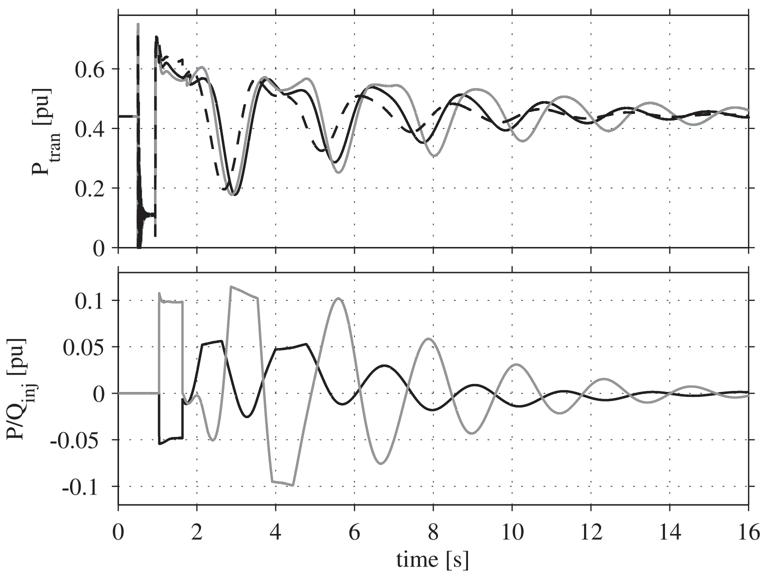

Fig. 7.10 TSE and POD performance with E-STATCOM connected at bus 7; Top: TSE and POD by $P_{\rm inj}$ (black), TSE and POD by $Q_{\rm inj}$ (gray) and TSE and POD by $P_{\rm inj}$ & $Q_{\rm inj}$ (black dashed); Bottom: $P_{\rm inj}$ (black) and $Q_{\rm inj}$ (gray) when $P_{\rm inj}$ & $Q_{\rm inj}$ are used for TSE and POD.

Impact of virtual machine to system stability

For the system in Fig. 7.1 and a compensator connected at bus 7, the TSE performance has been validated in Figs. 7.9 and 7.10 for a fault clearing time of 440 ms. Considering the same power system, the impact of controlling the E-STATCOM as a virtual machine on the power system stability is here investigated.

First, a similar three-phase fault is applied to the system in Fig. 7.1 for 440 ms on one of the transmission lines with the fault cleared by disconnecting the faulted line. As described previously, the implemented fault clearing time results in the loss of synchronism for the system when no compensator is connected. When a virtual inertia of $H_{\rm v} = 3.94$ s (about 15% of the total system inertia) is implemented in the E-STATCOM control, the system becomes transiently stable as shown in Fig. 7.11. With this choice of the virtual inertia, the controller results in a 2 Hz local oscillation in the system as it can be seen in the figure. By applying a 10% damping ratio for this oscillatory mode ($K_{\rm Dv} = 19.9$) in the control, the local oscillation is effectively damped.

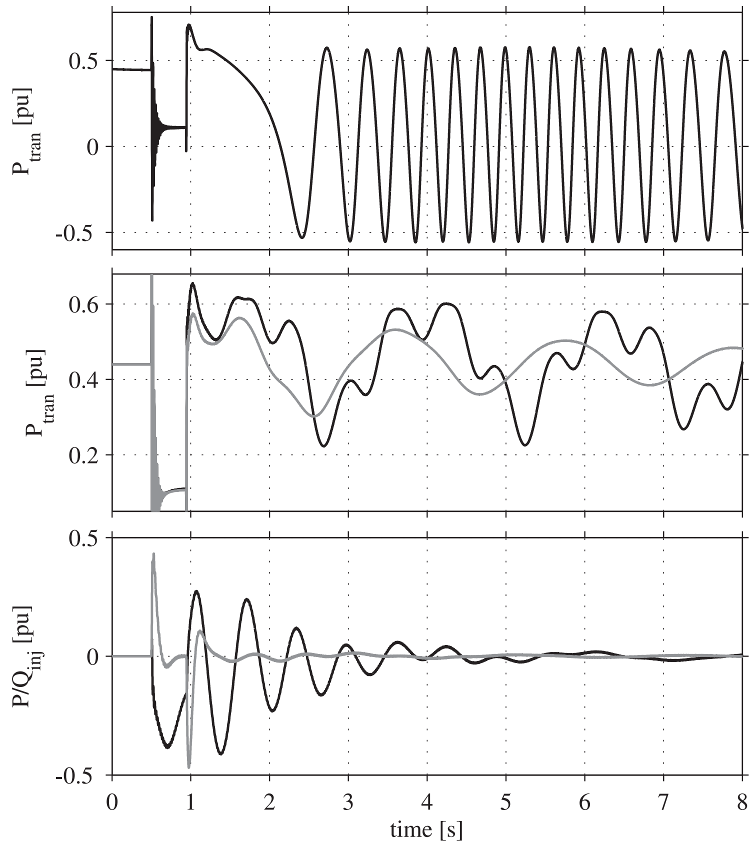

Fig. 7.11 Impact of virtual machine to system stability following fault; Top: transmitted power for no virtual machine connected; Middle: transmitted power for virtual machine with no damping (black) and with 10% damping ratio in the active power controller (gray); Bottom: injected active power (black) and reactive power (gray) for the virtual machine with 10% damping ratio in the active power controller.

Note that in the control implementation, the active power exchange from the compensator should be kept within its rating. Among the factors that influence the maximum active power exchange include the nature of the power system disturbance, location of the compensator, configuration of the power system and amount of virtual inertia to be implemented. As an example, Figure 7.12 shows the response of the controller for various cases, where the fault and compensator location are unchanged from the previous tests. As it can be observed from the results, the maximum injected power tends to increases with an increase in the virtual inertia and fault clearing time for this specific power system configuration.

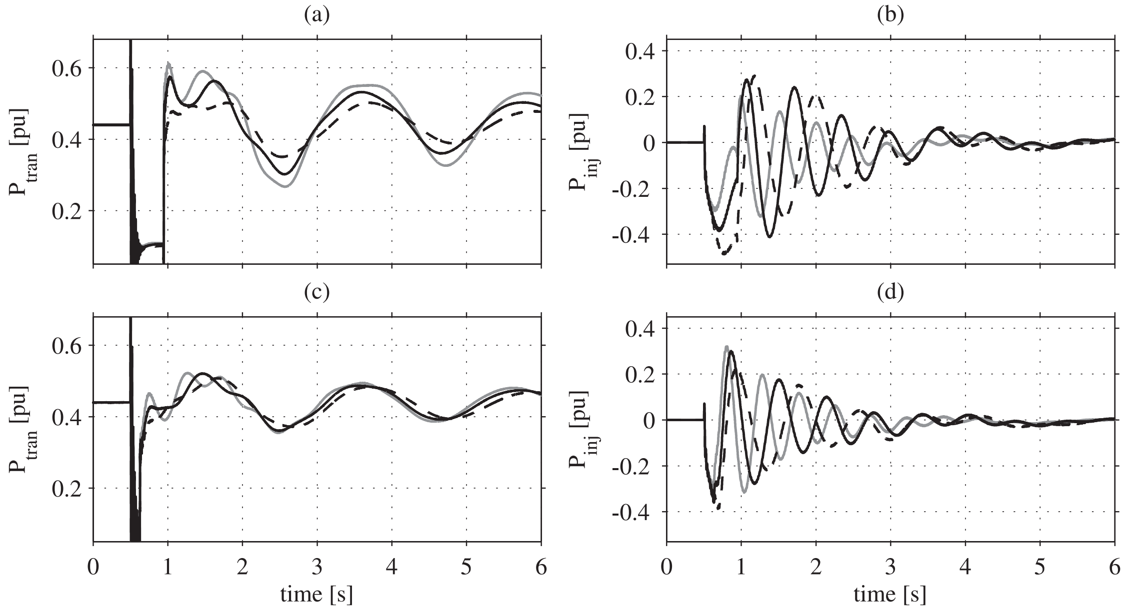

Fig. 7.12 Impact of virtual machine with various inertia constant and 10% damping ratio to system stability following various faults; (a) transmitted power for a fault clearing time of 440 ms; (b) injected active power for a fault clearing time of 440 ms; (c) transmitted power for a fault clearing time of 120 ms; (d) injected active power for a fault clearing time of 120 ms; The inertia constants for the different cases are $H_{\mathrm{v}} = 1.97$ s (gray curves), $H_{\mathrm{v}} = 3.94$ s (black solid curves) and $H_{\mathrm{v}} = 7.88$ s (black dashed curves).

Even if the performance of the virtual machine controller depends on the investigated case, a final test is performed to quantify the level of stability enhancement provided to the power system. For this purpose, a virtual inertia of $H_{\mathrm{v}} = 1.27$ (representing 5% of the total system inertia) with a 10% damping ratio has been implemented in the active power controller. The reactive current limit is set to 0.5 pu and is used to control the PCC voltage to 1 pu. The active current limit is set to 0.1 pu. For this test, the system will have a critical fault clearing time of 716 ms and the response of the controller is shown in Fig. 7.13. For comparison, the classical cascade controller is implemented with the same current limits and the response of the controller for the critical fault clearing time of 653 ms is shown in Fig. 7.14.

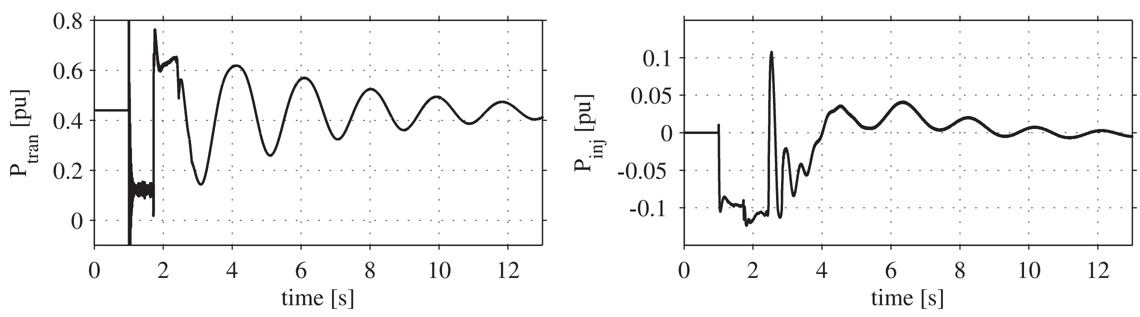

Fig. 7.13 Impact of virtual machine controller to system stability following a 716 ms three-phase fault; Left: transmitted power and Right: injected active power.

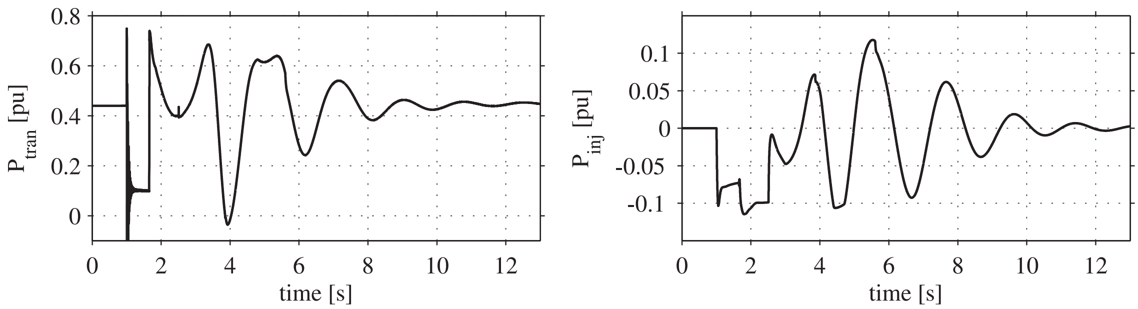

Fig. 7.14 Impact of classical cascade controller to system stability following a 653 ms three-phase fault; Left: transmitted power and Right: injected active power.

As the results show, the critical fault clearing time of 420 ms for the uncompensated system has been significantly increased using the two control approaches. The increase in the fault clearing time of the system due to the active power exchange is about 170 ms and 110 ms for the virtual machine controller and classical cascade controller, respectively. A better transient stability enhancement is achieved with the virtual machine controller due to the added inertia and the correct direction of the active power exchange from the E-STATCOM at bus 7. Moreover, no local or remote control signals are used to control the virtual machine controller and this is advantageous when compared to the classical cascade approach.

Using the control method described in Section 6.6, it is found that the classical cascade controller results in a similar stability enhancement when the compensator is connected at bus 9 in Fig. 7.1. On the other hand, the use of virtual machine controller with zero reference active power at bus 9 does not improve the stability of the system. This is due to the fact that the direction of active power exchange is decided by the dynamics of the virtual machine controller and at this location does not help in increasing the system stability. In this case, the reference active power should be modulated based on local or remote measurements similar to the classical cascade controller and the use of smaller inertia is more advantageous for faster response.

7.2.2 Three-area test system

In the previous section, a two-area test system has been considered to verify the POD and TSE control by E-STATCOM, where a single major oscillation component exists. To test the performance of the damping control algorithm for multiple oscillation modes using single and multiple compensators, time-domain simulations are performed using the three-area test system in Fig. 6.11.

To initiate the multimode oscillations, a three-phase short-circuit fault is applied for 80 ms in the transmission system between Generator 1 and Generator 2 close to Bus B_4 in the test system in Fig. 6.11. The output power of the generators when the compensators are in idle mode is shown in Fig. 7.15 for reference.

The output powers contain two oscillation modes, a 1 Hz (mode 1) and a 1.7 Hz (mode 2) oscillation, similar to the analysis in Section 6.5.2. The performance of the RLS estimator described in Section 6.5.1 for extracting these modes from measured power at the location of compensator

2 P_{t2}) is shown in Fig. 7.16 as an example.

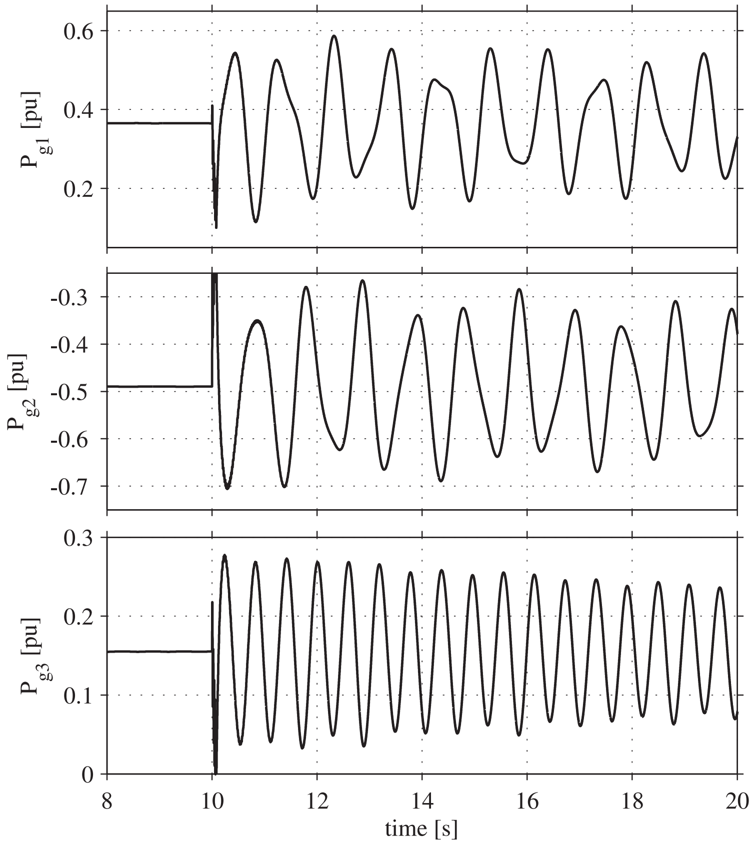

Fig. 7.15 Power output of generators following a three-phase fault with both compensators are in idle mode (i.e. the reference case).

First, the performance of the two compensators to control both oscillation modes is shown in Fig. 7.17. It can be observed that effective damping can be achieved by using both compensators at the same time. However, it can also be noted that Compensator 1 has small controllability on mode 2 oscillation (see the output power of Generator 3 in the figure). Hence, by choosing each compensator to provide damping to the mode, where its controllability is high, a more effective POD can be achieved. For this reason, another test is performed, where Compensator 1 and 2 are used to control mode 1 and mode 2 oscillations, respectively. The result on independent damping of each mode is shown in Figs. 7.18 and 7.19. Figure 7.18 shows that damping of mode 1 is achieved without affecting mode 2 and damping of mode 2 is achieved without affecting mode 1. This is possible by injecting active and reactive power only at the mode frequency to be controlled as shown in Fig. 7.19.

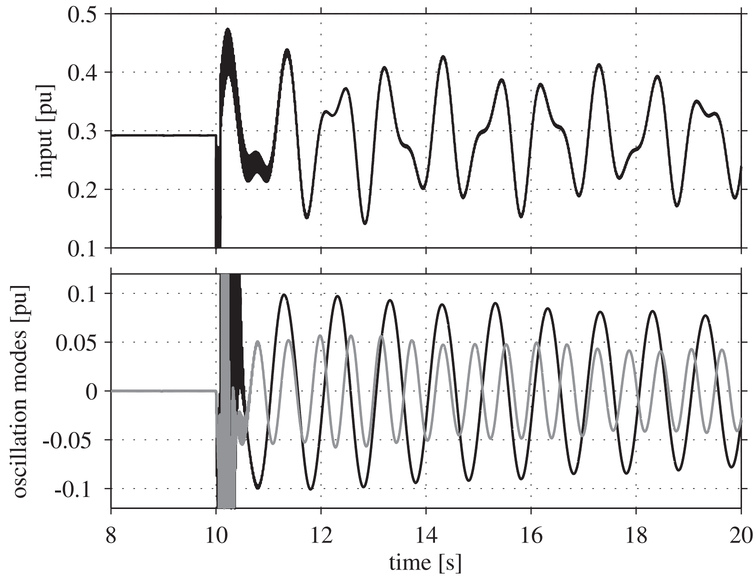

Fig. 7.16 RLS estimator performance to extract oscillation modes from measured power P_{t2}; top: input signal and bottom: oscillation mode 1 (black) and oscillation mode 2 (gray).

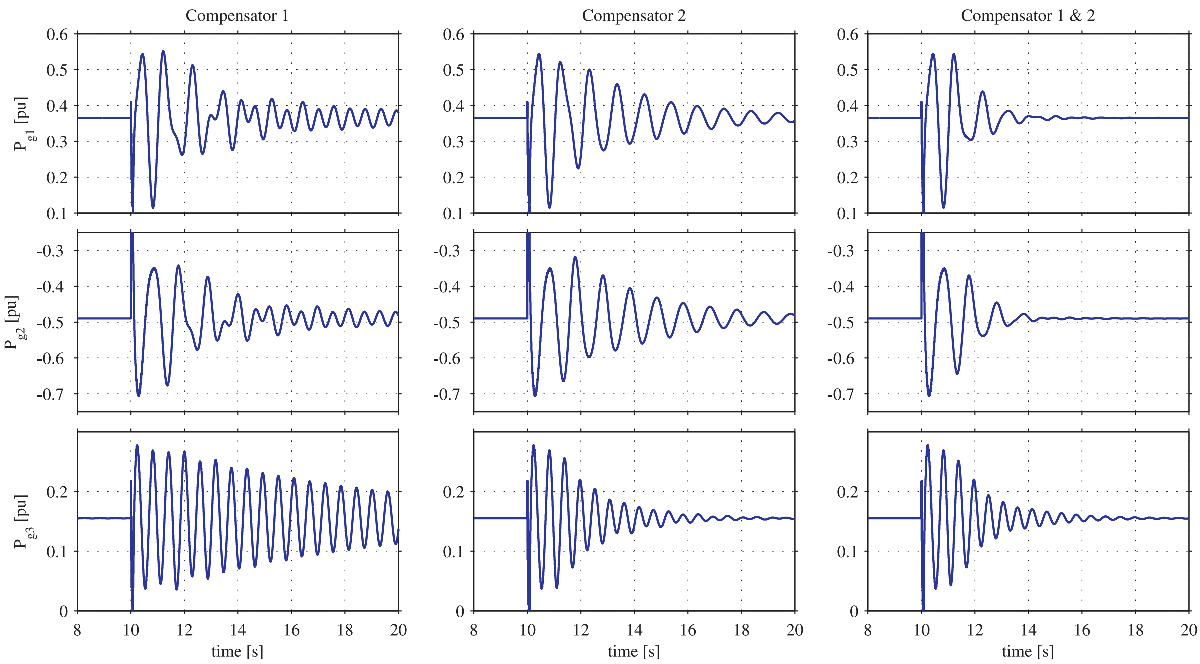

Fig. 7.17 Power output of generators following a three-phase fault with single and multiple compensators for POD.

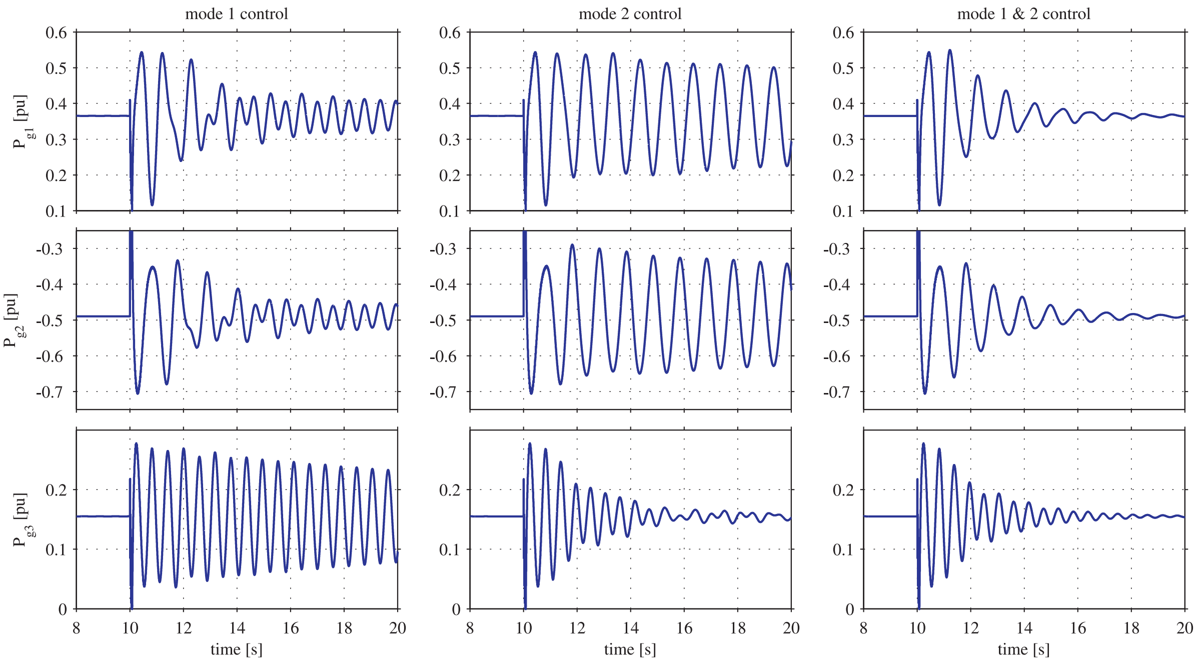

Fig. 7.18 Power output of generators following a three-phase fault with independent control of each mode.

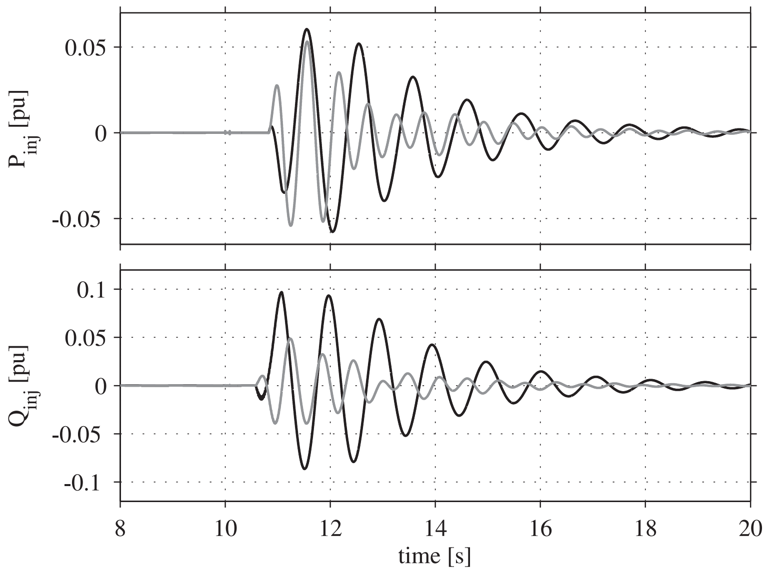

Fig. 7.19 Injection of active power (top) and reactive power (bottom) from compensator 1 (black) and compensator 2 (gray); Both compensators are used for POD.

In the results in Figs. 7.17 - 7.19, the tests have been performed assuming that the oscillation frequencies of the system are well known. A similar test is performed here considering that the system parameters are not well known. To realize this, the mode frequencies of the system are assumed to be 0.5 Hz and 1.5 Hz in the controller, while the actual values are 1 Hz and 1.7 Hz, respectively. Using both compensators for POD, the performance of the control method with and without the frequency adaptation mechanism is shown in Fig. 7.20. The estimate of the mode frequencies is shown in Fig. 7.21 when the frequency adaptation mechanism is activated. Unlike the conventional approaches, whose performance deteriorates during system parameter changes (gray plots in Fig. 7.20), the proposed method works well irrespective of inaccurate knowledge of system parameters (black plots in Fig. 7.20).

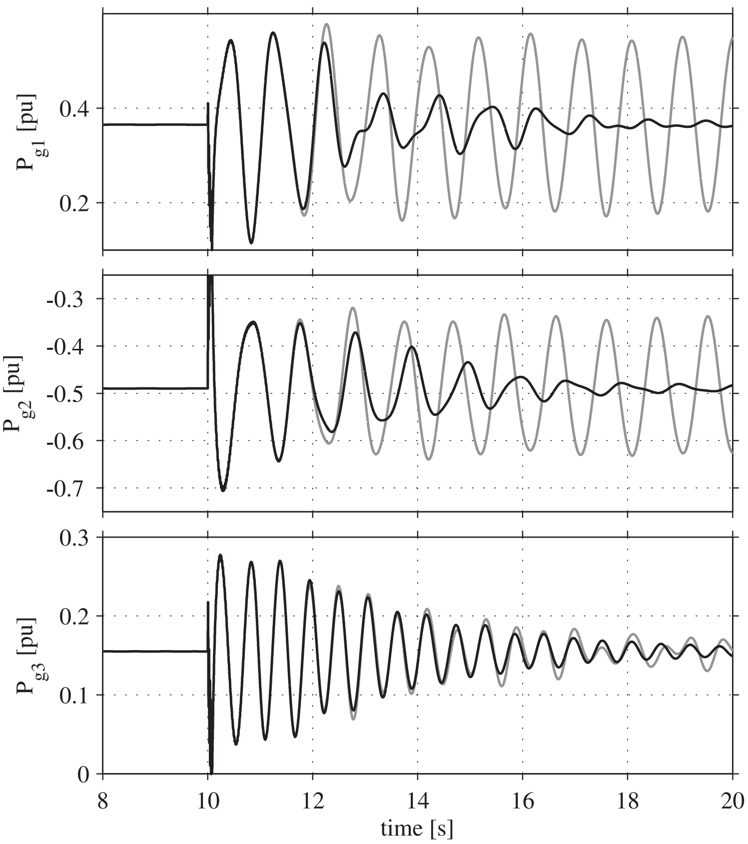

Fig. 7.20 Power output of generators following a three-phase fault; Controller with no frequency adaptation (gray) and with frequency adaptation (black).

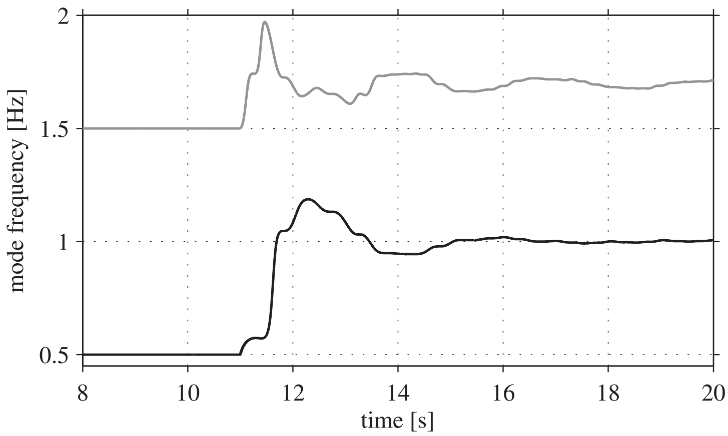

Fig. 7.21 Adaptation of the oscillation mode frequency; Mode 1 frequency (black) and mode 2 frequency (gray).

7.2.3 Large test system

The tests performed so far have been carried out on a simplified power system, in order to demonstrate the working principles of the various control strategies. A final simulation is made using the New England Test System [29], which consists of 10 machines and 39 buses as in Fig. 7.22. The parameters and loading of the transmission system are given in Appendix B.3.

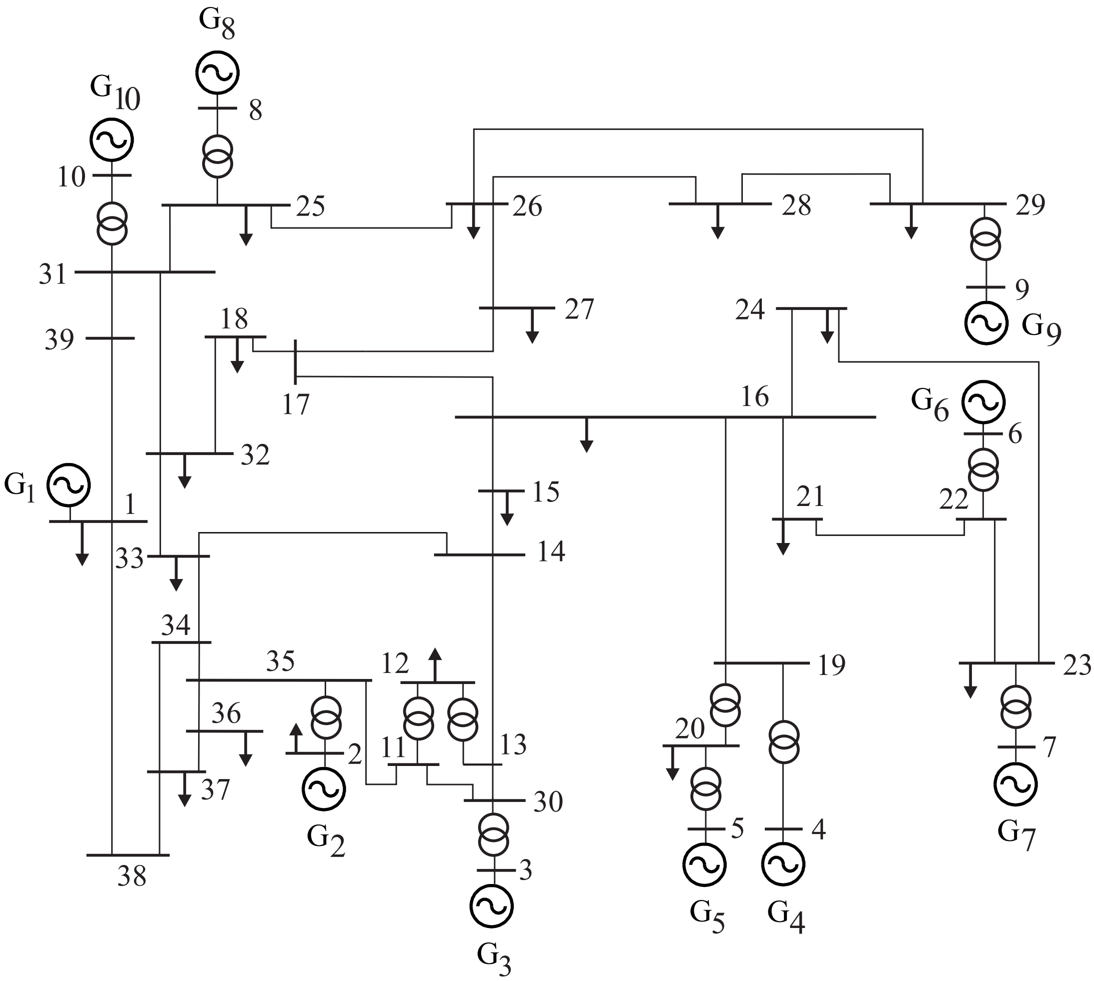

Fig. 7.22 A simplified 10 generator and 39 bus system for case study.

A three-phase short circuit fault is applied for 33 ms in the line between Bus 23 and Bus 24 close to Bus 23 to initiate the power oscillations. Even if the system is comprised of 10 generators, only two main oscillation modes (0.37 Hz and 0.73 Hz) are excited by the considered disturbance, with the critical mode (the most undamped component) being the lower frequency component. This is shown in the FFT plot of the speed of the generators (ω_{gi} with $i = 1, ..., 10$) in Fig. 7.23.

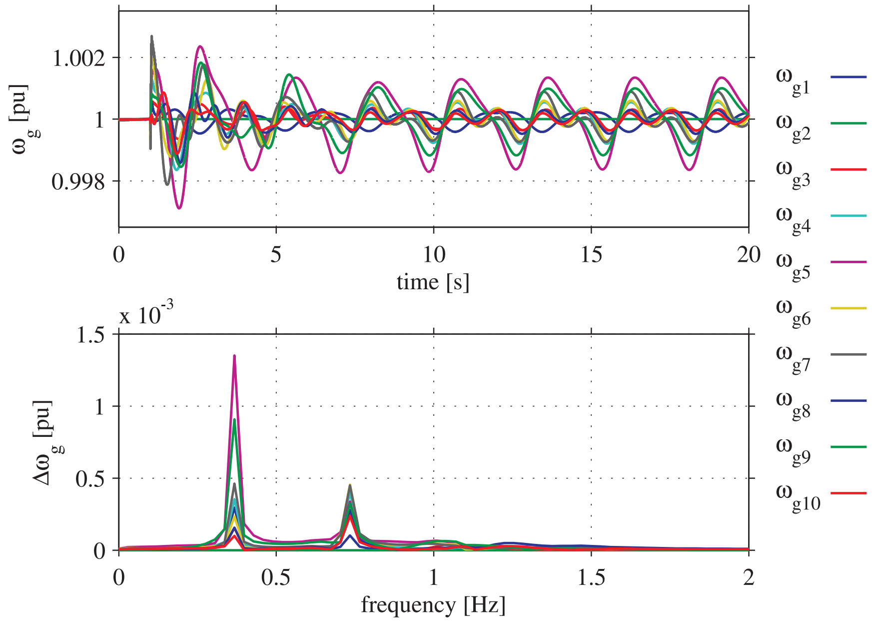

Fig. 7.23 Speed of generators (top) and FFT of speed deviation (bottom) following a three-phase fault with compensators in idle mode.

It is found that active power injection has high controllability on the 0.37 Hz oscillation mode at Bus 23, whereas reactive power injection has high controllability on the oscillation mode at Bus 28. For this reason, Compensators 1 and 2 are connected at Bus 23 and Bus 28, respectively. The performance of the POD controller to damp this critical 0.37 Hz oscillation mode is shown in Fig. 7.24. Similar to the results obtained for the simplified system in the previous sections, effective damping of the critical oscillation mode is achieved with injection of power at the critical mode frequency, as shown in Fig. 7.25, while using single or multiple compensators.

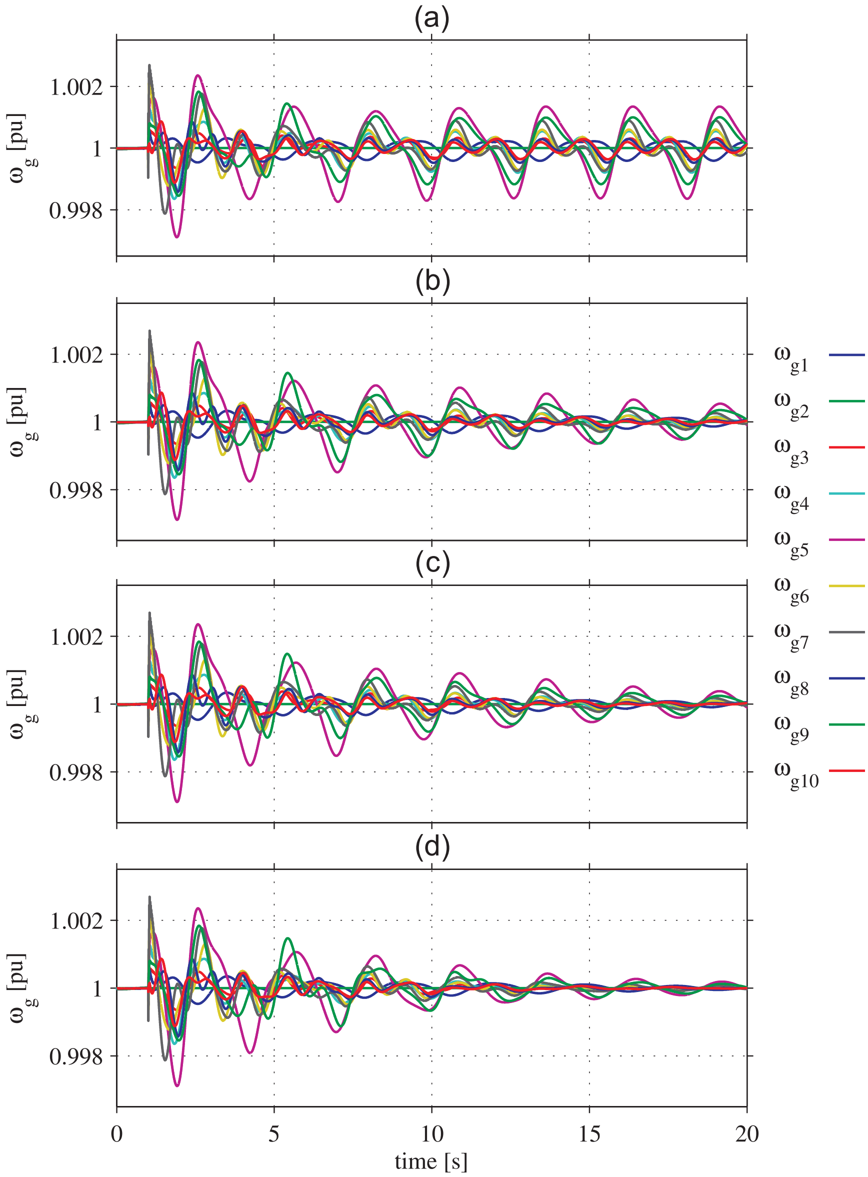

Fig. 7.24 Speed of generators following a three-phase fault; (a) both compensators are idle, (b) only compensator 1 is active, (c) only compensator 2 is active and (d) both compensators are active.

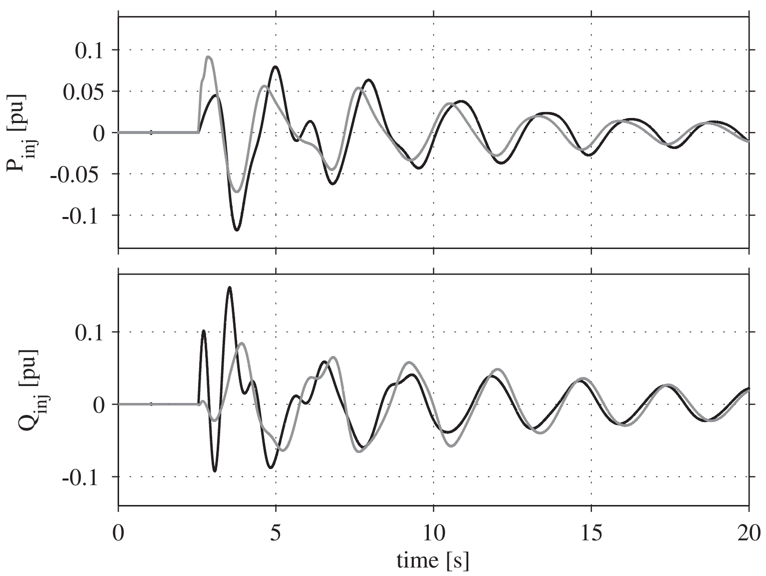

Fig. 7.25 Injection of active power (top) and reactive power (bottom) from compensator 1 (black) and compensator 2 (gray) when each compensator is used separately.

The results in Fig. 7.24 are obtained using a prior knowledge of the dominant oscillation mode frequency. A final test is again performed to evaluate the robustness of the control algorithm during system parameter uncertainties. For this, the critical oscillation mode frequency is assumed to be 0.6 Hz while the actual value is 0.37 Hz. The performance of the control algorithm with and without the frequency adaptation mechanism is shown in Fig. 7.26 with both compensators active. When the frequency adaptation mechanism is active, the update of the critical oscillation mode frequency at the two compensator's location is shown in Fig. 7.27. From the results, it can be concluded that the proposed method is again robust against system parameter changes in a realistic large power system.

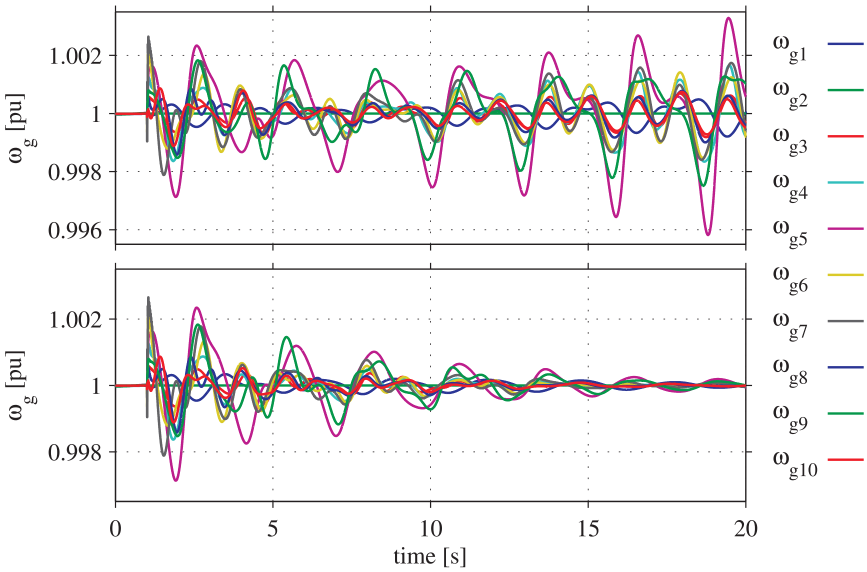

Fig. 7.26 Speed of generators with both compensators active during system change; Controller without mode frequency adaptation (top) and with mode frequency adaptation (bottom).

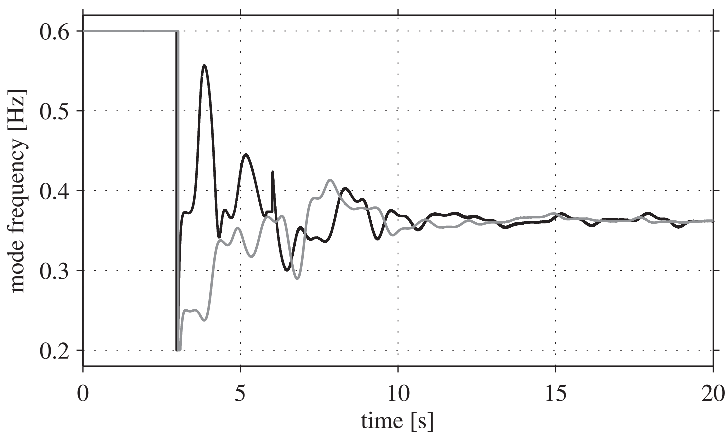

Fig. 7.27 Critical oscillation mode frequency update at compensator 1 location (black) and compensator 2 location (gray).

In the simulations performed so far for the system in Fig. 7.22, the three-phase fault applied results in an oscillation without causing system instability through loss of synchronism. The critical fault clearing time of the system is found to be 92 ms. To see which machines lose synchronism from the system, a similar three-phase fault is applied at 0.5 second and the fault is cleared after 93 ms. The plot of the generator's speed and angle deviation is shown in Fig. 7.28. It is shown in the figure that for the simulated case Generator 5 loses synchronism from the rest of the system. This means that any transient stability enhancement from the compensators should be prioritized at affecting the power output of this machine following the fault. For the system under investigation, the effective location of the compensator should be close to the generator that losses synchronism (Generator 5 in this case). Therefore, Bus 20 has been selected to test the impact of the compensator to improve transient stability of the system.

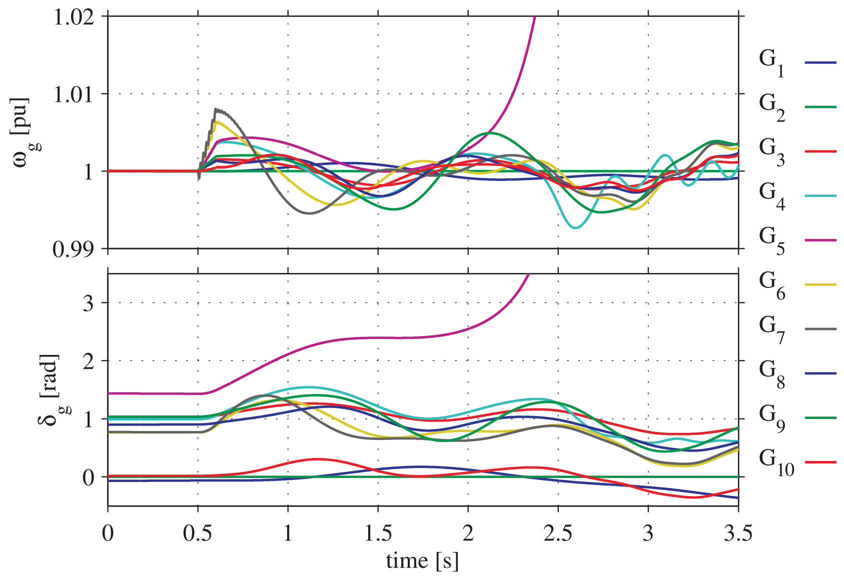

Fig. 7.28 Speed (top) and angle deviation (bottom) of generators following a 93 ms three-phase fault with the compensators in idle mode.

With the loading of Generator 5 as given in Table B.1, the inertia constant of Generator 5 is deliberately reduced by 6 s (i.e. from 26 s to 20 s). This simulates the case where a large power plant has been partially replaced by inertia-less generation, such as a wind power plant with full power converter turbines. The reduced inertia leads to a critical fault clearing time of 85 ms. Two control methods for the compensator connected at Bus 20 will be tested here to increase the critical fault clearing time of the ”new system” back to 92 ms.

The first simulation is to implement the TSE control as described in Section 6.6 for the large system. Due to the selected location of the compensator, the speed of Generator 5 can be used to control the injection of power for the first swing. Note that in this example, the maximum injection of active and reactive power is calculated to increase the critical fault clearing time of the system due to a loss of 6 s inertia from Generator 5. Figure 7.29 shows the swing of Generator 5 and injected powers for a fault applied to the new system for 92 ms. As the result shows, the stability of the system is guaranteed for the applied fault.

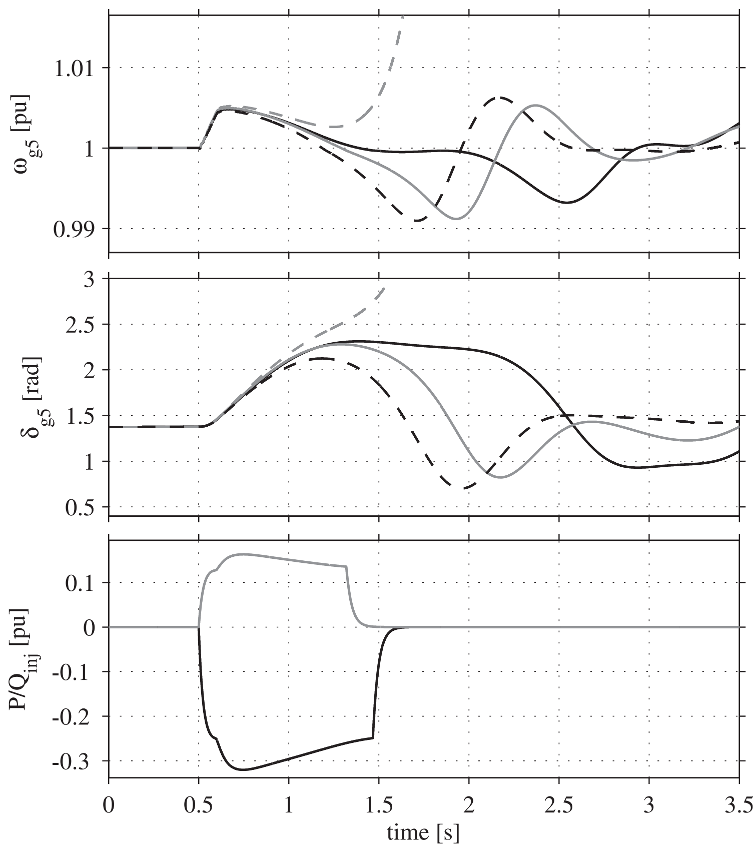

Fig. 7.29 Impact of TSE control of compensator connected at bus B_{14}; speed of Generator 5 (top), angle deviation of Generator 5 (middle) and injected active and reactive power (bottom); No TSE (gray dashed), TSE by active power injection only (black solid), TSE by reactive power injection only (gray solid) and TSE by active and reactive power injection (black dashed).

The second simulation is to implement a virtual machine control of the compensator as described in Section 5.4. The virtual inertia constant for the control is chosen as $H_{\mathrm{v}} = 6$ s to replace the reduced inertia of Generator 5 and the damping constant is chosen as $K_{\mathrm{Dv}} = 133$ to provide a damping ratio of 40% for the local oscillation mode of the controller. The integral constant for the reactive power control part is chosen as $K_{\mathrm{Qc}} = 50$. As described in Section 5.4, the reference active and reactive powers should be modulated based on power system disturbance to aid in TSE to the power system. For this simulation, the reference active power is set to zero so that the virtual machine controller works without any need of external control input signal. On the other hand, the reactive power reference is set according to the TSE control algorithm described in Section 6.6 as in the previous simulation and using the expression in (6.44). Figure 7.30 shows the swing of Generator 5 and injected powers. As the result shows, the stability of the system is guaranteed for the applied fault when a virtual inertia controller is implemented to the compensator.

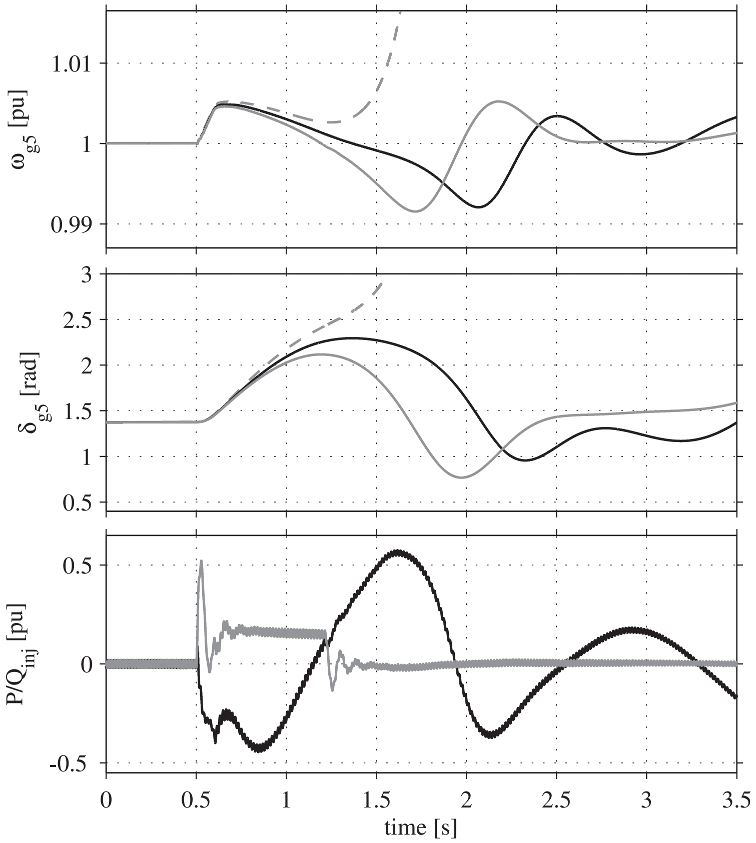

Fig. 7.30 Impact of virtual machine control of compensator connected at bus B_{14}; speed of Generator 5 (top), angle deviation of Generator 5 (middle) and injected active and reactive power (bottom); No virtual machine (gray dashed), virtual machine without reactive power injection (black solid) and virtual machine with reactive power injection (gray solid).

In the results in Figs. 7.29 and 7.30, it is shown that the transient stability of the large power system can be improved. However, the effectiveness of the compensator to provide TSE depends on the rating, the location and the control strategy of the compensator. As described in (6.42) and (6.43), the most difficult task in a large system to provide TSE function is to estimate the required control input signal for injection of active or reactive power. If the virtual machine controller for the active power part with zero active power reference is used for the compensator, no control input signal is necessary and this is advantageous. However, this control is used to add inertia to the system and the overall impact on the system stability depends on the location of the compensator and the added virtual inertia. Although it is not possible to generalize for all cases, a mere presence of the virtual inertia in the simulation in Fig. 7.30 (black curves) helps to improve the stability of the system.

7.3 Experimental Verification

To validate the results obtained via simulation for power system stability enhancement by E-STATCOM, experimental tests have been performed. In this section, a description of the setup together with the experimental results will be presented for the various control strategies described in the previous sections.

7.3.1 Laboratory setup

The schematic of the laboratory setup is shown in Fig. 7.31. The system consists of a 75 kVA, 400 V synchronous generator connected to a stiff AC grid through a transmission line model. A Voltage Source Converter (VSC) system can be connected at various locations in the transmission line.

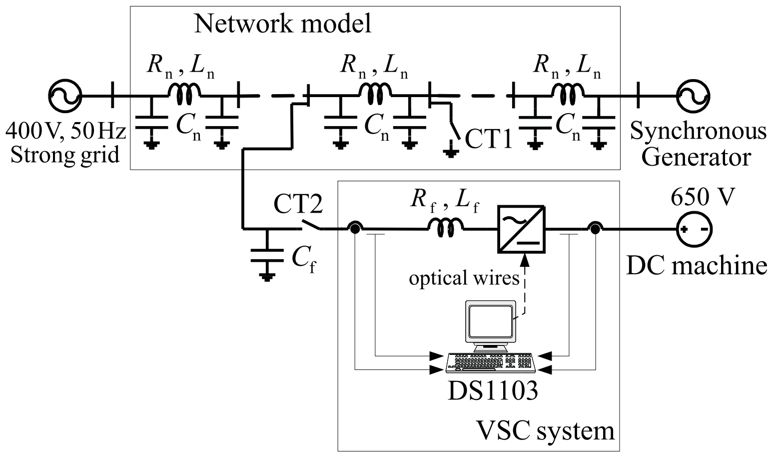

Fig. 7.31 Single-line diagram of the laboratory setup.

The description of the laboratory setup is given below.

1) VSC system: The VSC system consists of a two-level converter connected to the transmission line model through a series reactor with $L_f = 2$ mH, $R_f = 6.2$ mΩ and shunt capacitor with $C_f = 60$ μF. The VSC is controlled from a computer with a dSpace 1103 board. The DC-link of the VSC is connected to a DC machine rated 700 V, 60 A. The DC machine is equipped with field control and the terminal DC voltage is controlled to 650 V for all the experiments. The DC machine acts as the energy source providing active power injection capability to the VSC.

2) Network model: The network model is a down-scaled version of an actual Swedish 400 kV transmission system with the model rated at 400 V, 50 Hz. The transmission line model consists of six identical Π sections (with parameters L_n = 2.05 mH, R_n = 0.05 Ω and C_n = 46 μF), each corresponding to a portion of 150 km of the actual line [49]. As shown in Fig. 7.31, faults can be applied to the transmission system using the contactor (CT1).

3) Synchronous generator: The parameters of the synchronous generator are given in Table 7.1. The synchronous generator is driven by an 85 kW DC motor. The DC motor is fed from a thyristor converter and can be controlled by either speed or armature current, corresponding to frequency or active power control of the generator. A flywheel mounted on the shaft between the DC motor and the generator gives the model a similar mechanical time constant as the real power plant. The generator is equipped with a modern microprocessor-based voltage regulator that can control the generator terminal voltage, field current, reactive power or power factor. To enhance angular stability, a power system stabilizer (PSS) is also included in the voltage controller [49]. The PSS together with the speed controller from the DC motor gives the generator system a well damped system following faults during transient stability studies. For the purpose of these experiments, the speed controller of the DC motor is detuned and the PSS is disabled. This results in a poorly damped low-frequency electromechanical oscillation following short-circuit faults. For all the test performed, the ratings of the synchronous generator (75 kVA, 400 V) are used as base values.

TABLE 7.1. PARAMETERS OF THE SYNCHRONOUS GENERATOR

Rated power	75 kVA
Rated voltage	400 V
Synchronous reactance, X_d	2.93 Ω
Unsaturated transient reactance, X'_d	0.437 Ω
Unsaturated sub-transient reactance, X''_d	0.332 Ω
Armature resistance, R_s	0.081 Ω
Inertia constant (generator-turbine set), H_g	5.56 s

7.3.2 POD and TSE using classical cascade control of E-STATCOM

As described in Section 5.3.3, the outputs of the POD controller are active and reactive current references to be injected into the grid by the E-STATCOM. The outer control loops that have been investigated earlier in this chapter together with the current controller described in Section 5.3.1 are included in the control of the E-STATCOM. To verify the POD controller performance, the setup in Fig. 7.31, which represents a single-machine infinite-bus system with the E-STATCOM, is used. The single-line diagram of the setup is shown in Fig. 7.32, where the possible connection buses of the E-STATCOM are marked as 1 and 2. For the tests, the gain K_Q is chosen to get a damping ratio of 10% at bus 2 when reactive power is used for POD. For a fair comparison, the gain K_P is then adjusted to get a similar order of maximum active and reactive power injection for the tests. Once the values for the gains are selected, they are kept constant for all the experiments.

First, the power oscillation damping controller is tested for the two connection points of the E-STATCOM in Fig. 7.32. For this test, knowledge of the oscillatory frequency in the transmitted active power has been considered. To start the power oscillation, a three-phase fault is applied at bus 1 and the fault is cleared after 250 ms. The performance of the E-STATCOM for POD using the control strategy described in Section 6.3 is shown in Figs. 7.33 and 7.34. Observe that to facilitate the comparison, the presented measured signals have been filtered to remove noise and high-frequency harmonic components.

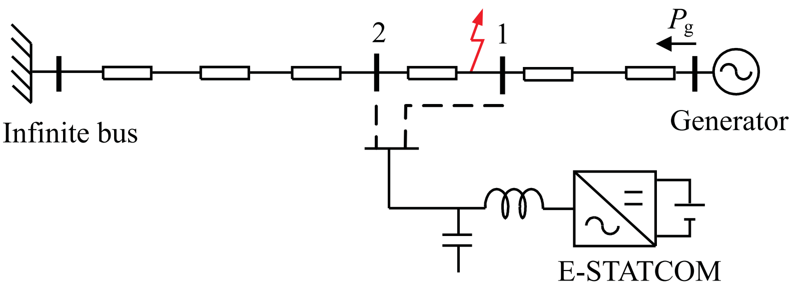

Fig. 7.32 Single line diagram of the laboratory setup for POD.

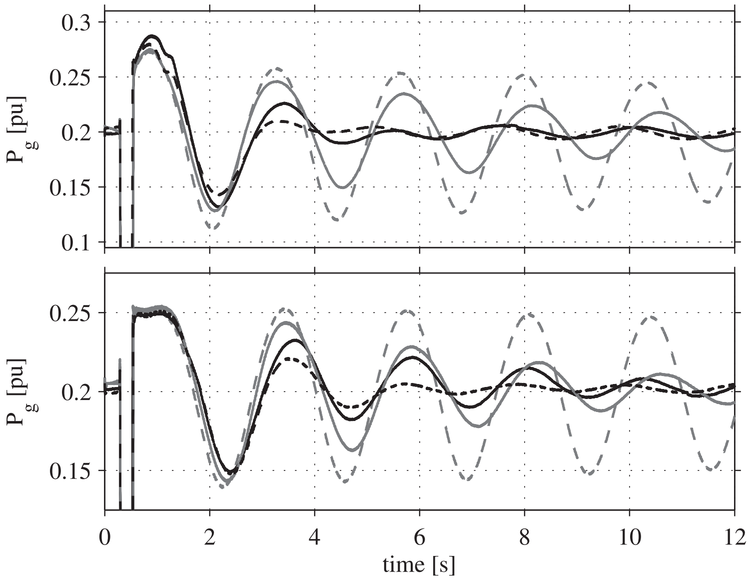

Fig. 7.33 Measured generator active power output following a three-phase fault with E-STATCOM connected at bus 1 (top) and bus 2 (bottom). POD by P_{inj} only (black solid), Q_{inj} only (gray solid), both P_{inj}, Q_{inj} (black dashed) and no POD (gray dashed).

As described in the small-signal analysis in Section 6.3.3, the injected active power decreases with the distance from the generator, where its impact to provide damping decreases (see Fig. 7.34). A better damping with active power injection is obtained when the E-STATCOM is closer to the generator, in this case at bus 1 (Fig. 7.33). With respect to reactive power injection, the damping provided by the compensator increases when moving closer to the electrical midpoint. As the transmitted power P_g is used to control the reactive power injected by the compensator, the same amount of injected reactive power is used at the two locations and a better damping action is achieved close to the electrical midpoint of the line, in this case at bus 2. With a proper choice of the control signals for injection of active and reactive power, effective power oscillation damping is provided by the E-STATCOM at both connection points of the compensator as shown in Fig. 7.33 (black dashed curves).

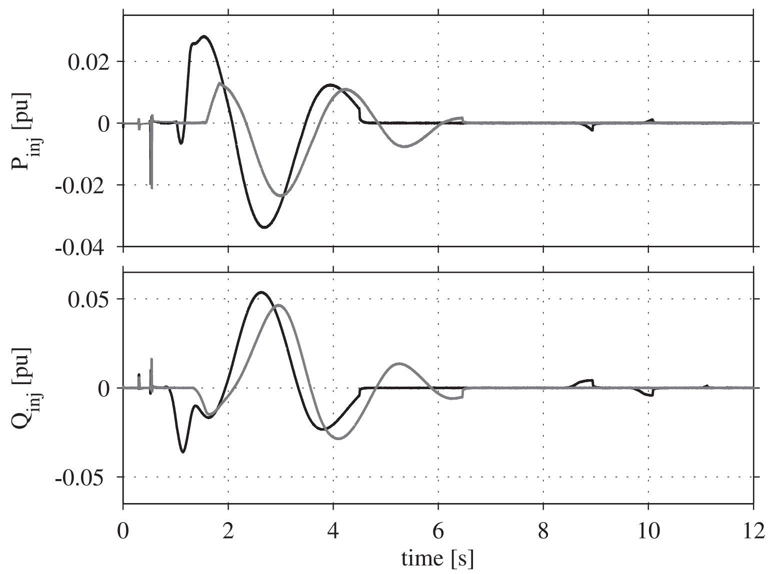

Fig. 7.34 Injected active and reactive power with E-STATCOM connected at bus 1 (black) and bus 2 (gray). Active power injection (top) and reactive power injection (bottom); both P_{inj} and Q_{inj} used for POD.

To test the dynamic performance of the investigated POD controller in case of system parameter changes, a second set of experiments has been carried out assuming an oscillation frequency of 0.9 Hz, where the actual measured oscillation frequency is 0.42 Hz. This means that an error of 100% in the estimated oscillation frequency is here considered. Figure 7.35 compares the performance of the POD controller with and without the oscillation frequency adaptation in the RLS estimator. In both cases, the E-STATCOM is connected at bus 2 and injection of active and reactive power is used for POD. By using the frequency adaption as described in Section 4.3.2, the phase of the oscillatory component in the input signal is correctly estimated, thus providing an effective damping. This is advantageous when compared to the classical approaches, where the correct phase-shift is provided in the estimation only at a particular oscillation frequency. As shown in Fig. 7.35 (gray solid plots), if the POD controller is not adapted to changes in the system, its performance is significantly reduced. This is also shown in Fig. 7.36, where the total energy exchange (W_{total}) between the E-STATCOM and the grid until the oscillations are completely damped for the two cases is displayed. The case without frequency adaptation is characterized by a longer settling time of the oscillation and therfore a larger amount of total energy exchange. This results in an uneconomical use of the energy storage.

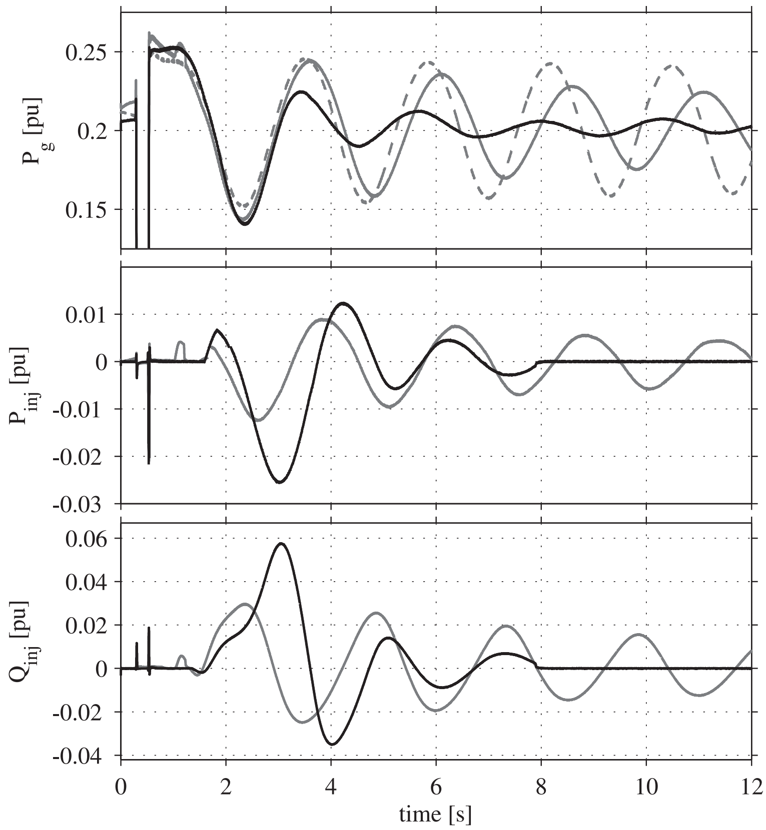

Fig. 7.35 Top: measured generator output power with frequency adaptation (black solid), without frequency adaptation (gray solid) and with no POD (gray dashed); Middle: Injected active power with frequency adaptation (black) and without frequency adaptation (gray); Bottom: Injected reactive power with frequency adaptation (black) and without frequency adaptation (gray).

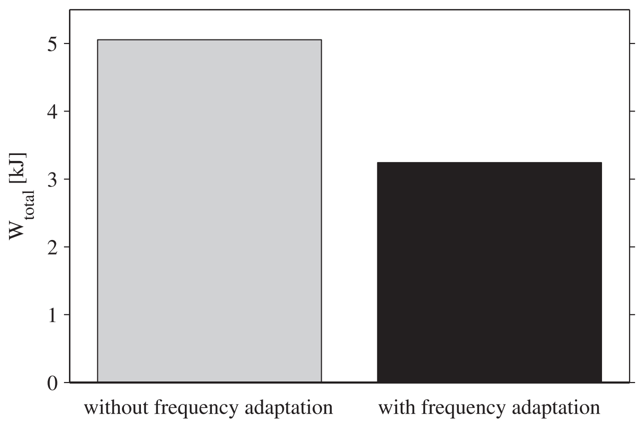

Fig. 7.36 Total energy exchange to damp oscillations with and without frequency adaptation.

In the experimental tests performed so far, the applied three-phase fault results in a sustained oscillation without any risk of transient instability. In case of larger disturbances, a TSE controller is needed to keep the generator from losing synchronism. The tendency of the generator to lose synchronism increases with the fault-clearing time and the amount of transmitted active power. It has been found that the critical fault clearing time of the uncompensated system in Fig. 7.32 is about to 550 ms. Thus, a larger fault clearing time of 600 ms is considered for a three-phase fault applied at bus 1 to test the effectiveness of the TSE controller described in Section 6.6. This fault causes the uncompensated system to lose synchronism, as indicated by a continuous increase of the estimated generator angle deviation in Fig. 7.37. The estimated generator angle ($\Delta\tilde{\delta}_{\mathrm{g}}$) and speed ($\Delta\tilde{\omega}_{\mathrm{g}}$) deviations following the disturbance are estimated using two PLLs, placed at the terminals of the generator and the infinite bus. By monitoring $\Delta\tilde{\omega}_{\mathrm{g}}$ as described in Section 6.6, the performance of the TSE controller is validated here.

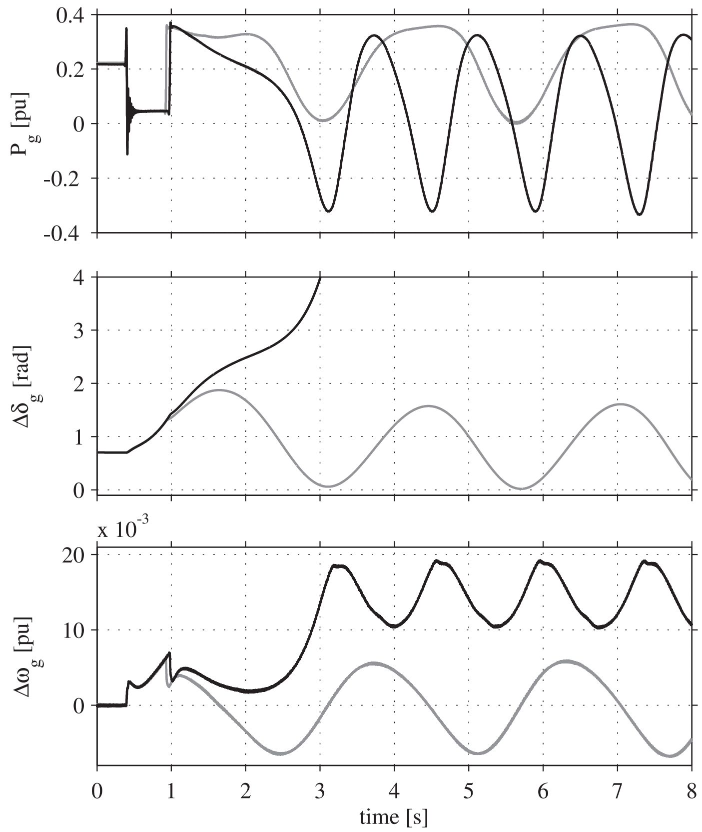

Fig. 7.37 Top: generator output power; Middle: estimate of generator angle deviation; Bottom: estimate of generator speed deviation; the E-STATCOM is in idle mode and the three-phase fault is applied for 550 ms (gray curves) and 600 ms (black curves).

For the 600 ms three-phase fault applied at bus 1 and the E-STATCOM connected at bus 2, Figure 7.38 shows the performance of the TSE and POD controllers. First, the TSE function without the POD controller is tested. As indicated in the figure in plots (a) and (b), the TSE controller guarantees the transient stability of the system. To damp the stable oscillation following the TSE action, the POD controller is also activated and the test is repeated. The results in plots (c) and (d) show that the sustained oscillations following the TSE operation are damped by the action of the POD controller. It can be seen in the results that the reactive power controller is limited even during the POD operation due to the high power swing of the generator power following the fault. As described in the previous chapter, the TSE function starts following the disturbance and will be applied during the first swing of the generator angle. By the end of the first swing, the control action switches to the POD operation. In this example case, it has been found that the critical fault clearing time of the system is increased at least by 50 ms when using a maximum active or reactive current injection of 0.16 pu, corresponding to 50% of the active current rating of the energy storage in this setup. When both active and reactive power injection is used, the fault clearing time can be increased in total by at least 100 ms.

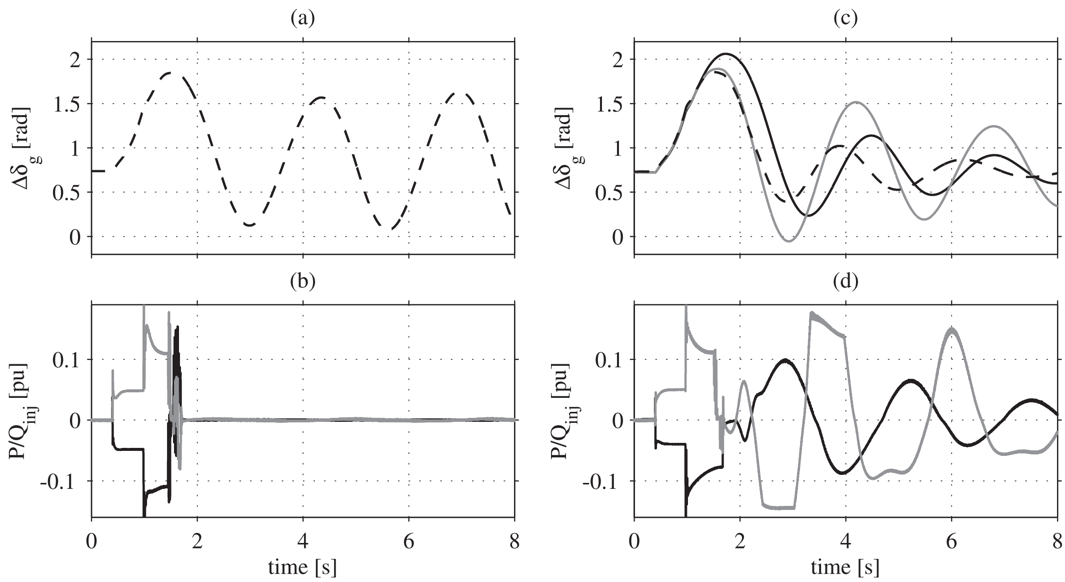

Fig. 7.38 TSE and POD performance with E-STATCOM connected at bus 2; (a) Generator angle deviation when active and reactive power are used for TSE only; (b) injected active power (black) and reactive power (gray) for TSE only; (c) Generator angle deviation during TSE and POD operation using only active power (black solid), only reactive power (gray) and both (black dashed); (d) injected active power (black) and reactive power (gray) for TSE and POD.

7.3.3 Impact of virtual machine control of E-STATCOM on stability

For the system in Fig. 7.32 and a compensator connected at bus 2, the TSE performance has been validated in Fig. 7.38 using the classical cascade controller for a fault clearing time of 600 ms. Considering the same power system and fault time, the impact of controlling the E-STATCOM as a virtual machine on the power system stability is investigated here. For this purpose, three different values of the virtual inertia (H_v) corresponding to 40, 50 and 60% of the generator inertia and two different values of the damping constant (K_Dv) have been selected for the active power controller. The reactive power controller is implemented using an intergral gain K_Qc of 18.5. The virtual machine is implemented to control the active and reactive power to zero during normal and fault conditions. Figure 7.39 shows the response of the system following the disturbance. For all the cases, the transient stability of the system is guaranteed and subsequent oscillations are successfully damped. The results show that the stability of the system tends to increase with an increase in the implemented virtual inertia. However, this leads to the active and reactive power exchange from the compensator to go into limitation for a longer time. In this case, the implemented machine behavior cannot be guaranteed and this might not improve the stability of the external system as much.

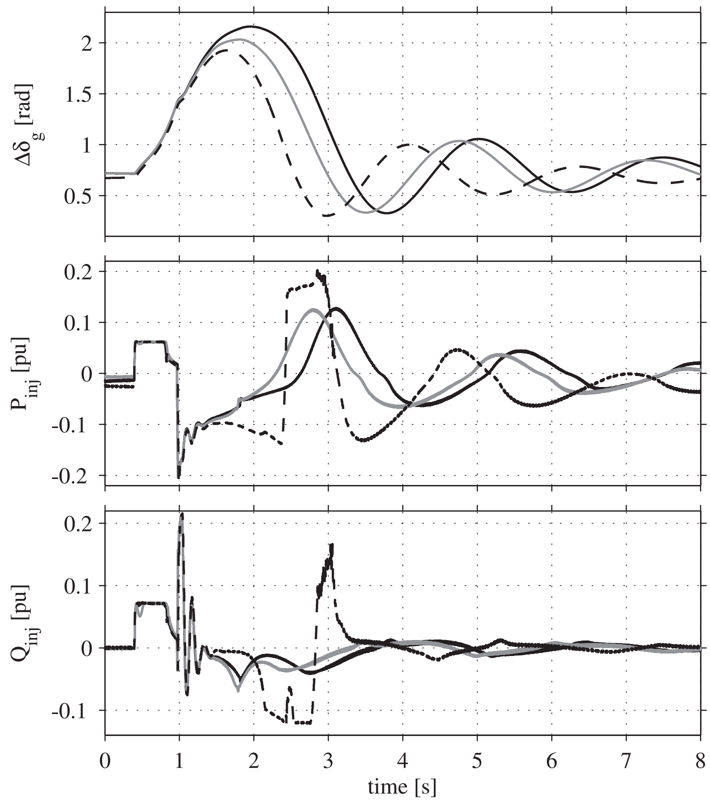

Fig. 7.39 Impact of virtual machine controller with $H_\mathrm{v} = 2.3$ s & $K_\mathrm{Dv} = 40$ (black solid), $H_\mathrm{v} = 2.8$ s & $K_\mathrm{Dv} = 40$ (gray solid) and $H_\mathrm{v} = 3.38$ s & $K_\mathrm{Dv} = 67.9$ (black dashed) on system stability; Top: estimate of generator angle deviation; middle: injected active power; Bottom: injected reactive power.

For the cases investigated, it is shown that both the classical cascade controller and the virtual machine controller increase the stability of the power system. In the first approach, it is shown that a continuous estimation of the state of the power system is necessary to implement the intended TSE function. In this case, as the estimation should be performed quickly and remote measurements are needed to be effective, this method presents a difficult challenge. However, with proper estimated control input signals, the classical cascade controller maximizes the use of active and reactive power injection to provide the intended TSE function. On the other hand, the virtual machine controller provides the stability enhancement function from its inherent behavior, without any need of external control signals. This is sometimes advantageous in cases where obtaining the required control signals for TSE is difficult, such as in a large power system. Moreover, if no control input signals are necessary, the controller acts immediately when a disturbance is sensed at the compensator location.

In the virtual machine controller, the stability enhancement comes from the added inertia from the compensator together with the power exchange to the external system. A disadvantage with this control method is that the implemented inertia will not be realized if a disturbance in the system leads to limitation of the power exchange. Moreover, as the power exchange to the external grid is dictated by the virtual machine control behavior instead of the external system response, the stability of the system might not be improved. To verify this, a final experiment is performed with the same setup as in the previous cases with a longer fault time of 650 ms and the result is shown in Fig. 7.40 when the two control approaches are used. The classical cascade controller guarantees the system stability for the longer fault. Even if the two control approaches enhance the system to a similar extent for a 600 ms fault as shown in the previous results, the virtual machine controller works in power limited mode for most of the time for the longer fault case and the intended stability enhancement is not achieved.

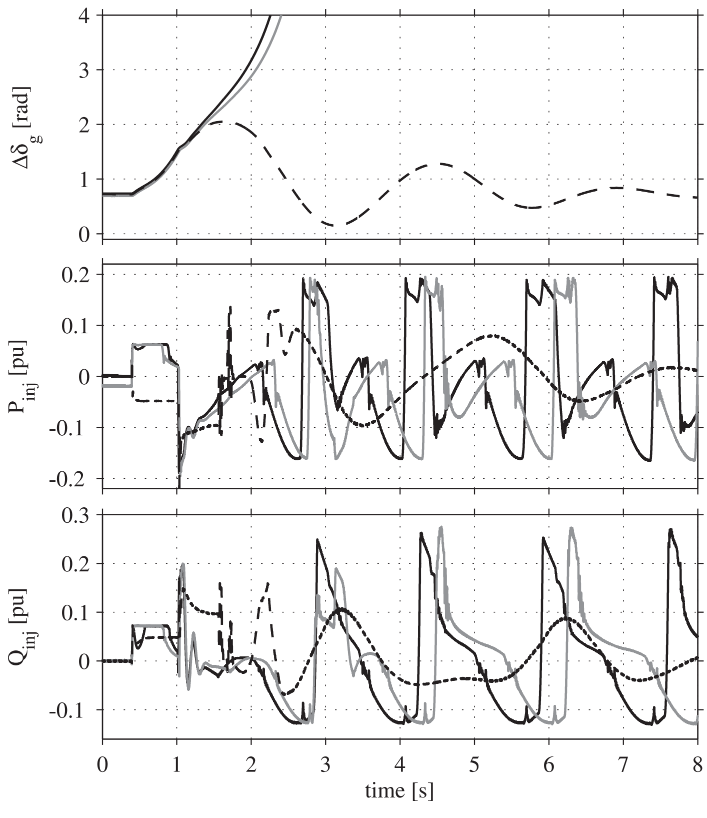

Fig. 7.40 Comparison of the classical cascade controller (black dashed) and virtual machine controller ($H_{\mathrm{v}} = 2.8$ s & $K_{\mathrm{Dv}} = 40$ (black solid) and $H_{\mathrm{v}} = 3.38$ s & $K_{\mathrm{Dv}} = 67.9$ (gray solid)) for a 650 ms fault; Top: estimate of generator angle deviation; Middle: injected active power; Bottom: injected reactive power.

7.4 Conclusions

In this chapter, the impact of the E-STATCOM on power system stability enhancement has been validated for various power system configurations through simulation and experiment. The robustness of the stability enhancement control algorithms against system parameter uncertainties has been investigated. It has been shown that injection of active power for POD is minimized at locations in the power system where its impact is negligible by using the frequency estimate output from the Phase Locked Loop (PLL) together with the proposed POD controller. The use of the proposed control method for damping multiple oscillation modes independently and the use of multiple compensators without negative interaction among themselves has been verified. To increase the transient stability of the power system, the use of the classical cascade controller and the virtual machine controller have been compared. It has been shown that by using both active and reactive power injection for POD and TSE with the proposed control strategies, stability enhancement can be achieved at different connection points of the E-STATCOM in the transmission system.

Chapter 8

Conclusions and future work

8.1 Conclusions

This thesis has dealt with the application of shunt-connected power electronic devices with optional active power injection capability for power system stability enhancement. In particular, the focus of the thesis has been on developing POD and TSE controllers that enable an efficient use of the available active and reactive power from the Power Electronic Devices.

To develop the control algorithm for POD, a novel signal estimation technique based on a Recursive Least Square (RLS) algorithm has been developed in Chapter 4. In this method, the conventional RLS approach has been improved to obtain a fast speed of response together with a good steady-state selectivity by the use of a variable forgetting factor. Furthermore, a method to be able to cope with inaccurate knowledge of the oscillatory frequency, which makes the estimation algorithm frequency adaptive, has been derived. Advantages of the proposed RLS estimation method over the conventional signal estimation techniques have been highlighted. The resulting RLS algorithm (here named improved RLS) gives a fast and selective estimation of low-frequency electromechanical oscillations in the measured signals. Moreover, the improved RLS method has been expanded for a generic signal estimation and its application for estimation of sequence and harmonic components in case of non-ideal conditions of the grid has also been verified through simulation and experimental tests.

To represent shunt-connected power electronics devices with optional active power injection capability, an E-STATCOM has been considered in this work. The overall control strategy for the device has been presented in Chapter 5. In this chapter, two control approaches have been described and their performances have been compared. First, a classical cascade controller based on vector control has been derived. The implemented controller consists of an inner vector-current controller and a number of outer control loops. For this case, the conventional vector current controller has been modified using the estimation technique described in Chapter 4 to counteract the impact of the grid-voltage harmonics on the injected currents in the case of connection to distorted grids. Next, an alternative approach to control the E-STATCOM to behave like a synchronous machine has been implemented. The performance of both control methods has been verified and compared through simulation and experimental tests.

A detailed description of the outer control loops of the E-STATCOM for power system stability enhancement has been developed using a simplified two-machine power system model in Chapter 6. First, the POD controller for active and reactive power injection has been derived using the signal estimation technique described in Chapter 4. It has been shown that injection of active power for POD is minimized at locations in the power system where its impact is negligible by using the frequency estimate of the Phase Locked Loop (PLL) in the controller. This leads to an effective use of the energy storage of the compensator. For example, it has been shown in Section 7.3.2 that by using the proposed control structure, a reduction of 40% in the size of the energy storage can be achieved for the specific case investigated. Moreover, the impact of load characteristics on the performance of POD controllers by shunt-connected FACTS devices has also been investigated. It has been found that the influence of loads is significant when reactive power injection is used and the location of the load is electrically close to the compensator. Secondly, it has been shown that control design dedicated to one oscillation mode could lead to system destabilization through interaction of the oscillation modes during system parameter changes. To avoid this problem, an independent multimode POD controller has been developed using the improved RLS algorithm. The estimator gives a selective and adaptive estimation of the various oscillation modes and the controller can provide damping at a particular mode of interest without influencing the damping of the other oscillation modes. The effectiveness of the proposed control method in presence of system parameter changes has been shown using both single and multiple shunt-connected power electronic devices for various power system configurations in Chapter 7. Moreover, it has been shown that the proposed damping controller helps to avoid any risk of interaction that could arise from multiple compensators, each designed independently to damp various oscillation modes. Finally, a control method for TSE from locally measured signals has been derived. To increase the transient stability of the power system, the use of the classical cascade controller and the virtual machine controller has been compared. It has been shown that by using both active and reactive power injection for POD and TSE with the control strategies as described, stability enhancement can be achieved at different connection points of the E-STATCOM in the transmission system. The performance of the various control methods has also been validated through simulation and experimental tests.

8.2 Future work

The main focus of the thesis has been on the development and analysis of an energy efficient control algorithm for POD and TSE using combined active and reactive power injection. The investigation carried out in this thesis has been made under the assumption of an ideal energy source connected to the DC-link of the voltage source converter. It can be of interest to expand the analysis by implementing the model of an actual energy storage (for example, batteries or capacitors, based on the required energy) and investigate the impact of its dynamics as well as the limited amount of available energy on the implemented control strategy. Moreover, the POD and TSE control methods can be adapted to actual power electronic devices with optional energy sources such as wind, solar and HVDC systems. Finally, it has been shown that in a large power system, the implementation of an effective TSE control requires knowledge of the system configuration and availability of remote signals following a disturbance. By using power system state estimation and signal processing techniques on various measurement signals, developing an effective and generalized TSE control algorithm could be an interesting task.

References

[1] N. G. Hingorani and L. Gyugyi, *Understanding FACTS. Concepts and technology of Flexible AC Transmission Systems*. New York: IEEE Press, 2000.

[2] Y. H. Song and A. T. Johns, *Flexible AC Transmission Systems (FACTS)*. London: The Institution of Electrical Engineers, 1999.

[3] G. Andersson, P. Donalek, R. Farmer, N. Hatziargyriou, I. Kamwa, P. Kundur, N. Martins, J. Paserba, P. Pourbeik, J. Sanchez-Gasca, R. Schulz, A. Stankovic, C. Taylor, and V. Vittal, “Causes of the 2003 major grid blackouts in north america and europe, and recommended means to improve system dynamic performance,” *IEEE Trans. Power Syst.*, vol. 20, no. 4, pp. 1922 – 1928, Nov. 2005.

[4] M. Klein, G. J. Rogers and P. Kundur, “A fundamental study of inter-area oscillations in power systems,” *IEEE Trans. Power Syst.*, vol. 6, no. 3, pp. 914–921, Aug. 1991.

[5] A. Domahidi, B. Chaudhuri, P. Korba, R. Majumder, and T. Green, “Self-tuning flexible ac transmission system controllers for power oscillation damping: a case study in real time,” *Generation, Transmission Distribution, IET*, vol. 3, no. 12, pp. 1079 –1089, Dec. 2009.

[6] L. Ängquist and C. Gama, “Damping algorithm based on phasor estimation,” in *Power Engineering Society Winter Meeting, 2001. IEEE*, vol. 3, 2001, pp. 1160 –1165 vol.3.

[7] M. Haque, “Improvement of first swing stability limit by utilizing full benefit of shunt facts devices,” *IEEE Trans. Power Syst.*, vol. 19, no. 4, pp. 1894 – 1902, Nov. 2004.

[8] G. Shahgholian, P. Shafaghi, S. Moalem, and M. Mahdavian, “Damping power system oscillations in single-machine infinite-bus power system using a STATCOM,” in *Computer and Electrical Engineering, 2009. ICCEE ’09. Second International Conference on*, vol. 1, Dec. 2009, pp. 130 –134.

[9] M. Beza and M. Bongiorno, “An adaptive power oscillation damping controller by STATCOM with energy storage,” *IEEE Trans. Power Syst.*, vol. 30, no. 1, pp. 484–493, Jan. 2015.

[10] ——, “Impact of different static load characteristics on power oscillation damping by shunt-connected facts devices,” in *Power Electronics and Applications (EPE), 2013 15th European Conference on*, Sept 2013, pp. 1–10.

[11] G. Cao, Z. Y. Dong, Y. Wang, P. Zhang and Y. T. Oh, “VSC based STATCOM controller for damping multi-mode oscillations,” in *Power and Energy Society General Meeting - Conversion and Delivery of Electrical Energy in the 21st Century, 2008 IEEE*, July 2008, pp. 1–8.

[12] M. Zarghami and M. Crow, “Damping inter-area oscillations in power systems by STATCOMs,” in *Power Symposium, 2008. NAPS ’08. 40th North American*, Sept. 2008, pp. 1 –6.

[13] J. Svensson, P. Jones and P. Halvarsson, “Improved power system stability and reliability using innovative energy storage technologies,” in *Proc. of* 8^{th} *IEEE International Conference on AC and DC Power Transmission*, vol. 2, Mar. 2006, pp. 220–224.

[14] Z. Yang, C. Shen, L. Zhang, M.L. Crow and S. Atcitty, “Integration of a STATCOM and battery energy storage,” *IEEE Trans. Power Syst.*, vol. 16, no. 2, pp. 254–260, May 2001.

[15] A. Arulampalam, J. B. Ekanayake and N. Jenkins, “Application study of a STATCOM with energy storage,” in *Generation, Transmission and Distribution, IEE Proceedings*, vol. 150, July 2003, pp. 373–384.

[16] N. Wade, P. Taylor, P. Lang, and J. Svensson, “Energy storage for power flow management and voltage control on an 11 kV UK distribution network,” CIRED paper 0824, Prague, Czech Republic, June 2009.

[17] P. Lang, N. Wade, P. Taylor, P. Jones, and T. Larsson, “Early findings of an energy storage practical demonstration,” in 21^{st} *International Conference on Electricity Distribution*, 2011, The Institution of Engineering and Technology, paper no. 0413.

[18] A. Adamczyk, R. Teodorescu, and P. Rodriguez, “Control of full-scale converter based wind power plants for damping of low frequency system oscillations,” in *PowerTech, 2011 IEEE Trondheim*, June 2011, pp. 1 –7.

[19] N. R. Ullah and T. Thiringer, “Variable speed wind turbines for power system stability enhancement,” *IEEE Trans. Energy Convers.*, vol. 22, no. 1, pp. 52 –60, Mar. 2007.

[20] H. Xie, “On Power-system Benefits, Main-circuit Design, and Control of Statcoms with Energy Storage,” Ph.D. dissertation, Royal Institute of Technology (KTH), Stockholm, Sweden, 2009.

[21] M. Benidris and J. Mitra, “Enhancing stability performance of renewable energy generators by utilizing virtual inertia,” in *Power and Energy Society General Meeting, 2012 IEEE*, July 2012, pp. 1–6.

[22] Q. C. Zhong and G. Weiss, “Synchronverters: Inverters that mimic synchronous generators,” *IEEE Trans. Ind. Electron.*, vol. 58, no. 4, pp. 1259–1267, April 2011.

[23] K. Kobayashi, M. Goto, K. Wu, Y. Yokomizu and T. Matsumura, “Power system stability improvement by energy storage type STATCOM,” in *Proc. of IEEE Power Tech Conference in Bologna*, vol. 2, June 2003.

[24] L. Zhang and Y. Liu, “Bulk power system low frequency oscillation suppression by FACTS/ESS,” in *Power Systems Conference and Exposition, 2004. IEEE PES*, Oct. 2004, pp. 219–226.

[25] R. Kuiava, R. A. Ramos and N. G. Bretas, “Control design of a STATCOM with energy storage system for stability and power quality improvements,” in *IEEE International Conference on Industrial Technology, 2009. ICIT 2009.*, Feb. 2009, pp. 1–6.

[26] P. Kundur, *Power System Stability and Control*. United States of America: McGraw-Hill, 1994.

[27] B. Chaudhuri, S. Ray, and R. Majumder, “Robust low-order controller design for multi-modal power oscillation damping using flexible ac transmission systems devices,” *Generation, Transmission Distribution, IET*, vol. 3, no. 5, pp. 448–459, 2009.

[28] A. Messina, O. Begovich, J. López, and E. Reyes, “Design of multiple facts controllers for damping inter-area oscillations: a decentralised control approach,” *Generation, Transmission Distribution, IET*, vol. 26, no. 1, pp. 19–29, January 2004.

[29] R. Sadikovic, P. Korba, and G. Andersson, “Application of facts devices for damping of power system oscillations,” in *Power Tech, 2005 IEEE Russia*, 2005, pp. 1–6.

[30] B. Chaudhuri, B. Pal, A. Zolotas, I. Jaimoukha, and T. Green, “Mixed-sensitivity approach to H-∞ control of power system oscillations employing multiple facts devices,” *IEEE Trans. Power Syst.*, vol. 18, no. 3, pp. 1149–1156, 2003.

[31] L. Hassan, M. Moghavvemi, H. Almurib, and K. Muttaqi, “A coordinated design of PSSs and UPFC-based stabilizer using genetic algorithm,” *IEEE Trans. Ind. Appl.*, vol. 50, no. 5, pp. 2957–2966, Sept 2014.

[32] M. Beza, “Control of Energy Storage Equipped Shunt-connected Converter for Electric Power System Stability Enhancement,” Chalmers University of Technology, Gothenburg, Sweden, Licentiate Thesis, 2012.

[33] Y. Li, N. Chiang, B.-K. Choi, Y. Chen, D.-H. Huang, and M. Lauby, “Representative static load models for transient stability analysis: development and examination,” *Generation, Transmission Distribution, IET*, vol. 1, no. 3, pp. 422–431, May 2007.

[34] V. Knyazkin, C. Canizares, and L. Soder, “On the parameter estimation and modeling of aggregate power system loads,” *IEEE Trans. Power Syst.*, vol. 19, no. 2, pp. 1023–1031, May 2004.

[35] J. Machowski, J. W. Bialek, and J. R. Bumby, *Power System Dynamics and Stability*. United States of America: John Wiley and Sons, 1997.

[36] L. Ängquist, “Synchronous Voltage Reversal Control of Thyristor Controlled Series Capacitor,” Ph.D. dissertation, Royal Institute of Technology (KTH), Stockholm, Sweden, 2002.

[37] L. Ängquist, B. Lundin and J. Samuelsson, "Power oscillation damping using controlled reactive power compensation - a comparison between series and shunt approaches," *IEEE Trans. Power Syst.*, vol. 8, no. 2, pp. 687–700, May 1993.

[38] P. Khayyer and U. Ozguner, "Decentralized control of large-scale storage-based renewable energy systems," *IEEE Trans. Smart Grid*, vol. 5, no. 3, pp. 1300–1307, May 2014.

[39] M. Beza and M. Bongiorno, "Application of recursive least squares algorithm with variable forgetting factor for frequency component estimation in a generic input signal," *IEEE Trans. Ind. Appl.*, vol. 50, no. 2, pp. 1168–1176, March 2014.

[40] R. Sadikovic, P. Korba, and G. Andersson, "Application of FACTS devices for damping of power system oscillations," in *Power Tech, 2005 IEEE Russia*, 2005, pp. 1–6.

[41] K. J. Åström and B. Wittenmark, *Adaptive Control*. Addison-Wesley, 1995.

[42] A. Vidal, F. Freijedo, A. Yepes, P. Fernandez-Comesañ anda, J. Malvar, O. Lopez, and J. Doval-Gandoy, "A fast, accurate and robust algorithm to detect fundamental and harmonic sequences," in *Energy Conversion Congress and Exposition (ECCE), 2010 IEEE*, Sept. 2010, pp. 1047 –1052.

[43] H.-S. Song, K. Nam, and P. Mutschler, "Very fast phase angle estimation algorithm for a single-phase system having sudden phase angle jumps," in *Industry Applications Conference, 2002. 37th IAS Annual Meeting. Conference Record of the*, vol. 2, Oct. 2002, pp. 925 –931 vol.2.

[44] P. Rodriguez, A. Luna, I. Candela, R. Mujal, R. Teodorescu, and F. Blaabjerg, "Multiresonant frequency-locked loop for grid synchronization of power converters under distorted grid conditions," *IEEE Trans. Ind. Electron.*, vol. 58, no. 1, pp. 127 –138, Jan. 2011.

[45] A. Timbus, T. Teodorescu, F. Blaabjerg, M. Liserre, and P. Rodriguez, "PLL algorithm for power generation systems robust to grid voltage faults," in *Power Electronics Specialists Conference, 2006. PESC '06. 37th IEEE*, June 2006, pp. 1 –7.

[46] P. Rodriguez, R. Teodorescu, I. Candela, A. Timbus, M. Liserre, and F. Blaabjerg, "New positive-sequence voltage detector for grid synchronization of power converters under faulty grid conditions," in *Power Electronics Specialists Conference, 2006. PESC '06. 37th IEEE*, June 2006, pp. 1 – 7.

[47] L. Ängquist and M. Bongiorno, "Auto-normalizing phase-locked loop for grid-connected converters," in *Energy Conversion Congress and Exposition, 2009. ECCE 2009. IEEE*, Sept. 2009, pp. 2957 –2964.

[48] L. Harnefors, "Modeling of three-phase dynamic systems using complex transfer functions and transfer matrices," *IEEE Trans. Ind. Electron.*, vol. 54, no. 4, pp. 2239–2248, Aug. 2007.

[49] M. Gustafsson and N. Krantz, "Voltage collapse in power systems," Chalmers University of Technology, Gothenburg, Sweden, Licentiate Thesis TR-215L, Dec. 1995.

[50] DS1103 PPC Controller Board, *Hardware Installation and Configuration*. Germany: dSPACE GmbH, 2009.

[51] N. Mohan, T. M. Underland, and W. P. Robbins, *Power Electronics: Converters, Applications and Design*. United States of America: John Wiley and Sons, 2003.

[52] M. Bongiorno, “Control of voltage source converters for voltage dip mitigation in shunt and series configurations,” Chalmers University of Technology, Gothenburg, Sweden, Licentiate Thesis, 2004.

[53] R. Teodorescu, F. Blaabjerg, M. Liserre, and P. Loh, “Proportional-resonant controllers and filters for grid-connected voltage-source converters,” *Electric Power Applications, IEE Proceedings*, vol. 153, no. 5, pp. 750 –762, september 2006.

[54] J. Hu, Y. He, L. Xu, and D. Zhi, “Predictive current control of grid-connected voltage source converters during,” *Power Electronics, IET*, vol. 3, no. 5, pp. 690 –701, september 2010.

[55] L. Harnefors, L. Zhang, and M. Bongiorno, “Frequency-domain passivity-based current controller design,” *Power Electronics, IET*, vol. 1, no. 4, pp. 455 –465, Dec. 2008.

[56] L. Harnefors and H.-P. Nee, “Model-based current control of ac machines using the internal model control method,” *IEEE Trans. Ind. Appl.*, vol. 34, no. 1, pp. 133 –141, Jan./Feb. 1998.

[57] M. Bongiorno, “On Control of Grid-Connected Voltage Source Converters,” Ph.D. dissertation, Chalmers University of Technology, Gothenburg, Sweden, 2007.

[58] Y. Quan, H. Nian, J. Hu, and J. Li, “Improved control of the grid-connected converter under the harmonically distorted grid voltage conditions,” in *Electrical Machines and Systems (ICEMS), 2010 International Conference on*, Oct. 2010, pp. 204 –209.

[59] P. Mattavelli, “Synchronous-frame harmonic control for high-performance ac power supplies,” *IEEE Trans. Ind. Appl.*, vol. 37, no. 3, pp. 864 –872, May/June 2001.

[60] E. Adzic, D. Marcetic, V. Katic, and M. Adzic, “Grid-connected voltage source converter operation under distorted grid voltage,” in *Power Electronics and Motion Control Conference (EPE/PEMC), 2010 14th International*, Sept. 2010, pp. T11–44 –T11–51.

[61] P. Chapman and S. Sudhoff, “A multiple reference frame synchronous estimator/regulator,” *IEEE Trans. Energy Convers.*, vol. 15, no. 2, pp. 197 –202, June 2000.

[62] M. Bongiorno and J. Svensson, “Voltage dip mitigation using shunt-connected voltage source converter,” *IEEE Trans. Power Electron.*, vol. 22, no. 5, pp. 1867 –1874, Sept. 2007.

[63] A. Arsoy, Liu Yilu, P. F. Ribeiro and F. Wang, “Power converter and SMES in controlling power system dynamics,” in *Industry Applications Conference, 2000*, vol. 4, Oct. 2000, pp. 2051–2057.

[64] H. Xie, L. L. Ängquist, and H.-P. Nee, "Design study of a converter interface interconnecting an energy storage with the dc-link of a VSC," in *Innovative Smart Grid Technologies Conference Europe (ISGT Europe), 2010 IEEE PES*, oct. 2010, pp. 1 –9.

[65] Q. C. Zhong, P. L. Nguyen, Z. Ma, and W. Sheng, "Self-synchronized synchronverters: Inverters without a dedicated synchronization unit," *IEEE Trans. Power Electron.*, vol. 29, no. 2, pp. 617–630, Feb 2014.

[66] L. Zhang, L. Harnefors, and H.-P. Nee, "Power-synchronization control of grid-connected voltage-source converters," *IEEE Trans. Power Syst.*, vol. 25, no. 2, pp. 809 –820, may 2010.

[67] R. Sadikovic, "Use of FACTS Devices for Power Flow Control and Damping of Oscillations in Power Systems," Ph.D. dissertation, Swiss Federal Institute of Technology, Zurich, Switzerland, 2006.

[68] "IEEE recommended practice for excitation system models for power system stability studies," *IEEE Std 421.5-1992*, 1992.

Appendix A

Transformations for three-phase systems

A.1 Introduction

In this appendix, the necessary transformations from three-phase quantities to vectors in stationary $\alpha\beta$ and rotating dq reference frames and vise versa will be described.

A.2 Transformation of three-phase quantities to vectors

A three-phase system constituted by three quantities $v_1(t)$, $v_2(t)$ and $v_3(t)$ can be transformed into a vector $\underline{v}_{\alpha\beta}(t)$ in a stationary complex reference frame, usually called $\alpha\beta$-frame, by applying the transformation defined by (A.1).

$$\underline{v}_{\alpha\beta}(t) = v_\alpha(t) + \mathrm{j}v_\beta(t) = K_{\mathrm{tran}}(v_1(t) + v_2(t)e^{\mathrm{j}\frac{2}{3}\pi} + v_3(t)e^{\mathrm{j}\frac{4}{3}\pi}) \tag{A.1}$$

The transformation constant K_{tran} can be chosen to be $\sqrt{2/3}$ or $2/3$ to ensure power invariant or amplitude invariant transformation respectively between the two systems. Equation (A.1) can be expressed in matrix form as in (A.2).

$$\begin{bmatrix} v_\alpha(t) \\ v_\beta(t) \end{bmatrix} = T_{32} \begin{bmatrix} v_1(t) \\ v_2(t) \\ v_3(t) \end{bmatrix} \tag{A.2}$$

where the matrix T_{32} is given by

$$T_{32} = K_{\mathrm{tran}} \begin{bmatrix} 1 & -\frac{1}{2} & -\frac{1}{2} \\ 0 & \frac{\sqrt{3}}{2} & -\frac{\sqrt{3}}{2} \end{bmatrix}$$

The inverse transformation, assuming no zero-sequence, is given by (A.3).

$$\begin{bmatrix} v_1(t) \\ v_2(t) \\ v_3(t) \end{bmatrix} = T_{23} \begin{bmatrix} v_\alpha(t) \\ v_\beta(t) \end{bmatrix} \tag{A.3}$$

with the matrix T_{23} given by

$$T_{23} = \frac{1}{K_{\text{tran}}} \begin{bmatrix} \frac{2}{3} & 0 \\ -\frac{1}{3} & \frac{1}{\sqrt(3)} \\ -\frac{1}{3} & -\frac{1}{\sqrt(3)} \end{bmatrix}$$

A.3 Transformation between fixed and rotating coordinate systems

For the vector $\underline{v}_{\alpha\beta}(t)$ rotating in the $\alpha\beta$-frame with the angular frequency $\omega(t)$ in the positive (counter-clockwise) direction, a dq-frame that rotates in the same direction with the same angular frequency $\omega(t)$ can be defined. The vector $\underline{v}_{\alpha\beta}(t)$ will appear as fixed vectors in this rotating reference frame. A projection of the vector $\underline{v}_{\alpha\beta}(t)$ in the d-axis and q-axis of the dq-frame gives the components of the vector in the dq-frame as illustrated in Fig.A.1.

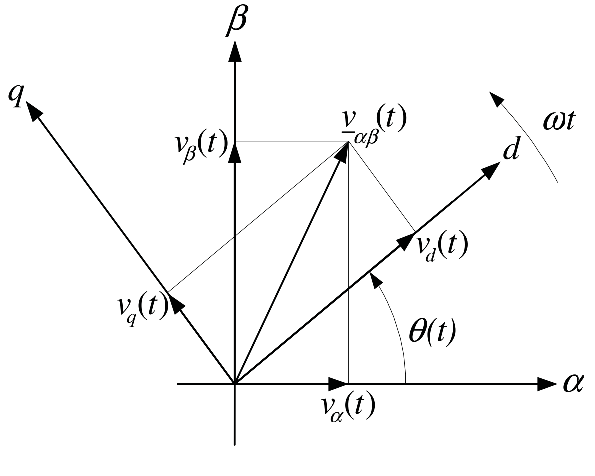

Figure A.1: Relation between $\alpha\beta$-frame and dq-frame.

The transformation can be written in vector form as in (A.4).

$$\underline{v}_{dq}(t) = v_d(t) + \mathrm{j}v_q(t) = \underline{v}_{\alpha\beta}(t)e^{-\mathrm{j}\theta(t)} \tag{A.4}$$

with the angle $\theta(t)$ in Fig.A.1 given by

$$\theta(t) = \theta_0 + \int_0^t \omega(\tau)d\tau$$

The inverse transformation, from the rotating dq-frame to the fixed $\alpha\beta$-frame is defined by (A.5).

$$\underline{v}_{\alpha\beta}(t) = \underline{v}_{dq}(t)e^{\mathrm{j}\theta(t)} \tag{A.5}$$

In matrix form, the transformation between the fixed $\alpha\beta$-frame and rotating dq-frame can be written as in (A.6) - (A.7).

$$\begin{bmatrix} v_d(t) \\ v_q(t) \end{bmatrix} = R(-\theta(t)) \begin{bmatrix} v_\alpha(t) \\ v_\beta(t) \end{bmatrix} \tag{A.6}$$

$$\begin{bmatrix} v_\alpha(t) \\ v_\beta(t) \end{bmatrix} = R(\theta(t)) \begin{bmatrix} v_d(t) \\ v_q(t) \end{bmatrix} \tag{A.7}$$

where the projection matrix is

$$R(\theta(t)) = \begin{bmatrix} \cos(\theta(t)) & -\sin(\theta(t)) \\ \sin(\theta(t)) & \cos(\theta(t)) \end{bmatrix}$$

Appendix B

Parameters of the test systems

B.1 Introduction

In this appendix, the system data for the simulation in Chapter 7 will be described.

B.2 Two-area four machine test system data

The parameters of the system in Fig. 7.1 will b given in this section [26]. It consists of two similar areas each with ratings of 900 MVA and 20 kV. The mechanical damping of all the generators are assumed zero and all other parameters on the rated MVA and kV base are given by

Armature resistance and leakage reactance (pu)	$R_{\mathrm{a}} = 0.0025$	$X_{\mathrm{l}} = 0.2$
d- and q-axis synchronous reactance (pu)	$X_{\mathrm{d}} = 1.8$	$X_{\mathrm{q}} = 1.7$
d- and q-axis transient reactance (pu)	$X'_{\mathrm{d}} = 0.3$	$X'_{\mathrm{q}} = 0.55$
d- and q-axis sub-transient reactance (pu)	$X''_{\mathrm{d}} = 0.25$	$X''_{\mathrm{q}} = 0.25$
d- and q-axis open-circuit transient time constant (s)	$T'_{\mathrm{d0}} = 8$	$T'_{\mathrm{q0}} = 0.4$
d- and q-axis open-circuit sub-transient time constant (s)	$T''_{\mathrm{d0}} = 0.03$	$T''_{\mathrm{q0}} = 0.05$
Inertia constant for G_1 and G_2 (s)	$H_{\mathrm{g1}} = 6.5$	$H_{\mathrm{g2}} = 6.5$
Inertia constant for G_3 and G_4 (s)	$H_{\mathrm{g3}} = 6.175$	$H_{\mathrm{g4}} = 6.175$

All generators are equipped with a high transient gain Thyristor exciter and a PSS. The gain and time constant of the excitation control are 200 and 0.001, respectively. On the other hand, the parameters of the PSS similar to the one in Fig. 3.6 and that uses a speed feedback of the corresponding generators are given by $G_{\mathrm{LL}} = 5$, $T_{\mathrm{w}} = 10$, $T_{\mathrm{L}} = 0.015$, $T_1 = 0.05$, $T_2 = 0.02$, $T_3 = 3$ and $T_4 = 5.4$.

Each step-up transformer rated 20/230 kV and 900 MVA has an impedance of $j0.15$ pu. The length and parameters of the transmission lines on a 100 MVA, 230 kV base are given by

series impedance, z (pu/km)	$0.0001 + j0.001$
shunt admittance, y (pu/km)	$j0.00175$
length of lines 5 - 6 and 10 - 11 (km)	25
length of lines 6 - 7 and 9 - 10 (km)	10
length of lines 7 - 8 and 8 - 9 (km)	110

The system is initially operating with Area 1 exporting 400 MW to Area 2 and the generating units are loaded as

	Active power (MW)	Reactive power (MVAr)	Terminal voltage (pu)
G_1	700	185	$1.03\angle 20.2°$
G_2	700	235	$1.01\angle 10.5°$
G_3	719	176	$1.03\angle -6.8°$
G_4	700	202	$1.01\angle -17.0°$

Loads are connected in the system at Buses 7 and 9. The active power component (P_{L}) and reactive power component (Q_{L}) of the loads have a constant current and constant impedance characteristics, respectively. Moreover, shunt capacitors for reactive power support (Q_{C}) are connected at the two Buses. The magnitude of the loads are given by

	Bus 7	Bus 9
Active power load, P_{L} (MW)	967	1767
Reactive power load, Q_{L} (MVAr)	100	100
Reactive power support, Q_{C} (MVAr)	200	350

B.3 IEEE 10 Generator 39 Bus test system data

Using a base value of 100 MVA and 20/230 kV, the parameters of the system in Fig. 7.22, which consists of 10 Generators and 39 Buses will be given in this section. This system is well known as the New-England power system, where Generator 1 represents an aggregate of a large number of generators [67].

The armature resistance and mechanical damping of all generators are assumed to be zero and all other parameters for the generators are given in Table B.1. The IEEE type DC1A excitation system [26][68] is used for all the generators and the parameters are as given in Table B.2. Generator 2 is chosen as the swing node and the load data at various buses is given in Table B.3. Note that all the loads are assumed to have a constant power characteristics. Finally, the transmission line data is given in Table B.4.

TABLE B.1. PARAMETERS OF THE GENERATORS

	X_l	X_d	X'_d	T'_d0	X_q	X'_q	T'_q0	H_g	E_t	P_g
G_1	0.003	0.02	0.006	7.0	0.019	0.008	0.7	500	1.03	10.0
G_2	0.035	0.295	0.0697	6.56	0.282	0.170	1.5	30.3	0.982	-
G_3	0.0304	0.2495	0.0531	5.7	0.237	0.0876	1.5	35.8	0.983	6.50
G_4	0.0295	0.262	0.0436	5.69	0.258	0.166	1.5	28.6	0.997	6.32
G_5	0.054	0.67	0.132	5.4	0.62	0.166	0.44	26.0	1.011	5.08
G_6	0.0224	0.254	0.05	7.3	0.241	0.0814	0.4	34.8	1.050	6.50
G_7	0.0322	0.295	0.049	5.66	0.292	0.186	1.5	26.4	1.063	5.60
G_8	0.028	0.29	0.057	6.7	0.280	0.0911	0.41	24.3	1.0278	5.40
G_9	0.0298	0.2106	0.057	4.79	0.205	0.0587	1.96	34.5	1.0265	8.30
G_{10}	0.0125	0.1	0.031	10.2	0.069	0.008	0.0	42.0	1.045	2.50

TABLE B.2. PARAMETERS OF THE EXCITATION SYSTEM FOR THE GENERATORS

	K_A	T_A	V_RMIN	V_RMAX	K_E	T_E	A_EX	B_EX	K_F	T_F
G_1	0	0	0	0	0	0	0	0	0	0
G_2	6.2	0.05	-1.0	1.0	0	0.405	0.0470	2.0252	0.057	0.5
G_3	5.0	0.06	-1.0	1.0	0	0.5	0.0015	1.6988	0.08	1.0
G_4	5.0	0.06	-1.0	1.0	0	0.5	0.0003	2.0787	0.08	1.0
G_5	40.0	0.02	-10.0	10.0	0	0.785	0.0000	1.0384	0.03	1.0
G_6	5.0	0.02	-1.0	1.0	0	0.471	0.0002	1.6608	0.0754	1.246
G_7	40.0	0.02	-6.5	6.5	0	0.73	0.0328	0.2830	0.03	1.0
G_8	5.0	0.02	-1.0	1.0	0	0.528	0.0003	1.8645	0.0854	1.26
G_9	40.0	0.02	-10.5	10.5	0	1.4	0.0483	0.1953	0.03	1.0
G_{10}	5.0	0.06	-1.0	1.0	0	0.25	0.0008	1.5249	0.04	1.0

TABLE B.3. LOAD BUS DATA

Bus	Active power	Reactive power	Bus	Active power	Reactive power
12	0.075	0.88	26	1.39	0.17
15	3.20	1.53	27	2.81	0.755
16	3.29	0.32	28	2.06	0.276
18	1.58	0.30	29	2.835	0.269
20	6.28	1.03	32	3.22	0.024
21	2.74	1.15	33	5.00	1.84
23	2.47	0.846	36	2.338	0.84
24	3.086	-0.92	37	5.22	1.76
25	2.24	0.472			

TABLE B.4. TRANSMISSION LINE DATA

From Bus	To Bus	Resistance	Reactance	Susceptance	Tap ratio
1	38	0.0010	0.0250	1.2000	0.00
1	39	0.0010	0.0250	0.7500	0.00
2	35	0.0000	0.0250	0.0000	1.070
3	30	0.0000	0.0200	0.0000	1.070
4	19	0.0007	0.0142	0.0000	1.070
5	20	0.0009	0.0180	0.0000	1.009
6	22	0.0000	0.0143	0.0000	1.025
7	23	0.0005	0.0272	0.0000	0.00
8	25	0.0006	0.0232	0.0000	1.025
9	29	0.0008	0.0156	0.0000	1.025
10	31	0.0000	0.0181	0.0000	1.025
11	12	0.0016	0.0435	0.0000	1.006
11	30	0.0004	0.0043	0.0729	0.00
11	35	0.0007	0.0082	0.1389	0.00
12	13	0.0016	0.0435	0.0000	1.006
13	14	0.0009	0.0101	0.1723	0.00
13	30	0.0004	0.0043	0.0729	0.00
14	15	0.0018	0.0217	0.3660	0.00
14	33	0.0008	0.0129	0.1382	0.00
15	16	0.0009	0.0094	0.1710	0.00
16	17	0.0007	0.0089	0.1342	0.00
16	19	0.0016	0.0195	0.3040	0.00
16	21	0.0008	0.0135	0.2548	0.00
16	24	0.0003	0.0059	0.0680	0.00
17	18	0.0007	0.0082	0.1319	0.00
17	27	0.0013	0.0173	0.3216	0.00
18	32	0.0011	0.0133	0.2138	0.00
19	20	0.0007	0.0138	0.0000	1.060
21	22	0.0008	0.0140	0.2565	0.00
22	23	0.0006	0.0096	0.1846	0.00
23	24	0.0022	0.0350	0.3610	0.00
25	26	0.0032	0.0323	0.5130	0.00
25	31	0.0070	0.0086	0.1460	0.00
26	27	0.0014	0.0147	0.2396	0.00
26	28	0.0043	0.0474	0.7802	0.00
26	29	0.0057	0.0625	1.0290	0.00
28	29	0.0014	0.0151	0.2490	0.00

Continued to next page

Continued from previous page

From Bus	To Bus	Resistance	Reactance	Susceptance	Tap ratio
31	32	0.0013	0.0151	0.2572	0.00
31	39	0.0035	0.0411	0.6987	0.00
32	33	0.0013	0.0213	0.2214	0.00
33	34	0.0008	0.0128	0.1342	0.00
34	35	0.0002	0.0026	0.0434	0.00
34	37	0.0008	0.0112	0.1476	0.00
35	36	0.0006	0.0092	0.1130	0.00
36	37	0.0004	0.0046	0.0780	0.00
37	38	0.0023	0.0363	0.3804	0.00